Mechanochemical synthesis and structural characterization of bimetallic and hybrid tetrahydridoborates

Burazer, Sanja

Doctoral thesis / Disertacija

2019

Degree Grantor / Ustanova koja je dodijelila akademski / stručni stupanj: **University of Zagreb, Faculty of Science / Sveučilište u Zagrebu, Prirodoslovno-matematički fakultet**

Permanent link / Trajna poveznica: https://urn.nsk.hr/urn:nbn:hr:217:131290

Rights / Prava: In copyright/Zaštićeno autorskim pravom.

Download date / Datum preuzimanja: **2025-01-10**

University of Zagreb
FACULTY OF SCIENCE

Sanja Burazer

MECHANOCHEMICAL SYNTHESIS AND STRUCTURAL CHARACTERIZATION OF BIMETALLIC AND HYBRID TETRAHYDRIDOBORATES

DOCTORAL THESIS

Zagreb, 2019

Sveučilište u Zagrebu

PRIRODOSLOVNO-MATEMATIČKI FAKULTET

Sanja Burazer

MEHANOKEMIJSKA SINTEZA I STRUKTURNA KARAKTERIZACIJA DIMETALNIH I HIBRIDNIH TETRAHIDRIDOBORATA

DOKTORSKI RAD

Mentor: dr. sc. Jasminka Popović

Zagreb, 2019.

University of Zagreb

FACULTY OF SCIENCE

Sanja Burazer

MECHANOCHEMICAL SYNTHESIS AND STRUCTURAL CHARACTERIZATION OF BIMETALLIC AND HYBRID TETRAHYDRIDOBORATES

DOCTORAL THESIS

Supervisor: Dr. Jasminka Popović

Zagreb, 2019.

Acknowledgements

Usually there are people with whom you have to work, but I am rarely lucky person who works on RBI with beautiful people and great collaborators which, if I had a chance, would pick even by myself: Martina Vrankić, Marijana Jurić and Lidija Androš Dubraja. Thank you for making our office such a great place.

I would like to thank to whole group of Prof. Radovan Černy which made my stay in his laboratory in Geneva feel like home. Lidija Kanižaj, thank you for making our mornings brighter, full of calmness and joy. Abra Penezić and Claribel Dominguez, thank you for making Geneva even better place. All the working days during experiments in Ljubljana would be endlessly long without laugh and company of my dear friends and colleagues Petra Kuzman and Marija Živković. Thank you all for your positive energy. I am thankful to my all dear friends who were great life support and support during my PhD, especially to Ivana and Mirna, Tea, Anita, Daniela.

I am thankful to my sister for encouraging me to be better and stronger and pushing me forward in her unique way.

There are no words which can describe my gratitude to my parents, both here and somewhere in the sky. Thank you for selfless support you gave me through every mine decision, for unconditional love and faith in me, for making me what I am today, for everything!

All my success would be impossible without endless love and support I had from my wonderful husband Mirko. Thank you for all your patience and understanding throughout my studies and PhD. Above all, thank you for reaching the greatest life success with me, having our beautiful girl, Tonka, the meaning of my life.

Contents

Sveučilište u Zagrebu   Doktorska disertacija

Prirodoslovno-matematički fakultet

Kemijski odsjek

SAŽETAK

MEHANOKEMIJSKA SINTEZA I STRUKTURNA KARAKTERIZACIJA DIMETALNIH I HIBRIDNIH TETRAHIDRIDOBORATA

Sanja Burazer

Zavod za fiziku materijala

Institut Ruđer Bošković

Bijenička cesta 54, 10000 Zagreb, Hrvatska

Istražene su mehanokemijske reakcije metalnih tetrahidridoborata i metalnih imidazolata te strukturne značajke dobivenih produkata. Rendgenska difrakcija u polikristalu na laboratorijskom difraktometru te *in-situ* visokotemperaturna difrakcija na sinkrotronskoj liniji najvažnije su eksperimentalne tehnike korištene u ovom radu, a neki uzorci dodatno su okarakterizirani pomoću nuklearne magnetske rezonancije u čvrstom stanju. Poboljšan je sintetski put priprave hibridne metalohidridne organske mreže, Li_2ImBH_4, nastale kombinacijom molekulskih građevnih blokova litijevog borohidrida, $LiBH_4$, i litijevog imidazolata, LiIm, uz visok stupanj konverzije. Otkrivena je nova skupina dimetalnih magnezijevih imidazolata, prvih imidazolatnih spojeva koji sadrže alkalijske i zemnoalkalijske metalne centre, $AMgIm_3$ (A = Na, K). Priređeni su novi dimetalni spojevi manganovog imidazolata s alkalijskim metalnim centrima, $AMnIm_3$ (A = Na, K). Određivanje struktura novih spojeva provedeno je iz difrakcijskh podataka polikristalnih uzoraka pomoću metoda u direktnom prostoru. Otkriven je nov način pripreme kristalnog magnezijevog imidazolata, $MgIm_2$, te visokotemperaturnog (HT) polimorfa natrijevog imidazolata, HT-NaIm, čija struktura je određena iz difrakcijskih podataka jediničnog kristala.

(116 stranica, 75 slika, 27 tablica, 157 literaturnih navoda, jezik izvornika: engleski)

University of Zagreb   Doctoral Thesis

Faculty of Science

Department of Chemistry

ABSTRACT

MECHANOCHEMICAL SYNTHESIS AND STRUCTURAL CHARACTERIZATION OF BIMETALLIC AND HYBRID TETRAHYDRIDOBORATES

Sanja Burazer

Division for Materials Physics

Ruđer Bošković Institute

Bijenička cesta 54, HR-10000 Zagreb, Croatia

Mechanochemical reactions of metal tetrahydridoborates and metal imidazolates, as well as the structural characteristics of the obtained products were investigated. X-ray powder diffraction, both at the laboratory diffractometer and *in-situ* high-temperature diffraction under the synchrotron radiation was mainly used experimental technique. NMR was used as a complementary technique. Combination of molecular building blocks of lithium borohydride, $LiBH_4$, and lithium imidazolate, LiIm, led to the formation of hybrid Li_2ImBH_4 with a high conversion rate. New compounds containing alkali and alkaline earth metal centers, $AMgIm_3$ (A = Na, K), were found. New compounds of manganese imidazolates with alkaline metal centers were prepared, $AMnIm_3$ (A = Na, K). Crystal structure determination of the new compounds was carried out from the powder diffraction data using methods in the direct space. New methods of preparation of crystalline magnesium imidazolate, $MgIm_2$, and high-temperature polymorph of sodium imidazolate, HT-NaIm, are described. Structure of HT-NaIm was determined from the single crystal diffraction data.

(116 pages, 75 figures, 27 tables, 157 references, original in English)

Sveučilište u Zagrebu
Prirodoslovno-matematički fakultet
Kemijski odsjek

Doktorska disertacija

PROŠIRENI SAŽETAK

Zbog štetnih utjecaja na okoliš, posljednjih godina pokušava se smanjiti uporaba fosilnih goriva. Inicijativom Europske komisije o klimatskim promjenama utvrđeno je da razvoj novih održivih energijskih sustava, sposobnih zadovoljiti sve veće potrebe za energijom, predstavlja jedan od najvećih izazova današnjice.[I] Materijalom budućnosti često se smatra vodik, jer se može jednostavno proizvesti iz vode i drugih obnovljivih izvora energije. Zbog male mase i reaktivnosti, glavni izazov vodikove ekonomije je njegovo sigurno i efikasno skladištenje. Uobičajeno, vodik se skladišti u spremnicima pod tlakom ili pri niskoj temperaturi, kao plin ili ukapljeni vodik, dok se veća sigurnost i efikasnost skladištenja može postići kemijskim vezanjem ili fizikalnom adsorpcijom vodika u različite materijale u čvrstom stanju.[II,III]

Hidridi predstavljaju dobro istraženu skupinu spojeva u kojima se vodik skladišti kemisorpcijski. Hidridi mogu vezati veliku količinu vodika, skladištiti ga, ali i reverzibilno otpustiti pri blagim uvjetima. Zbog visoke gustoće apsorpcije vodika, među hidridima se posebno ističe skupina kompleksnih hidrida, tetrahidridoborati opće formule $M(BH_4)_n$, koji se sastoje od metalnog kationa, M^{n+}, i borohidridnog aniona, BH_4^-. Najefikasniji u ovoj grupi su metalni tetrahidridoborati iz skupine alkalijskih i zemnoalkalijskih metala, [IV,V,VI,VII] pogotovo mješoviti koji sadrže i prijelazne metale d-bloka.[VIII] Tetrahidridoborati se uobičajeno, ali i u

[I] I. A. Züttel, u A. Züttel, A. Borgschulte i L. Schlapbach (ed.), *Hydrogen as a Future Energy Carrier*, Vol. 1, Wiley–VCH Verlag GmbH&Co. KGaA, Weinheim, 2008, stranica 1–6.
[II] R. Mohtadi i S.–I. Orimo, *Nat. Rev. Mater.* **2** (2016) 16091.
[III] https://www.energy.gov/eere/fuelcells/hydrogen–storage (pristupano 15. ožujka 2019.)
[IV] B.D. James i M.G.H. Wallbridge, *Prog. Inorg.Chem.* **11** (1970) 99–231.
[V] T.J. Marks i J.R. Kolb, *Chem. Rev.* **77** (1977) 263–293.
[VI] W. Grochala i P.P. Edwards, *Chem. Rev.* **104** (2004) 1283–1315.
[VII] Y. Filinchuk, D. Chernyshov i V. Dmitriev, u U.B. Demirci i P. Miele (Ed.), *Boron hydrides, high potential hydrogen storage materials*, Nova Publishers, New York, 2010.

[VIII] D.B. Ravnsbæk, Y. Filinchuk, R. Černý i T.R. Jensen, *Z. Kristallogr.* **225** (2010) 557–569.

literaturi gotovo bez iznimke, nazivaju borohidridima, stoga će taj naziv biti korišten u daljnjem tekstu ove disertacije. Magnezijev borohidrid, γ-Mg(BH$_4$)$_2$,[IX] ima poroznu strukturu, sa šupljinama dovoljno velikima za prihvat male molekule, poput vode. S druge strane, manganov borohidrid, Mn(BH$_4$)$_2$, različiti dimetalni borohidridi, A$_n$Li$_m$(BH$_4$)$_{n+m}$ (A = Rb, Cs)[X] te prvi priređeni trimetalni borohidrid, Li$_3$MZn$_5$(BH$_4$)$_{15}$ (M = Mg, Mn),[XI] iako kod njih nije uočena poroznost, posjeduju jake i usmjerene veze metal-BH$_4$ koje određuju strukturu.

Metaloorganske mreže, tzv. MOF-ovi (*eng*. Metal-Organic Frameworks, MOFs), trodimenzionalni su koordinacijski polimeri građeni od metalnih kationa ili blokova metalnih kationa te organskih poveznica (liganada) i predstavljaju skupinu spojeva koja se istražuje zbog mogućnosti adsorpcije vodika.[XII]

Posebnu skupinu koordinacijskih mreža čine metalohidridne organske mreže[XIII] (*eng*. Metal-Hydride-Organic-Frameworks, HOFs), novi hibridni materijali dizajnirani kombinacijom molekulskih građevnih jedinica kompleksnih hidrida male molekulske mase s organskim poveznicama, ligandima, razvijenima primarno za sintezu koordinacijskih mreža. Fleksibilnost borohidridnog aniona može omogućiti nove koordinacije metalnih kationa, drukčije od onih uobičajeno nađenih u koordinacijskim mrežama. Dodatne mogućnosti za strukturnu raznolikost pruža korištenje usmjerenih organskih liganada, primjerice imidazolata, izonikotinata te njihovih derivata. U ovom doktoratu izbor liganada je pripao imidazolatima, prije svega zbog sličnosti kristalnih struktura; kut metal-imidazolat-metal iznosi 145°, što odgovara kutu metal-borohidrid-metal u molekuli Mg(BH$_4$)$_2$.[IX] Prvi, i jedini dosad publicirani primjer hibridnog spoja koji sadrži i borohidridni i organski imidazolatni ligand je Li$_2$ImBH$_4$.[XIV]

Nerijetko je željene produkte teško, pa čak i nemoguće sintetizirati u otopini, zbog čega se sve više razvijaju sintetske metode temeljene na mehanokemijskim reakcijama, budući da su čišće, brže i često učinkovitije. Uključuju mehaničko mljevenje za pripravu različitih spojeva, bilo

---

[IX] Y. Filinchuk, B. Richter, T.R. Jensen, V. Dmitriev, D. Chernyshov i H. Hagemann, *Angew. Chem. Int. Ed.* **50** (2011) 11162–11166.

[X] R. Černý, neobjavljeni rezultati.

[XI] R. Černý, P. Schouwink, Y. Sadikin, K. Stare, Ĺ. Smrčok, B. Richter i T.R. Jensen, Inorg. Chem. **52** (2013) 9941–9947.

[XII] U. Eberle, M. Felderhoff i F. Schüth, *Angew. Chem. Int. Ed.* **48** (2009) 6608–6630.

[XIII] Projekt „Metal–Hydride Organic Frameworks (HOF)–new solids for gas adsorption and separation", Geneva, 2015.

[XIV] F. Morelle, V. Ban i Y. Filinchuk, Towards hydridic nanoporous frameworks: the first imidazolate–borohydride compound Li$_2$ImBH$_4$ (Im = [C$_3$H$_3$N$_2$]$^-$). International symposium on metal–hydrogen systems (MH2014); Manchester, UK, July 20–25, 2014.

organskih, supramolekulskih ili organometalnih spojeva.[XV] Najveća prednost je smanjena uporaba otapala i samim time manje zagađenje okoliša. Zbog nemogućnosti izravnog praćenja promjena na atomsko-molekulskoj razini, mehanizmi i trajanje mehanokemijskih reakcija još su uvijek uvelike nepoznati. Površina reaktanata mehanički se aktivira u kontaktu s kuglicom, nastaju različite vrste defekata koje dovode do fizikalno-kemijskih reakcija.[XVI] Postoje dvije vrste mehanokemijskih reakcija: suho mljevenje (*eng.* neat grinding, NG) i mljevenje potpomognuto tekućinom (*eng.* liquid assisted grinding, LAG).[XV,XVII] Mljevenje se najčešće provodi u kugličnim mlinovima, a u ovoj doktorskoj disertaciji korišten je planetarni mlin.[XVIII]

Metalni borohidridi nalaze se u fokusu mnogih istraživanja zbog svoje strukturne fleksibilnosti, kemijske reaktivnosti, različitih kemijskih i fizikalnih svojstava te primjene u skadištenju vodika, baterijskim sustavima i ionskim vodičima.[IX,XIX–XXIV] Kod monometalnih borohidrida alkalijskih i zemnoalkalijskih metala otkriveno je više polimorfnih struktura, do čijih faznih pretvorbi najčešće dolazi pod utjecajem temperature ili tlaka.[XIX] Dosad istraženi dimetalni i trimetalni borohidridi sadrže alkalijske i zemnoalkalijske metale, najčešće s prijelaznim metalima, primjerice $AZn(BH_4)_3$ (A = Na, K), $AZn_2(BH_4)_5$ (A = Li, Na), $Li_3MZn_5(BH_4)_{15}$ (M = Mg, Mn).[XXXII–XXXIV,XLIV, XLV] Svi borohidridi izuzetno su osjetljivi na zrak i vlagu, stoga je sinteze nužno provoditi pažljivo i u inertnom okruženju.

Hibridni materijali posjeduju karakteristike zasebnih komponenti, čime se pospješuje mogućnost njihove primjene i povećava učestalost korištenja. Hibridni borohidridi mogu se prirediti anionskom zamjenom borohidridnog aniona s nekim drugim anionom ili modifikacijom borohidrida s neutralnim molekulama (npr. NH_3, NH_3BH_3, N_2H_4).[XXV] Hibridni Li_2ImBH_4[XIV] kristalizira s rompskom ćelijom, u prostornoj grupi *Imma* tijekom mehanokemijske reakcije LiIm i $LiBH_4$ s malim količinama otapala ili prilikom termičke obrade pri 100 °C. Imidazolatni anion okružen je sa četiri litijeva atoma, po dva vezana na svakom atomu dušika smještena ispod i iznad ravnine aromatskog prstena. Duljina Li–N veze

[XV] S.L. James, C.J. Adams,C. Bolm, D. Braga, P. Collier, T. Friščić, F. Grepioni, K.D.M. Harris, G. Hyett, W. Jones, A. Krebs, J. Mack, L. Maini, A.G. Orpen, I.P. Parkin, W.C. Shearouse, J.W. Steedk i D.C. Waddelli, *Chem. Soc. Rev.* **41** (2012) 413–447.

[XVI] V.V. Boldyrev, *Russ. Chem. Rev.* **75** (2006) 177–189.

[XVII] T. Friščić, I. Halasz, V. Štrukil, M. Eckert–Maksić i R.E. Dinnebierd, *Croat. Chem. Acta* **85** (2012) 367–378.

[XVIII] https://www.fritsch–international.com/sample–preparation/milling/planetary–mills/details/product/pulverisette–7–premium–line/ (pristupano 18. ožujka 2019.)

[XIX] M. Paskevicius, L.H. Jepsen, P. Schouwink, R. Černý, D.B. Ravnsbæk, Y. Filinchuk, M. Dornheim, F. Besenbacher i T.R. Jensen, *Chem. Soc. Rev.* **46** (2017) 1565–1634.

iznosi 2,085 Å. BH$_4$ skupina koordinirana je sa četiri litijeva atoma u kvadratno-planarnom okruženju. Litijev kation veže se na dva imidazolata i dvije borohidridne skupine u deformiranoj tetraedarskoj koordinaciji.[XIV] Kako priređeni spoj nije potpuno čist, već se radi o 75 %-tnoj konverziji, i to uz upotrebu otapala ili visoke temperature, važno je ispitati nove sintetske puteve kojima bi se navedeni spoj moglo prirediti.

Važno je naglasiti da imidazolati, reaktanti u spomenutim rekacijama s borohidridima, također predstavljaju skupinu spojeva koja je unatoč izuzetno bogatoj strukturnoj raznolikosti, nedovoljno istražena. Dimetalni imidazolati u literaturi izuzetno su rijetki, a među poznatim spojevima primjerice nisu zabilježene strukture dimetalnih imidazolata s alkalijskim i zemnoalkalijskim metalima.[XX,XXI,XXII,XXIII] Alkalijski imidazolati (LiIm, NaIm, KIm) formiraju guste i hiperkoordinirane strukture, a koordinacijski zahtjevi metalnih kationa rastu s povećanjem njihovog ionskog radijusa. Tako Li$^+$ preferira heteroleptične strukture, dok K$^+$ koordinaciju na imidazolatni prsten radi preko π-veza. Zanimljivo, magnezijev imidazolat stvara poroznu zeolitnu mrežu.[XXIV,XXV] Priprava alkalijskih i zemnoalkalijskih imidazolata nedovoljno je istražena. Primjerice, magnezijev imidazolat dobiva se mehanokemijskom reakcijom, ali u amorfnom obliku stoga je od interesa istražiti alternativne puteve sinteze koji će omogućiti bržu i efikasniju pripravu zemnoalkalijskih imidazolatnih mreža.

Rendgenska difrakcija jedna je od najvažnijih metoda istraživanja strukture tvari, analitička, nedestruktivna metoda za identifikaciju i kvantitativnu karakterizaciju različitih kristalnih formi i faza prisutnih u krutim uzorcima.[XXVI] Elektronska gustoća može se rekonstruirati iz difrakcijske slike dobivene raspršenjem rendgenskih zraka na periodično raspoređenim atomima u kristalu. Tako se iz prostornog rasporeda i intenziteta raspršenih zraka mogu dobiti informacije o periodičnom rasporedu atoma, drugim riječima, difrakcijska slika kristalnog materijala Fourierova je transformacija uređene atomske strukture u recipročnom prostoru. To

---

[XX] Y.–Q. Tian, H.–J. Xu, Y.–Z. Li i X.–Z. You, *Z. Anorg. Allg. Chem.* **630** (2004) 1371–1373.

[XXI] D.M. Schubert, M.Z. Visi i C.B. Knobler, *Main Group Chem.* **7** (2008) 311–322.

[XXII] J.A. Graden, L.M. Ellerby, J.A. Roe i J.S. Valentine, *J. Am. Chem. Soc*. **116** (1994) 9743–9744.

[XXIII] N.T.T. Nguyen, T.N.H. Lo, J. Kim, H.T.D. Nguyen, T.B. Le, K.E. Cordova i H. Furukawa, *Inorg. Chem.* **55** (2016) 6201–6207.

[XXIV] F. Morelle, Hybrid hydridic frameworks by the combination of complex hydrides and nitrogen–based organic ligands. Doktorska disertacija, Univerité catholique de Louvain, Louvain–la–Neuve, 2017.

[XXV] D.A. Safin, K. Robeyns i Y. Filinchuk, *Acta Crystallogr., Sect. A: Found. Adv.* **72** (2016) 402.

[XXVI] V.K. Pecharsky i P.Y. Zavalij, *Fundamentals of powder diffraction and structural characterization of materials, Springer, New York, 2009.*

znači da se trodimenzionalan raspored atoma u ćeliji, direktna slika kristala, može rekonstruirati nakon što se difrakcijsku sliku transformira u direktni prostor pomoću Fourierovih transformacija, no za taj korak potrebno je znati apsolutne vrijednosti strukturnih amplituda, ali i njihove faze. Strukturne amplitude mogu se jednostavno odrediti iz difrakcije u monokristalu i polikristalu, ali se faze gube tijekom eksperimenta, zbog čega moraju biti povraćene odgovarajućim numeričkim tehnikama.[XXXII] Nakon provedenih Fourierovih transformacija dobiva se mapa elektronske gustoće čiji maksimumi prikazuju položaj atoma što omogućuje određivanje kristalne strukture.

Određivanje kristalne strukture iz difrakcije u polikristalu nerijetko je značajno zahtjevniji postupak u odnosu na određivanje strukture iz monokristala. S druge strane, unatoč složenijem postupku, difrakcija u polikristalu nezaobilazna je metoda jer omogućava strukturnu karakterizaciju različitih uzoraka koje nije moguće prirediti u obliku monokristala. Ostale prednosti difrakcije u polikristalu su jednostavnost pripreme uzorka, brže prikupljanje difrakcijskih podataka te mogućnost analize višefaznih uzoraka.[XXVII]

Rezultati koji se mogu izvući iz difraktograma praha ovise, prije svega, o kvaliteti difrakcijske snimke. Bez premca, najbolju kvalitetu podataka pružaju difrakcijska mjerenja provedena pomoću sinkrotronskog zračenja budući da se postiže bolja kutna rezolucija i vrlo brzo se prikupljaju podaci. Intenzitet sinkrotronskog zračenja najmanje je pet puta jači, a često i značajno mnogostruko jači u odnosu na laboratorijske izvore zračenja. Zbog kratkog vremena prikupljanja podataka moguće je snimiti i uzorke osjetljive na ionizirajuće zračenje. [XXVIII]

Unatoč stalnom napretku u metodologiji i algoritmima za određivanje kristalne strukture iz polikristalnih materijala, to je i dalje vrlo zahtjevan, a ponekad i nedostižan proces. Rješavanje kristalne strukture iz polikristala sastoji se od nekoliko koraka: prikupljanje podataka, indeksiranje difrakcijske slike, određivanje prostorne grupe, dekompozicija (raščlanjivanje) difrakcijske slike (kada je potrebno), određivanje strukture, optimizacija modela (ako je nepotpun) te završno strukturno utočnjavanje.[XXXII] Indeksiranje i određivanje prostorne grupe često su "uska grla procesa" i kako bi se odredila točna struktura, neophodno je da ovi koraci

---

[XXVII] Q.Q. Pan, P. Guo, J. Duan, Q. Cheng i H. Li, *Chin Sci Bull* **57** (2012) 3867–3871.
[XXVIII] https://www.psi.ch/sites/default/files/import/sls–techno–trans–ag/HomeEN/ScienceOmega3–ESS–August7th–2.pdf (pristupano 24. ožujka 2019)

budu precizni i točni.[XXIX,XXX] Postoji veliki broj različitih algoritama za indeksiranje difrakcijskih slika pa ako početni pokušaj bude neuspješan, dobro je pokušati s drugim algoritmom. Najčešće korišteni programi za indeksiranje su: DICVOL04,[XXXI] N-TREOR,[XXXII] McMaille,[XXXIII] FOX,[XXXIV,XXXV] EXPO2004,[XXXVI] Topas,[XXXVII] X-Cell.[XXXVIII] Određivanje prostorne grupe temelji se na pravilima pogašenja određenih difrakcijskih linija, no preklapanje difrakcijskih maksimuma nerijetko dovodi do nepouzdanosti u procjeni pogašenja. Metode rješavanja mogu se općenito podijeliti na: *i*) metode u recipročnom prostoru koje uključuju ekstrakciju intenziteta (LeBailovom[XXXIX] ili Pawleyevom[XL] metodom), a koriste se kada su dostupni podaci visoke rezolucije koji omogućuju točno određivanje faza, *ii*) metode modeliranja u direktom prostoru (metode globalne optimizacije: simulirano aniliranje i paralelno temperiranje). Procedura završava kada se postigne najbolje slaganje računate i eksperimentalne difrakcijske slike. Konačno, struktura se utočnjava Rietveldovom metodom, metodom najmanjih kvadrata koja se provodi s ciljem minimiziranja razlike između eksperimentalnog i izračunatog difrakcijskog profila.[XLI] Difrakcijska slika polikristalnog uzorka sadrži i informacije o njegovoj mikrostrukturi; pomoću Warren-Averbachove metode proširenja linija moguće je odrediti veličinu kristalita (veličinu koherentne difrakcijske domene) i udio deformacije kristalne rešetke.[XLII]

Nuklearna magnetska rezonancija u čvrstom stanju (NMR) metoda je karakterizacije koja pruža uvid u strukturu na atomskoj razini. NMR u čvrstom stanju, kao metoda komplementarna rendgenskoj strukturnoj analizi, oslanja se na postojanje dalekodosežnog uređenja dajući sliku prosječne kristalne strukture. NMR-spektroskopija vrlo je važna za određivanje odnosa između

[XXIX] A. Meden, *Croat. Chem. Acta* **71** *(*1998) 615–633.
[XXX] R. Černý, *Crystals* **7** (2017) 142–152.
[XXXI] A. Boultif, D. Louër, *J. Appl. Crystallogr.* **37** (2004) 724–731.
[XXXII] A. Altomare, C. Giacovazzo, A. Guagliardi, A.G.G. Moliterni, R. Rizzi i P.–E. Werner, *J. Appl. Crystallogr.* **33** (2000) 1180–1186.
[XXXIII] A. Le Bail, *Powder Diffraction* **19** (2004) 249–254.
[XXXIV] V. Favre–Nicolin i R. Černý, *J. Appl. Crystallogr.* **35** (2002) 734–743.
[XXXV] R. Černý, V. Favre–Nicolin, J. Rohlíček, M. Hušak, Z. Matej i R. Kužel, *CPD Newsl.* **35** (2007) 16–19.
[XXXVI] A. Altomare, M.C. Burla, M. Camalli, B. Carrozzini, G.L. Cascarano, C. Giacovazzo, A. Guagliardi, A.G.G. Moliterni, G. Polidori i R. Rizzi, *J. Appl. Crystallogr.* **32** (1999) 339–340.
[XXXVII] R. W. Cheary i A.A. Coelho, *J. Appl. Crystallogr.* **25** (1992) 109–121.
[XXXVIII] M.A. Neumann, *J. Appl. Crystallogr.* **36** (2003) 356–365.
[XXXIX] A. LeBail, H. Duray i J. L. Fourquet, *Mat. Res. Bull.* **23** (1988) 447–452.
[XL] G. S. Pawley, *J. Appl. Crystallogr.* **14** (1981) 357–361.
[XLI] R. A. Young (Ed.), *The Rietveld Method,* University Press, Oxford, 1993.
[XLII] B.E. Warren i B.L. Averbach, *J. Appl. Phys.* **21** (1950) 595–599.

strukture i funkcionalnosti. Njome je moguće dokazati ili opovrgnuti predloženi model dobiven rendgenskom analizom. Također se koristi za određivanje jakosti interakcija između adsorbiranih molekula i MOF-matrica.[XLIII]

Svi uzorci opisani u disertaciji priređeni su mehanokemijskom sintezom, mljevenjem pomoću kuglica u mlinu *Planetary Micro Mill Fritsch Pulverisette 7 premium line*. Za mljevenje su korištene dvije posudice od nehrđajućeg čelika u koje su stavljene kuglice od nehrđajućeg čelika promjera 5 mm, mase 0,5 g i reaktanti. Omjer mase kuglica i mase reaktanata bio je 25:1. Kako bi se izbjeglo pregrijavanje sustava, mljevenje je provedeno u ciklusima od 10 min mljevenja i 5 min pauze. Kako bi se optimizirale sinteze, korištena je različita duljina i trajanje (2–9 h), brzina mljevenja (400–700 rpm) te raličiti omjeri reaktanata. Rukovanje reaktantima i produktima je zbog osjetljivosti borohidrida na vlagu provedeno u gloveboxu marke mBRAUN, punjenom dušikom (FKKT, Ljubljana) ili argonom (Geneva).

Korišteni borohidridi $M(BH_4)_n$ (M = Li, Na, K, Mg, Mn), $ZnCl_2$ i otapala: tetrahidrofuran (THF), diklorometan (DCM), acetonitril (ACN), dimetilsulfoksid (DMSO), kloroform (CF) analitičke čistoće su komercijalni (Sigma Aldrich), a organski su imidazolati $M(Im)_n$ (M = Li, Na, K, Mg), pripremljeni na Sveučilištu u Louvainu, u Belgiji.[XXX]

Oznake uzoraka i detalji o reakcijskim uvjetima navedeni su u tablici I.

[XLIII] G. Mali, in F. Zafar i E. Sharmin, *Looking into Metal–Organic Frameworks with Solid–State NMR Spectroscopy*, IntechOpen, 2016.

Tablica I. Oznake uzoraka i reakcijski uvjeti.

Uzorak	Reakcija	Reakcijski uvjeti
P1	$NaBH_4$:$ZnCl_2$ = 3:1	suho mljevenje, 600 r/min, 2h
P2	2:1	suho mljevenje, 600 r/min, 2h
P3		P1 centrifugiran s DCM
P4		P1 centrifugiran sa CF
1D1	$NaZn(BH_4)_3$:NaIm = 1:1	suho mljevenje, 600 r/min, 2h
1D2	$NaZn(BH_4)_3$:NaIm = 2:1	suho mljevenje, 600 r/min, 2h
1D3	$NaZn(BH_4)_3$:NaIm = 3:1	suho mljevenje, 600 r/min, 2h
1D4	$NaZn(BH_4)_3$:NaIm = 1:2	suho mljevenje, 600 r/min, 2h
1D5	$NaZn(BH_4)_3$:NaIm = 1:3	suho mljevenje, 600 r/min, 2h
1D6	$NaZn(BH_4)_3$:NaIm = 1:1	suho mljevenje, 600 r/min, 4h
1D7	$NaZn(BH_4)_3$:NaIm = 1:1	suho mljevenje, 600 r/min, 9h
1S1	1:1	mljevenje s otapalom THF, 600 r/min, 2h
1S1-DCM		1S1 centrifugiran s DCM
1S1-CF		1S1 centrifugiran sa CF
1S2	1:1	mljevenje s otapalom ACN, 600 r/min, 2h
1S3	1:1	mljevenje s otapalom DMSO, 600 r/min, 2h
1S3a		1S3 nakon 3 mjeseca starenja
2D1	$NaBH_4$:$ZnCl_2$:NaIm = 1:1:1	suho mljevenje, 600 r/min, 2h
2D2	$NaBH_4$:$ZnCl_2$:NaIm = 1:1:3	suho mljevenje, 600 r/min, 2h
3D1	$LiBH_4$:LiIm = 3:1	suho mljevenje, 600 r/min, 2h
3D2	$NaBH_4$:NaIm = 1:6	suho mljevenje, 600 r/min, 2h
3D3	$NaBH_4$:NaIm = 1:4	suho mljevenje, 600 r/min, 2h
3D4	$NaBH_4$:NaIm = 1:2	suho mljevenje, 600 r/min, 2h
3D5	$NaBH_4$:NaIm = 1:1	suho mljevenje, 600 r/min, 2h
3D6	$NaBH_4$:NaIm = 4:1	suho mljevenje, 600 r/min, 2h
3D7	$NaBH_4$:NaIm = 6:1	suho mljevenje, 600 r/min, 2h
3D8	$NaBH_4$:NaIm = 6:1	suho mljevenje, 600 r/min, 2h
3S1	$NaBH_4$:NaIm = 1:1+50 μl ACN	mljevenje s otapalom ACN, 600 r/min, 2h
3S2	$NaBH_4$:NaIm = 1:1+50 μl DMSO	mljevenje s otapalom DMSO, 600 r/min, 2h
3D9	KBH_4:KIm = 1:6	suho mljevenje, 600 r/min, 2h
3D10	KBH_4:KIm = 1:2	suho mljevenje, 600 r/min, 2h
3D11	KBH_4:KIm = 1:1	suho mljevenje, 600 r/min, 2h
4D1	$Mg(BH_4)_2$:NaIm = 1:1	suho mljevenje, 550 r/min, 3h
4D2	$Mg(BH_4)_2$:NaIm = 1:2	suho mljevenje, 550 r/min, 3h
4D3	$Mg(BH_4)_2$:NaIm = 1:6	suho mljevenje, 550 r/min, 3h
4D4	$Mg(BH_4)_2$:LiIm = 1:1	suho mljevenje, 550 r/min, 3h
4D5	$Mg(BH_4)_2$:LiIm = 1:2	suho mljevenje, 550 r/min, 3h
4D6	$Mg(BH_4)_2$:KIm = 1:2	suho mljevenje, 550 r/min, 3h
4D7	$Mg(BH_4)_2$:KIm = 1:6	suho mljevenje, 550 r/min, 3h
5D1	$Mg(BH_4)_2$:NaIm = 1:1	suho mljevenje, 550 r/min, 3h
5D2	$Mg(BH_4)_2$:KIm = 1:1	suho mljevenje, 550 r/min, 3h
5D3	$Mg(BH_4)_2$:LiIm = 1:1	suho mljevenje, 550 r/min, 3h
6D1	$Mn(BH_4)_2$:NaIm = 1:6	suho mljevenje, 550 r/min, 3h
6D2	$Mn(BH_4)_2$:NaIm = 1:2	suho mljevenje, 550 r/min, 3h
6D3	$Mn(BH_4)_2$:KIm = 1:6	suho mljevenje, 550 r/min, 3h
6D4	$Mn(BH_4)_2$:KIm = 1:2	suho mljevenje, 550 r/min, 3h
6D5	$Mn(BH_4)_2$:LiIm = 1:6	suho mljevenje, 550 r/min, 3h
6D6	$Mn(BH_4)_2$:LiIm = 1:2	suho mljevenje, 550 r/min, 3h

Produkti reakcija preliminarno su kvalitativno i kvantitativno analizirani pomoću rendgenske difrakcije u polikristalu na difraktometrima PANalytical X'Pert PRO MPD ili STOE IPDS-P s CuKα1 izvorom zračenja ($\lambda = 1{,}54060$ Å). Uzorci su zbog osjetljivosti na zrak montirani u 0,5– 1 mm staklene ili borosilikatne kapilare unutar suhe komore, a podaci su prikupljeni pri sobnoj temperaturi (*eng.* room temperature, RT) u rasponu od 2 do 100° 2θ, 40 s/korak. Monokristalni uzorci mjereni su na difraktometru STOE IPDS-II s MoKα zračenjem ($\lambda = 0{,}7107$ Å). Višefazni spojevi, amorfni uzorci, kao i uzorci za koje je nakon laboratorijskih PXRD (*eng.* powder X-ray diffraction) mjerenja utvrđeno da sadrže nove faze, analizirani su nadalje pomoću *in-situ* SR-PXRD (*eng.* synchrotron radiation powder X-ray diffraction) mjerenja na sinkrotronu SNBL, BM01, ESRF, Grenoble, Francuska. $\lambda_1 = 0{,}8187$ Å, $\lambda_2 = 0{,}7149$ Å, rotacija uzorka 0– 40°, vrijeme izloženosti rendgenskom zračenju 40 s, udaljenost uzorka od detektora 200–400 mm, grijanje uzoraka od sobne temperature do 250–500 °C s brzinom grijanja 5–10 °C/min. Strukture novih spojeva riješene su upravo iz sinkrotronskih podataka. Indeksiranje, određivanje prostorne grupe, kao i sam proces rješavanja strukture provedeni su koristeći program FOX,[XL,XLI] upotrebom metoda u direktnom prostoru, i to metode paralelnog aniliranja. Kod uzoraka 6D1–6D6 korištena je metoda najmanjih kvadrata, jer je paralelno aniliranje vodilo u lažni minimum nudeći krivu strukturu kao konačno rješenje.[XXXVI] Rietveldovo utočnjavanje provedeno je u programu Fullprof[XLIV] utočnjavajući parametre ćelije, oblik difrakcijskog maksimuma, pozadinske parametre te u nekim slučajevima i temperaturne faktore. Imidazolatni anion tretiran je kao kruto tijelo, a mijenjani su jedino njegov položaj i orijentacija u ćeliji. Mikrostrukturni parametri, veličina kristalita i deformacija rešetke određeni su koristeći algoritam implemetiran u program HighScore Xpert plus. Za vizualizaciju kristalnih struktura korišten je program VESTA.[XLV] NMR mjerenja provedena su na NMR-sustavu 600 MHz Varian opremljenim s 3,2 mm Varian T3 HX MAS sondom. Mjeren je MAS-spektar (*eng.* magic angle spinning) i dvodimenzijski *spin-diffusion* spektar.

Osnovna ideja tijekom planiranja eksperimentalnog dijela doktorata je optimizirati već poznate sinteze. Promjenom reakcijskih uvjeta cilj je postići bolju usmjerenost liganada, ispitati utjecaj različitih uvjeta na promjene u sastavu produkata, na vezanje i na termalna svojstva, te se želi

[XLIV] J. Rodriguez-Carvajal, *Phys. B* **192** (1993) 55−69.
[XLV] K. Momma i F. Izumi, *J. Appl. Crystallogr.* **44** (2011) 1272−1276.

pojednostavniti reakcijske puteve. Cilj je bio istražiti mogućnost nastajanja spojeva u kojima je borohidridni anion ionskom izmjenom zamijenjen drugim anionom, kao što je, primjerice, imidazolat.

Dimetalni borohidridi priređeni su suhim mljevenjem $NaBH_4$ i $ZnCl_2$ u omjeru 2:1 i 3:1, kao što je prikazano na shemi I.
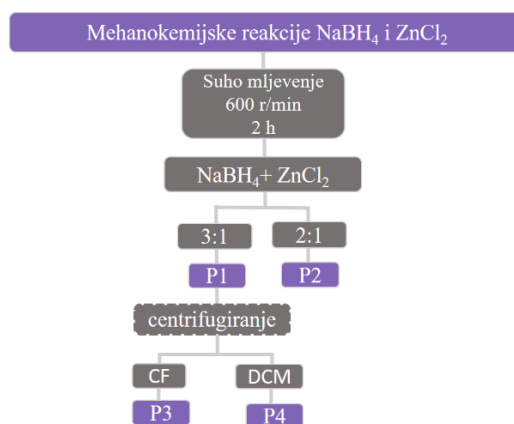
Shema I. Mehanokemijske reakcije natrijevog borohidrida i cinkovog klorida.

Rezultati fazne analize pokazali su da uzorak P1 sadrži $NaZn(BH_4)_3$ te natrijev klorid. Uzorak P2 dodatno sadrži i $NaZn_2(BH_4)_5$ te neidentificiranu kristalnu fazu, zbog čega je kao prekursor za daljnje reakcije s NaIm korišten samo prekursor P1 dobiven mehanokemijskom reakcijom iz omjera reaktanata 3:1. Pokušaj uklanjanja NaCl iz smjese proveden je centrifugiranjem uzorka P1 s kloroformom (CF) i diklorometanom (DCM), što je rezultiralo djelomičnim raspadom glavnog produkta $NaZn(BH_4)_3$, ali ne i uklanjanjem NaCl. S obzirom da se pokazalo da je NaCl inertan u reakcijama dimetalnih prekursora s imidazolatima odustalo se od daljnjih pokušaja uklanjanja natrijevog klorida.

Kako bi se ispitala reaktivnost borohidridnog prekursora $NaZn(BH_4)_3$ i NaIm, priređena je serija uzoraka mehanokemijskim reakcijama navedenih reaktanata u različitim omjerima. Ispitane su reakcije suhog mljevenja, ali i mljevenja potpomognutog otapalom (THF, ACN, DMSO), kao što je prikazano na shemi II.

Mehanokemijske reakcije NaZn(BH₄)₃ P1 i NaIm

| Suho mljevenje 600 r/min 2 h | Suho mljevenje 600 r/min 4 h | Suho mljevenje 600 r/min 9 h | Mljevenje s tekućinom 600 r/min 2 h |

1:1 — 1D1 2:1 — 1D2 3:1 — 1D3 1:2 — 1D4 1:3 — 1D5

1:1 — 1D6

1:1 — 1D7

THF ACN DMSO
1:1 — 1S1 1:1 — 1S2 1:1 — 1S3
centrifugiranje starenje 1S3a
DCM CF
1S1-DCM 1S1-CF
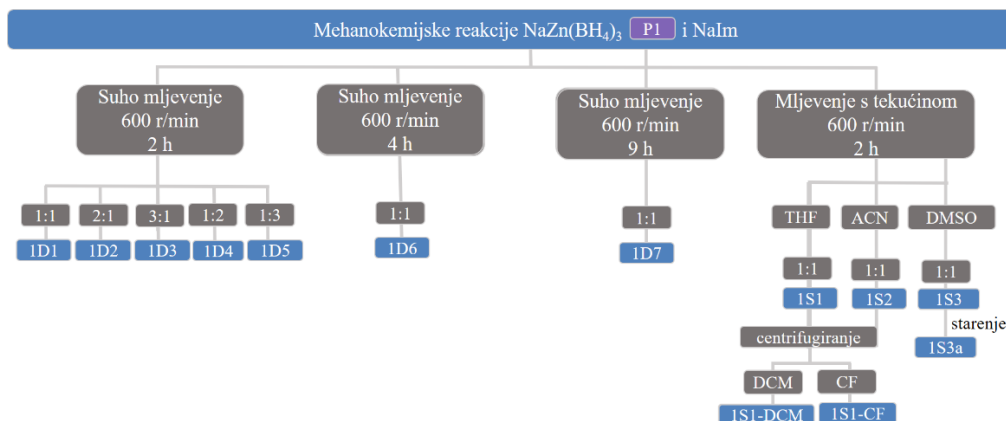
Shema II. Mehanokemijske reakcije dimetalnog borohidridnog prekursora i natrijevog imidazolata.

Produkti provedenih reakcija većinom su neizreagirani reaktanti (NaCl, NaZn(BH₄)₃) ili produkti raspada dimetalnog prekursora (NaBH₄). U reakcijama sa suviškom NaBH₄, NaCl može formirati čvrstu otopinu sastava $NaCl_{0.5}(BH_4)_{0.5}$. U uzorku 1D5 primijećen je značajan udio amorfne faze, stoga su dodatno provedena sinkrotronska difrakcijska mjerenja pri visokim temperaturama. Nađeno je da pri 165 °C dolazi do kristalizacije iz amorfnog produkta pri čemu nastaje cinkov imidazolat koji kristalizira kao zeolitna imidazolatna mreža ZIF (IMIDZB01).

Kod otapalom potpomognutog mljevenja, kada je kao otapalo korišten DMSO (shema II) (uzorak 1S3), nastao je nepoznati spoj, zboč čega su dodatno provedena sinkrotronska difrakcijska mjerenja pri visokim temperaturama, kao i nuklerana magnetska rezonancija u čvrstom stanju. Ispitivan je svježe priređeni uzorak i uzorak koji je tri mjeseca stajao u staklenoj posudici u suhoj komori (1S3a). Strukturna analiza pokazala je postojanje dviju novih faza, od kojih je jedna stabilna do 60 °C, a druga do 132 °C, a istovremeno s nestankom druge nepoznate faze dolazi do kristalizacije ZIF-a (IMIDZB01). Budući da kod odstajalog uzorka (1S3a) nije bila prisutna niti jedna od dviju nepoznatih faza iz uzorka 1S3, može se zaključiti da se one raspadaju tijekom stajanja pri sobnoj temperaturi prilikom čega nastaje nova faza. Faza prisutna u uzorku 1S3a stabilna je do 160 °C. Indeksiranje je provedeno u programu FOX,[LXIII,LXIV] kao i određivanje prostorne grupe; nađeno je da spoj kristalizira u prostornoj grupi *P*2/c s parametrima ćelije $a = 13{,}20675(2)$ Å, $b = 12{,}6095(3)$ Å, $c = 18{,}2684(7)$ Å i $\beta = 93{,}641°$. Kako algoritmi implementirani u programe EXPO[LXV] i FOX[LXIII,LXIV] nisu mogli ponuditi zadovoljavajući strukturni model, uzorak je dodatno istražen NMR mjerenjima u čvrstom stanju. Signali protona iz imidazolata u ¹H NMR spektru nalaze se na oko 7 ppm. Ovi protoni nalaze se prostorno vrlo blizu protonu s rezonancijom na oko 0 ppm koji se pripisuje protonskim jezgrama iz borohidridne skupine. Ti rezultati sugeriraju da je nastala faza vrlo vjerojatno

hibridni spoj koji sadrži oba aniona. Štoviše, protoni koji potječu od DMSO nisu spregnuti ni s jednim drugim protonom (u 2D-spektru nema odgovarajućih sprežnih signala koji se ne nalaze na dijagonali) što sugerira da se DMSO ne nalazi u istoj kristalnoj strukturi koja sadrži imidazolatni i borohidridni anion, već se vrlo vjerojatno nalazi u amorfnoj fazi. Zaključno, suho mljevenje dimetalnog borohidridnog prekursora s imidazolatima rezultira raspadom prekursora i amorfizacijom sustava koji zagrijavanjem najčešće daje ZIF i neizreagirani $NaBH_4$. Prema rezultatima NMR u čvrstom stanju, mljevenje potpomognuto otapalom može dovesti do stvaranja hibridnog spoja koji sadrži borohiridni i imidazolatni anion.

Nakon ispitanih reakcija dimetalnih borohidridnih prekursora s imidazolatima, fokus istraživanja preusmjeren je na manje kompleksne sustave koji uključuju reakcije monometalnih borohidrida MBH_4 (M = Na, K, Li) i alkalijskih imidazolata MIm (M = Na, K, Li) u različitim omjerima, kako je prikazano na shemi III.
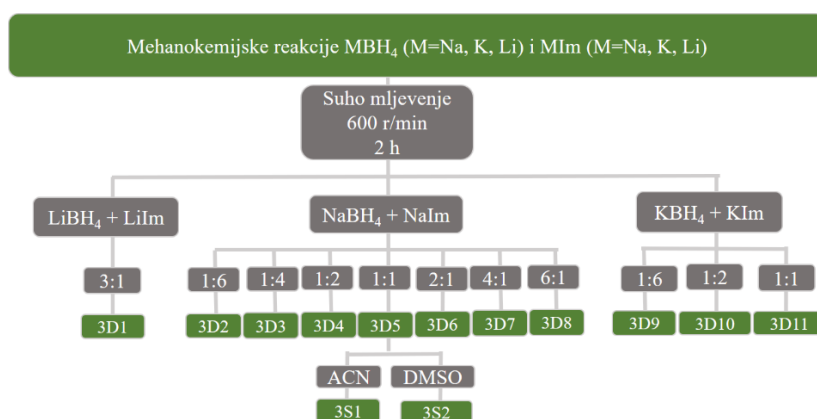
Shema III. Mehanokemijske reakcije monometalnih alkalijskih borohidrida i alkalijskih imidazolata.

Mehanokemijska reakcija između $LiBH_4$ i LiIm u omjeru 3:1 (uzorak 3D1) rezultirala je nastankom hibridnog spoja Li_2ImBH_4, čija je određena struktura jedina do danas poznata koja sadrži borohidridni i imidazolatni anion. Novi sintetski put za dobivanje Li_2ImBH_4 koji je pronađen tijekom izrade ove disertacije značajno je jednostavniji od dosada poznatih te ne zahtijeva uporabu otapala niti termičke obrade.[XIV]

Tijekom mehanokemijskih reakcija $NaBH_4$ i NaIm u različitim omjerima (uzorci 3D2-3D8) uočeno je stvaranje nove kristalne faze, prisutne u svim uzorcima neovisno o početnom omjeru rekatanata. Pored nove kristalne faze, uzorci 3D2–3D8 sadrže i određenu količinu neizgreagiranih komponenata te amorfne faze. Uzorak 3D5, priređen iz omjera $NaBH_4$:NaIm = 1:1, pokazao je najmanju količinu amorfne faze te je dodatno ispitan NMR-om

u čvrstom stanju. Zanimljivo, na NMR spektrima uočava se jedan [11]B signal koji potječe od borovog atoma u NaBH$_4$ te samo dva [23]Na signala što bi odgovaralo natrijevim atomima u NaIm i NaBH$_4$. Bilo je potrebno odrediti elemente prisutne u trećoj, novoj kristalnoj fazi koja je uočena u difrakcijskoj snimci. Činjenica da NMR-spektri ukazuju na prisutstvo samo dvije faze koje sadrže natrijev atom, bila je indikacija da tijekom mjerenja (koje uključuje vrtnju te posljedično porast temperature) dolazi do fazne promjene jedne od faza, ili NaIm ili NaBH$_4$, odnosno da nije nastao hibridni spoj.

S ciljem određivanja kristalne strukture novog spoja, visokotemperaturna difrakcijska mjerenja pomoću sinkrotronskog zračenja provedena su na uzorku 3D5; ustanovljeno je da nepoznata faza odgovara visokotemperaturnom (*eng.* high temperature) polimorfu natrijevog imidazolata (HT-NaIm). Udio visokotemperaturnog polimorfa raste postepeno s porastom temperature, faznom pretvorbom iz niskotemperaturnog polimorfa NaIm pri oko 190 °C. Priređeni HT-NaIm tali se oko 210 °C i rekristalizira ispod 190 °C tijekom hlađenja.

Zanimljiv efekt primijećen je tijekom rekristalizacije visokotemperaturnog polimorfa NaIm; rastom kristalnih zrna dolazi do pojave difuznog raspršenja oko prve difrakcijske linije, koje se daljnjim hlađenjem pretvara u zrakaste pruge, umjesto difrakcijskih prstenova. Uzorak se morfološki znatno promijenio, iz finog praha u zrnati uzorak s mnoštvom velikih monokristala. Ovakva difuzna značajka tipična je za prisutnost defekata ili nereda u strukturi. Iako je difrakcijska slika prikupljena pri 139 °C uspješno indeksirana u trigonskoj ćeliji, značajno preklapanje difrakcijskih linija, kao i neuređenost u strukturi, onemogućili su uspješno određivanje strukture, zbog čega je uzorak priređen u obliku monokristala. Praškasti uzorak 3D5 zagrijavan je u kapilari na uljnoj kupelji pri 190 °C 10 min. Sporo hlađenje rastaljenog uzorka na sobnu temperaturu dovodi do kristalizacije monokristala. Nađeno je da visokotemperaturni polimorf NaIm kristalizira u trigonskoj prostornoj grupi, $P3_112$, s parametrima ćelije $a = 10{,}3164(4)$ Å i $c = 21{,}4192(11)$ Å, potvrđujući točnost procesa indeksiranja difrakcijske slike iz polikristalnog uzorka. Struktura je riješena kao racemični sraslac, što općenito znači da se radi o agregatu u kojem su različite domene srasle zajedno prema specifičnoj simetrijskoj operaciji, odnosno zakonu sraštanja. Postupak rješavanja sastoji se od rotacije, refleksije ili inverzije difrakcijskih slika dobivenih od različitih domena jedne u odnosu na drugu, te težinske prilagodbe svake slike ovisno o količini pojedine domene prisutne u kristalu. Difrakcijsku sliku dobivenu tijekom snimanja ovakvog uzorka čine sve navedene komponente. Sraslace se može podijeliti u dvije kategorije; onu u kojoj su svi refleksi zahvaćeni

preklapanjem i onu u kojoj je samo dio refleksa pod utjecajem preklapanja. Tijekom utočnjavanja strukture samo su Na1 i Na2 položaji utočnjeni kao potpuno zaposjednuti, dok su preostali atomi prisutni u omjeru 73/27 (slika Ia).

Struktura sadrži dva različita lanca s vijčanom osi 3_1 duž osi *c,* međusobno premoštena formirajući sloj paralelan osi *b*. Prvi lanac sadrži atome Na1 i Na2, a drugi Na3 i Na4. Ponavljajuća jedinka može se opisati kao trimerna jedinica formule Na_3Im_6 koja je sastavljena od dva Na1 i jednog Na2 atoma u slučaju prvog lanca te dva Na3 atoma i jednog Na4 atoma u slučaju drugog lanca (slika Ib). Natrijevi atomi nalaze se u različitim okruženjima; Na2 i Na4 oktaedarski su koordinirani dušikovim atomima iz šest imidazolatnih prstenova, dok su Na1 i Na3 koordinirani sa četiri imidazolatna liganda, stvarajući izrazito deformirani tetraedar. Različita okruženja imidazolatnih prstenova prikazana su na slici Ib. Imidazolatni prsten ImA ponaša se kao premosni ligand prema četiri natrijeva atoma, Na1 i Na2. Imidazolat ImB postiže još kompleksnije okruženje, atomi Na2, Na3, Na4 te dva atoma Na1 nalaze se na udaljenostim u rasponu od 2,4–2,8 Å od imidazolatnih dušikovih atoma. ImC je okružen s Na1, Na2, Na4 i dva Na3 atoma na sličnim udaljenostima kao i u slučaju ImB. Slojevi su međusobno spojeni u smjeru osi *a* tvoreći vrlo složenu trodimenzijsku mrežu.
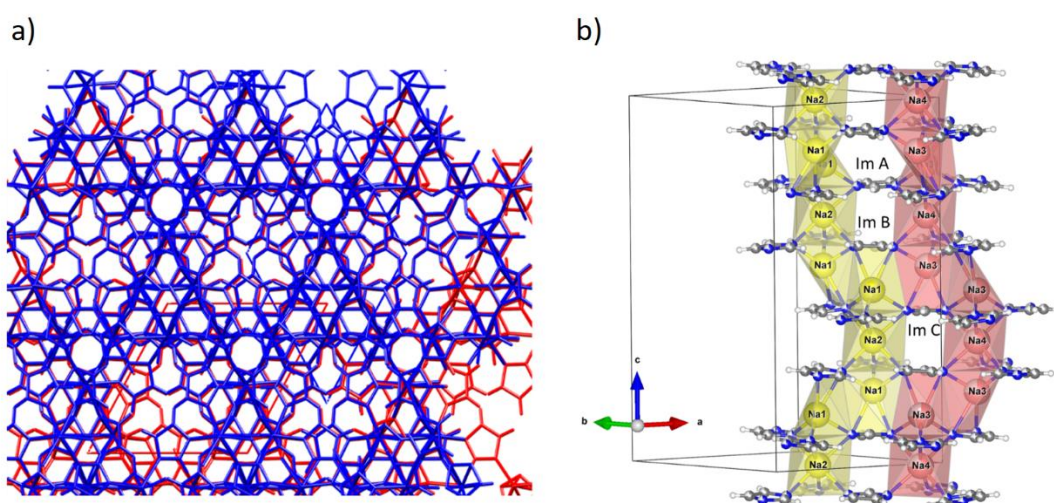
Slika I. a) Preklopljene strukture HT-NaIm s omjerom zaposjednuća atomskih položaja Na3 i Na4 natrijevih atoma 73/27. Crvenom bojom označen je model s većim zaposjednućem natrijevih atoma (73%), a plavom model s manjim zaposjednućem (27%). b) Različita okruženja imidazolatnih prstena u strukturi HT-NaIm.

Za razliku od niskotemperaturnog polimorfa koji pokazuje samo tetraedarsku koordinaciju natrijevih atoma,[XXX] visokotemperaturni polimorf natrijevog imidazolata posjeduje i tetraedarski i oktaedarski koordinirane natrijeve atome. Međuatomne udaljenosti natrijevog atoma i dušikovog atoma iz imidazolatnog prstena veće su za tetraedarski natrij kod niskotemperaturnog polimorfa nego kod visokotemperaturnog $d(Na_{tet}-N_{Im})_{NaIm} = 2,45(3)$ Å, $d(Na_{tet}-N_{Im})_{HT-NaIm} = 2,39(3)$ Å. Oktaedarski koordinirani natrij iz visokotemperaturnog NaIm radi duže veze s dušikom iz imidazolatnog prstena, što je i očekivano, s obzirom na viši koordinacijski broj, $d(Na_{okt}-N_{Im})_{HT-NaIm} = 2,65(2)$ Å.

Ispitane su i reakcije između $NaBH_4$ i NaIm potpomognute otapalima ACN i DMSO(3S1 i 3S2, shema III). Osim prisutne amorfne faze, kristalni produkti sadržavali su neizreagirane reaktante, ali i novi kristalni produkt, solvat NaIm i DMSO.

Kako bi se provjerila sličnost u ponašanju alkalijskih metala, suhim mehanokemijskim reakcijama u različitim omjerima podvrgnuti su KBH_4 i KIm (3D9-3D11, shema III). Dobiveni kristalni produkti bili su neizreagirani reaktanti i nekoliko neidentificiranih difrakcijskih linija. Povišenjem temperature nije došlo do reakcije između neizreagiranih reaktanata, niti je omogućena identifikacija neidentificiranih difrakcijskih linija.

Zaključno, stabilnost i reaktivnost borohidrida i imidazolata vrlo je različita za metale unutar grupe alkalijskih elemenata. U ovom radu prikazana je sinteza hibridnog spoja, Li_2ImBH_4 samo suhim mljevenjem $LiBH_4$ i LiIm, bez potrebe za dodavanjem otapala ili povišene temperature. Reakcije natrijevih i kalijevih spojeva nisu rezultirale hibridnim spojem, ali je priređen novi polimorf natrijevog imidazolata. Spoj je posebice zanimljiv zbog strukture u kojoj se natrijevi atomi nalaze između slojeva imidazola; ukoliko se pokaže da su natrijevi atomi unutar te strukture pokretni, ovaj polimorf bi se mogao istraživati kao potencijalni elektrolit u čvrstom stanju. Zbog same primjene, važno je da se HT-NaIm može prirediti i zagrijavanjem pri 210 °C, pri čemu ovaj spoj ostaje stabilan i nepromijenjen i nakon hlađenja na sobnu temperaturu.

Nakon ispitivanja reakcija između alkalijskih imidazolata i alkalijskih monometalnih borohidrida, istraživanje je prošireno na reakcije zemnoalkalijskih borohidrida $Mg(BH_4)_2$ s alkalijskim imidazolatima MIm (M = Na, Li, K) u različitim omjerima (shema IV).
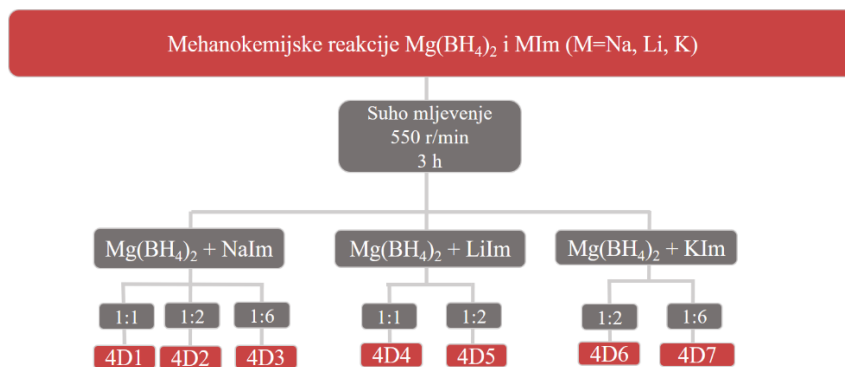
Shema IV. Mehanokemijske reakcije zemnoalkalijskog monometalnog borohidrida i alkalijskih imidazolata.

Strukturnom analizom utvrđeno je da su priređeni kristalni produkti ovih reakcija uglavnom neizreagirani reaktanti ili produkti ionske zamjene, a također navedenim reakcijama nastaj amorfnafaza. U nekim se slučajevima na snimkama uočavaju difrakcijske linije koje pripadaju novim neidentificiranim fazama. Odabrani uzorci, 4D3 i 4D5, ispitivani su visokotemperaturnim difrakcijskim *in-situ* mjerenjima pomoću sinkrotronskog zračenja, dok je uzorak 4D7 grijan *ex-situ* u autoklavu. Uzorak 4D3 pri sobnoj temperaturi sadrži neizreagirani NaIm i znatan udio amorfa. Difrakcijske slike prikupljene tijekom grijanja u temperaturnom intervalu 25–385 °C i tijekom hlađenja do 25 °C, kao i fazni sastav uzorka pri odabranim temperaturama prikazan je na slici II.
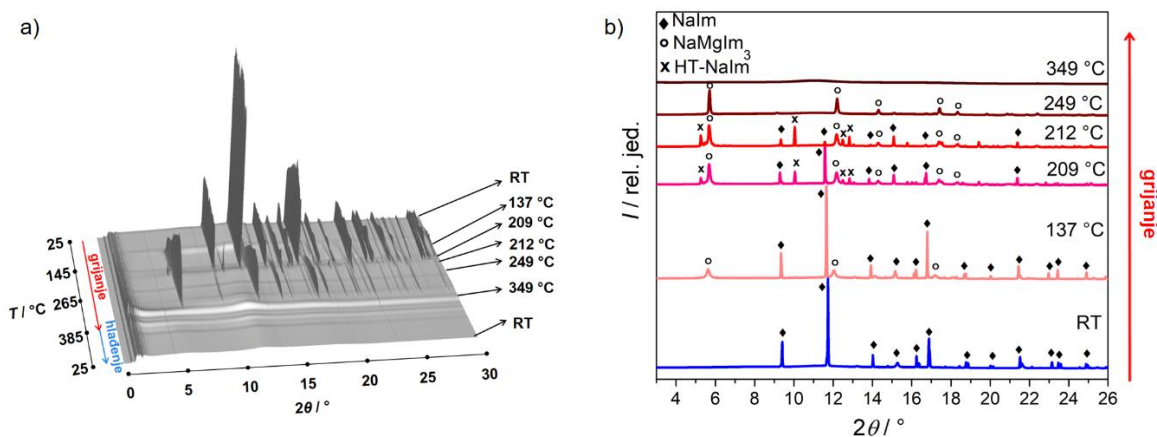
Slika II. a) Difrakcijske slike uzorka 4D3 prikupljene tijekom grijanja u temperaturnom intervalu 25–385 °C te tijekom ciklusa hlađenja do 25 °C. b) Fazni sastav uzorka 4D3 pri 25, 137, 209, 212, 249 i 349 °C. Difrakcijske linije faze NaMgIm$_3$ označene su kružićima, NaIm rombovima, dok su difrakcijske linije visokotemperaturnog polimorfa NaIm označene križićem.

Pri 118 °C dolazi do kristalizacije nepoznate faze, za koju će daljnje istraživanje pokazati da se radi o novom spoju, NaMgIm$_3$. Difrakcijske linije NaIm nestaju pri 209 °C daljnjim

zagrijavanjem. Istovremeno, visokotemperaturni polimorf NaIm (slika I) kristalizira i stabilan je u uskom temperaturnom intervalu. Između 218 °C i 340 °C u uzorku je prisutna samo faza NaMgIm$_3$.

Uzorak 4D5 pri sobnoj temperaturi sadrži samo LiIm i LiBH$_4$, što ukazuje na djelomičnu ionsku izmjenu. Određeni dio uzorka je amorfan. Fazna analiza uzorka 4D5 pri temperaturama 32, 198 i 320 °C prikazana je na slici III. Zagrijavanjem iznad 100 °C nastaje hibridni spoj Li$_2$ImBH$_4$. Istovremeno s nestankom ovog spoja, oko 240 °C počinje kristalizacija MgIm$_2$ koji ostaje stabilan kao jedina kristalna faza u sustavu sve do 450 °C kao i tijekom hlađenja na sobnu temperaturu.

Slika III. a) Difrakcijske slike uzorka 4D5 prikupljene tijekom grijanja u temperaturnom intervalu 25–450 °C te tijekom ciklusa hlađenja do 25 °C; b) Fazni sasatav uzorka 4D5 pri 25, 198 i 320 °C. Difrakcijske linije MgIm$_2$ označene su kvadratima, Li$_2$ImBH$_4$ s κ, LiIm zvjezdicom, a LiBH$_4$ s ι. ($\lambda = 0.8212$ Å).

Zagrijavanje uzorka 4D7 nastalog tijekom reakcije Mg(BH$_4$)$_2$ i KIm u omjeru 1:6, u autoklavu pri 155 °C rezultiralo je pojavom nove faze. Detaljnom strukturnom analizom ustanovljeno je da se radi o KMgIm$_3$.

Ovim je potvrđeno da se Li$_2$ImBH$_4$ može pripremiti ne samo iz monometalnog litijevog sustava, već i reakcijom magnezijevog borohidrida s litijevim imidazolatom. Budući daprvo dolazi do reakcije ionske zamjene i nastanka LiBH$_4$, uzorak je potrebno zagrijati kako bi se potakla reakcija između LiBH$_4$ i LiIm. Daljnjim zagrijavanjem ovog uzorka uočeno je da nestankom Li$_2$ImBH$_4$ oko 240 °C kristalizira magnezijev imidazolat. Tijekom zagrijavanja do 450 °C ne dolazi do termičkog raspada MgIm$_2$ kao ni hlađenjem do sobne temperature. Do ovih istraživanja MgIm$_2$ se u kristalnom obliku priređivao samo otopinskom sintezom. Kristalizacija

MgIm$_2$ nije uočena kada su u reakciji korišten natrijev ili kalijev imidazolat, kada nastaju dimetalni imidazolati.

Kako bi se dobio bolji uvid u strukturne promjene i termičku stabilnost novopriređenih spojeva, provedene su i direktne mehanokemijske reakcije između MgIm$_2$ i alkalijskih imidazolata (NaIm, KIm i LiIm) u molarnom omjeru 1:1 (shema V).

Shema V. Mehanokemijske reakcije zemnoalkalijskog monometalnog imidazolata i alkalijskih imidazolata.

Uzorak 5D1 dobiven rekacijom MgIm$_2$ i NaIm, pri sobnoj temperaturi u potpunosti je amorfan. Difrakcijske slike prikupljene tijekom grijanja u temperaturnom intervalu 25–390 °C i hlađenjem do 25 °C, te fazni sastav uzorka na odabranim temperaturama prikazan je na slici IV.
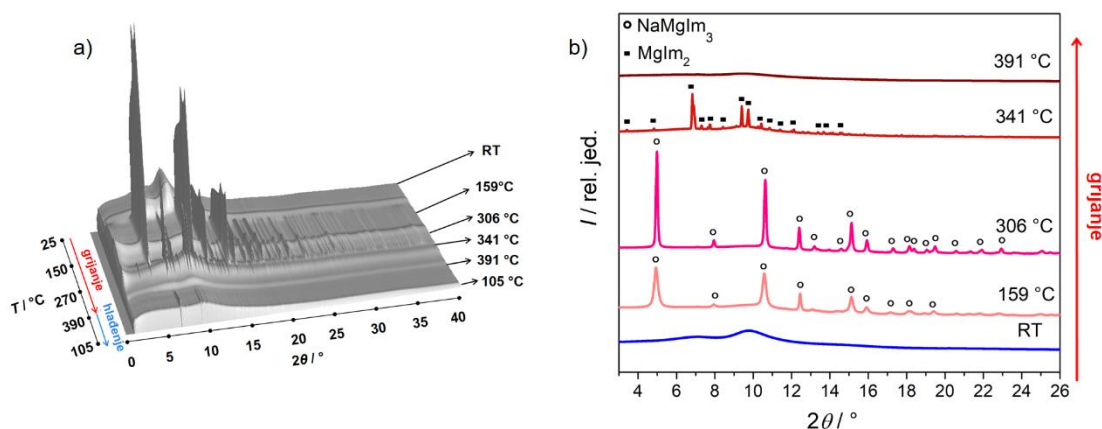
Slika IV. a) Difrakcijske slike uzorka 5D1 prikupljene tijekom grijanja u temperaturnom intervalu 25–390 °C te tijekom ciklusa hlađenja do 25 °C. b) Fazni sasatav uzorka 5D1 pri 25, 159, 306, 341 °C i 391 °C. Difrakcijske linije NaMgIm$_3$ označene su kružićima, dok su difrakcijske linije MgIm$_2$ označene kvadratićima.

Kristalizacija NaMgIm$_3$ počinje iznad 149 °C, a spoj ostaje stabilan do 310 °C kada kristalizira MgIm$_2$ do 366 °C. Zanimljivo je uočiti da je NaMgIm$_3$ stabilan u širem temperaturnom intervalu uz prisutnost borohidrida (118–340 °C), nego u slučaju kada je priređen iz odgovarajućih imidazolata (149–310 °C). Kristalna struktura NaMgIm$_3$ (slika V) određena je iz difrakcijskih podataka prikupljenih pri 333 °C. Nađeno je da spoj kristalizira u heksagonskom kristalnom sustavu, s prostornom grupom $P6_3$22.
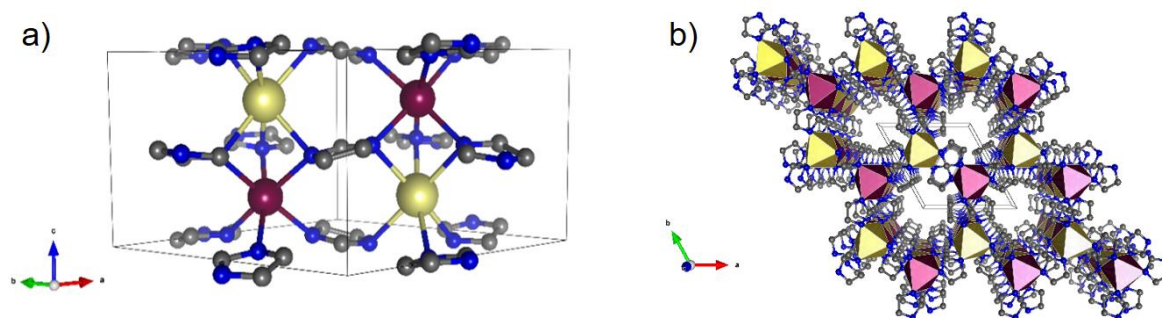
Slika V. a) Kristalna struktura NaMgIm$_3$. Magnezijevi atomi prikazani su purpurnom bojom, natrijevi atomi prikazani su žutom, ugljikovi atomi sivom, dok su dušikovi atomi prikazani plavom bojom. b) Kristalno pakiranje NaMgIm koje prikazuje kanale duž osi *c*.

Za razliku od monometalnih imidazolata poput NaIm i MgIm$_2$ u kojima su metali tetraedarski koordinirani, u NaMgIm$_3$ i Na i Mg kationi nalaze se u deformiranoj oktaedarskoj koordinaciji. Međuatomne udaljenosti između metala i dušikovog atoma iz imidazolatnog prstena veće su kod miješanog imidazolata, što je bilo i očekivano obzirom na veći koordinacijski broj. Imidazolatni ligand okružen je sa četiri metalna kationa, pri čemu je svaki dušikov atom iz imidazolatnog aniona koordiniran s dva kationa formirajući kompleksnu trodimenzijsku mrežu. Duž osi *c*, Na i Mg povezani su preko premošćujućih dušikovih atoma iz tri imidazolatna prstena stvarajući lanac oktaedara povezanih preko zajedničkih ploha. Lanci su međusobno povezani na način da tvore *cik-cak* mrežu duž ravnine *ab*. U smjeru osi *c* nalaze se kanali smješteni na vijčanoj osi šestog reda. Promjer kanala iznosi ~6.6 Å, a raspoloživi volumen je 28.5 Å^3 (pretpostavljajući sferu polumjera *r* = 1.4 Å). Topološki NaMgIm$_3$ pripada *stp* mreži,[LXXVIII] koju posjeduje i nekoliko MOF-ova te anorganskih spojeva, a zajednički im je strukturni tip koji pripada željezovom fosfonatu Fe$_2$(HPO$_3$)$_3$.

Kada je kao alkalijski imidazolat korišten KIm, za razliku od NaIm, mehanokemijska reakcija već nakon samog mljevenja, a bez dodatne termičke obrade, rezultirala je stvaranjem miješanog metalnog imidazolata, KMgIm$_3$. Difrakcijske slike prikupljene tijekom grijanja u temperaturnom intervalu 25–325 °C i tijekom hlađenja na sobnu temperaturu te fazni sastav uzorka 5D2 na odabranim temperaturama prikazan je na slici VI.
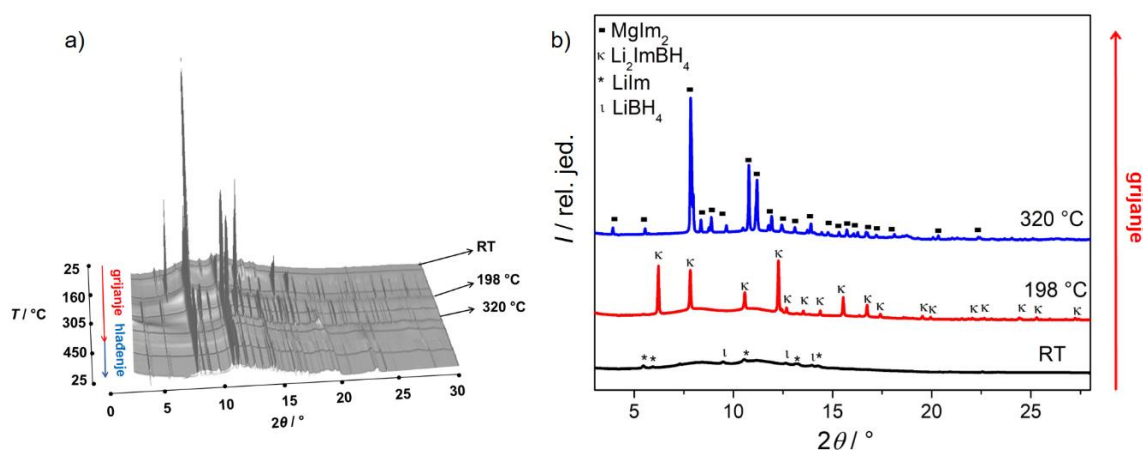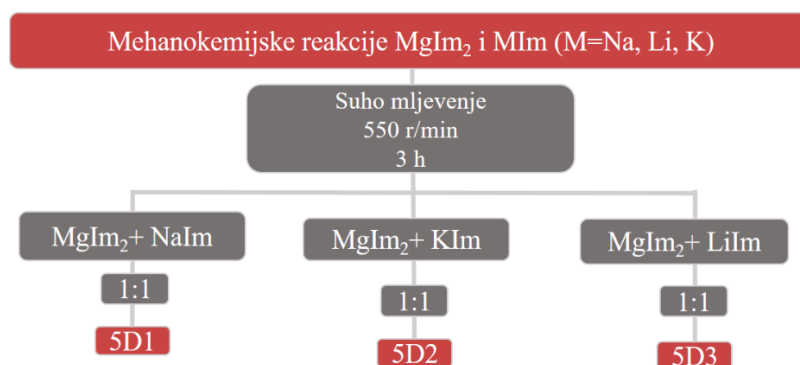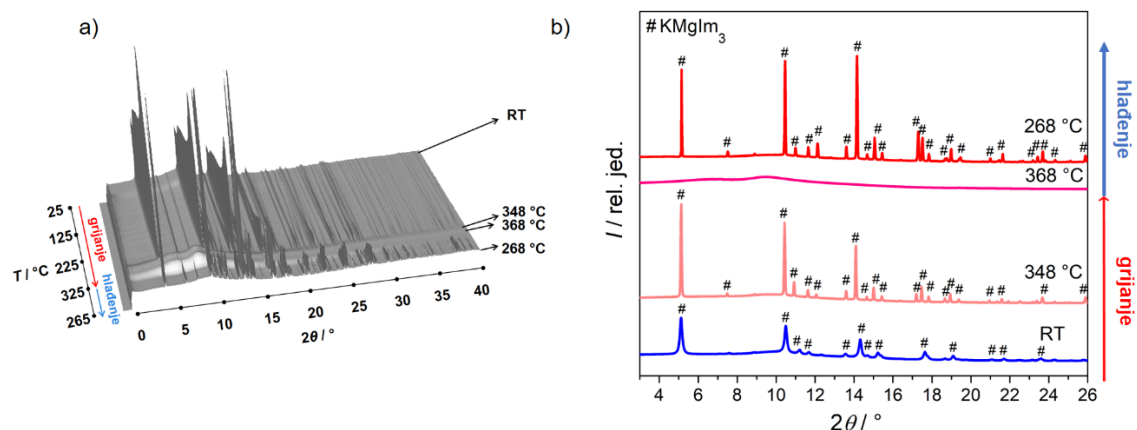
Slika VI. a) Difrakcijske slike uzorka 5D2 prikupljene tijekom grijanja u temperaturnom intervalu 25–325 °C te tijekom ciklusa hlađenja do 25 °C. b) Fazni sasatav uzorka 5D2 pri 348 °C, 368 °C, te 268 °C u hlađenju. Difrakcijske linije KMgIm$_3$ označene su ljestvama.

Spoj je stabilan u jako širokom temperaturnom intervalu (25–353 °C), nakon čega se tali. Prilikom hlađenja rekristalizira ispod 298 °C. Kristalna struktura (slika VII) određena je iz difrakcijske slike prikupljene pri 333 °C.
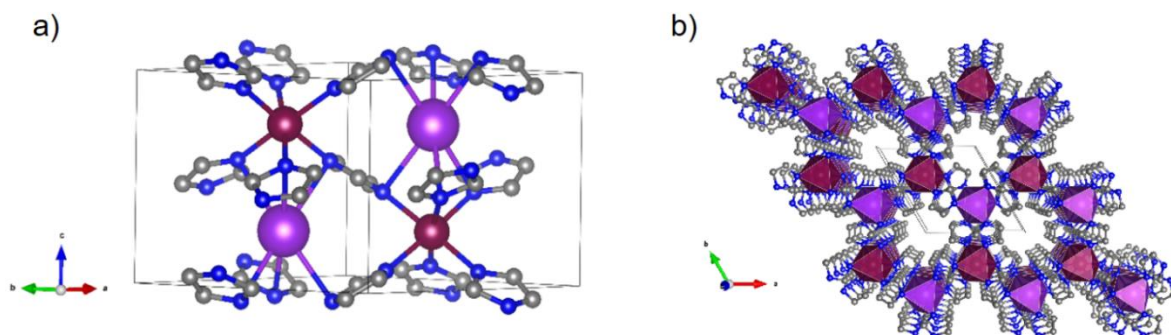
Slika VII. a) Kristalna struktura KMgIm$_3$. Magnezijevi atomi prikazani su purpurnom bojom, kalijevi atomi ljubičastom, ugljikovi atomi sivom, dok su dušikovi atomi prikazani plavom bojom. b) Kristalno pakiranje KMgIm prikazuje kanale u strukturi duž osi *c*.

Struktura KMgIm$_3$ slična je strukturi NaMgIm$_3$, a najznačajnija razlika odnosi se na orijentaciju imidazolatnog prstena. U slučaju NaMgIm$_3$ prsten minimalno odstupa od idealne planarne konfiguracije te se smatra gotovo paralelnim s ravninom *ab*, što nije slučaj u strukturi KMgIm$_3$. Također, spojevi se razlikuju po stupnju deformacije poliedra oko alkalijskog metalnog centra, pri čemu je deformacija izraženija u strukturi NaMgIm$_3$. Obje su strukture potvrđene izračunom BVS[LXXIX] (*eng.* bond valence sum).

Kako je prikazano i slikom VIII, kada je LiIm korišten u reakciji s MgIm$_2$, uzorak 5D3 pri sobnoj temperaturi sadrži samo amorfnu fazu. Difrakcijske linije LiIm pojavljuju se pri 149 °C,

a drugi reaktant, MgIm$_2$, kristalizira pri 185 °C. Obje faze ostale su stabilne do 296 °C te ne dolazi do nastanka miješanog metalnog imidazolata.
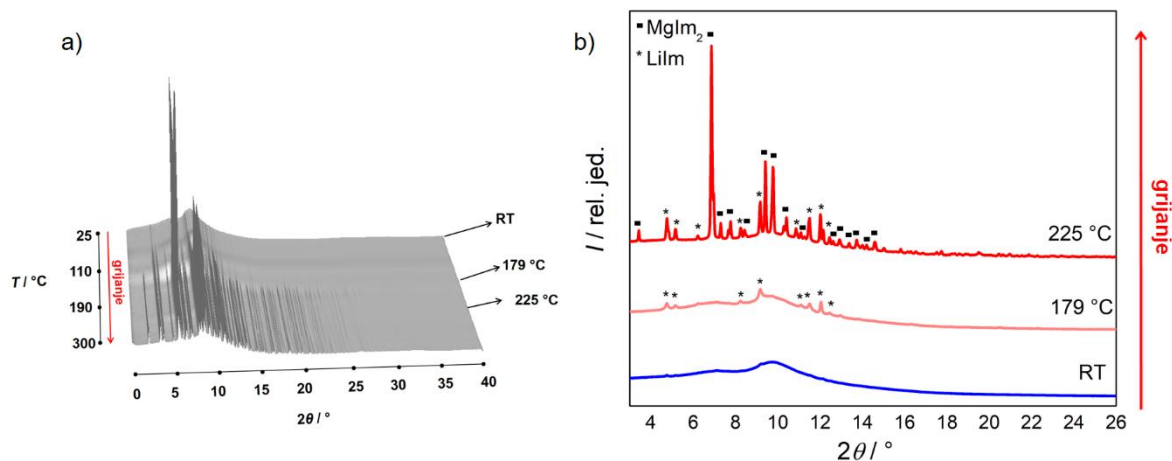
Slika VIII. a) Difrakcijske slike uzorka 5D3 prikupljene tijekom grijanja u temperaturnom intervalu 25–300 °C. b) Fazni sastav uzorka 5D3 na 25, 179 i 225 °C. Difrakcijske linije LiIm označene su zvjezdicama, dok su difrakcijske linije MgIm$_2$ označene kvadratima.

Zaključno, nastanak miješanih metalnih imidazolata AMgIm$_3$ (A = Li, Na, K) uvjetovan je, s jedne strane termodinamičkom stabilnošću imidazolata alkalijskih metala, te energijom miješanih metalnih imidazolata s druge. Nađeno je da litijev imidazolat ne reagira s magnezijevim imidazolatom, vjerojatno zbog ograničenja uzrokovanih malim litijevim kationom koji nije dovoljno velik da ispuni potrebe koordinacijskog broja 6 koji A kationi u AMgIm$_3$ imaju. Za razliku od litijevog imidazolata, kalijev imidazolat vrlo brzo reagira s MgIm$_2$ stvarajući KMgIm$_3$.

Kako su reakcije između alkalijskih imidazolata i magnezijevog imidazolata ili borohidrida rezultirale stvaranjem nove grupe dimetalnih imidazolata, istraživanje je usmjereno ka reakcijama prijelaznih metala, točnije manganovog borohidrida, s imidazolatima alkalijskih metala MIm (M = Na, K, Li) u različitim omjerima kako je prikazano na shemi VI.
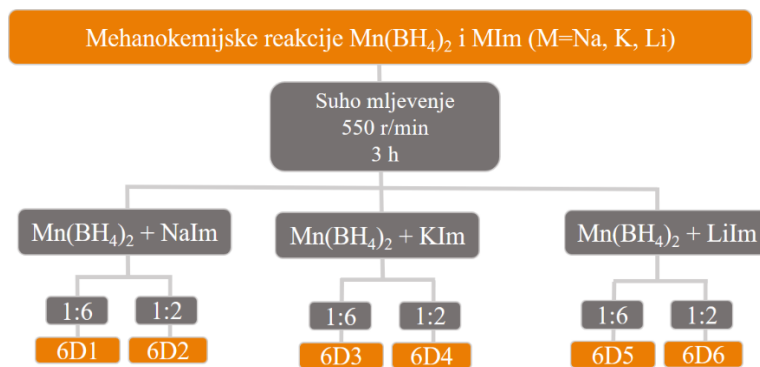
Shema VI. Mehanokemijske reakcije monometalnog borohidrida prijelaznog metala i alkalijskih imidazolata.

Rietveldovim utočnjavanjem utvrđeno je da je, slično kao i kod magnezijevih spojeva, s Mn(BH$_4$)$_2$ najlakše reagirao KIm, stvarajući novu fazu već prilikom mljevenja, dok su u slučaju mehanokemijskih reakcija s NaIm ili LiIm primijećeni neizreagirani reaktanti, produkti ionske zamjene i/ili amorfna faza.

Zagrijavanjem uzorka 6D1 u autoklavu na 220 °C dolazi do smanjenja udjela amorfne faze i kristalizacije nove faze, što je bila indikacija za provedbu *in-situ* visokotemperaturnih difrakcijskih mjerenja pomoću sinkrotronog zračenja. Uzorak na sobnoj temperaturi sadrži samo neizreagirani Mn(BH$_4$)$_2$ te NaBH$_4$ koji je nastao ionskom zamjenom, te znatan udio amorfne faze. Difrakcijske slike prikupljene tijekom grijanja u temperaturnom intervalu 25–295 °C i u hlađenju do 25 °C te fazni sastav uzorka na odabranim temperaturama prikazan je na slici IX.
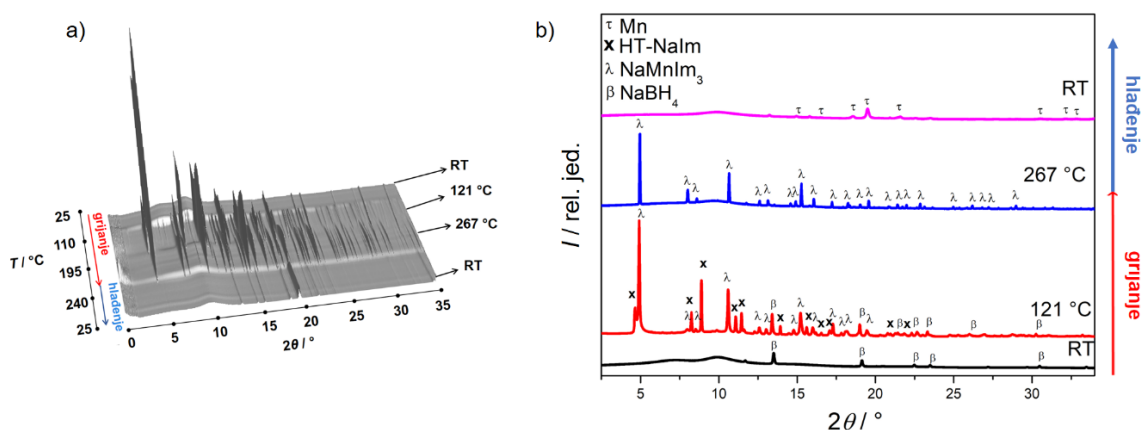
Slika IX. a) Difrakcijske slike uzorka 6D1 prikupljene tijekom grijanja u temperaturnom intervalu 25–295 °C te tijekom ciklusa hlađenja do 25 °C b) Fazni sasatav uzorka 6D1 na 25, 121, 267te 25 °C u hlađenju. Difrakcijske linije visokotemperaturnog polimorfa NaIm označene su s x, NaMnIm$_3$ s λ, Mn s τ, dok je NaBH$_4$ označen s β.

Na 87 °C dolazi do kristalizacije nove faze, koja će naknadno biti identificirana kao NaMnIm$_3$. Istovremeno dolazi i do kristalizacije visokotemperaturnog polimorfa NaIm koji je stabilan do 180 °C. Daljnjim povišenjem temperature u uzorku prisutan je samo NaMnIm$_3$ koji ostaje stabilan do taljenja pri 280 °C.

Kristalna struktura NaMnIm$_3$ (slika X) određena je iz uzorka 6D1, iz difrakcijske slike prikupljene tijekom grijanja na 200 °C. Nađeno je da spoj kristalizira u heksagonskom sustavu, u prostornoj grupi $P6_3 22$.
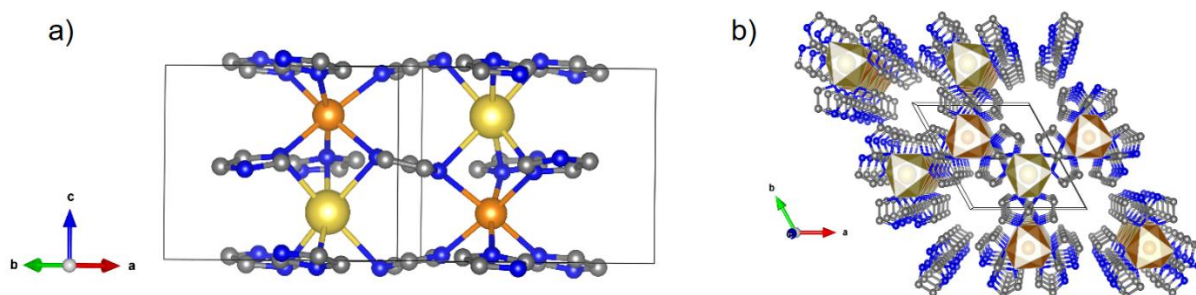
Slika X. a) Kristalna struktura NaMnIm$_3$. Manganovi atomi prikazani su narančastom bojom, natrijevi atomi žutom, ugljikovi atomi sivom dok su dušikovi atomi prikazani plavom bojom. b) Kristalno pakiranje NaMnIm$_3$ koje prikazuje kanale u strukturi duž osi c.

NaMnIm$_3$ izostrukturan je s magnezijevim analogom, NaMgIm$_3$, što je i očekivano, posebice ako se u obzir uzmu strukturne sličnosti između manganovih i magnezijevih borohidridnih spojeva. Veze između natrijevog atoma i dušikovog atoma iz imidazolatnog prstena u NaMnIm$_3$ [d(Na−N$_{Im}$)$_{NaMnIm3}$ = 2,66859(3) Å] nešto su duže nego u strukturi NaMgIm$_3$ [d(Na−N$_{Im}$)$_{NaMgIm3}$ = 2,5851(2) Å]. Također, međuatomna udaljenost između manganovog atoma i dušikovog atoma iz imidazolatnog prstena u NaMnIm$_3$ [d(Mn−N$_{Im}$)$_{NaMnIm3}$ = 2,37226(2) Å] veća je od veze između magnezijevog atoma i dušikovog atoma iz imidazolatnog prstena u NaMgIm$_3$ (d(Mg−N$_{Im}$)$_{NaMgIm3}$ = 2,3701(2) Å). Kao što je to slučaj i kod borohidrida, γ-Mn(BH$_4$)$_2$ i γ-Mg(BH$_4$), veći manganov atom i ovdje stvara nešto veću ćeliju u usporedbi s magnezijevim analogom ($V_{NaMnIm3}$ = 529,674(18) Å^3, $V_{NaMgIm3}$ = 514,55(5) Å^3).

Uzorak 6D3, pripremljen iz Mn(BH$_4$)$_2$ i KIm u molarnom omjeru 1:6, već nakon mljevenja pokazao je prisustvo nove faze (kasnijim rezultatima dokazano je da se radi o KMnIm$_3$). Zagrijavanje u autoklavu pri 175 °C dovodi do porasta udjela KMnIm$_3$, no značajan udio amorfne faze još uvijek ostaje, stoga su provedena dodatna *in-situ* viskotemperaturna difrakcijska mjerenja pomoću sinkrotronskog zračenja. Na sobnoj temperaturi uz KMnIm$_3$ u uzorku prisutni su neizreagirani KIm i KBH$_4$ koji je nastao ionskom zamjenom. Difrakcijske

slike prikupljene tijekom grijanja u temperaturnom intervalu 25–290 °C i u hlađenju do 25 °C te fazni sastav uzorka pri odabranim temperaturama prikazan je na slici XI.
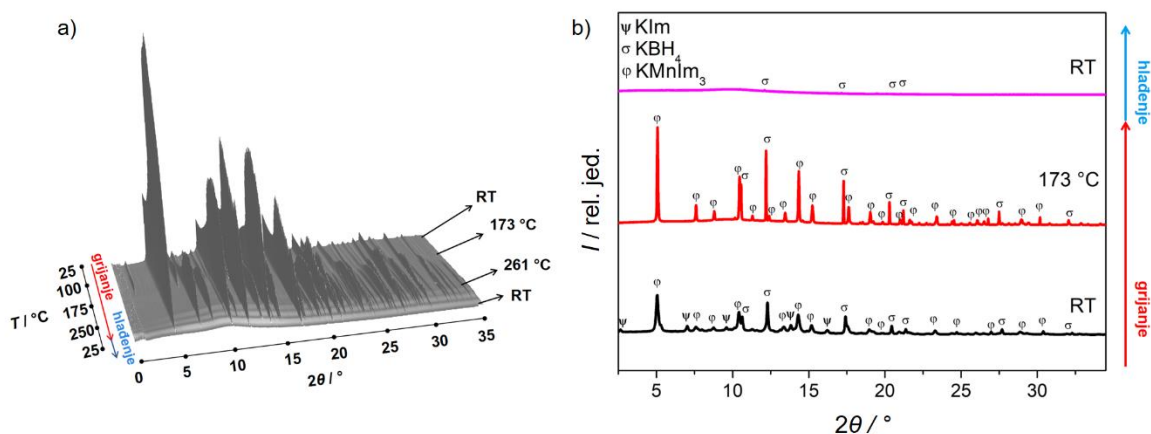
Slika XI. a) Difrakcijske slike uzorka 6D3 prikupljene tijekom grijanja u temperaturnom intervalu 25–290 °C te tijekom ciklusa hlađenja do 25 °C; b) Fazni sasatav uzorka 6D3 pri 25, 173, te 25 °C u hlađenju. Difrakcijske linije KIm označene su s ψ, KBH_4 s σ, dok je $KMnIm_3$ označen s φ.

KIm se tali pri 152 °C, a $KMnIm_3$ je stabilan do 289 °C. Iznad te temperature KBH_4 je jedina kristalna faza u uzorku.

Kako je $KMnIm_3$ (slika XII) svo vrijeme prisutan u sustavu zajedno s KBH_4, određivanje kristalne strukture bilo je nešto zahtjevnije nego u slučaju $NaMnIm_3$. Struktura je određena zagrijavanjem uzorka pri 173 °C, indeksiranjem difrakcijskih linija u heksagonskom sustavu, u prostornoj grupi $P6_322$.
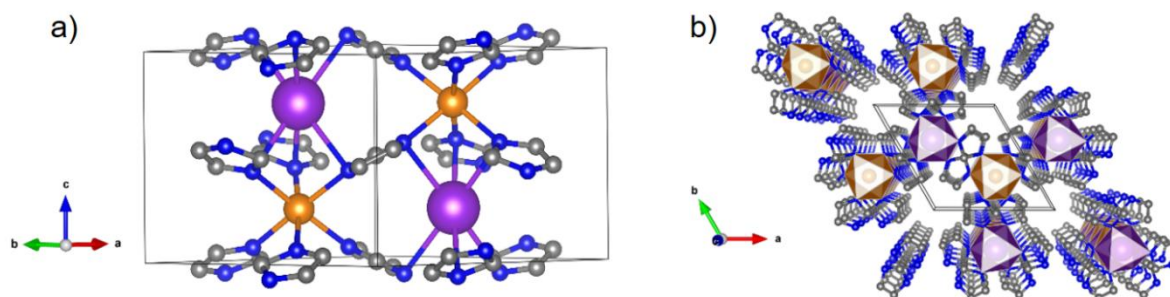

Slika XII. a) Kristalna struktura $KMnIm_3$. Manganovi atomi prikazani su narančastom bojom, kalijevi atomi ljubičastom, ugljikovi atomi sivom, dok su dušikovi atomi prikazani plavom bojom. b) Kristalno pakiranje $KMnIm_3$ koje prikazuje kanale u strukturi duž osi *c*.

Sličnosti vidljive za $NaMgIm_3$ i $KMgIm_3$, primjetne su i prilikom usporedbe kristalnih struktura $KMnIm_3$ i $NaMnIm_3$; osnovna razlika između natrijevih i kalijevih spojeva je u orijentaciji

imidazolatnog prstena koji je u slučaju natrijevog spoja gotovo paralelan s ravninom *ab*, dok u kalijevom spoju nije.

Kao što je već spomenuto, strukture $AMgIm_3$ i $AMnIm_3$ (A = Na, K) određene su iz difrakcijskih podataka iz polikristala. Strukture $AMgIm_3$ određene su procesom paralelnog temperiranja, koristeći milijardu pokušaja po koraku, no u slučaju $AMnIm_3$ isti uvjeti paralelnog temperiranja bili su neuspješni i rezultirali su modelom iz lažnog energijskog minimuma, što znači, netočnim rješenjem u kojem su imidazolatni prstenovi udvostručeni. Stoga je za određivanje strukture $AMnIm_3$ primijenjena druga strategija procesa globalne optimizacije, kako je objašnjeno u preglednom radu,[LIX] a koja uključuje upotrebu malog broja pokušaja i koraka, ali koristeći utočnjavanje metodom najmanjih kvadrata nakon svakog koraka. U oba slučaja imidazolatni prstenovi tretirani su kao kruto tijelo, bez mogućnosti rotacije oko veza, te su korištene odgovarajuće vrijednosti ograničenja međuatomnih udaljenosti za svaki par atoma.

Zaključno, manganov borohidrid u reakcijama s alkalijskim imidazolatima ponaša se vrlo slično magnezijevom borohidridu, pri čemu u slučaju natrijevog i kalijevog imidazolata nastaju miješani metalni imidazolati $AMnIm_3$, dok u slučaju litijevog imidazolata nastaje hibridni spoj Li_2ImBH_4, te pri višim temperaturama kristalizira nepoznata faza koja vjerojatno odgovoara manganovom imidazolatu $MnIm_2$.

U sklopu ovog istraživanja ispitane su mehanokemijske reakcije monometalnih i dimetalnih borohidrida s imidazolatima alkalijskih i zemnoalkalijskih metala. Zaključno, zanimljivo je uočiti da, osim litija, nijedan metal ne tvori hibridni spoj koji uključuje i borohidridni i imidazolatni anion. Ipak, u većini ispitanih sustava, mljevenje je induciralo mehanokemijsku reakciju pri čemu je stvorena nova grupa miješanih metalnih imidazolata. Li_2ImBH_4 je i ranije sintetiziran, ali otopinskom metodom ili pri visokim temperaturama, dok je u ovom radu pokazano kako se isti spoj može pripremiti jednostavnim suhim mljevenjem $LiBH_4$ i LiIm, gdje Li_2ImBH_4 nastaje već pri sobnoj temperaturi kao jedina kristalna faza. Li_2ImBH_4 nastaje i u reakcijama LiIm s $Mg(BH_4)_2$ ili $Mn(BH_4)_2$, no u tim slučajevima sustav je potrebno podvrgnuti zagrijavanju. Za razliku od litijevog sustava, NaIm u reakciji s $NaBH_4$ nije dao novi hibridni spoj, ali je formiran novi, visokotemperaturni polimorf NaIm, čija struktura je riješena kao racemični sraslac. Ova struktura sadrži dva različita lanca s 3_1 vijčanom osi duž osi *c,* koji međusobno stvaraju složenu trodimenzionalnu mrežu. Isti spoj nastaje i u

reakcijama NaIm s Mg(BH$_4$)$_2$ ili Mn(BH$_4$)$_2$, no tek nakon izlaganja povišenoj temperaturi, dok u reakciji s NaBH$_4$ kristalizira pri sobnoj temperaturi, bez potrebe za dodatnim zagrijavanjem. Posebno zanimljive rezultate dala je reakcija NaIm s Mg(BH$_4$)$_2$ u kojoj nastaje dimetalni imidazolat formule NaMgIm$_3$. Za razliku od monometalnih imidazolata (NaIm i MgIm$_2$) u kojima su metali tetraedarski koordinirani, ovdje i natrijev i magnezijev atom imaju deformiranu oktaedarsku koordinaciju. Strukturu NaMgIm$_3$ karakteriziraju kanali promjera $d \sim 6{,}6$ Å duž osi c. Isti spoj priređen je reakcijom MgIm$_2$ i NaIm, no širi temperaturni raspon u kojem je ovaj spoj stabilan uočen je kada je u reakciji prisutan borohidrid. Ispitane su reakcije MgIm$_2$ i s KIm i LiIm i uočeno je da je stvaranje AMgIm$_3$ (A = Na, K) određeno termodinamičkom stabilnošću imidazolata alkalijskih metala i energijom stvaranja miješanih metalnih imidazolata. Razlog tome je činjenica da litijev imidazolat ne reagira s MgIm$_2$, vjerojatno zbog male veličine litijevog kationa, dok kalijev imidazolat vrlo brzo reagira s MgIm$_2$ i tvori KMgIm$_3$. Spojevi iz skupine AMgIm$_3$ (A = Na, K) prvi su članovi dimetalnih imidazolatnih mreža s *stp* topologijom. Spojevi opće formule AMnIm$_3$ izostrukturni su skupini AMgIm$_3$ (A = Na, K) i priređeni su reakcijom manganovog borohidrida i imidazolata alkalijskog metala AIm (A = Na, K).

Ovim istraživanjem također je utvrđeno da se kristalni magnezijev imidazolat, koji je dosad priređen samo reakcijom u tekućem amonijaku, može priprediti djelomičnom ionskom zamjenom tijekom mljevenja LiIm i Mg(BH$_4$)$_2$ i grijanjem pri 240 °C. Tako pripremljen MgIm$_2$ stabilan je nakon hlađenja na sobnu temperaturu. Ovaj novi sintetski put predstavlja odličnu zamjenu već poznatoj reakciji u kojoj je iznimno važno paziti na agresivnu redoks reakciju između NH$_2^-$ i NO$_3^-$. Reakcije između NaZn(BH$_4$)$_3$ i NaIm nisu dale novi hibridni spoj i uglavnom su rezultirale samo neizreagiranim reaktantima, produktima raspada ili amorfnim produktima, a dodatnim temperaturnim tretmanom kristalizirale su i neke od poznatih zeolitnih imidazolatnih mreža (IMIDZB01). Ipak, uzevši u obzir rezultate NMR-a u čvrstom stanju, reakcija potpomognuta otapalom (DMSO) možda rezultira kristalizacijom hibridnog spoja. Kako se signali protona iz imidazolata u ^{1}H NMR spektru na oko 7 ppm nalaze prostorno vrlo blizu protonu s rezonancijom na oko 0 ppm, koji se pripisuje protonskim jezgrama iz borohidridne skupine, može se očekivati da je nastala faza vrlo vjerojatno hibridni spoj koji sadrži oba aniona. Koristeći navedene činjenice, bit će poduzeti daljnji koraci potrebni za određivanje kristalne strukture novog spoja.

§ 1.   INTRODUCTION

Increasing energy demands of our modern society cause air polution and high atmospheric CO_2 concentrations therefore the development of efficient sorption materials and processes that allow CO_2 purification will allow a reduction in the complexity of utilization technologies and in the subsequent costs. Furthermore, increased consumption requires the development of convenient energy storage devices wherefore hydrogen might be a good solution. Problem of its safe and efficient storage can be solved by utilization of solid state media.[1–5] Tetrahydridoborates, commonly called borohydrides, can be used for this purpose.[6–13] Even more promising are novel hybrid materials designed by combining the molecular building blocks of light-weight complex hydrides with organic linkers.[14–20] Due to the specific nature of unique complex-hydride ligands in a special group of coordination frameworks, metal-hydride organic frameworks, HOFs, interesting properties (guest-host interactions, dehydrogenation properties) can be expected. HOFs are novel hybrid materials designed by combining molecular building blocks of light weight complex hydrides with organic linkers, ligands developed for coordination frameworks. Crystal engineering principles of coordination frameworks, which are used for HOF design, should result in interesting structural and microstructural characteristics of materials, such as high porosity, wherefore HOFs show potential for gas adsorption and separation.[21,22] Flexibility of the borohydride complex anion present in HOFs allows cation coordination unusual for coordination frameworks, thus they can be considered a new type of frameworks. Usage of directional anionic ligands other than hydrides (imidazolates, isonicotinates or derivatives) gives the possibility of additional structural diversity. The most promising ligand is imidazolate as the metal-N(imidazolate)-metal angle of 145° is very similar to metal-borohydride-metal angle observed for example in $Mg(BH_4)_2$.[7] In all reactions, mechanochemical synthesis is used, as a clean, efficient and fast synthetic route.[24–75] Among the borohydrides, alkali metal borohydrides, alkaline earth metal borohydrides and especially those containing also d-transition metals are investigated.[76–109] The only known example where the borohydride anion is enclosed in the same structure with an organic ligand (imidazole) and forms hybrid material is Li_2ImBH_4.[110] All examples of bimetallic imidazolates known from literature include transition metal atoms, but no study on the mixed-metal imidazolates containing alkali and alkaline earth metals has been reported.[111–116]

Aim of this research is to investigate, adjust and optimize mechanochemical synthesis of different borohydrides of molecular formula MM'(BH$_4$)$_n$ (M = alkali/alkaline earth metal, M' = transition metal) and furthermore investigate reactions of monometallic or bimetallic borohydrides with organic linkers (imidazolates).

In the scope of this disertation, all reactions are performed by grinding in the planetary ball-mill, the influence of reactant ratio, speed or time of milling on final product composition is investigated. Due to the sensitivity of borohydrides to air and humidity, all manipulation, both with reactants and final products, is performed in an inert atmosphere, in a glovebox filled with nitrogen or argon. Reaction of borohydride and water is explosive therefore all hygroscopic reactants and solvents are dried by using the vacuum line. Mechanochemistry is clean, fast and efficient way for the preparation of different types of compounds which sometimes cannot be prepared by solvent, but only by using a mechanical force. The rotation of jars and jar holder and collision of milling balls lead to a chemical reaction. There are two types of the mechanochemical reactions: neat grinding, NG, and liquid assisted grinding, LAG, and both types will be used in the course this thesis.

Due to the fact that the chosen synthetic route always results in formation of polycrystalline products, structural characterization is done by X-ray powder diffraction, XRPD, on laboratory diffractometer[117–121] and synchrotron beamline.[122–124] Not only structural, but also a microstructural characterization of the samples is performed. In the last few years, tremendous development in the instrumentation, programs and methods for structure solution from polycrystalline data was achieved. For structure solution of polycrystalline sample, direct methods or methods in direct space (global optimization methods-simulated annealing, parallel tempering) can be applied. Structure solution, starting from pattern indexing, space group determination from systematical absences, all over to the determination of a structural model,[125–144] are performed in programs EXPO2014[131] and FOX.[129,130] The Rietveld method[139] is used for structure refinement implemented within the HighScoreX'pert plus. By this procedures, the structural characteristics of the investigated materials are determined: unit cell parameters, atomic positions, temperature factors, bond lenghts and angles, crystallite sizes and lattice strains. Solid state NMR (ss-NMR) is used as complementary technique to diffraction techniques and it relies on the existence of short-range order and provides a picture of an average crystal structure.[145,146]

Hybrid materials prepared from metal hydrides and organic linkers show structural characteristics of both groups of compounds, thus it can be expected they will have porous structures. Different reactivity among the group of alkali metal borohydrides and imidazolates is revealed and this research contributes to better understanding of the crystallization processes, stability and structural characteristics, which is a necessary prerequisite for the development of new materials for hydrogen storage.

§ 2. STATE OF THE ART

2.1. HYDROGEN STORAGE

Pronounced energy demands in the world today are caused by both the increase of population as well as life standards of modern society. Non-renewable fossil fuels are still mostly used for energy production, while, as the consequence, we are witnessing the whole range of negative impacts on the Earth and climate changes. In due time, the world supplies of fossil fuels will disappear, therefore transition towards a sustainable and carbon-free energy systems represents one of the greatest challenges of the 21st century.[1] Those sustainable systems should be renewable and able to offer safe alternative for the people and the environment. Element, which is already recognized as an alternative energy carrier, and possesses all the above-mentioned characteristics, is hydrogen. It can be conveniently produced from the renewable energy and water. Prior to the efficient exploitation of huge amounts of energy stored in hydrogen, a major problem, safe and efficient mean of hydrogen storage, must be properly addressed and resolved. Most of the systems used until now are based on compressed or liquefied hydrogen and have limited application due to the technical difficulties, such as real time production, the safe and convenient storage and the efficient combustion of hydrogen. For example, the US Department of Energy (DOE) has set the hydrogen storage targets (Table 1) for automotive applications in terms of gravimetric and volumetric density which are 1.7 and 2.9 times higher than the best values measured in high pressure (350–700 bar) tanks.[1–3] On a mass basis, hydrogen has nearly three times the energy content of gasoline-120 MJ/kg for hydrogen versus 44 MJ/kg for gasoline. On a volume basis, however, the situation is reversed; liquid hydrogen has an energy density of 8 MJ/L whereas gasoline has an energy density of 32 MJ/L. Onboard hydrogen storage capacities of 5–13 kg hydrogen will be required to meet the driving range for the full range of light-duty vehicle platforms.[4]

Table 1. DOE targets for on-board hydrogen storage systems for light-duty vehicles.[4,5]

Storage system parameter	Original 2010 target (accepted in 2007)	Revised 2010 target (accepted in 2009)	2017 target	Ultimate target
Gravimetric capacity, kgH$_2$/kg system	6%	4.5%	5.5%	7.5%
Volumetric capacity, gH$_2$/L system	45	28	40	70
Operational cycle life	1000	1000	1500	1500
Fill time (min. for 5 kg)	3	4.2	3.3	2.5
Minimum full flow rate (gH$_2$/s/kW)	0.02	0.02	0.02	0.02
Min. delivery pressure at 85 °C (atm.)	8	5	4	3
Fuel purity	99.99%	99.97%	99.97%	99.97%

Solid state storage has the greatest potential to fulfil this challenge, either by chemical bonding in crystalline compounds *via* formation of hydrogen-containing compounds (chemisorption) or by physical adsorption of molecular hydrogen (physical adsorbents) in porous materials (Figure 1).[4]
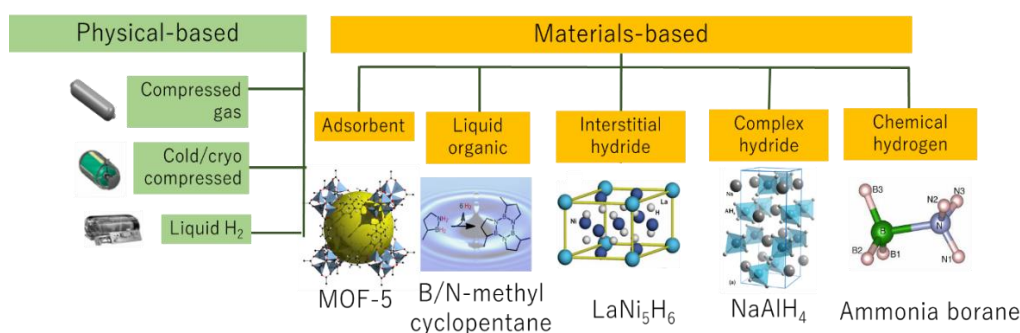
Figure 1. Scheme representing ways of hydrogen storage.[4]

2.1.1. Chemisorption

Best examples, where hydrogen is stored by chemisorption, are hydride compounds that are characterized by the presence of a hydrogen atom bound with various elements to form covalent, ionic or interstitial (metallic) systems. Main advantage is their ability to uptake large amounts of hydrogen, store and reversibly release under moderate conditions. Initial launch of fuel cell vehicles which used hydrides to run was stimulated by the mentioned facts.[1–3]

Hydrogen storage materials were first investigated as so-called interstitial or metal hydrides where hydrogen is stored in the atomic form at the interstitial sites of the crystal lattice, such as AB$_2$, A$_2$B, AB and AB$_5$, where "A" is the element which makes very stable AH$_x$ hydrides

(usually a lanthanide element, Ca or rare earth metal mixture), while "B" is the element which makes unstable BH_x hydrides (Ni, substituted by Co, Al, Mn, Fe, Sn, Cu, Ti etc). Since more than a decade the attention of the hydrogen storage community has shifted towards complex and chemical hydrides (Figure 2). Metal hydrides have advantages because of their reversibility, rapid kinetics close to room temperature, high volumetric hydrogen storage density (comparable to that of liquid hydrogen), but they also have big disadvantage, inferior gravimetric hydrogen densities compared to high-pressure tank systems, what has shifted research interests to other classes of hydrides. Complex and chemical hydrides, such as borohydrides (with boron) or alanates (with aluminum), are capable of holding at least double the amount of hydrogen than what is available in metal hydrides. Here, hydrogen is partially charged and covalently bonded to a central atom with a highly localized charge (boron, aluminum, nitrogen). Access to this hydrogen is possible by thermal decomposition of these materials. Problem with this group of compounds is related to the fact that hydrogen release is not that straightforward as it is for metal hydrides due to a multistep decomposition reaction in which mass transport, ionic diffusion and element segregation take place. Among complex hydrides tetrahydridoborates with a general formula $M(BH_4)_n$, consisting of metal cations M^{n+}, and borohydride anions, BH_4^-, are the most promising because of the high hydrogen sorption densities. Common name for tetrahydridoborates is borohydrides, and this name will be used further on in this dissertation. One disadvantage that all types of hydrides have in common is a high activation barrier, which results in slow kinetics. Solution lays in tuning of the thermodynamics parameters or heat of reaction of hydrogen release, possibly by formation of composite materials.[1–3]
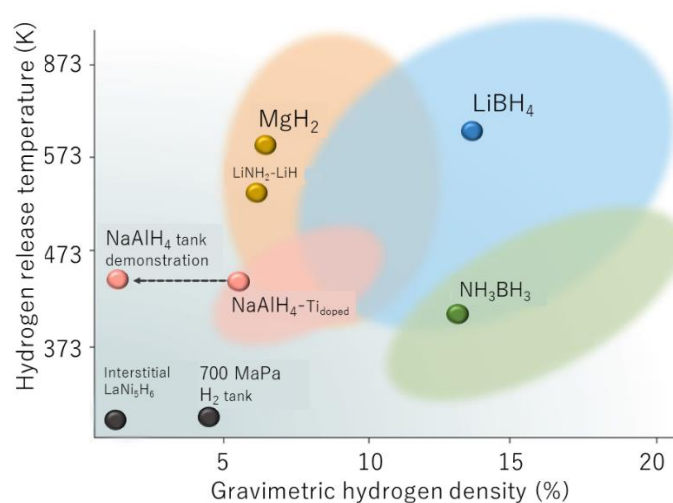
Figure 2. Hydride compounds with hydrogen storage properties based on their gravimetric hydrogen storage content and release temperature, taken from the literature.[3]

Important example is magnesium borohydride, $Mg(BH_4)_2$, which exhibits seven different polymorphs all characterized by the bidentate coordination of four BH_4 groups to each magnesium atom, forming framework structures.[6] Its structure will be shown and explained in details in Section 2.3.1.4. These polymorphs have very different densities, γ- and δ-$Mg(BH_4)_2$ are characterized by the densities of 0.55 and 0.99 g/mL and volumetric hydrogen densities of 82 and 147 g H_2/L, respectively.[7]

Metal (alkali and alkaline earth) borohydrides, as well as those containing also *d*-transition metals forming bimetallic borohydrides, are very promising for hydrogen solid state storage, because of the high hydrogen sorption densities (Table 2).[8–12]

Table 2. Structural, hydrogen adsorption and thermal stability data of bimetallic borohydrides.[13]

	$LiZn_2(BH_4)_5$	$NaZn_2(BH_4)_5$	$NaZn(BH_4)_3$
Space group	*Cmca*	$P2_1/c$	$P2_1/c$
a / Å	8.6244(3)	9.397(2)	8.2714(16)
b / Å	17.8970(8)	16.635(3)	4.5240(7)
c / Å	15.4114(8)	9.1359(16)	18.757(3)
β / °	90	112.658(19)	101.689(11)
Z	8	4	4
V / Å	2378.76(19)	1318.0(5)	687.3(2)
M / gmol^{-1}	211.93	227.98	132.91
ρ / gcm^{-3}	1.18	1.15	1.28
ρ_v (H_2) / kgH$_2$m^{-3}	112.6	101.6	116.9
ρ_m (H_2) /wt. %	9.51	8.84	9.10
T_{dec} / °C	127	95	103

2.1.2. Physisorption

Physisorption of hydrogen on the surface of the pores takes place in wide range of the materials such as Metal-Organic Frameworks (MOFs), porous carbons and zeolites. Although among the youngest members in the class of porous materials, one of the most extensively studied materials for hydrogen storage by physical adsorption are MOFs with defined inorganic-organic hybrid structures and permanent porosities. In MOFs, metal ions are linked together by the organic ligands forming a material with high surface areas. They are usually stable, cheap, and susceptible to chemical modification after the assembly of the framework and often show high gas adsorption capacities that are, of course, dependent on the surface area and pore volume.[14] Their biggest advantage is a fast adsorption and desorption kinetics. However, problems occur due to the fact that van der Waals interactions between hydrogen and the surface of the sorbents

are quite weak; lot of these materials have high storage capacities at liquid nitrogen temperature and high pressures, but at ambient temperature and pressure their capacities become very low due to the weak hydrogen-to-framework interactions. Main goal of the current research in this field is to improve hydrogen binding energies in MOFs by the optimization of pore volumes for hydrogen molecule adsorption or by the formation of additional hydrogen sorption sites within the frameworks.[15,16] The highest excess H_2 storage capacity reported so far for MOFs is 99.5 mg g^{-1} at 56 bar and 77 K in NU-100 (NU = Northwestern University), which is based on a hexatopic carboxylate ligand, LH6, and has a total capacity of 164 mg g^{-1} at 77 K and 70 bar.[17] The highest total H_2 storage capacity reported is 176 mg g^{-1} (excess 86 mg g^{-1}) in MOF-210 at 77 K and 80 bar.[18] The initial H_2 storage data reported for MOF-5 in 2003 (4.5 wt. % at 77 K and 1 atm) were later corrected to the maximum H_2 uptake to vary from 1.3 to 5.2 excess wt. % at 77 K depending on the preparation and handling conditions.[15,19]

2.1.3. Hybrid compounds

The new family of the coordination frameworks, Metal-Hydride-Organic-Frameworks (HOFs) are especially interesting for gas adsorption and separation, as well as for hydrogen storage. Their synthesis and characterization combine methodologies developed in the two relatively distant disciplines; HOFs can be designed by the combination of complex borohydrides as a molecular building blocks with the ligands, typically N-donor ligands, developed for the coordination frameworks. HOFs are expected to exhibit new properties defined by the nature of the unique complex-hydride ligands, such as guest-host interactions and dehydrogenation properties. They should also have interesting structural and microstructural characteristics, such as high porosity, wherefore HOFs show potential for gas adsorption and separation.[20] The reduction of atmospheric CO_2 concentrations can be achieved by its utilization as feedstock to obtain fuels, chemicals and materials, closing in this way the carbon cycling as nature does. To realize the important goal of industrial valorisation the first step is the capture and purification of CO_2 from different sources to be converted in useful products. In the majority of CO_2 transformation technologies its purity is crucial for its subsequent exploitation. However, flue gases from combustion of fossil fuels and industrial processes contain a wide variety of compounds, mainly N_2, CO, O_2, H_2O, NO_x, VOCs and variable CO_2 concentrations. Therefore the development of efficient sorption materials is needed.

The flexibility of the borohydride complex anion allows other cation coordinations, those that are not typically found within the coordination frameworks. Introducing directional anionic ligands, other than hydrides, such as imidazolates, isonicotinates or their derivatives offer the possibility of additional structural diversity. Imidazolate is the most promising ligand because the metal-imidazolate-metal angle (Figure 3) of 145° is very similar to metal-borohydride-metal angle[22, 23] observed for example in $Mg(BH_4)_2$.[7] Until now there has been no material that embodies both moieties, a hydride and an organic ligand in such manner to form a porous structure. However, polymeric anionic units $[Li_n(BH_4)_{n+1}]^-$ have been formed[21] and also observed as simple or complex chains, sheets and frameworks in bimetallic alkali-metal borohydrides $A_mLi_n(BH_4)_{n+m}$ (A = Rb, Cs).[22] Highly porous borohydride framework was observed in γ-$Mg(BH_4)_2$, the framework which is thermally stable, adsorbs reversibly guest species and withstands compression to 1 GPa. Change of the coordination environment for the Mg atom from a trigonal bipyramid to a tetrahedron as a consequence of desolvation at higher temperatures causes formation of denser structures.[7] The only known example where the borohydride anion is enclosed in the same structure with an organic ligand (imidazole) and forms a hybrid material is Li_2ImBH_4, which will be described more detail in 5.3.3.
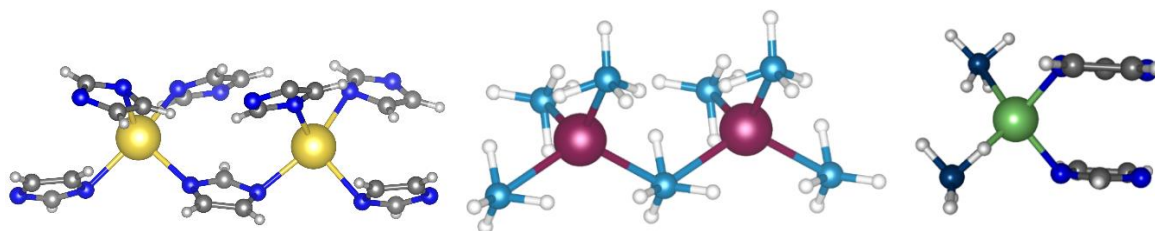
Figure 3. Similarity of metal-N(imidazolate)-metal and metal-borohydride-metal bond angle.[23]

2.2. MECHANOCHEMICAL SYNTHESIS

The importance of mechanochemistry as a method for synthesis of the solids was reported by Faraday in 1820, when he demonstrated the reduction of AgCl to Ag by grinding in a mortar and pestle a mixture of AgCl and Zn.[24] During the past few decades, mechanochemical synthesis has become one of the most popular methods for the preparation of a variety of compounds and has huge potential for development of novel approaches, such as solvent free synthesis methods in 'green chemistry'.[25] Several recent reviews,[26] provide an exhaustive overview of topics actively pursued and related to the application of mechanical energy for different chemical and structural transformations. A working definition from the mentioned review is: "*mechanochemistry refers to reactions, normally of solids, induced by the impact of*

mechanical energy such as grinding in ball mills". Other, considered formal definition by IUPAC states: "a mechanochemical reaction is a chemical reaction that is induced by mechanical energy".[27] Main processes occurring during the mechanochemical reactions are changes in the molecular structure which include both making and breaking of covalent bonds as well as the alterations in non-covalent interactions. In general, mechanochemical synthesis is a very effective preparation route that promotes reactions of solids quickly and quantitatively, with the minimal amounts of solvents or without any solvent at all. This feature is especially important because current dependence on solvents is unsustainable; they are environmentally problematic, hazardous and energy-demanding with regard to production, purification and recycling.[26]

Chemical interactions between solids happen exclusively at contacts between the particles, neither in the entire volume of the reacting compounds nor on their entire surface. The total number of such contacts between reacting particles is the basis at the initial steps of a solid-state reaction. That is why is always desirable to grind and mix components so that the aggregation of the particles of the same component is prevented.[28] A general term which describes mechanical action by hard surfaces on a material is grinding which usually happens in order to break up the material and reduce its particle size (Figure 4). This may be achieved by a manual method, such as mortar and pestle, or non-manual methods, such as ball milling, extrusion or similar. Grinding can be carried out without adding of solvents, so-called neat grinding (NG), or with a very small amount of added liquid, when it is called liquid assisted grinding (LAG). It is known that substances can react very differently in the solid state compared to the solution and even a very small amount of liquid may have a significant impact on the outcome of the solid-solid reaction.[26] Highly promising method of directing the structure by grinding starting materials with a small amount of an ionic salt additive is called ILAG (ion- and liquid-assisted grinding).[29]
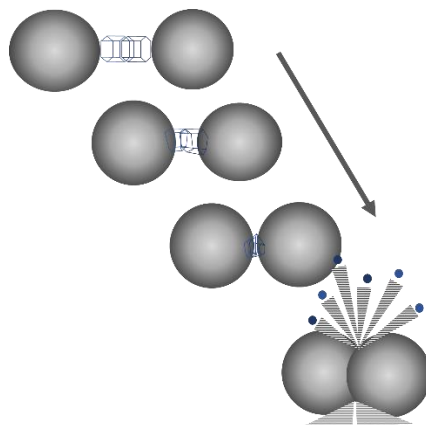
Figure 4. Scheme of the material grinding during ball milling, simplified from the literature.[30]

The most popular choice in research laboratories is high energy ball mill.[31,32] It includes one or more containers in which powder and balls are placed. Ball mills are widely available in different sizes and designs (Figure 5).[33] In attritor the balls are set in motion by rotation of the central shaft on which secondary arms are fixed and cylinder is fixed. Horizontal mill has cylinder which rotates around its horizontal axis and causes centrifugal force which in combination with gravity cause the balls to rise and fall onto the powder particles. In vibrational or shaker mill the vessel is set in vertical oscillatory motion and under this action, if the mill is one-dimensional, the ball rises and falls back onto the powder particles, and if it is three-dimensional, the balls collide with the side walls of the container (friction and impacts), but also with its floor and ceiling. Planetary mill has the containers which are fixed on a table which rotates in one direction and the containers themselves also rotate in the opposite direction. The centrifugal force causes the ground sample material and grinding balls to bounce off the inner wall of the grinding bowl, cross the bowl diagonally at an extremely high speed and impact the material to be ground on the opposite wall of the bowl.[34]
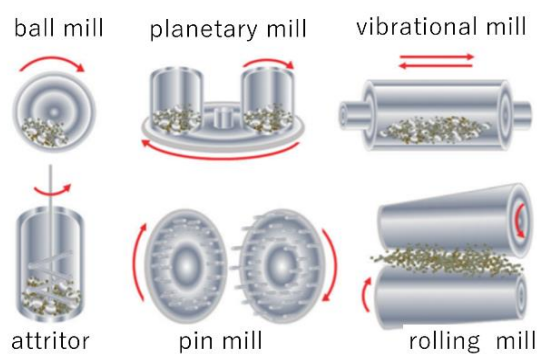
Figure 5. Types of mills for high-energy milling.[32]

2.2.1. Application and development of mechanochemical synthesis

Mechanochemistry has already been applied with success in different fields, starting with organic synthesis,[35–41] supramolecular chemistry[42–44] all the way to process engineering.[45] Often it is extensively used for the preparation of different types of compounds, such as biomaterials, catalysts,[46] nanoparticles,[32,47,48] biomaterials,[49,50] oxides,[51] materials for hydrogen storage,[52] cocrystals in pharmaceutical industry[54] and many other.[26,28,36,47]

There are some materials which cannot form in any other way but exclusively by the mechanochemical synthesis. Mechanochemistry can solve the problem of poor solubility of many organic compounds. Such example is the lack of solubility of fullerenes in ordinary solvents, but chemical reaction occurs when induced by milling.[54] However, if solubility is good, mechanochemical milling can improve the speed and selectivity of reaction. Such example is shown for some metal-organic complexes.[55] There are also reactions which are essentially thermochemical, where milling is needed only to bring together the reactants in appropriate relative configurations.[56] That is important because mechanical milling does not need to break covalent bonds which will break usually, it just needs to bring reactants so that required groups come into proximity and a click reaction takes place and the unique molecule forms.[57]

Although synthetic scope and methodology[58–60] in the field of mechanochemistry is progressing rapidly, the mechanistic understanding of mechanochemical reactions has remained unattainable.[61–63] It has been proposed that continuous mechanical stress and impact in a mechanochemical reaction environment promote unusual reactivity or intermediate phases different than those recorded using conventional chemistry.[64] Lack of evidence for such expectations can be assigned to a lack of methods that would permit direct, real-time insight into the rapidly agitated environment of an operating ball mill. The first methodology for time-resolved *in-situ* powder X-ray diffraction (PXRD) monitoring of mechanochemical reactions has been reported.[65] It utilizes the synchrotron radiation and offers an unique opportunity to monitor mechanochemical pathways and observe possible intermediate crystalline phases.[66] *In-situ* and real-time X-ray diffraction monitoring of mechanochemical synthesis[67] of zeolitic imidazolate framework, ZIF-8, revealed an unexpected amorphization-crystallization process which involves the intermediate formation of an unknown MOF, a metastable polymorph of ZIF-8.

A new type of *in-situ* ball mill setup has been developed at the Materials Science beamline (SLS, PSI, Switzerland). Improvements have been made in its geometry, what resulted in PXRD data displaying significantly lower background and much sharper Bragg peaks. This, in turn, allows more sophisticated analysis of mechanochemical processes, extending the limits of the technique.[68] Further improvement have been done and reported by the same group.[69] They have described an easy way to design and manufacture ball milling jars by three-dimensional printing. A reduced background/absorption and higher angular resolution, with the prospect for use at lower-energy beamlines, is reached by a modification of wall thickness and the use of a thin-walled sampling groove and a two-chamber design, where the milling and diffraction take place in two communicating volumes.[69]

2.2.2. Mechanochemical synthesis of borohydrides

In last few decades, novel metal borohydrides have been prepared mechanochemically [70] by the ball milling of alkali borohydrides, MBH_4 (M = Li, Na or K) with $ZnCl_2$. This reaction was firstly applied and reported in 1989.[71] During mechanochemical reaction small deviations in the composition of reactants may lead to significant difference in reaction products, both considering the stoichiometry and the structural topology. The structures of $NaZn_2(BH_4)_5$ and $NaZn(BH_4)_3$ are significantly different, so that may suggest that the underlying formation mechanism for these compounds is also different.[72]

$$2ZnCl_2 + 5NaBH_4 \rightarrow NaZn_2(BH_4)_5 + 4NaCl$$

$$ZnCl_2 + 3NaBH_4 \rightarrow NaZn(BH_4)_3 + 2NaCl$$
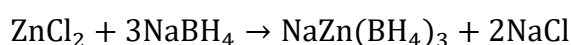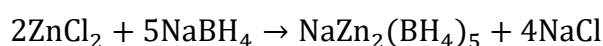
More detailed insight into chemical and structural diversity of the borohydride family of compounds will be given in Section 5.3.

2.2.3. Mechanochemical synthesis of porous MOFs

The first solvent-free mechanochemical synthesis of a microporous MOF was demonstrated in the acid-base reaction of copper acetate and isonicotinic acid (HINA).[73] The reaction led to the formation of the open framework $Cu(INA)_2$ containing robust 3D connectivity, with the acetic acid and water byproducts most likely included in the pores. Product was formed without any applied heating, what implies that energy of mechanochemical reaction was strong enough for the preparation of microporous MOF.[73,74] HKUST-1, an industrially relevant open framework

with pore diameter of about 9 Å is constructed by the same procedure, by neat grinding of copper(II) acetate and trimesic acid.[75]

The effect of LAG and ILAG has been reported by James *et al.*[26] Comparison between neat grinding and LAG in the presence of a small amount of water or AgCl with ethylenethiourea revealed the difference in the final products. AgCl(ethylenethiourea)$_3$ is the product in both synthesis, but neat grinding resulted in a slow partial formation of product while LAG yielded a quantitative formation of the product within 1 min. Difference in neat grinding products and products obtained by adding catalytic amounts of a liquid phase is observed in the reaction of silver iodide with ethylenethiourea; neat grinding did not lead to the formation of a product while LAG using small amount of water resulted in the quantitative formation of AgI(ethylenethiourea)$_2$.[26]

2.3. BOROHYDRIDES

Over the past decade, metal borohydrides have received increasing interest, because of their extremely rich chemistry, fascinating structural flexibility and different compositions and physical properties.[7,76–81] Borohydrides have a large potential for a variety of future applications, especially for the energy storage because of their high hydrogen density and possible uses in batteries and solid-state ion conductors. Here, boron and hydrogen form a simplest hydroborate anion BH_4^{-1}, commonly called borohydride, which is counterbalanced by metal cations. The boron-hydrogen bond in the complex anion, e.g. BH_4^-, is covalent, whereas the coordination to metals in the solid state is more diverse, ranging from ionic to more covalent with well-defined directionality.

Table 3 shows physical properties of light borohydrides. Most of these compounds are solids at ambient conditions, except liquid $Al(BH_4)_3$ with the melting point at -65 °C. They are sensitive to air and moisture, especially Al and Be borohydrides, so all handling and manipulation should be performed under inert atmosphere.

Table 3. Physical properties of selected metal borohydrides [82, 83]

Complex hydride	Weight (g/mol)	Density (g/cm^3)	Gravimetric hydrogen density (wt. %)	Volumetric hydrogen density (kg/m^3)	T_m (°C)	ΔH_f° (kJ/mol)
LiBH$_4$	21.78	0.66	18.36	122.5	268	-194
NaBH$_4$	37.83	1.07	10.57	113.1	505	-191
KBH$_4$	53.94	1.17	7.42	87.1	585	-229
RbBH$_4$	100.28	1.92	3.99	77.2		

CsBH$_4$	147.72	2.405	2.71	65.66	
Be(BH$_4$)$_2$	38.69	0.702	20.67	145.1	123^d
Ca(BH$_4$)$_2$	69.76	1.072	11.47	124.07	260^d
Mg(BH$_4$)$_2$	53.99	0.989	14.82	146.5	320^d
Al(BH$_4$)$_3$	71.51	0.7866	16.78	132	44.5^d

^{d}-decomposition before melting

Conventional X-ray, synchrotron X-ray and neutron powder diffraction methods are mainly used for investigation of the crystal structures of borohydrides.[84]

Usually, alkali and alkaline earth metal borohydrides are prepared by reactions in solution from NaBH$_4$ or LiBH$_4$ and metal chlorides or hydroxides. In the case of heavier alkaline earth borohydrides, the synthesis should be performed in cold methanol.[85] The biggest disadvantages of reactions in solution is that the final products often crystallize in the form of solvates, and sometimes is impossible to remove solvent molecules (for example Mg(BH$_4$)$_2$ from the THF solution, because the solvent removal leads to Mg-borohydride decomposition). Some other solvent, such as ether, is possible to remove by thermal treatment at 150 °C, as it is a case with Y(BH$_4$)$_3$.[86]

The production process of, for example, NaBH$_4$ has remained almost the same since 1950s, when synthetic pathways developed by Brown and Schlesinger[87] became commercial. Few economically more reasonable processes become viable.

Main step in this process is the reaction of sodium hydride (NaH) and trimethylborate (B(OCH$_3$)$_3$), TMB).

$$4NaH + B(OCH_3)_3 \rightarrow NaBH_4 + 3NaOCH_3$$
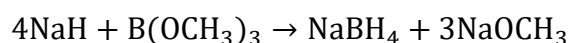
This procedure is expensive so several new procedures are or have been in operation, such as direct use of carbon, hydrocarbon or hydrogen reducing agents, multi-step thermo-chemical reaction pathways, reactions which utilize metals as reducing agents. Alternative ways include microwave and nuclear radiation synthesis or mechanochemical synthesis.[88]

Mechanochemical methods are often used as it was already mentioned in Chapter 5.2.2. Bi- and trimetallic borohydrides can also be prepared mechanochemically from monometallic borohydride precursors.

$$2CsBH_4(s) + LiBH_4(s) + Y(BH_4)_3(s) \rightarrow Cs_2LiY(BH_4)_6(s)$$
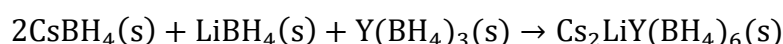
2.3.1. Monometallic borohydrides

For preparation of monometallic borohydrides, metathesis reactions, such as double substitution of metal halide and metal borohydride can be used, however problems related to the removal of halogen salt are possible.

$$MnCl_2(s) + 2LiBH_4(s) \rightarrow Mn(BH_4)_2(s) + 2LiCl(s)$$
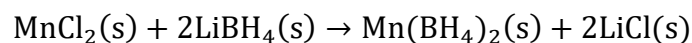
2.3.1.1. Lithium borohydride

Lithium borohydride, $LiBH_4$, is a reducing agent in organic and inorganic chemistry and is a potential hydrogen storage material. Structure of $LiBH_4$ has been studied by synchrotron X-ray powder diffraction at room temperature and at 408 K. Room temperature polymorph exhibits orthorhombic symmetry in the *Pnma* space group, $a = 7.17858(4)$, $b = 4.43686(2)$, $c = 6.80321(4)$ Å. Borohydride anions with tetrahedral geometry are aligned along two orthogonal directions and are strongly distorted with respect to bond lengths B–H = 1.04(2)–1.28(1) Å and bond angles H–B–H = 85.1(9)°–120.1(9)°. Upon heating, the structure undergoes transition and becomes hexagonal (*P6₃mc*); (Figure 6).[89]
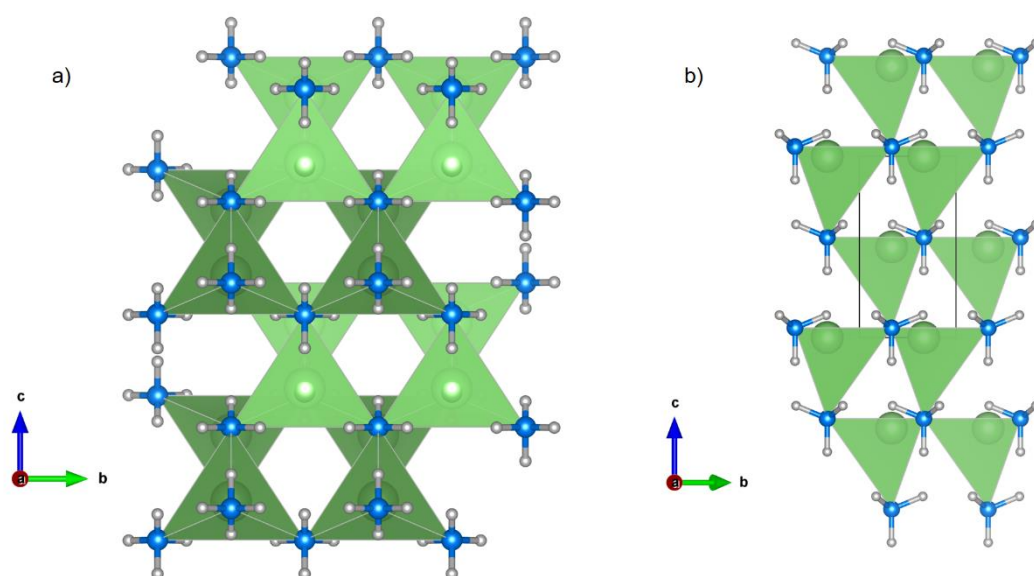
Figure 6. Crystal structure of $LiBH_4$ at a) room temperature (*Pnma*), and at b) 408 K (*P6₃mc*).

2.3.1.2. Sodium borohydride, NaBH₄

Sodium borohydride, $NaBH_4$, is a versatile reducing agent used in a number of industrial processes and can be used to store and generate hydrogen gas *via* a hydrolysis reaction.

Few different structures of $NaBH_4$ have been reported in the literature.[88, 90, 91] It is known that $NaBH_4$ can crystallize in three different polymorphs. At ambient conditions, the cubic α-phase is the most stable.[92] The α-phase crystallizes in a face-centered structure, space group $F\bar{4}3m$ and lattice parameter $a = 6.20$ Å. The high temperature (HT) phase is also cubic, with space group $Fm\bar{3}m$, and contains orientationally disordered BH_4 groups.[93–95] Cooling below 190 K reveals the transformation from the disordered cubic phase to the closely related ordered tetragonal phase which crystallizes in $P4_2/nmc$, but earlier it was solved in lower symmetry, in space group $P\bar{4}2_1c$ (Figure 7).

Stability and hydrogen desorption of $NaBH_4$ is investigated by dynamic pressure, concentration and temperature measurements under constant hydrogen flow. The decomposition occurs in one step and only one plateau is visible in the pressure composition isotherms. Possible decomposition products are given in Table 4.[88,90]

Table 4. Calculated thermodynamic data and lattice parameters of possible decomposition products.[88,90]

Species	$\Delta_f H$/kJmol⁻¹	a, b, c/Å	Space group	remarks
$NaBH_4$	-245.500	6.199	$F\bar{4}3m$	face-centred cubic
Na	0.0	4.214	$Im3m$	body-centred cubic
α–B	0.0	4.860, 4.860, 12.414	$R3m$	hexagonal
NaH	-45.519	4.867	$Fm\bar{3}m$	face-centred cubic
Na_2B_{29}	-105.213	10.240, 8.230, 5.755	$Im2m$	body-centred orthorhombic
Na_2B_{30}	-281.157	10.186, 8.339, 5.777	$Imam$	body-centred orthorhombic
Na_3B_{20}	-200.718	18.492, 5.623, 4.106	$Cmmm$	centred orthorhombic

The low-temperature phase shows tetragonal deformation, but cubic and tetragonal phases are closely related, with Na atoms and borohydride groups octahedrally coordinated in both structures. Difference between these phases lays in the patterns of H⋯H contacts. The shortest repulsive H⋯H interactions between the adjacent borohydride groups in the cubic phase favor disorder and their number is half of that in the hypothetical ordered $F\bar{4}3m$ structure. Lowering of the temperature causes shortening of the H⋯H distances which increases repulsions. When lattice symmetry in the tetragonal phase is lowered, ordering of the borohydride groups in a different way is allowed and number of the shortest H⋯H contacts is further reduced by one-third, while keeping the H⋯H distances nearly unaffected. That is why an isotropic disordered

3D network of the repulsive H⋯H contacts in the cubic phase transforms to an ordered 2D network which is oriented in the *ab* plane of the tetragonal cell.[90]
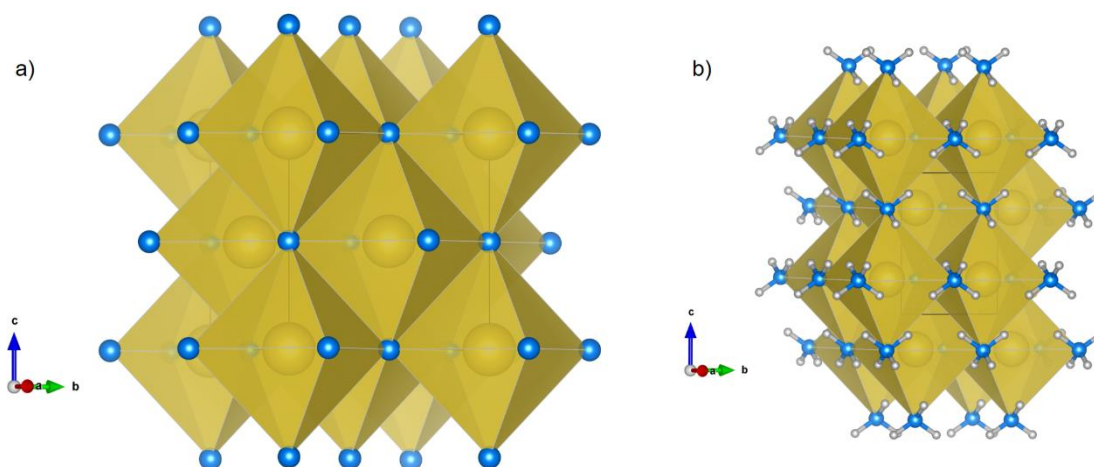
Figure 7. Crystal structure of NaBH$_4$ phases **a)** in $Fm\overline{3}m$ and **b)** $P4_2/nmc$.

2.3.1.3. Potassium borohydride, KBH$_4$

The room temperature structure of KBH$_4$ has cubic symmetry and it is isomorphous to that of NaBH$_4$ with space group $Fm\overline{3}m$, $a = 6.7306(1)$ Å. Transformation into a tetragonal low temperature phase which crystallizes in $P4_2/nmc$, $a = 4.7003(2)$ Å, $c = 6.5979(3)$, occurs at 65–70 K, at lower temperature than it is the case for the Na analogue (Figure 8).

Babanova[90] described how interatomic interactions have a determining effect on the physical properties of alkali metal borohydrides. As it was already mentioned, transformation temperature for KBH$_4$ is lower than for NaBH$_4$. This transition is driven by reducing the number of repulsive H⋯H interactions which are weaker in the case of KBH$_4$. That is because the larger potassium ions allow a bigger space between BH$_4$ anions. This weakening is expected to be accompanied by strengthening of the metal-hydrogen interactions (M⋯H).
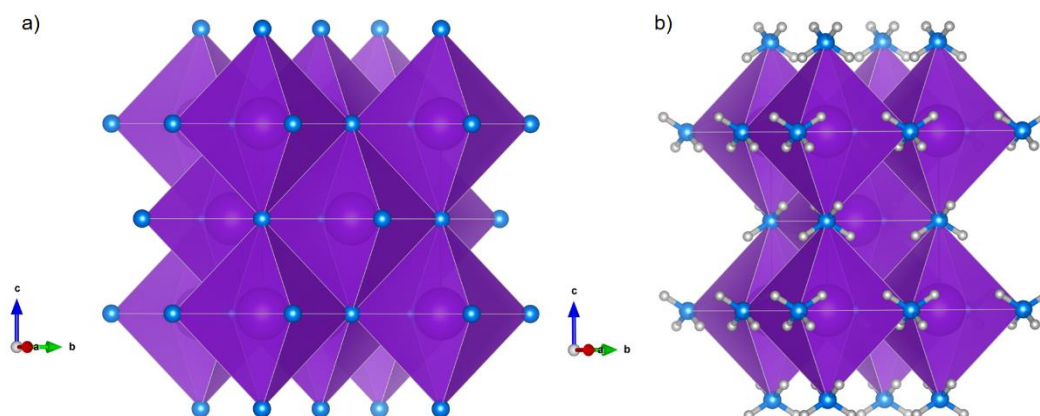
Figure 8. Crystal structure of KBH$_4$, **a)** at 295 K ($Fm\overline{3}m$) and **b)** at 10 K ($P4_2/nmc$).

2.3.1.4. Magnesium borohydride, Mg(BH₄)₂

Magnesium borohydride is a great example of an extreme structural flexibility among the family of metal borohydrides with seven, very different, crystalline polymorphs: α-, β-, β'-, ε-, ζ-, γ- and δ-Mg(BH$_4$)$_2$.[7,96–102]

Crystal structure of the most stable polymorph, α-Mg(BH$_4$)$_2$ was solved and refined by combination of synchrotron and neutron powder diffraction data, in the $P6_1$ space group. Although synchrotron data provided most of the needed information for structure solution, without neutron data, the correct orientation of the rigid borohydride tetrahedra could not have been determined.[98] Later, this structure has been revised in the space group $P6_122$ from single-crystal data[103] because in the $P6_1$ model, location of the H atoms from powder data posed the main problem for the identification of the correct symmetry.

Transformation from α-phase to β-phase occurs above 490 K. The high temperature structure can be described in the space group $Immm$, but modelling of all peaks was better in the 8 times bigger supercell with $Fddd$ symmetry.[97]

All magnesium borohydride structures are complex (Figure 9). The hexagonal structure (α-polymorph) has three symmetry independent Mg^{2+} cations and six symmetry independent borohydride anions. Borohydride groups bridge magnesium atoms, forming a framework with a novel 3D topology. It contains an unoccupied void of 37 Å^3; this volume is large enough to fit a small molecule, such as H$_2$O. The orthorhombic structure (β-polymorph) has two symmetry independent Mg^{2+} cations and five symmetry independent borohydride anions which by bridging magnesium atoms form a 3D framework. This structure contains no voids.
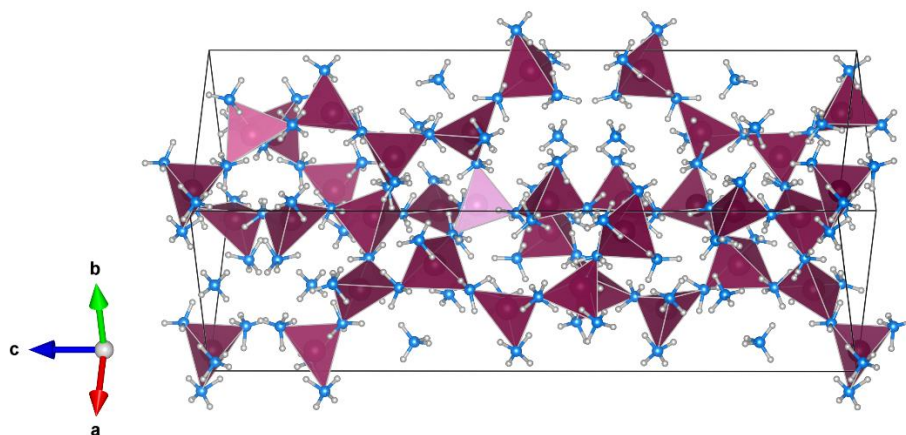
Figure 9. Crystal structure of α-Mg(BH$_4$)$_2$ ($P6_122$).

From the solvent-based synthesis, a dimethylsulfide (DMS) solvate of magnesium borohydride appears but DMS can be extracted at moderate conditions below 100 °C, resulting in the formation of highly symmetric cubic structure of γ-Mg(BH$_4$)$_2$ in the $Ia\bar{3}d$ space group with the magnesium atom tetrahedrally coordinated to the borohydride anions. This is the first hydride to have a large permanent porosity, with a 3D network of interpenetrated channels, where the narrowest part of the pore channel is defined by a 5.8 Å distance between hydrogen atoms. This magnesium borohydride polymorph has the framework topology isomorphic to both a hypothetical zeolite type polymorph of SiO$_2$ and porous zinc imidazolate framework, ZIF-72.[7,104] The most interesting feature of this compound is the amorphization of this porous compound at RT and recrystallization of porous compound upon heating at 80 °C. This polymorph transforms to δ-Mg(BH$_4$)$_2$ polymorph at high pressures (Figure 10).
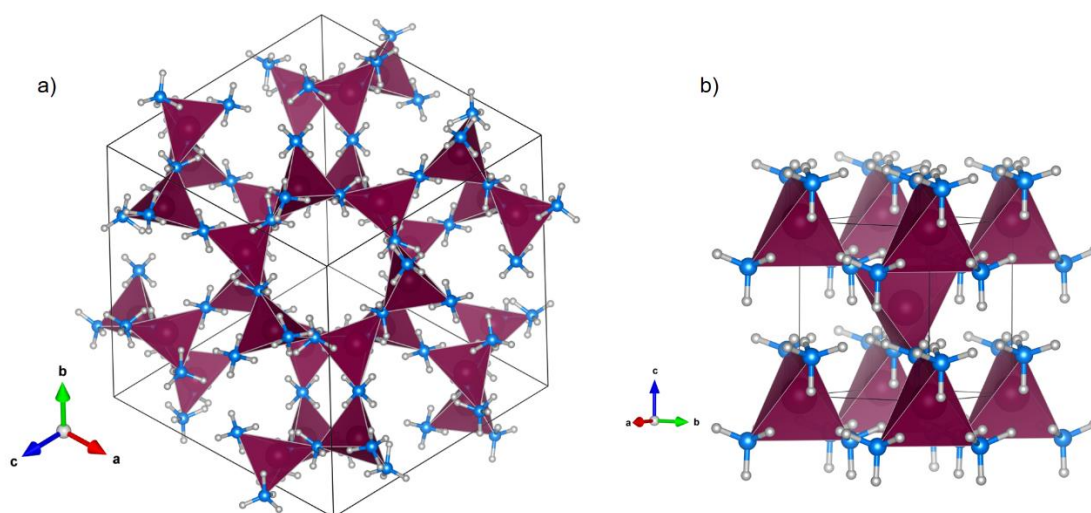
Figure 10. Crystal structure of Mg(BH$_4$)$_2$: **a)** γ-form and **b)** δ-form.

All Mg(BH$_4$)$_2$ polymorphs consist of BH$_4$ groups coordinated to two Mg cations *via* opposite tetrahedral edges with Mg–B–Mg angles deviating 3–20° from linearity. The interaction Mg···BH$_4$ is highly directional, and fragments Mg–BH$_4$–Mg can be considered as fundamental building blocks in all the structures. Strongly deformed tetrahedral environment is observed for magnesium atoms which coordinated to four BH$_4$ tetrahedra.

2.3.1.5. Manganese borohydride, Mn(BH₄)₂

In 2009, manganese borohydride was the first transition metal borohydride to be described and it was denoted as α-Mn(BH$_4$)$_2$, prepared mechanochemically from MnCl$_2$ and LiBH$_4$.[85] This polymorph is isostructural with ζ-Mg(BH$_4$)$_2$.[105] Today, four manganese borohydride polymorphs are known.[105–107] When dimethylsulfide is used as a solvent, different solvates can be prepared and gentle removal of the solvent provides a porous polymorph, γ-Mn(BH$_4$)$_2$, isostructural to the magnesium analogue described in the previous chapter, γ-Mg(BH$_4$)$_2$. The larger Mn^{2+} cation gives a bit larger unit cell volume for γ-Mn(BH$_4$)$_2$ compared to γ-Mg(BH$_4$)$_2$.[105]
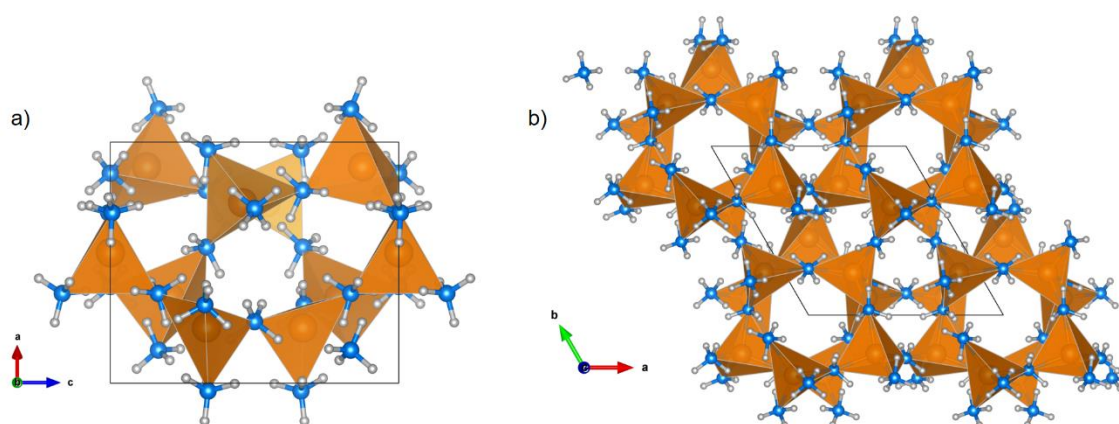
Figure 11. Mn(BH$_4$)$_2$ crystal structure viewed along **a)** *b* direction and **b)** *c* direction.

Crystal structure of α-Mn(BH$_4$)$_2$ consists two independent Mn atoms around which are four borohydride units exhibiting a deformed tetrahedral coordination. Each borohydride anion is nearly linearly coordinated by two Mn atoms through the opposite tetrahedral edges, same as in magnesium borohydrides. Same as α-Mg(BH$_4$)$_2$, α-Mn(BH$_4$)$_2$ has some degree of porosity in the structure, with the isolated voids of an estimated volume of 21 Å^3. Transformations from this phase to the high-pressure δ-phase is either to $P\bar{4}n2$ or $I4_1/acd$ space group (Figure 11).[107]

2.3.2. Mixed-metal borohydrides

Most of the bimetallic borohydrides consist of complex metal borohydride anions counterbalanced by alkali cations, where more electronegative metal constitutes the central atom in the complex anion by coordination to a number of borohydride units. Bimetallic

borohydrides can be divided into few groups, those based on *s*-block metals only, based on a *d*- or *f*-block metals with alkali metal and those based on a *p*-block metal and an alkali metal.

Here, group of alkali metal zinc borohydrides will be mentioned more detailed. Zinc coordination in several alkali metal zinc borohydrides is trigonal, where zinc is connected in a planar fashion to three BH_4 units forming a complex discrete anions, $AZn(BH_4)_3$ (A = Na, K). Two independent zinc atoms in $NaZn_2(BH_4)_5$ are coordinated by three BH_4 groups in nearly planar trigonal coordination with coordination number (CN) 3. Sodium atom have a saddle-like coordination (CN = 4). All BH_4 groups in $NaZn_2(BH_4)_5$ are linearly coordinated by two metal atoms forming a motif similar as in $Mg(BH_4)_2$.[96–98] The BH_4 groups are coordinated through the two opposite tetrahedral edges, bridging either two Zn atoms or one Zn and one Na atom. This structure consists of two identical doubly interpenetrated three dimensional (3D) frameworks. In $NaZn(BH_4)_3$, the Zn atoms have a distorted tetrahedral coordination with CN = 4 and, similar to more zinc rich compounds $AZn_2(BH_4)_5$ (A = Li, Na), Na atom has saddle-like coordination of four BH_4 groups (Figure 12). Here, metal atoms and BH_4 groups form a 3D network.[108]
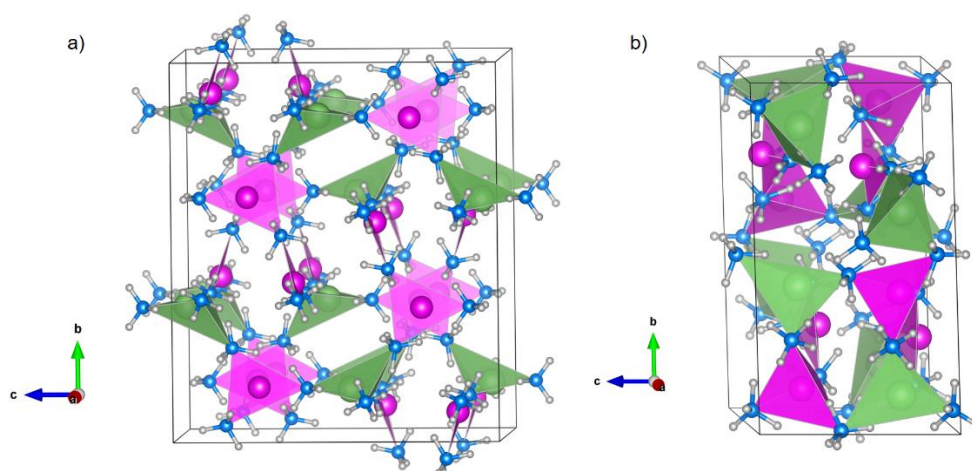
Figure 12. Crystal structure: **a)** $LiZn_2(BH_4)_5$ and **b)** $LiZn(BH_4)_3$

Two isostructural compounds have been found and characterized as the first trimetallic homoleptic borohydride compounds, $Li_3MZn_5(BH_4)_{15}$ (M = Mg, Mn) (Figure 13). They crystallize in $P6_3/mcm$ space group. The framework contains channels built from face sharing $[M(BH_4)_6]$ octahedra with triangularly coordinated lithium occupying the faces and consists of two interpenetrated frameworks. These compounds are potentially interesting as solid-state electrolytes, if the lithium mobility within the octahedral channels is improved by disordering

the site *via* heterovalent substitution. Decomposition of these two compound results in the formation of the more stable mono- and bimetallic borohydrides.[109]
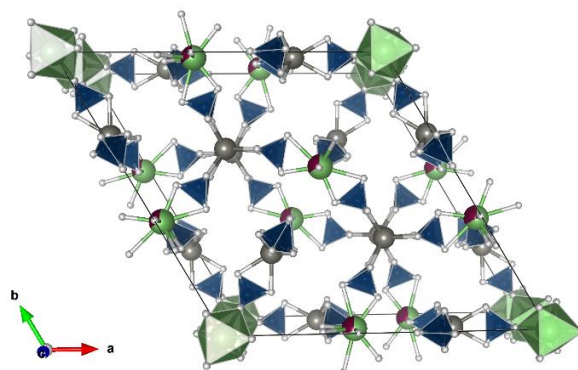
Figure 13. Crystal structure of first trimetallic homoleptic borohydride compounds, $Li_3MZn_5(BH_4)_{15}$ (M = Mg, Mn)

2.3.3. Hybrid borohydrides

By a combination of two different and independently acting compounds into one covalently linked hybrid compound, synergy from the effects of both independently acting moieties to the new composite compound can be conveyed, leading to the application properties greater than the sum of each individual moiety's potencies for application (such as lowering the decomposition temperature in the case of borohydrides).

Among the class of metal borohydride derivatives, two major groups should be mentioned: *i)* anion-substituted compounds where the complex borohydride anion, BH_4^-, is replaced by another anion (halide or amide) and *ii)* metal borohydrides modified with neutral molecules (NH_3, NH_3BH_3, N_2H_4). When talking about anion-substituted compounds, halide substitution in metal borohydrides is a valuable approach for tailoring physical and chemical properties and their structures can be either fully ordered, partly ordered or disordered. Boron-nitrogen compounds where borohydride anion is substituted by amide are also investigated intensively due to their hydrogen storage and ion conductivity properties.[70]

Metal borohydrides modified with neutral molecules possess competitive hydrogen storage properties. Compounds such as ammonia react with metal borohydrides by coordination tothe metals and by formation of dihydrogen bonds to borohydride groups.[2,70] NH_3, which can be catalytically decomposed to H_2 and N_2 is a great candidate for potential on-board hydrogen storage, mostly due to its high hydrogen content (17.3 wt. %).

Li₂ImBH₄ (Figure 14) is a hybrid material, the only known example where borohydride anion is embodied in the same structure with the organic ligand, namely imidazolate. It can be synthesized either by milling of LiIm and LiBH₄ with small amounts of solvent (DMS or diethyl ether), or by heat treatment at 100 °C. It crystallizes in ortorhombic cell, in the space group *Imma*. Crystal structure has been solved from synchrotron radiation powder data, but the orientation of the borohydride group could not have been determined from PXRD data, so neutron diffraction has been carried out in order to fully elucidate structural features. Imidazolate anion is coordinated with four Li atoms, two Li atoms on every nitrogen atom, below and above the plane of aromatic rings. The Li–N bond length is 2.085 Å. The borohydride anion is coordinated with four Li atoms, in a square coordination. The Li cation is connected to two imidazolates and two borohydride groups in a deformed tetrahedral coordination.[110]
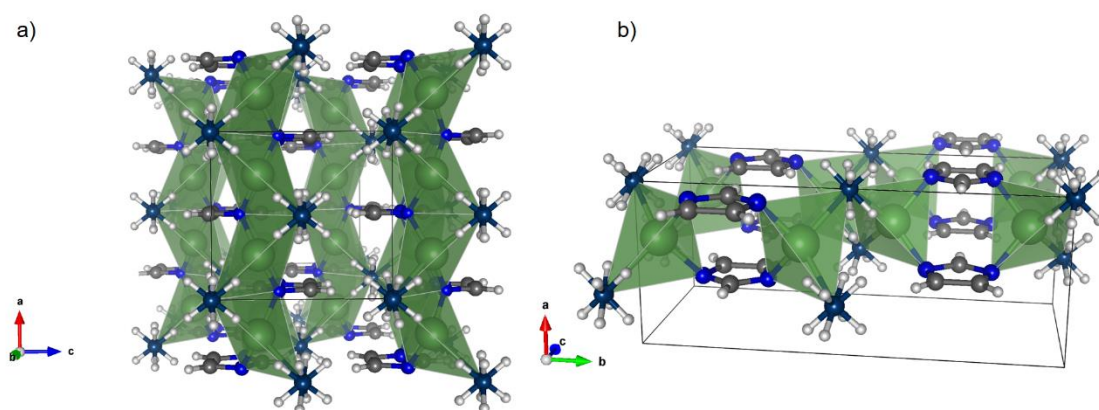
Figure 14. Crystal structure of Li₂ImBH₄, **a)** chains of tetrahedrally coordinated lithium atoms in *c*-direction and **b)** sheet parallel to the *bc* plane.

2.4. BIMETALLIC IMIDAZOLATES

Bimetallic imidazolates are particularly scarce in the literature, although imidazolates, in general, possess extremely rich and versatile coordination potential.[96, 110] Among the few known, the 2D grid-shaped coordination polymer [Co^{II}Cu$^{I}_2$(Im)₄] has been reported.[111] The asymmetric unit consist of a tetrahedrally coordinated cobalt(II) atom and a linearly coordinated copper(I) ion. Metal centers are bridged by a deprotonated imidazole molecule. The structure of Cu₂ZnIm₆ shows an interesting network of alternating zinc and copper atoms bridged by imidazolate moieties. Copper and zinc atoms are surrounded by two and four imidazolate nitrogen atoms, respectively.[112] It is interesting to highlight that bridge Cu(I)–Im–Zn(II) is analogous to those found in copper-zinc superoxide dismutase metalloenzymes.[113]

The zeolitic imidazolate frameworks are not restricted to exclusively tetrahedral nets; octahedral coordination environment of indium(III) is found in an imidazolate based bimetallic coordination net, $In_2Zn_3(Im)_{12}$, with a topology of the $Al_2Si_3O_{12}$ part of a garnet.[23] Great dynamic uptake selectivity for CO_2 over methane under wet conditions has been demonstrated for bimetallic imidazolates.[114] Considering all mentioned, it is safe to conclude that there is, indeed, a very rich and versatile structural chemistry awaiting systematic exploration of imidazolates.

All mentioned examples of bimetallic imidazolates include transition metal atoms, but no study on the mixed-metal imidazolates containing alkali and alkaline earth metals has been reported. Alkali imidazolates (LiIm, NaIm, KIm) (Figures 15 and 16) form the dense and hypercoordinated structures and coordinative demands of the metal cations increase with an increase of the ionic radii, so Li^+ cation likes to form heteroleptic structures, while K^+ coordinates imidazolate ring through the π-system.[115]
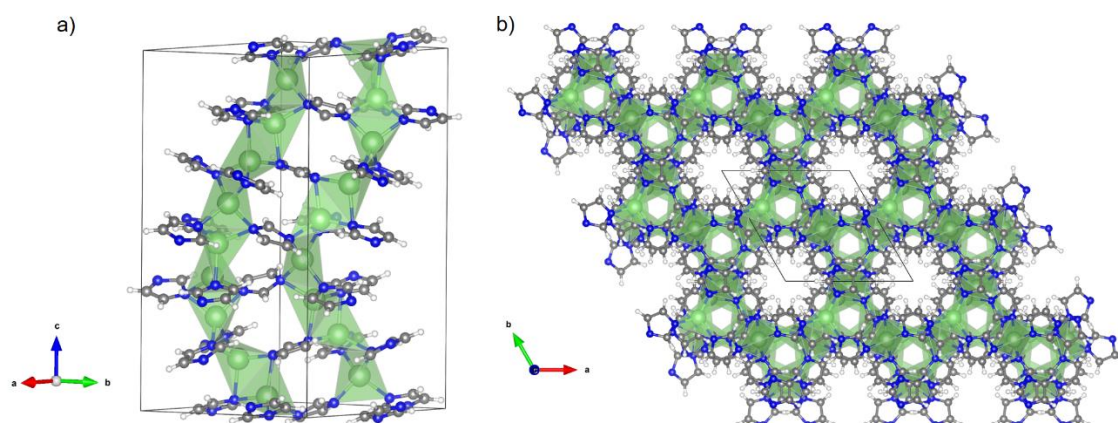
Figure 15. Crystal structure of LiIm , **a)** chains of tetrahedrally coordinated lithium atoms, in the *c*-direction and **b)** three-dimensional dense framework viewed along the *c*-direction.
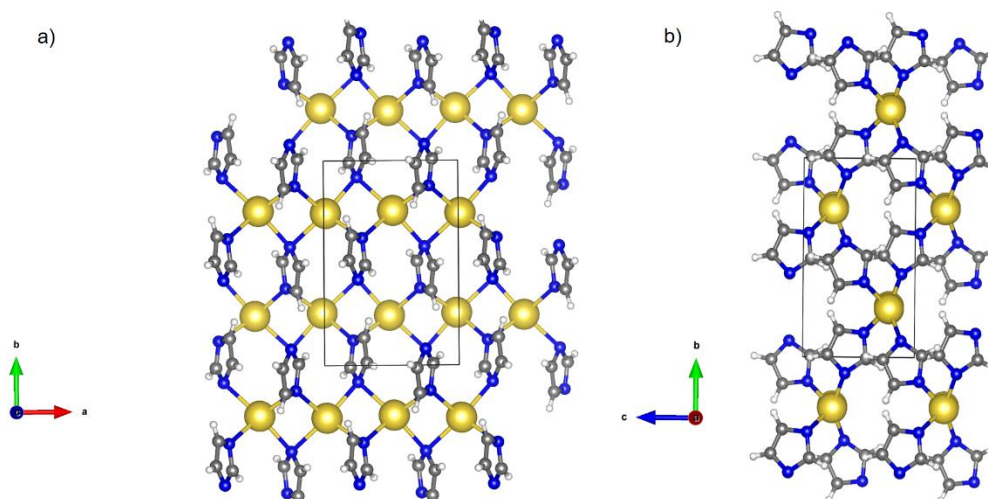
Figure 16. Three-dimensional dense framework of NaIm viewed along: **a)** *c*-direction and **b)** *a*-direction.

When alkaline earth metal was utilized, porous zeolitic imidazolate framework was observed in the case of magnesium imidazolate (MgIm$_2$) (Figure 17).[115, 116]
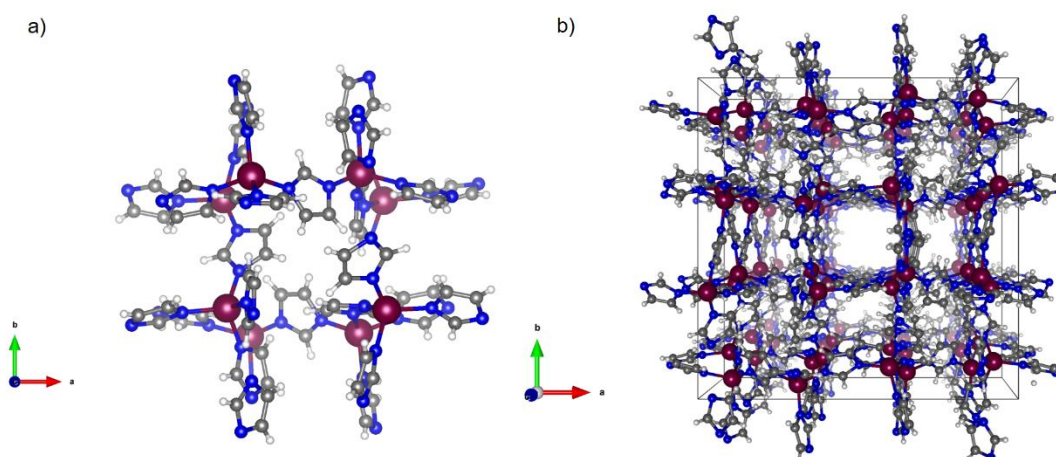
Figure 17. Three-dimensional porous structure of MgIm$_2$ viewed along the *c*-direction **a)** magnesium atoms connection *via* bridging imidazolates and **b)** cage-like extended packing showing channels along the *c*-direction

2.5. THEORETICAL DESCRIPTION OF THE EXPERIMENTAL METHODS

2.5.1. X-ray diffraction

2.5.1.1. Physical background

X-ray crystallography is considered to be an experimental technique which exploits the fact that X-rays are diffracted by crystals. It is a versatile, non-destructive analytical technique for identification and quantitative determination of the various crystalline forms and phases, present in crystalline samples. The X-rays wavelength is in the Ångström range (1 Å = 10^{-10} m), so they can be scattered by the electron cloud of an atom of comparable size. Electron density can be reconstructed from the diffraction pattern obtained from X-ray scattering off the periodic assembly of molecules or atoms in the crystal. So the spatial distribution and intensity of scattered X-rays or electrons provide information on the arrangement of atoms in a periodic sample.[2, 117, 118] Each atom contains multiple electrons which are distributed around a nucleus, so scattering power of atoms is proportional to the total number of electrons, Z. The atomic scattering function, $f(\theta)$, also called the form factor, is property of every element and it presents an intrinsic angular dependence of the X-ray amplitude on scattering angle θ. So, the diffraction pattern of stationary, periodically arranged atoms is the result of a superposition of interface and the corresponding squared scattering function.

Basic relation which describes how the periodic lattice produces diffraction maxima at specific angles defined by both the lattice repeat distances (*a, b, c*) and the X-ray wavelength (*λ*) is Braggs' law (Equation 1). d_{hkl} is the distance between crystallographic planes, θ_{hkl} is the angle of the diffracted beam, *n* is integer (order of reflection) and λ is the X-ray wavelength.

$$2d_{hkl}\sin\theta_{hkl} = n\lambda \tag{1}$$

F_{hkl}, the structure factor, is defined by the details of the crystal structure of the material: coordinates and types of atoms, their distribution among different lattice sites and thermal motion. Therefore, a diffraction pattern produced by a crystal is also a function of the triplet of Miller indices (*hkl*). The intensities of reciprocal lattice nods (*hkl*) in the reciprocal space are proportional to the squared structure factor moduli (Equation 2)

$$I(hkl) \propto |F_{hkl}|^2 \tag{2}$$

Structure factor can be described from the known coordinates for the *j* atom of x_j, y_j and z_j according to Equation 3.

$$F_{hkl} = \sum_j f_j \exp(2\pi i (hx_j + ky_j + lz_j)) \qquad (3)$$

The diffraction pattern of a crystal material is a transformation into reciprocal space of its ordered atomic structure. That means that the 3D distribution of the atoms in the lattice, the direct image of the crystal, can be restored only after the diffraction pattern has been transformed back into direct space, what is done by Fourier transformation with the calculated phase information. In order to complete the reconstruction, additional phase information must be extracted either from the diffraction data or from additional diffraction experiments. To obtain a quite accurate molecular structure, a model should be progressively built into the experimental electron density and refined against the data. The maximum on the electron density map shows the positions of the atoms, from which the crystal structure might be solved.[118, 119]

Although restoring a crystal structure by applying Fourier transformation to diffraction data is a quite simple process, the fact that the structure amplitude is a complex quantity creates the "phase problem". To locate atoms in the unit cell, both the absolute values of the structure amplitudes and their phases are needed. The structure amplitudes can easily be determined both from single crystal or powder diffraction data, but their phases are lost during the experiment. During the crystal structure solution process, the lost phase angles must be recovered using a suitable numerical technique. It is important to separate this from the refinement process which improves the structural parameters of the approximately or partially known model, usually by using the least squares minimization against available diffraction data. So the least squares method is not applicable to the ab initio structure solution because the structure amplitude is a non-linear function of multiple individual atomic parameters.[118]

2.5.1.2. Comparison of single and powder X-ray diffraction

Single-crystal and powder X-ray diffraction are the two main methods in the field of materials structures research. A sample is considered to be a single crystal or monocrystalline if the lattice is continuous and unbroken in the entire sample and it is optically clear with no grain boundaries. The size of the single crystal should be small, preferably in the range from 0.1 to 0.2 mm.[118, 119]

The powder diffraction pattern can only be obtained from a sample containing an "infinite" number of individual particles realizing an "infinite" number of orientations in the irradiated volume. That means that the particles in the specimen should have a completely random

distribution of crystallographic orientations of grains or crystallites with respect to one another. It is obvious that this ideal situation is impossible to achieve, but if one takes in account a 10 mm diameter and 0.1 m deep sample holder filled with 50 μm diameter spherical particles, it will hold nearly $9 \cdot 10^4$ of such particles, assuming close packing of the spheres. With reduced sizes even more particles can fill the same volume. Due to the fact that these are large numbers, it may be considered sufficient to approximate the infinite quantity of particles required for collecting powder diffraction data. The majority of materials examined by powder diffraction are not initially in the state suitable for the straightforward preparation of the specimen. If the material is not already in the form of a fine powder with average particle size between 10 and 50 μm, the size of the particles should be reduced.[118]

It is obvious that it would be a time consuming operation to reorient the single crystal in order to measure the angle θ and determine the d-spacing for all atomic planes. A faster way is to use fine powder where thousands of grains have random orientations, and to simply assume that most of the different atomic planes lie parallel to the surface in some of the grains.[120] Structure solution from powder diffraction data can be considered as problem-solving process; although it is quite complicated, complex and non-trivial task compared to determination of structures from single crystal data, the big advantage of this technique is that the huge variety of products from different types of synthesis, such as mechanochemical synthesis, can be structurally characterized.[121] Additional advantages of the technique are: simplicity of sample preparation, rapid measurement and the ability to analyze the mixture of phases. The downside of technique is based on the fundamental fact; plenty of information is lost by the collapse of the 3D space onto a 1D axis. Nevertheless, a nice example, ilustrating the power of powder diffraction, is given by Pan, where they have compared crystal structure of griseofulvin ($C_{17}H_{17}ClO_6$) solved from single crystal diffraction and powder diffraction data (Figure 18). Lattice parameters from powder data are: $a = b = 8.9759$ Å, $c = 19.9345$ Å, $V = 1605.99$ Å^3. From single crystal data these values are: $a = b = 8.9714$ Å, $c = 19.8848$ Å, $V = 1600.46$ Å^3. From these results, single-crystal X-ray diffraction has validated the accuracy of PXRD. The slight difference of molecular structure may be attributed to obscured diffraction intensities which result from the loss of 3D single-crystal data when transformed into 1D powder diffraction data.[121]
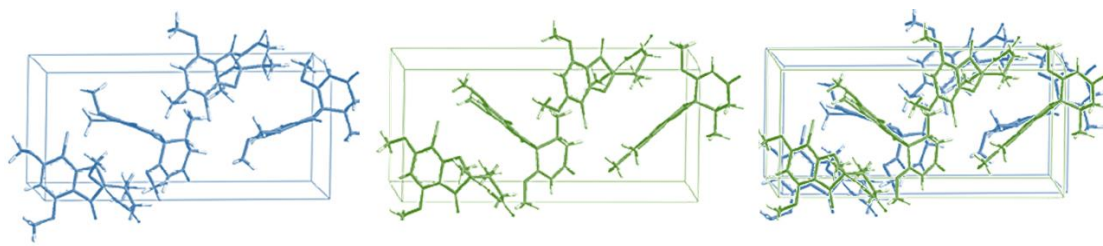
Figure 18. Crystal structure of griseofulvin as determined by powder X-ray diffraction (blue), and single-crystal X-ray diffraction (green). Both models are also shown in an overlap manner.[121]

2.5.1.3. Information encoded in a powder diffraction pattern

In order to understand how structural information is encoded in a powder diffraction pattern (Figure 19), that pattern is considered as a set of discrete diffraction peaks (Bragg reflections) superimposed over a continuous background. Background can be used to extract some information about the crystallinitiy of the sample, but the aim is to minimize it during the experiment.
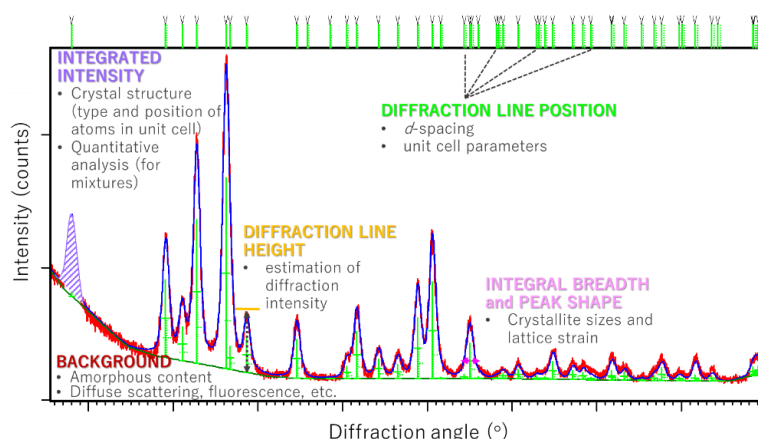
Figure 19. Anatomy of powder diffraction pattern.

For structure determination from powder data, individual Bragg peaks should be located on the pattern, their positions and intensities should be determined by fitting to a certain peak shape function, including the background (Table 5). To establish the unit cell symmetry, both parameters and content, peak positions are used. To determine space group symmetry and coordinates of an atom, peak intensities are used. To refine all crystallographic and peak shape function parameters, including background, the entire diffraction pattern is used.

A lot of factors have an impact on the precise determination of peak intensities. Those are the intrinsic structural factors, dependent on the crystal periodicity itself, the specimen factors owing to its microstructure i.e. shape and size, grain size and distribution and other sample-related features, or finally, instrumental factors which depend on the radiation, type of focusing

geometry, properties of the detector, slit or monochromator geometry. Structural factors depend on the internal, atomic, structure of the crystal, described by relative positions of atoms in the unit cell, their types and other characteristics, for example thermal motion and population parameters.[118]

Table 5. Powder diffraction pattern as a function of various crystal structure, specimen and instrumental parameters, taken from the Ref. [118]

Pattern component	Crystal structure	Specimen property	Instrumental parameter
Diffraction line position	Unit cell parameters: $(a, b, c, \alpha, \beta, \gamma)$	Absorption Porosity	Radiation (wavelength) Instrument/sample alignment Axial divergence of the beam
Integrated intensity of diffraction line	Atomic parameters $(x, y, z, B, \text{etc.})$	Pref. orientation Absorption Porosity	Geometry and configuration Radiation (Lorentz, polarization)
Peak shape	Crystallinity Disorder Defects	Grain size Strain Stress	Radiation (spectral purity) Geometry Beam conditioning

2.5.1.4. Synchrotron radiation X-ray powder diffraction

The accuracy and reliability of the technique, same as the wealth of the information that can be extracted, is defined by the quality of an XRPD pattern. Synchrotron radiation X-ray powder diffraction (SR-XRPD) holds the first place in data quality. It is widely superior to laboratory XRPD in terms of angular resolution, counting statistics energy tunability and fast acquisition time.

The X-rays here are generated by a synchrotron facility and are at least five orders of magnitude more intense than the best laboratory source. The efficient data collection with acquisition times ranging from milliseconds to few minutes allow the control of the inevitable radiation damage of organic compounds. Also, it is possible to perform kinetic studies of structural changes during the chemical reactions or under temperature and pressure variations.[122]

There are number of advantages of synchrotron radiation in comparison with laboratory sources, but most important are: high brightness and high intensity, many orders of magnitude more than X-rays from X-ray tube; high collimation, small angular divergence of the beam; high level of polarization; low emittance, the product of source cross section and solid angle of emission is small; large tunability in wavelength by monochromatization; pulsed light emission which allows ultra-fast time-resolved studies. Other techniques which may be carried out at synchrotron sources are absorption, imaging, diffraction tomography.[122, 123]

For tracking the thermal expansion of solids or temperature-induced structural changes, the best way is to use high temperature XRPD measurements. These studies can be fulfilled on synchrotrons gaining high resolution and high flux. Samples can be loaded in glass capillaries and heated using a hot-air blower.

The importance of high resolution for correct determination of the number of reflections contributing to the observed maxima, is their positions and intensities.[124] Figure 20 shows a comparison of three powder diffraction data sets of the same compound (monoclinic $(C_2N_2H_9)[MnPO_4]\cdot H_2O$), collected with three different instruments using the same wavelength.
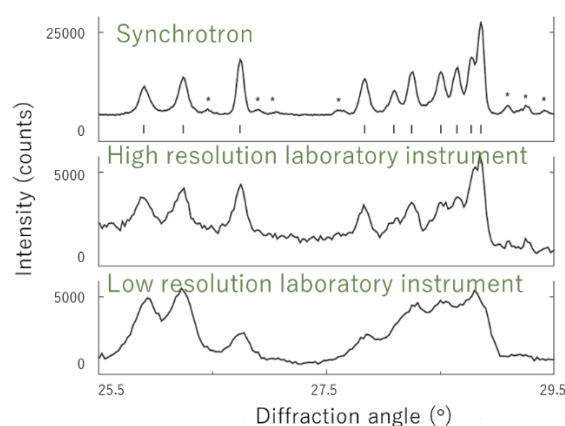
Figure 20. Comparison of diffraction data of $(C_2N_2H_9)[MnPO_4]\cdot H_2O$ collected on three different instruments using the same wavelength.[124]

2.5.2. Crystal structure solution from powder X-ray diffraction

Although the structure solution from powder diffraction evolves all the time, still is far from being routine. Currently, major challenges of powder crystallography refer to *ab initio* crystal structure determination on real samples of new materials with specific microstructures, characterization of intermediate reaction products from *in situ* and *in operando* studies and novel phases from *in situ* studies of phase diagrams.[125]

2.5.2.1. Steps of the procedure of crystal solution from PXRD

The procedure of crystal structure determination from powder diffraction data can be divided into the following steps:

    a) data collection,

    b) indexing,

    c) space group determination,

d) pattern decomposition (when needed),

e) structure solution,

f) completion of the structure (if model is not complete)/optimization of model and

g) final refinement.

Decision at most of the steps is usually not unique and some steps depend on the other. Final structure is achieved if it gives a good fit with a chemically reasonable model.

a) Data collection

Prerogative for structure solution from PXRD is diffraction data collection of highest possible quality. High resolution can be achieved by the utilization of narrow slits and large diffractometer radii (synchrotron source-based diffractometers reach great resolution). Good angular accuracy can be attained by modern diffractometers with certain geometries (Debye-Scherrer and Bragg-Brentano) and by careful mounting of the sample. Finally, accurate intensities are most difficult to obtain because lot of parameters should be fulfilled: optimal size of the crystallites, absorption for capillary measurements should be taken into account, surface roughness and preferred orientation should be avoided for flat plate geometry.

b) Indexing

Due to the fact that powder pattern contains only information of interplanar spacings and no information on the angles between crystal planes, indexing can be, despite an intense development in indexing algorithms, a bottleneck of the structure solution in the case of low-resolution powder patterns, in the case of multiphase systems or in the case of low symmetry structures (monoclinic and triclinic). Powder indexing often is carried out easily on high quality diffraction data, but on pure data indexing procedure is everything but straightforward. If the initial trials fail, the advice is to try another program which uses a different algorithm. The most popular indexing programs are: DICVOL04,[126] N-TREOR,[127] McMaille,[128] FOX,[129, 130] EXPO2004,[131] Topas,[132] X-Cell.[133] Among the indexing algorithms, dichotomy algorithm is mostly used in this thesis. The dichotomy algorithm is very fast (especially in FOX) and robust towards low data quality. In multiphase system problem of correct indexing can be solved in several ways. For example, in the case when sample composition is completely unknown several approaches are considered valuable in order to determine the structure: dividing peaks into groups of sharp and broad, resynthesis or recrystallization under different experimental conditions or heating of sample where one phase may disappear at elevated temperatures.[125, 134]

c) Space group determination

Determination of the space group is based on the extinction rules for reflections. The biggest problem is reflection overlap that often prevents finding out which reflections are absent; that is particularly pronounced at higher diffraction angles. This might lead to uncertainty regarding the choice of correct space group among several proposed all of which are possible. Very complicated case happens in monoclinic system where the extinction rules for $P2_1/c$, $A2$, Am, $A2/m$ are equal for the first few isolated reflections but the overlap at higher angles prevents an ambiguous decision, what is shown in Figure 21 for pattern of $C_7F_{15}COOH$. Unfortunately, when there is no way to distinguish which group is the correct, the only solution is to try all possibilities. If none of the possibilities provides correct structure solution, good way is to return to earlier stages of the structure solution process in order to correct wrong decisions in previous steps, such as incorrect indexing.[124]
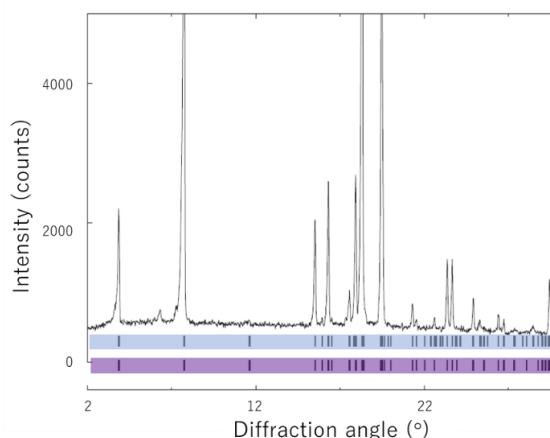
Figure 21. The extinction rules for $P2_1/c$ (upper bars), $A2$, Am and $A2/m$ (lower bars) are equal for the first few isolated reflections but the overlap at higher angles prevents an ambiguous decision. [124]

d) Powder Pattern Decomposition

This procedure is performed in order to extract a "single-crystal-like" data set from the powder pattern. After this, all methods used for single crystal, can be applied for powder data also. With powder data there are always errors in the extracted intensities caused by the overlap of reflections. Extraction is done by fitting the powder pattern by varying the unit cell parameters, profile parameters and intensities of allowed reflections in the assumed space group. Usually, this is done by LeBail's[135] method or Pawley's[136] method. Pawley's method treats intensities as individual variables in the least squares fitting what might cause negative values of some of

these intensities, what is not physically reasonable. Bayesian statistics[137] is used for improvement of this feature. In LeBail's procedure, an iterative redistribution of initial intensities is widely used. Intensity of each point in the pattern is distributed among the contributing reflections, taking into account the profile of reflections. LeBail's method can start both from unbiased model where all intensities are initially set to 1 and from a biased model where the initial intensities are calculated from a partial structural model. The use of former option automatically leads to equipartition of overlapping reflections and latter gives a data set with better partitioning. That means that distribution of the intensities of reflections contributing to a single observed diffraction maximum is better when starting from a biased model and this model can be used as a feedback in an iterative solving process. On the other hand, the unbiased extraction is used to obtain a starting rough structural model which then improves the extracted intensities which give a better model.

This step of powder pattern decomposition is not necessary for all methods of structure solution from powder data.

e)   Methods for structure solution

General classification of the structure solution methods is into two groups: intensity extraction (IE)-based algorithms which work with reciprocal space (so called reciprocal space methods) and pattern modelling (PM)-based algorithms which work in the direct space and use the chemical knowledge from that space (so called direct space methods or global optimization methods). Algorithms working in the direct space have to know how to define basic structural units of the crystal which will be then optimized by the algorithm. From that it is obvious that molecular or non-molecular boundary is relevant for the choice of a structure determination method. Reciprocal space methods are used when high resolution powder patterns are available. Direct space methods are slower, but used for real conditions of crystallization, in situ studies of reactions and phase transitions. These methods work with patterns containing broadened, overlapped peaks, with patterns of low-resolution powder data of ~2 Å and there is no need for extraction of integrated intensities. Mostly used algorithms are parallel tempering, simulated annealing and reversed Monte Carlo.[125] In this thesis direct space methods have been used mostly. When solving a structure ab-initio in direct space, that means that structure is described through a number (N) of degrees of freedom (DoF), such as translation and rotation of the molecule of polyhedron or internal DoF like torsion angles, bond length and bond angles. By

randomly changing these parameters, minimal cost which indicates best agreement between the calculated and experimental powder pattern should be found (Figure 22).[138]
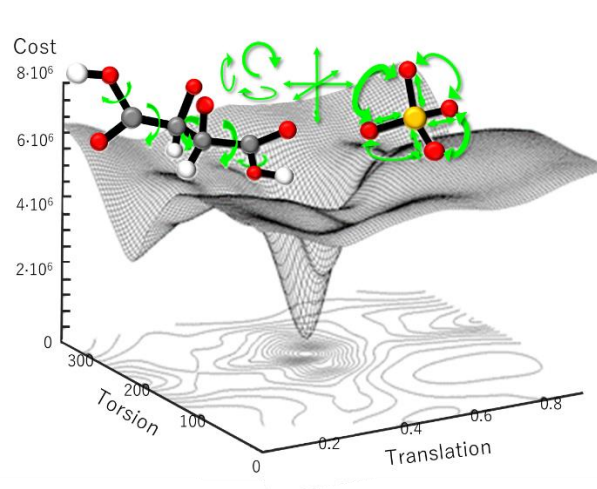
Figure 22. Ab-initio direct space methods for structure solution-finding the minimal energy.[138]

f) Structure completion

In cases when only a partial structural model is obtained during solving procedure, there are few ways to complete the structure. For example, recycling can be done, like in biased extraction. The most commonly used approaches are geometrical modelling and Fourier recycling, which is the same as for single crystal data, only with different sharpness of the Fourier maps. These methods are used together and may be combined with a partial Rietveld refinement.[124]

g) Structural refinement

Obtained structural parameters have to be fitted in such a way to achieve as good fit of the calculated diffraction pattern in respect to the observed pattern as possible, while keeping the structural model chemically reasonable. Widely used, Rietveld[139] refinement will be explained more detailed in next chapter.

2.5.2.2. Rietveld refinement in X-ray powder diffraction

Mostly used in practice, as well as in this thesis, is the Rietveld method[139] for the refinement of crystal structures. It utilizes the least-squares refinement in order to minimize the difference between the observed and calculated profiles from the whole pattern (Figure 23). Following parameters are typically refined: background parameters, a zero-point error for the detector, scale factor, lattice parameters, atomic coordinates, temperature factors, as well as the

parameters which describe the half-width with scattering angle and the peak shape. The peak shapes are modelled by combination of Gaussian/Lorentzian peak shape (profile) functions. The calculated intensities y_{ci} are determined from the structural model $|F_{hkl}|^2$ by summing the background y_{bi} and calculated contributions from neighboring Bragg reflections, which contribute to the intensity y_i, the intensity observed at any arbitrary chosen point, i (Equation 4).

$$y_{ci} = s \sum_{hkl} L_{hkl} |F_{hkl}|^2 \, \phi(2\theta_i - 2\theta_{hkl}) P_{hkl} A + y_{bi} \qquad (4)$$

s is the scale factor, L_{hkl} contains the Lorentz polarization and multiplicity factors, ϕ is the reflection profile function, P_{hkl} is the preferred orientation function, A is an absorption factor. The criteria of structure fit and convergence can be taken from all the calculated and observed points, in the form of the "weighted profile R-factor" (Equation 5).[2]

$$R_{wp} = \frac{\sum \omega |y_i(obs) - y_i(calc)|}{\sum \omega y_i(obs)} \qquad (5)$$
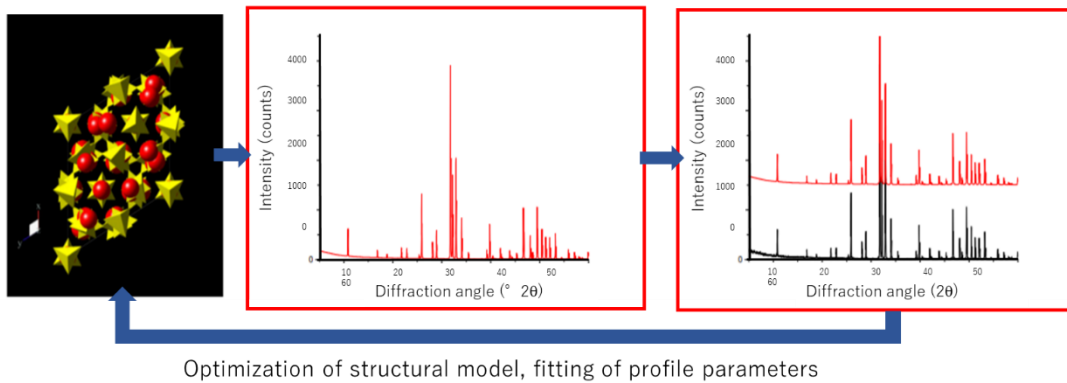
Figure 23. Rietveld refinement procedure scheme.[140]

Rietveld refinement extracts much more information from PXRD data, such as: unit cell dimension, phase quantities, crystallite sizes/shapes, atomic coordinates/bond lengths, micro-strain in crystal lattice, texture effects, substitutions/vacancies.[140]

2.5.2.3. Diffraction-line broadening analysis

Two main types of broadening have been introduced by Warren and Averbach: the size and strain components.[141]Size component depends on the size of coherent domains or incoherently diffracting domains in a sense that they diffract incoherently to one another. This is not limited to the grains but may include effects of stacking and twin faults and subgrain structures, such

as small-angle boundaries. The strain component is caused by any lattice imperfection, such as dislocations and different point defects.

The diffraction lines are broadened both by instrument and specimen and the observed profile is a convolution of those contributions (Equation 6).[142]

$$h(x) = g(x) \star f(x) + \text{background} \qquad (6)$$

Instrumental profile consists of wavelength distribution and geometrical aberrations (Equation 7).

$$g(x) = \omega(x) \star \gamma(x) \qquad (7)$$

In order to obtain microstructural parameters of the specimen, the physically broadened profile, f, related to specimen, must be extracted from the observed profile, h.

Specimen broadening can be caused by any lattice imperfection: dislocations, vacancies, interstitials, substitutional or similar defects which cause the lattice strain. Domain-size broadening occurs if a crystal is broken into smaller incoherently diffracting domains by dislocation arrays (small-angle boundaries), stacking faults, twins, large-angle boundaries (grains) or similar.

Before diffraction-line broadening analysis, it is necessary to correct the observed line profiles for instrumental effects. This can be done by a careful scan of a suitable standard sample which shows minimal physical broadening, what will define the instrumental contribution to broadening.[143]

The adsorption properties of porous materials is governed by the microstructure, such as the specific surface area, pore size distribution, pore volume and surface chemical property, such as functional groups. Wei[144] has proven that active carbon obtained from coconut shells could be improved for hydrogen adsorption by treatment with HF (5.5% improvement) or $NH_3 \cdot H_2O$ (3.6% improvement). No obvious effect was noted in treatment with HNO_3 and negative effect on the hydrogen adsorption capacity was detected after the treatment with H_3PO_4 (18% decrease of the hydrogen uptake) (Figure 24). All of the effects could be accounted for by changes in the specific surface area, pore size distribution and surface chemistry of the active carbon samples, where the specific surface area of carbon samples was the dominant factor for hydrogen adsorption, no matter what kind of treatment was performed. Higher hydrogen adsorption capacity is detected for small micropores which were favorable for larger specific surface areas and stronger adsorption fields.
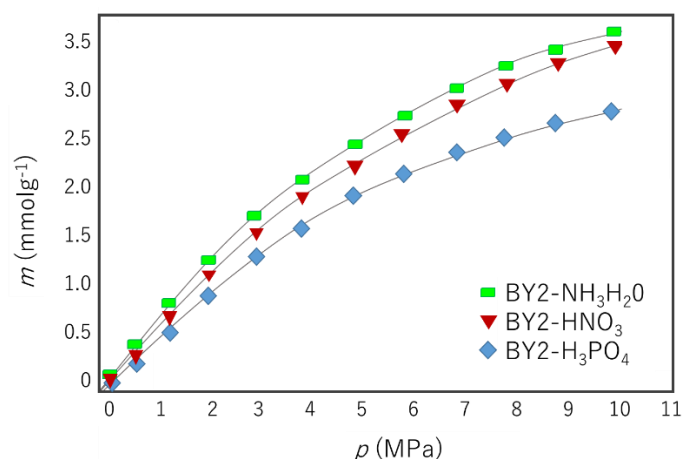
Figure 24. Effects of surface chemical modification on the hydrogen uptake.[144]

2.5.3. Solid state NMR

MOFs used for most applications requires both knowledge about the atomic-scale structures but also understanding of the atomic-scale processes if used for catalysis, gas separation and storage or drug delivery. This knowledge and understanding can be gained by a set of complementary techniques that elucidate short- and long-range structural motifs, static and dynamic properties, interactions among the frameworks and the adsorbates, such as modelling and spectroscopic investigations. Solid-state nuclear magnetic resonance (NMR) is considered to be one of the most powerful characterization techniques which can provide element-specific atomic-resolution insight into materials. Except use in studies of MOF formation, their structure determination or *in-situ* studies of their performance, solid-state NMR can be used as a local spectroscopic tool, as complementary technique to diffraction techniques that rely on the existence of long-range order and that provide a picture of an average crystal structure. NMR spectroscopy is very important for deducing relationship between structure and functionality. It can prove or disprove the proposed model, strength of interactions between the adsorbed molecules and the MOF matrices. NMR results can follow gradual adsorption or desorption of molecules into pores, locate or quantify these molecules and on this way can complement the data obtained by the thermal and sorption analysis.[145]

Literature[146] reports cases when PXRD failed to identify the presence of polymorphs, while the solid-state NMR proved to be more efficient. Experiments were done on a sweetener neotame, whose anhydrous form is capable of existing in several polymorphic forms and as an amorphous form. Drying the monohydrate under vacuum revealed various crystalline forms which can be detected by ^{13}C SSNMR.

§ 3. EXPERIMENTAL PART

3.1. MATERIALS AND SYNTHESIS

In this thesis, samples have been prepared by the mechanochemical synthesis by ball milling in Planetary Micro Mill Fritsch Pulverisette 7 premium line (Figure 25).

Figure 25. Planetary Micro Mill Fritsch Pulverisette 7 premium line, taken from the literature.[147]

Two stainless steel vials of 25 ml were used for loading reactants into them. Stainless steel balls ($d = 0.5$ mm, $m = 0.5$ g) were used for milling. Balls-to-sample mass ratio which was used in all synthesis was 25:1.

In order to optimize synthesis, different milling times, different speed of rotation and different ratios were examined during synthesis of the precursors, as it will be explained in next chapters. Independent of total milling time, the procedure always carried out in cycles of 10 min of milling followed by 5 min waiting period in order to avoid the overheating of the system. Milling times varied from 2 h up to 9 h. All mechanochemical reactions were set up equally with milling balls at the bottom and milling material at the top. Different speeds of milling have been examined (from 400 rpm to 700 rpm). As the discussion will show, 2 h or 3 h of milling and 550 rpm or 600 rpm have often been chosen as optimal values, judging both by the XRD results and visual inspection of the homogeneity of the samples.

Due to the moisture sensitivity of borohydrides, all handling and manipulation of the chemicals were performed in a mBRAUN nitrogen-filled glovebox located at the Faculty for Chemistry and Chemical Engineering, University of Ljubljana, Slovenia and an mBRAUN argon-filled

glovebox located on Faculty of Science, Department for Physics, University of Geneva, Switzerland (Figure 26).

Figure 26. mBRAUN glovebox, Geneva, taken from the literature.[148]

Monometallic borohydrides $M(BH_4)_n$ (M = Li, Na, K, Mg, Mn), as well as $ZnCl_2$ and solvents (THF, DCM, ACN, DMSO, CF) were of analytical purity and purchased from Sigma Aldrich. Organic imidazolates, $M(Im)_n$ (M = Li, Na, K, Mg), were prepared by collaborators from Université catholique de Louvain, Ottignies-Louvain-la-Neuve, Belgium, by the procedure reported elsewhere.[115]

3.1.1. Mechanochemical reactions of bimetallic borohydride precursor $NaZn(BH_4)_3$ with sodium imidazolate NaIm

3.1.1.1. Synthesis of bimetallic borohydride precursor $NaZn(BH_4)_3$

Bimetallic borohydrides, $NaZn_n(BH_4)_m$, were prepared by ball milling from $NaBH_4$ and $ZnCl_2$, in the molar ratios 2:1 and 3:1 as proposed by Ravnsbæk.[13] All reactions were performed by neat grinding i.e. dry synthesis without any addition of solvents.

Prior to the mechanochemical reactions, zinc chloride, being very hygroscopic, was dried under vacuum overnight on a Schlenk line before every use (Figure 27).

Attempts to remove the by-product of the reaction, NaCl, by centrifugation from different aprotic solvents (acetonitrile, tetrahydrofuran, chloroform, dichloromethane) have been carried out. Prior to the centrifugation, all solvents were dried for several hours under the vacuum on a Schlenk line.
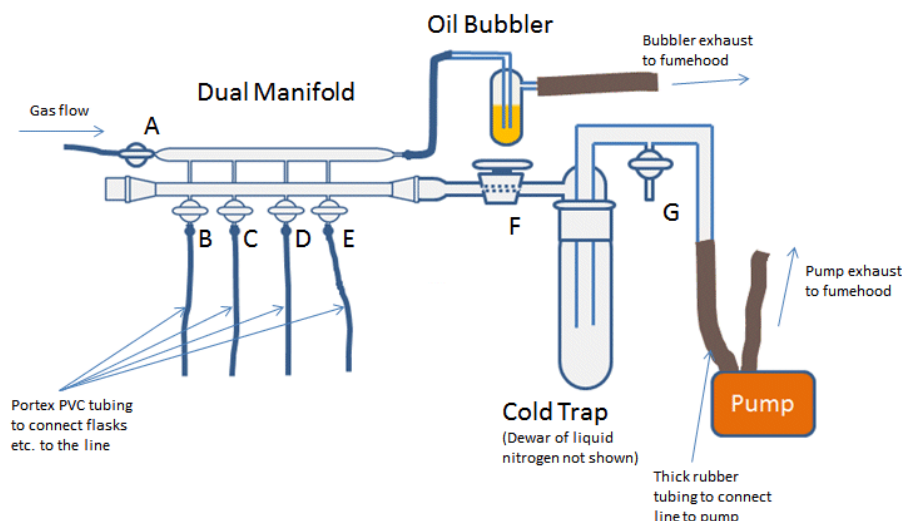
Figure 27. Schlenk line setup taken from the literature.[149]

As it will be discussed in next chapters, centrifugation has not yielded expected results, so it was abandoned in further synthesis attempts. Additionally, discussion will show that 2:1 ratio typically resulted in the formation of multiple phases mixtures, thus it was also abandoned and the focus was set on investigation of reactions in the 3:1 ratio i.e. on the synthesis of NaZn(BH$_4$)$_3$. Prepared NaZn(BH$_4$)$_3$ samples have been used in reactions with imidazolates, so are denoted as precursors in the further text. Schematic representation for the preparation of precursors is given in Table 6.

Table 6. Synthesis of bimetallic borohydride precursor NaZn(BH$_4$)$_3$

Sample	NaBH$_4$: ZnCl$_2$ molar ratio	Reaction conditions
P1	3:1	NG, 600 rpm, 2h
P2	2:1	NG, 600 rpm, 2h
P3		P1 centrifuged with DCM
P4		P1 centrifuged with CF

3.1.1.2. Mechanochemical reactions of bimetallic borohydride precursor NaZn(BH$_4$)$_3$ with sodium imidazolate NaIm

a) Dry mechanochemical reaction (neat grinding) of NaZn(BH$_4$)$_3$ and NaIm

The reaction was performed by ball-milling of NaZn(BH$_4$)$_3$ precursors with NaIm for 2 h at 600 rpm in the different molar ratios: 1:1, 2:1, 3:1, 1:2 and 1:3. Additionally, the effect of ball-milling time (2 h, 4 h and 9 h) on the final product composition was examined in the case of the 1:1 molar ratio (Table 7).

Table 7. Dry mechanochemical reaction (neat grinding) of NaZn(BH$_4$)$_3$ and NaIm

Sample	NaZn(BH$_4$)$_{3:}$ NaIm molar ratio	Reaction conditions
1D1	1:1	NG, 600 rpm, 2h
1D2	2:1	NG, 600 rpm, 2h
1D3	3:1	NG, 600 rpm, 2h
1D4	1:2	NG, 600 rpm, 2h
1D5	1:3	NG, 600 rpm, 2h
1D6	1:1	NG, 600 rpm, 4h
1D7	1:1	NG, 600 rpm, 9h

b) Liquid assisted grinding of NaZn(BH$_4$)$_3$ and NaIm

The reaction was performed by ball-milling of the NaZn(BH$_4$)$_3$ precursor with NaIm for 2 h at 600 rpm in the molar ratios 1:1 together with 50 µl of solvent. Synthesis was tried with different organic solvents, such as THF, ACN, and DMSO. For centrifugation of the products in the form of suspension dichloromethane and chloroform were used (Table 8).

Table 8. Liquid assisted grinding of NaZn(BH$_4$)$_3$ and NaIm

Sample	NaZn(BH$_4$)$_{3:}$ NaIm molar ratio	Reaction conditions
1S1	1:1	LAG THF, 600 rpm, 2h
1S1-DCM		1S1 centrifuged with DCM
1S1-CF		1S1 centrifuged with CF
1S2	1:1	LAG ACN, 600 rpm, 2h
1S3	1:1	LAG DMSO, 600 rpm, 2h
1S3a		1S3 after 3 month of aging

c) Mechanochemical reactions of NaBH$_4$, ZnCl$_2$ and NaIm

Reactions of NaBH$_4$, ZnCl$_2$ and NaIm in the ratio 1:1:1 and 1:1:3 have been done. LAG was conducted by direct adding of all components to the bowl at the same time, with addition of 50 µl of ACN or DMSO. The molar ratio of the solid reactants in LAG was NaBH$_4$:ZnCl$_2$:NaIm = 1:1:1 (Table 9).

Table 9. Mechanochemical reactions of NaBH$_4$, ZnCl$_2$ and NaIm

Sample	NaBH$_4$:ZnCl$_2$:NaIm molar ratio	Reaction conditions
2D1	1:1:1	NG, 600 rpm, 2h
2D2	1:1:3	NG, 600 rpm, 2h

3.1.2. Mechanochemical reactions of monometallic alkali borohydrides MBH$_4$ (M = Li, Na and K) with alkali metal imidazolates MIm (M = Li, Na and K)

Mechanochemical reactions, in which the monometallic borohydrides MBH$_4$ (M = Li, Na and K) have been mixed with alkali metal imidazolates MIm (M = Li, Na and K) directly in the milling vial, were done as neat grinding. Starting reactants and corresponding ratios are shown in Table 10.

Table 10. Reactions of MBH$_4$ (M = Li, Na and K) and MIm (M = Li, Na and K)

Sample	Reactants molar ratio	Reaction conditions
3D1	LiBH$_4$:LiIm = 3:1	NG, 600 rpm, 2h
3D2	NaBH$_4$:NaIm = 1:6	NG, 600 rpm, 2h
3D3	NaBH$_4$:NaIm = 1:4	NG, 600 rpm, 2h
3D4	NaBH$_4$:NaIm = 1:2	NG, 600 rpm, 2h
3D5	NaBH$_4$:NaIm = 1:1	NG, 600 rpm, 2h
3D6	NaBH$_4$:NaIm = 4:1	NG, 600 rpm, 2h
3D7	NaBH$_4$:NaIm = 6:1	NG, 600 rpm, 2h
3D8	NaBH$_4$:NaIm = 6:1	NG, 600 rpm, 2h
3S1	NaBH$_4$:NaIm = 1:1+50 μl ACN	LAG ACN, 600 rpm, 2h
3S2	NaBH$_4$:NaIm = 1:1+50 μl DMSO	LAG DMSO, 600 rpm, 2h
3D9	KBH$_4$:KIm = 1:6	NG, 600 rpm, 2h
3D10	KBH$_4$:KIm = 1:2	NG, 600 rpm, 2h
3D11	KBH$_4$:KIm = 1:1	NG, 600 rpm, 2h

The reactions were performed by ball-milling of LiBH$_4$ with LiIm in the 1:1 molar ratio; NaBH$_4$ with NaIm in 1:6, 1:4, 1:2, 1:1, 2:1, 4:1 and 6:1 molar ratios; KBH$_4$ with KIm in the 1:6, 1:2 and 1:1 molar ratio for 2 hours at 600 rpm. Additionally, the effect of 50 μl of solvent (ACN, DMSO) on the reaction of NaBH$_4$ and NaIm in the 1:1 molar ratio has been explored.

3.1.3. Mechanochemical reactions of monometallic alkaline earth borohydride Mg(BH$_4$)$_2$ with alkali metal imidazolates MIm (M = Na, Li and K)

Mechanochemical reactions, in which the monometallic alkaline earth borohydride Mg(BH$_4$)$_2$ has been mixed with alkali metal imidazolates MIm (M = Li, Na and K) directly in the milling vial, were done as neat grinding. Starting reactants and the corresponding ratios are shown in Table 11.

Table 11. Reactions of $Mg(BH_4)_2$ and MIm (M = Li, Na and K)

Sample	Reactants molar ratio	Reaction conditions
4D1	$Mg(BH_4)_2$:NaIm = 1:1	NG, 550 rpm, 3h
4D2	$Mg(BH_4)_2$:NaIm = 1:2	NG, 550 rpm, 3h
4D3	$Mg(BH_4)_2$:NaIm = 1:6	NG, 550 rpm, 3h
4D4	$Mg(BH_4)_2$:LiIm = 1:1	NG, 550 rpm, 3h
4D5	$Mg(BH_4)_2$:LiIm = 1:2	NG, 550 rpm, 3h
4D6	$Mg(BH_4)_2$:KIm = 1:2	NG, 550 rpm, 3h
4D7	$Mg(BH_4)_2$:KIm = 1:6	NG, 550 rpm, 3h

The reactions were performed by ball-milling of $Mg(BH_4)_2$ with NaIm in the 1:1, 1:2 and 1:6 molar ratios; $Mg(BH_4)_2$ with LiIm in the 1:1 and 1:2 molar ratios; $Mg(BH_4)_2$ with KIm in the 1:2 and 1:6 molar ratios for 3 hours at 550 rpm.

3.1.4. Mechanochemical reactions of monometallic alkaline earth imidazolate $Mg(Im)_2$ with alkali metal imidazolates MIm (M = Na, Li and K)

Mechanochemical reactions, in which the monometallic alkaline earth imidazolate $MgIm_2$ was mixed with alkali metal imidazolates MIm (M = Li, Na and K) directly in the milling vial, were done as neat grinding. Starting reactants and corresponding ratios are shown in Table 12.

Table 12. Reactions of $MgIm_2$ and MIm (M = Li, Na and K)

Sample	Reactants molar ratio	Reaction conditions
5D1	$Mg(BH_4)_2$:NaIm = 1:1	NG, 550 rpm, 3h
5D2	$Mg(BH_4)_2$:KIm = 1:1	NG, 550 rpm, 3h
5D3	$Mg(BH_4)_2$:LiIm = 1:1	NG, 550 rpm, 3h

The reactions were performed by ball-milling of $MgIm_2$ with NaIm in the 1:1 molar ratio; $MgIm_2$ with KIm in the 1:1 molar ratio and $MgIm_2$ with LiIm in the 1:1 molar ratio for 3 hours at 550 rpm.

3.1.5. Mechanochemical reactions of monometallic transitional borohydride $Mn(BH_4)_2$ with alkali metal imidazolates MIm (M = Na, K and Li)

Mechanochemical reactions, in which the monometallic transitional borohydride $Mn(BH_4)_2$ has been mixed with alkali metal imidazolates MIm (M = Li, Na and K) directly in the milling vial, were done as neat grinding. Starting reactants and corresponding ratios are shown in Table 13.

Table 13. Reactions of $Mn(BH_4)_2$ and MIm (M = Li, Na and K)

Sample	Reactants molar ratio	Reaction conditions
6D1	$Mn(BH_4)_2$:NaIm = 1:6	NG, 550 rpm, 3h
6D2	$Mn(BH_4)_2$:NaIm = 1:2	NG, 550 rpm, 3h
6D3	$Mn(BH_4)_2$:KIm = 1:6	NG, 550 rpm, 3h
6D4	$Mn(BH_4)_2$:KIm = 1:2	NG, 550 rpm, 3h
6D5	$Mn(BH_4)_2$:LiIm = 1:6	NG, 550 rpm, 3h
6D6	$Mn(BH_4)_2$:LiIm = 1:2	NG, 550 rpm, 3h

The reactions were performed by ball-milling of $Mn(BH_4)_2$ with NaIm in the 1:6 and 1:2 molar ratios; $Mn(BH_4)_2$ with KIm in the 1:6 and 1:2 molar ratios and $Mn(BH_4)_2$ with LiIm in the 1:6 and 1:2 molar ratios for 3 hours at 550 rpm.

3.2. METHODS

3.2.1. Laboratory X-ray diffraction

Products of each reaction were initially investigated by the means of X-ray powder diffraction (XRPD) using a powder diffractometer PANalytical X'Pert PRO MPD or STOE IPDS-P diffractometer (Figure 28) with a curved image plate detector, both with monochromated CuKα1 radiation ($\lambda = 1.54060$ Å). Air sensitive samples were packed into 0.5–1 mm glass or borosilicate capillaries within the glovebox and then sealed with vacuum grease. Data was collected at RT, in the 2θ range: 2–100° with counting time of 40 s/step. Products obtained by the mechanochemical reactions were characterized by PXRD qualitative and quantitative analysis.
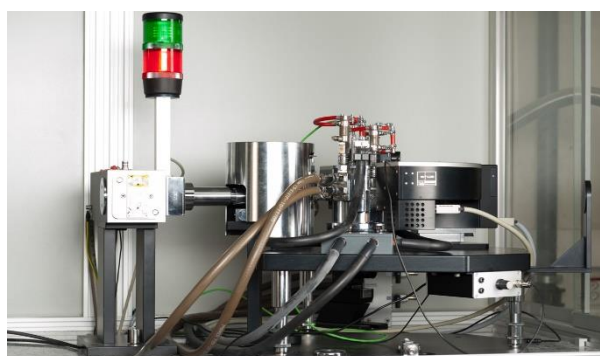
Figure 28. Powder diffractometer STOE, taken from the literature.[150]

Single crystals were measured on a single crystal diffractometer STOE IPDS-II, with MoKα radiation ($\lambda = 0.7107$ Å) and equipped with a two-dimensional image plate detector (Figure 29).
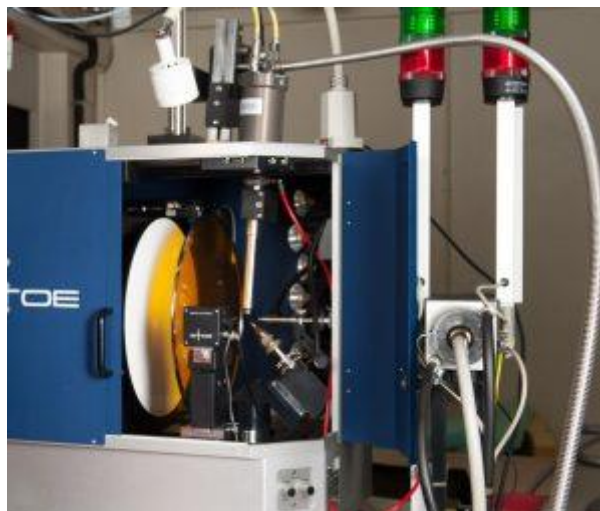
Figure 29. Single crystal diffractometer STOE IPDS-II, taken from the literature.[151]

3.2.2. In-situ synchrotron radiation X-ray powder diffraction

Multiphase samples, amorphous samples or samples containing novel phases with unknown structure were further analyzed by *in-situ* synchrotron radiation X-ray powder diffraction on Swiss-Norwegian Beamline (SNBL), BM01A, at the European Synchrotron Radiation Facility (ESRF), Grenoble, France. The samples were mounted into 0.5 mm borosilicate capillaries and sealed with the vacuum grease. Measurement parameters were: $\lambda_1 = 0.8187$ Å, $\lambda_2 = 0.7149$ Å, sample rotation 0–40°, X-ray exposure time 40 s. The Dectris Pilatus 2M detector was used for recording 2D powder data at the sample-to-detector distances of 200 or 400 mm. Samples were heated in the temperature range from RT to 250–500 °C (heating rate 5–10 °C/min) by a heat blower. 2D images were integrated and treated with the local program Bubble.[152]

3.2.3. Crystal structure solution from powder X-ray diffraction

Crystal structures of new compounds were solved and refined from the SR-PXRD data. Indexing, space group determination as well as structure solution was carried out using the FOX program.[129,130] The background was automatically estimated, firstly using a linear interpolation, followed by a spline fitting. Indexing of the crystalline phase is usually the limiting step. Here, the dichotomy algorithm was used for indexing process. For space group determination, the "space group explorer" widget is available in FOX and follows the following protocol: given the unit cell, all possible group settings starting from $P1$ are tested using least squares profile fitting,[125] and the χ^2 as well as the number of systematic extinctions is recorded for each space group. Program FOX performs direct-space structure determination, allowing a modular

description of the structure as a combination of atoms, polyhedra and molecules. It is possible to choose between two algorithms for structure solution: parallel tempering and simulated annealing. Parallel Tempering is mostly used. Some structures were partially solved by Parallel Tempering so the least squares refinement, also implemented in the FOX program, was used for additional improvements of the structural model. The crucial step during Parallel Tempering structure solution process was setting the exactly correct values of antibump restraints, for each pair of atoms, and treating ligands (borohydride, imidazolate) as a rigid body.

Bond valence sum (BVS) calculations were used for validation of the obtained structural models. Crystallographic positions, as determined by XRPD, were used for BVS calculation. Soft bond valence parameters R_{ij} and b were taken from the literature.[153] Results calculated from the most commonly adopted empirical expression for the variation of the length d_{ij} of a bond with valence $v_{ij} = \exp\big[(R_{ij} - d_{ij})/b\big]$, were summed up to get the sum of all the valences from a given atom.

The structural models were finally refined by Rietveld method using the Fullprof program.[154] Cell parameters, peak shape parameters, background parameters and, for some structures, isotropic temperature factors were refined. The imidazolate anion was treated as a rigid body and only its position and orientation in the unit cell was varied. Microstructural parameters, crystallite sizes and lattice strain, were determined by the size-strain algorithm implemented in HigScore Xpert plus.

The topology analysis of the underlying net in the novel crystal structures was performed within the program TOPOS.[155]

The program VESTA was used for visualization of crystal structures and crystal packings.[156]

3.2.4. Solid state NMR

NMR measurements were carried out on a 600 MHz Varian NMR system equipped with a 3.2 mm Varian T3 HX MAS probe. Larmor frequencies for ^1H, ^{13}C, ^{11}B and ^{23}Na were 599.50 MHz, 150.74 MHz, 192.34 MHz and 158.58 MHz, respectively. ^1H magic angle spinning (MAS) NMR spectra were obtained by using single 90-degree pulse excitation (2.3 µs) and sample rotation frequency of 20 kHz. Two-dimensional ^1H spin-diffusion spectra were obtained with spin-diffusion mixing time of 16 ms. The measurement consisted of 190 increments along t_1 with 16 scans per increment and repetition delay of 5 s. Spectral width along the indirectly-detected dimension was equal to sample rotation frequency (20 kHz). For all other

measurements, sample rotation frequency was 16 kHz. ^{1}H–^{13}C cross-polarization (CP) MAS NMR spectra were recorded by first exciting protons and transferring polarization to carbon nuclei using the amplitude-ramped CP block with a duration of 5 ms. During the acquisition, high-power XiX heteronuclear decoupling was applied; repetition delay was 20 s and 480 scans were collected. ^{11}B MAS NMR spectra were obtained using a short-pulse excitation (0.8 µs) and XiX heteronuclear decoupling during acquisition. Repetition delay was 10 s and number of repetitions was 16. ^{1}H–^{11}B CP MAS NMR measurement employed 0.8 ms CP block and XiX decoupling. Four scans were collected, and repetition delay was 20 s. ^{23}Na MAS NMR spectra were also recorded using short-pulse excitation (0.8 µs) and XiX decoupling; number of scans was 80 and delay between the scans was 10 s. ^{1}H–^{23}Na CP MAS NMR spectra were obtained with a 0.8 ms CP block, repetition delay of 20 s and 64 collected scans. Frequency axes for ^{1}H and ^{13}C NMR spectra were referenced to the corresponding signals of TMS, whereas frequency axes of ^{11}B and ^{23}Na spectra were referenced to the signals of H_3BO_3 and NaCl in solution.

§ 4. RESULTS AND DISCUSSION

In the scope of this work the mechanochemical reactions of various monometallic and bimetallic borohydrides with alkali and alkaline earth metal imidazolates have been investigated in a very comprehensive and systematic manner.

4.1. MECHANOCHEMICAL REACTIONS OF BIMETALLIC BOROHYDRIDE PRECURSOR NaZn(BH₄)₃ WITH SODIUM IMIDAZOLATE NaIm

4.1.1. Synthesis of bimetallic borohydride precursor NaZn(BH₄)₃

Bimetallic borohydrides containing an alkali cation (Na) and a transition metal (Zn) were prepared by the dry mechanochemical reaction (neat grinding) of $NaBH_4$ and $ZnCl_2$ in the 2:1 and 3:1 molar ratio according to Scheme 1.
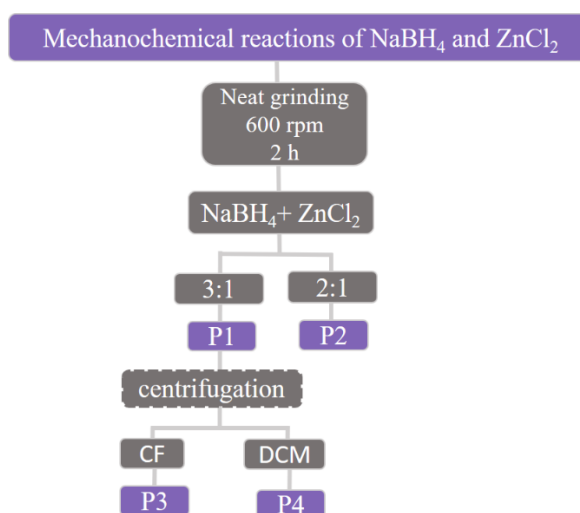
Scheme 1. Mechanochemical reactions of sodium borohydride and zinc chloride.

As it has already been demonstrated in the literature,[13] small deviation in the ratio of reactants leads to the significant difference in the composition of final products, both in the respect to stoichiometry as well as structural topology.

Rietveld structure refinement of samples P1 and P2, obtained by the reaction of $NaBH_4$ and $ZnCl_2$ in the 3:1 and 2:1 molar ratio, are shown in Figure 30. Qualitative analysis showed that the sample P1 contains almost 50 wt. % of $NaZn(BH_4)_3$ and 50 wt. % of NaCl. The 2:1 molar ratio (sample P2) resulted in the formation of a mixture containing 51.1 wt. % $NaZn_2(BH_4)_5$,

48.9 wt. % NaCl, and some unidentified phase, as shown in Figure 26b. Since the phase composition of sample P2 could not have been fully elucidated, decision was made not to pursue the 2:1 ratio any further.
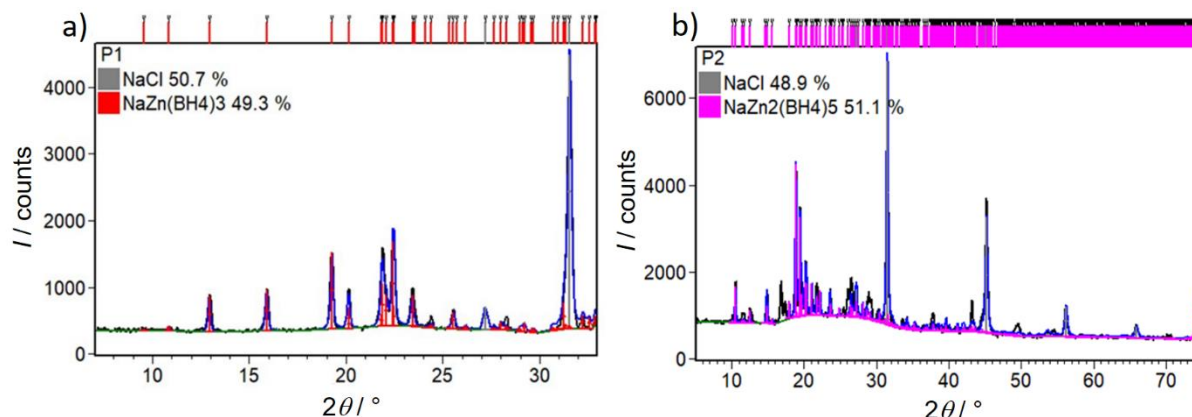
Figure 30. Rietveld structure refinement of sample **a)** P1 and **b)** P2 obtained after the reaction of $NaBH_4$ and $ZnCl_2$ in 3:1 and 2:1 molar ratio, respectively. Experimental diffraction data are shown in black, while calculated patterns are given in blue. Positions of the diffraction lines of $NaZn(BH_4)_3$ are colored in red, $NaZn_2(BH_4)_5$ is colored with pink color while the position of NaCl diffraction lines are grey.

The byproduct of the mechanochemical reaction in 3:1 ratio (P1) was sodium chloride so several attempts to remove it by centrifugation in chloroform (CF) and dichloromethane (DCM) were undertaken (P3 and P4), as shown on Figure 31.
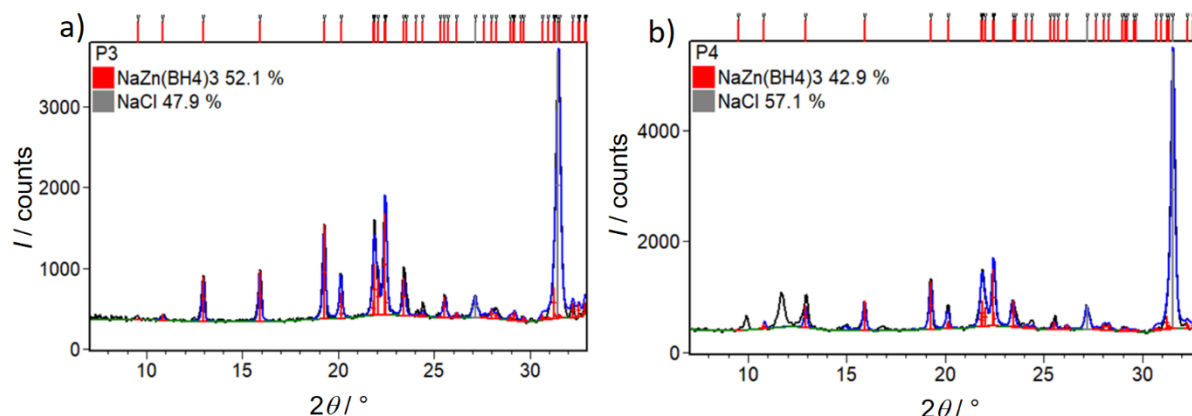
Figure 31. Rietveld refinement of samples P3 and P4 obtained after the centrifugation of P1 in: **a)** cloroform and **b)** DCM. Experimental diffraction data are shown in black, while calculated patterns are given in blue. Diffraction lines position of $NaZn(BH_4)_3$ are represented by red vertical marks while the positions of NaCl diffraction lines are given in grey.

Centrifugation of P1 in DCM resulted in the partial decomposition of $NaZn(BH_4)_3$ as it was evident even during conduction of the experiment because hydrogen release has been noticed during centrifugation. Rietveld refinement confirmed degradation of bimetallic borohydride;

the sample prior to centrifugation contained 49.3 wt. % of $NaZn(BH_4)_3$ while after centrifugation the content of $NaZn(BH_4)_3$ decreased to 42.9 wt. % (Figures 30a and 31b). Attempts to remove NaCl by centrifugation with cloroform also proved to be nonbeneficial; although the degradation of $NaZn(BH_4)_3$ had not taken place, unlike in the case of DCM, the amount of NaCl after the centrifugation has not decreased significantly. Due to the problems caused by the hydrogen release and ineffectiveness of the procedure itself, purification of the precursor in respect to NaCl was abandoned. Further discussion will show that sodium chloride was, in fact, inert in the subsequent mechanochemical reaction. Therefore, since it has been found that NaCl only dissolves excess BH_4, and does not react with any other reactants, $NaZn(BH_4)_3$/NaCl mixture (P1) has been used as the precursor in the as-prepared form.

4.1.2. Mechanochemical reactions of bimetallic borohydride precursor $NaZn(BH_4)_3$ with sodium imidazolate NaIm

Mechanochemical reactions of the bimetallic borohydride precursor, $NaZn(BH_4)_3$, and the sodium imidazolate, NaIm, were carried out in different molar ratios by the utilization of two approaches, as shown in Scheme 2. First approach was neat grinding without presence of any solvent. Additionally, a liquid-assisted mechanochemical grinding was explored as well.
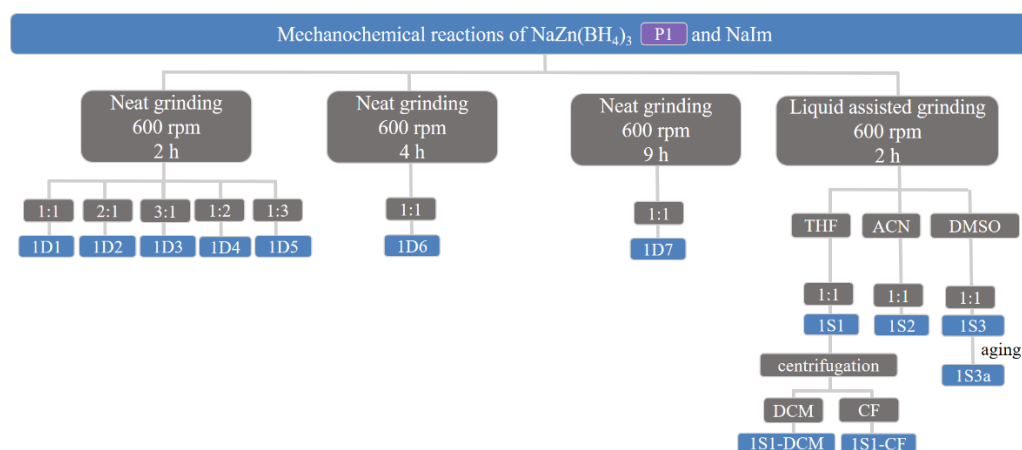
Scheme 2. Mechanochemical reactions of bimetallic borohydride precursor $NaZn(BH_4)_3$ with sodium imidazolate NaIm.

In the case of neat grinding, the effect of grinding time on the final composition of the reaction products have been systematically investigated.

4.1.2.1. Neat grinding of NaZn(BH₄)₃ and NaIm

Rietveld refinements for samples 1D1–1D5, obtained by the dry mechanochemical reactions of NaZn(BH$_4$)$_3$ precursor and NaIm in different molar ratios, are given in Figure 32. Figure 33 shows the Rietveld refinements for samples 1D6 and 1D7, obtained for ratio 1:1 by different grinding times (Scheme 2).
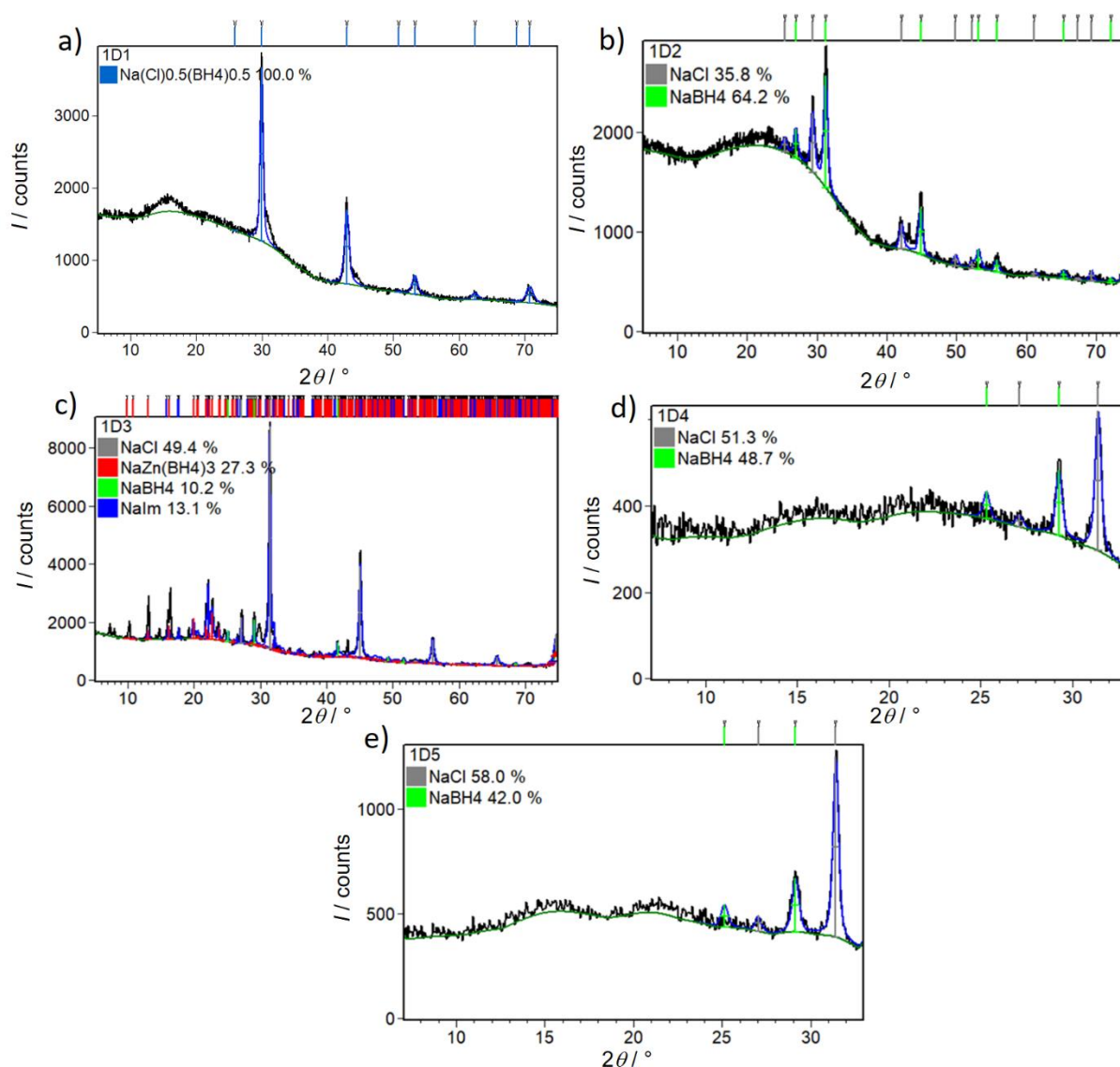
Figure 32. Rietveld refinement of samples 1D1–1D5 obtained by the neat grinding of NaZn(BH$_4$)$_3$ precursor and NaIm in different molar ratios: **a)** 1:1, **b)** 2:1, **c)** 3:1, **d)** 1:2 and **e)** 1:3. Experimental diffraction data are shown in black, while calculated patterns are given in blue. Diffraction lines position of NaBH$_4$ are represented by green vertical marks, NaCl by grey, NaCl$_{0.5}$(BH$_4$)$_{0.5}$ by blue, NaIm by deep blue while the vertical marks in the case of NaZn(BH$_4$)$_3$ are colored in red.
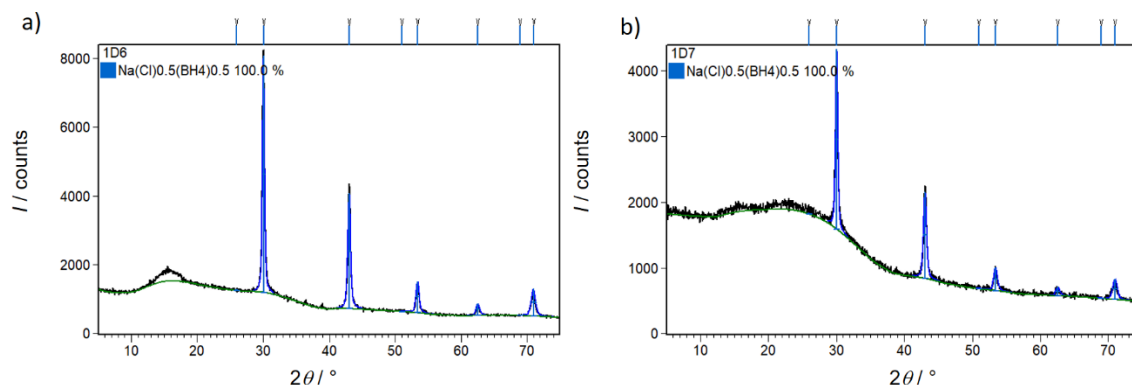
Figure 33. Rietveld refinement of samples 1D6 and 1D7 obtained by the neat grinding of $NaZn(BH_4)_3$ precursor and NaIm in 1:1 molar ratio after different grinding times: **a)** 4 h and **b)** 9 h. Experimental diffraction data are shown in black, while calculated patterns are given in blue. Diffraction lines position of $NaCl_{0.5}(BH_4)_{0.5}$ are represented by blue vertical marks.

Quantitative composition of mechanochemical products (samples 1D1–1D7) are summarized in Table 14.

Table 14. Quantitative composition of crystalline products in samples 1D1–1D7.

Sample	$NaZn(BH_4)_3$: NaIm molar ratio	Milling time	Crystalline products composition as determined by the Rietveld refinement
1D1	1:1	2	amorphous phase, $NaCl_{0.5}(BH_4)_{0.5}$ (100 wt. %)
1D2	2:1	2	amorphous phase, NaCl (35.8 wt. %) and $NaBH_4$ (64.2 wt. %)
1D3	3:1	2	NaCl (49.4 wt. %), NaIm (13.1 wt. %), $NaZn(BH_4)_3$ (27.3 wt. %), $NaBH_4$ (13.1 wt. %) and unidentified phase(s)
1D4	1:2	2	amorphous phase, $NaBH_4$ (48.7 wt. %) and NaCl (51.3 wt. %)
1D5	1:3	2	amorphous phase, $NaBH_4$ (42.0 wt. %) and NaCl (58.0 wt. %)
1D6	1:1	4	amorphous phase, $NaCl_{0.5}(BH_4)_{0.5}$ (100 wt. %)
1D7	1:1	9	amorphous phase, $NaCl_{0.5}(BH_4)_{0.5}$ (100 wt. %)

The only crystalline product in sample 1D1, obtained after the mechanochemical reaction for 2 h in 1:1 ratio was solid solution $NaCl_{0.5}(BH_4)_{0.5}$. Here, $NaCl_{0.5}(BH_4)_{0.5}$ is observed instead of NaCl which was expected from the theoretical reaction $3NaBH_4 + ZnCl_2 \rightarrow NaZn(BH_4)_3 + 2NaCl$. The BH_4 comes from the decomposition product of $NaZn(BH_4)_3$, $NaBH_4$, which immediately reacts with NaCl, as explained in Černý,[157] while the other decomposition products (Zn, diborane, hydrogen) are amorphous. Additionally, for the 1:1 ratio the effect of a ball-milling time on the final product composition was examined. It was showed that longer milling time does not have any significant impact on the final product composition; both samples 1D6 and 1D7 contain solid solution $NaCl_{0.5}(BH_4)_{0.5}$ as an only crystalline product. Samples 1D2 and 1D3 contain sodium chloride as dominant phase. Significant amount of $NaBH_4$ was noticed in

sample 1D2 which indicates that neat grinding in the 2:1 ratio resulted in decomposition of the NaZn(BH$_4$)$_3$ precursor. Besides NaCl, sample 1D3 contains a significant amounts of starting reactants NaIm and NaZn(BH$_4$)$_3$ indicating that the mechanochemical reaction, in fact, has not occurred for the 3:1 ratio. Sample 1D5, obtained by the same synthetic procedure in 1:3 ratio, similar to sample 1D4 obtained from 1:2 ratio, contained a significant amount of amorphous products and thus it was further examined by the *in-situ* high temperature synchrotron radiation X-ray powder diffraction.

XRD patterns of the sample 1D5 collected during heating run in the temperature range from RT to 290 °C are shown in Figure 34a, while Figure 34b shows phase analysis at temperatures: RT, 154 and 272 °C.
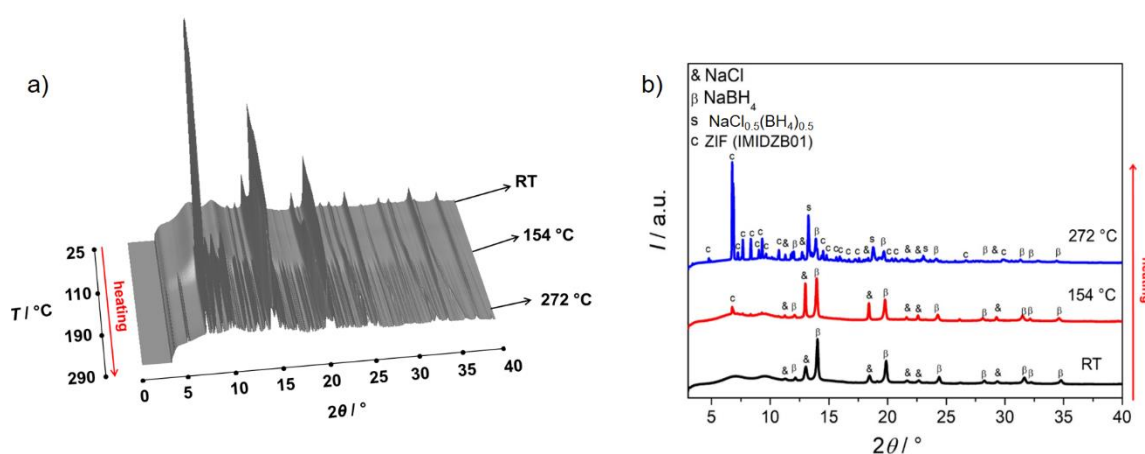
Figure 34. a) XRD patterns of sample 1D5 collected during heating run in temperature range from RT to 290 °C. **b)** Phase composition of sample 1D5 at RT, 154 and 272 °C. ($\lambda = 0.69449$ Å) Diffraction lines belonging to NaCl are marked with &, diffraction lines belonging to ZIF (IMIDZB01) with α, those belonging to NaCl$_{0.5}$(BH$_4$)$_{0.5}$ with s, while the diffraction lines belonging to NaBH$_4$ phase are marked with β.

From the *T*-ramp it can be seen that sample 1D5 at RT contained an amorphous phase, unreacted NaCl and decomposition product of P1–NaBH$_4$. Zinc imidazolate, having a zeolitic imidazolate framework structure (IMIDZB01), started to crystallize from the amorphous phase around 152 °C, while solid solution NaCl$_{0.5}$(BH$_4$)$_{0.5}$ appeared around 270 °C when NaBH$_4$ disappeared. The NaCl is present in the system all the time.

4.1.2.2. Liquid assisted grinding of NaZn(BH$_4$)$_3$ and NaIm

Rietveld refinements for samples 1S1–1S3, obtained by the liquid-assisted mechanochemical reactions of NaZn(BH$_4$)$_3$ precursor and NaIm in 1:1 molar ratio with different solvents (Scheme 2) are given in Figure 35.
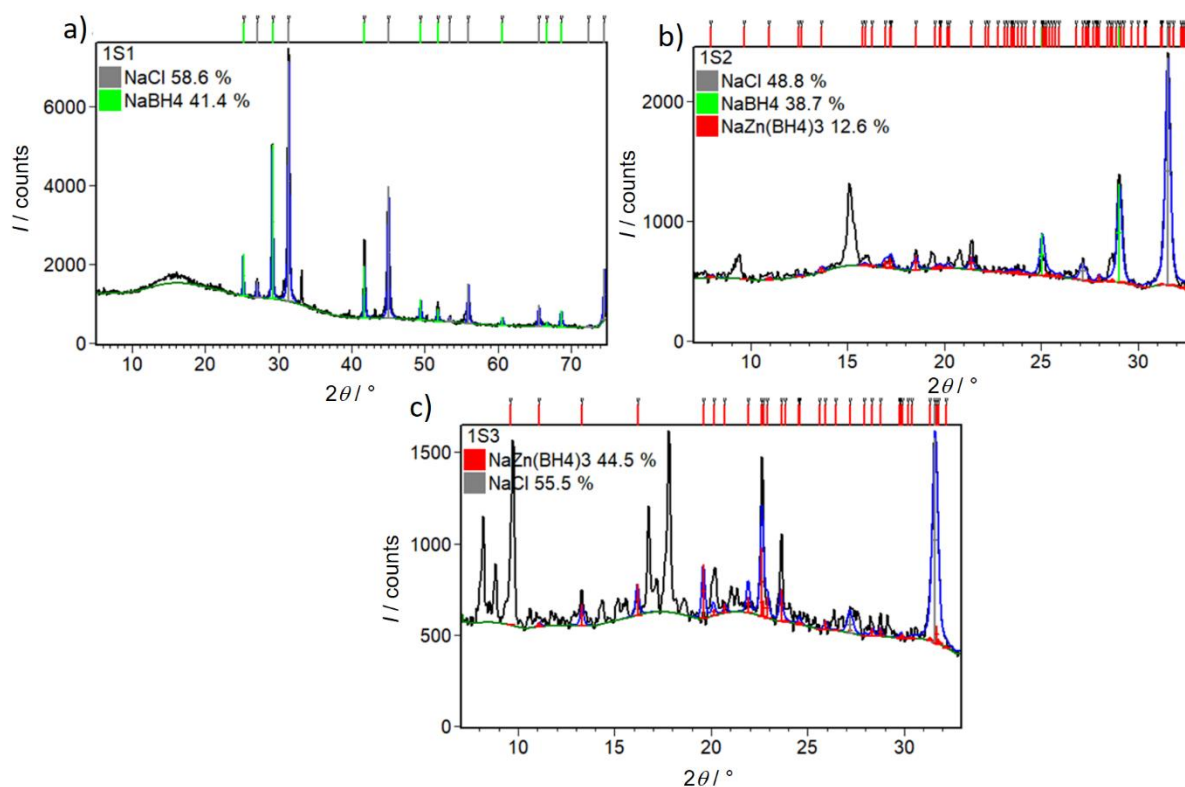
Figure 35. Rietveld refinements for samples 1S1–1S3, obtained by the liquid-assisted mechanochemical reactions of $NaZn(BH_4)_3$ precursor and NaIm in 1:1 molar ratio with different solvents: **a)** THF, **b)** ACN and **c)** DMSO. Experimental diffraction data are shown in black, while calculated patterns are given in blue. Diffraction lines position of $NaBH_4$ are represented by green vertical marks, NaCl by grey while the vertical marks in the case of $NaZn(BH_4)_3$ are colored in red.

The quantitative composition of mechanochemical products (samples 1S1–1S3) summarized in Table 15.

Table 15. Quantitative composition of crystalline products in samples 1S1–1S3.

Sample	$NaZn(BH_4)_3$:NaIm ratio	Solvent	Crystalline products composition as determined by the Rietveld refinement
1S1	1:1	THF	NaCl (58.6 wt. %) and $NaBH_4$ (41.4 wt.%) and few unidentified diffraction lines
1S2	1:1	ACN	NaCl (48.8 wt. %), $NaBH_4$ (38.7 wt. %), $NaZn(BH_4)_3$ (12.6 wt. %) and few unidentified diffraction lines
1S3	1:1	DMSO	NaCl (55.5 wt. %), $NaZn(BH_4)_3$ (44.5 wt. %) and unidentified phase(s)

Besides sodium chloride, dominant phases in all samples, 1S1–1S3, are either one of the starting reactants $NaZn(BH_4)_3$ or the product of its decomposition–$NaBH_4$. On the other hand, diffraction lines that would correspond to second reactant NaIm are not present, thus it can be

assumed that unidentified phases in all samples correspond to the compounds that, in some form, contain imidazole.

As it was discussed before, sodium chloride appeared as a by-product during the synthesis of the $NaZn(BH_4)_3$ precursor and the centrifugation was proved to be unsuccessful for the removal of NaCl. Considering reactions were conducted as neat grinding, at this point while performing liquid-assisted mechanochemical reactions, the potential of centrifugation was reevaluated once again. Rietveld refinements for samples 1S1-CF and 1S1-DCM (Scheme 2), obtained after the centrifugation of 1S1 sample in CF and DCM, are shown in Table 16 and Figure 36.
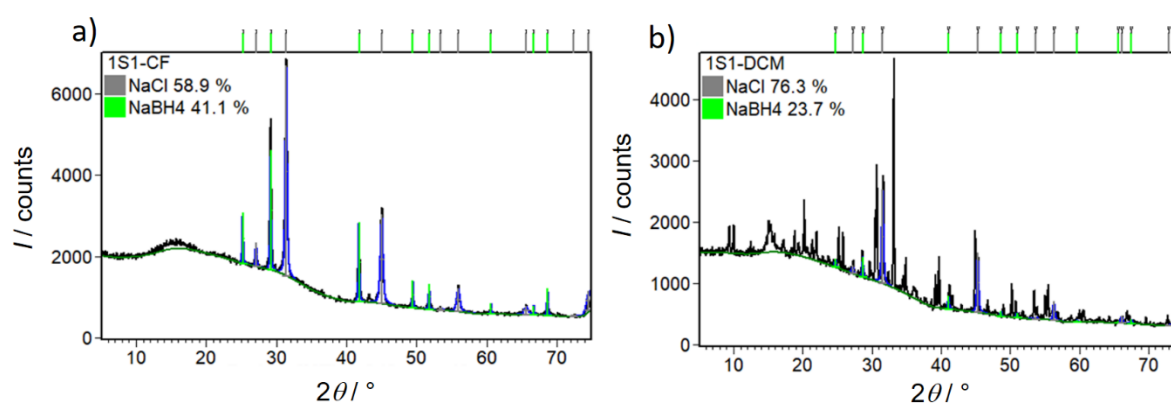
Figure 36. Rietveld refinement on samples 1S1-CF and 1S1-DCM obtained after the centrifugation of 1S1 in **a)** CF and **b)** DCM. Experimental diffraction data are shown in black, while calculated patterns are given in blue. Position of diffraction lines corresponding to $NaBH_4$ phase are given by green vertical marks while the vertical marks in the case of NaCl are grey.

Table 16. Quantitative composition of crystalline products in samples 1S1-CF and 1S1-DCM.

Sample	Centrifugation	Crystalline products composition as determined by the Rietveld refinement
1S1-CF	chloroform	NaCl (58.9 wt. %), $NaBH_4$ (41.1 wt. %)
1S1-DCM	dichloromethane	NaCl (76.3 wt. %), $NaBH_4$ (23.7 wt. %) and unknown phase(s)

Quantitative analysis revealed that unidentified diffraction lines present in sample 1S1 are removed by the centrifugation in CF. On the other hand, centrifugation of the sample 1S1 in DCM resulted in the formation of a new phase which was not present in sample 1S1. However, in neither case centrifugation was useful for the removal of sodium chloride.

Diffraction pattern of sample 1S2 (Scheme 2) showed the presence of few unidentified diffraction lines but unfortunately, even the temperature treatment during the *in-situ* SR-XRPD,

has not induced enhancement of crystallization that would allow the identification and/or structure solution (Figure AI SI, Table AI SI). Diffraction lines of an unidentified phase present in sample 1S3 (Scheme 2) obtained using DMSO seemed quite defined thus it has also been further investigated by *in-situ* SR-XRPD as well as by solid state NMR. As-prepared 1S3 sample as well as the sample after three months of aging, 1S3a, have been characterized.

XRD patterns of sample 1S3 collected during the heating run in the temperature range from RT to 445 °C and during the cooling run back to RT are shown in Figure 37a, while Figure 37b shows phase analysis at temperatures: RT, 70, 190, 240 and 280 °C in heating and RT after a cooling cycle.
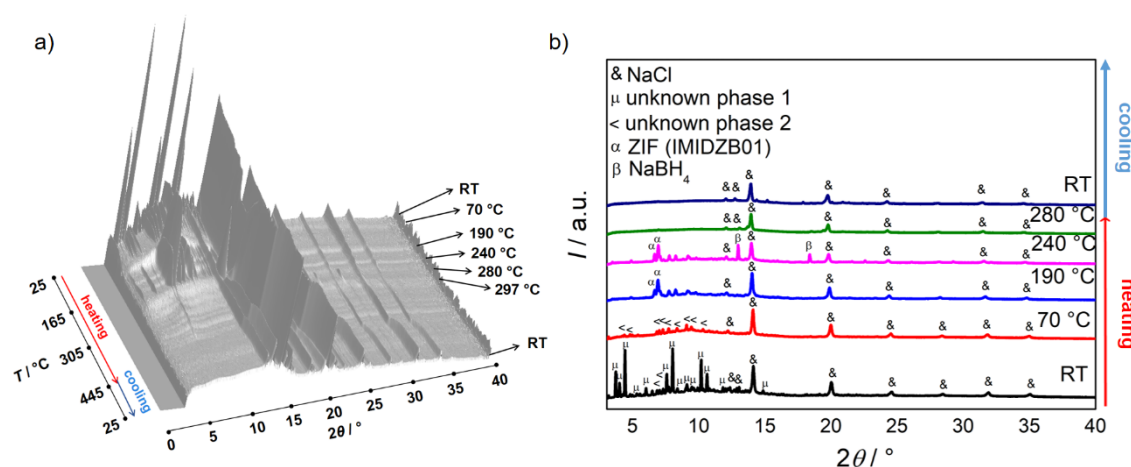
Figure 37. a) XRD patterns of sample 1S3 collected during heating run in temperature range from RT to 445 °C and during cooling run back to RT. **b)** Phase composition of sample 1S3 at RT, 70, 190, 240 and 280 °C and RT after cooling. Diffraction lines belonging to NaCl are marked with &, diffraction lines belonging to ZIF (IMIDZB01) with α, those belonging to unknown phases with μ and <, respectively while the diffraction lines belonging to $NaBH_4$ phase are marked with β.

From the *T*-ramp it becomes obvious that the composition of sample 1S3 changed during the period between data collection at the laboratory diffractometer and data collection at the synchrotron; sample 1S3 at RT does not contain only one unidentified phase, yet instead two unknown phases coexist; first one disappeared at 60 °C while the second one remained stable up to 132 °C. Simultaneously with disappearance of the second unidentified phase, zinc imidazolate (ZIF-IMIDZB01) begins to crystallize. With further increase in temperature, at 229 °C crystallization of $NaBH_4$ is observed. Both ZIF and $NaBH_4$ decompose around 270 °C. Sodium chloride is present in the system from room temperature and stays present in the system all the time. No recrystallization products are observed during the cooling run.

XRD patterns of the sample 1S3a collected during a heating run in the temperature range from RT to 445 °C and during the cooling run back to RT are shown in Figure 38a, while Figure 38b shows phase analysis at temperatures: RT, 125 and 190 °C and RT after the cooling cycle.
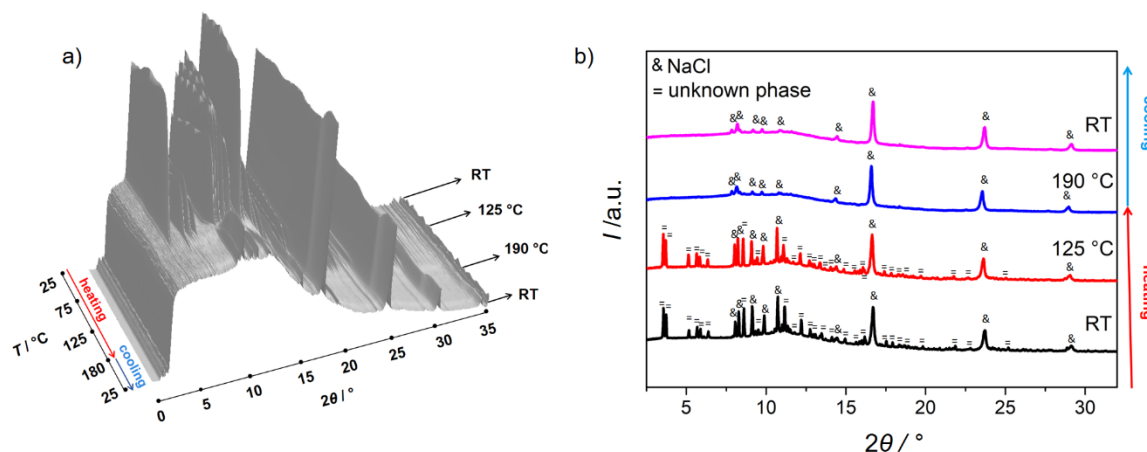
Figure 38. a) XRD patterns of sample 1S3a collected during heating run in temperature range from RT to 445 °C and during cooling run back to RT. **b)** Phase composition of sample 1S3a at RT, 125 and 190 °C and RT after cooling. Diffraction lines of NaCl phase are marked with & while the diffraction lines belonging to the unknown phase are represented by =.

Unlike in the case of the as-prepared sample 1S3, aged sample 1S3a showed the presence of only one unidentified phase, that different from those present in sample 1S3, which indicated that both unidentified phases present in 1S3 are some kind of solvate compounds with DMSO which can decompose at RT with aging. This phase remains stable up to 160 °C. Sodium chloride is present in the system from room temperature and stays present in the system all the time. No recrystallization products are observed during the cooling run. This new phase present in the sample 1S3a was indexed and space group was assigned from the systematic absences using the program FOX.[129,130] The phase crystallizes in the *P2/c* or *Pc* space group with the unit-cell parameters $a = 13.20675(2)$ Å $b = 12.6095(3)$ Å, $c = 18.2684(7)$ Å and $\beta = 93.641°$. Full pattern decomposition, as obtained in program EXPO[131] is shown in Figure 39.
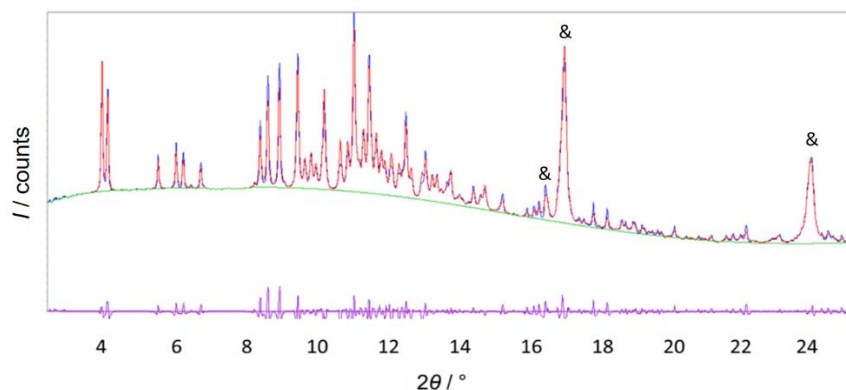
Figure 39. Whole pattern decomposition of sample 1S3a in the *P*2/*c* space group. Experimental pattern is given as blue line, calculated pattern as red while the difference is shown below in purple. NaCl diffraction lines are denoted with &.

Unfortunately, the structure was too complex for powder diffraction. From the cell volume, there should be 16 independent Zn-centers in the structure if the symmetry is *P*2/*c*. The structure-solution algorithms, both in EXPO or FOX, were not able to offer any plausible structure model thus this compound was additionally characterized by the solid-state NMR (ss-NMR).

The ^{1}H, ^{13}C, ^{23}Na and ^{11}B ss-NMR spectra of sample 1S3a are shown in Figure 40, together with the spectra of the as prepared sample 1S3. It is important to highlight that sample 1S3a, when ss-NMR measurement were collected, had the same phase composition, NaCl and one unidentified phase, as it was determined by the synchrotron diffraction experiment at RT. However the composition of the as-prepared 1S3 sample has changed. While the as-prepared 1S3 sample, measured at synchrotron contained two unidentified phases and NaCl, by the time ss-NMR was measured phase composition has changed to some intermediate composition that no longer contained those two phases yet instead a new phase that is present in the 1S3a sample. As the discussion will show, 1S3 sample, at the time when ss-NMR was measured contains NaCl, NaBH$_4$ and the new phase (the same as in the aged 1S3a sample).
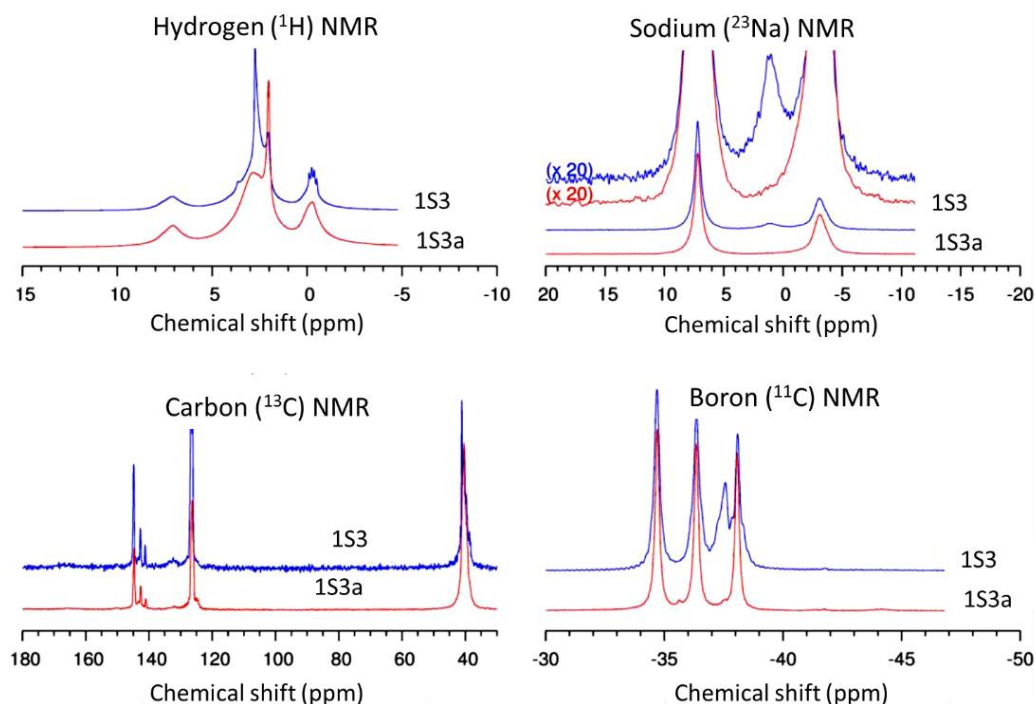
Figure 40. [1]H, ^{13}C, ^{23}Na and ^{11}B ss-NMR spectra of samples 1S3a and 1S3.

The ^{1}H, ^{13}C, [23]Na and [11]B spectra are characterized by narrow signals. Narrow signals usually indicate either a very good crystallinity of the material (very ordered phase(s)) or a fast motion of constituent atoms or groups of atoms, leading to efficient averaging of anisotropic contributions. The most prominent difference between the spectra of samples 1S3 and 1S3a is the disappearance of one [23]Na signal (resonating at 1 ppm) and one [11]B signal (resonating at -37.6 ppm). The sodium signal represented about 10% of the total sodium signal, and the boron signal represented about 20% of the total boron signal. In the proton NMR spectrum, a sharp signal at about 2.8 ppm is also missing. The changes in the carbon spectrum are less pronounced.

In order to gain insight into the structural features of the phase present in sample 1S3a, a careful examination of ss-NMR spectra have been carried out. The carbon signal at about 40 ppm can be assigned to DMSO. The corresponding proton signal might be the very narrow signal at about 2.1 ppm. Carbon signals resonating between 120 and 150 ppm belong to imidazole carbons; several signals can clearly be resolved which points out that not all imidazole moieties experience equal environments. The sodium NMR spectrum shows two clearly resolved signals with the intensity ratio of about 3 (signal at 7 ppm) to 2 (signal at -3 ppm). None of the signals exhibits a quadrupolar line shape, suggesting again that all sodium occupies very symmetric sites. In the boron NMR spectrum three almost equally strong signals can be detected that are

even narrower than the sodium signals. The fact that the outer two signals (the leftmost and the rightmost) are equally displaced from the middle, induces some doubt that the three signals belong to three different B sites; it might be that the signals belong to one site and that the 'splitting' of the observed signal is due to *J* coupling. Three signals would suggest coupling with an environment which has a total nuclear spin equal to one; such an environment could be due to two ^{1}H nuclei. Cross polarization between ^{1}H and [11]B is very efficient.

Additionally, sample 1S3a was also subjected to two 2D measurements, [1]H–[11]B HETCOR and [1]H–[1]H spin diffusion measurement shown on Figure 41.
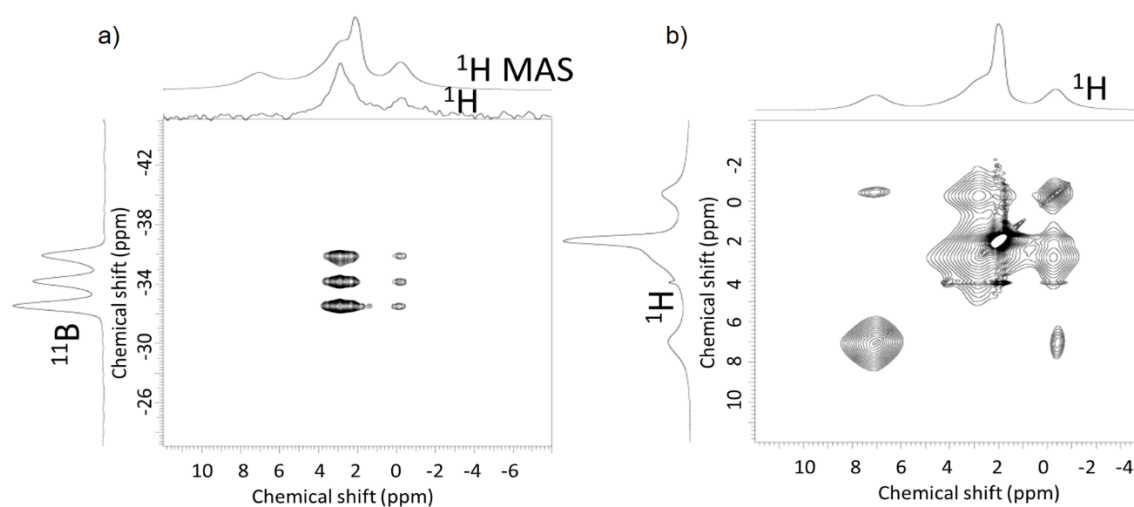
Figure 41. a) [1]H–[11]B HETCOR. **b)** ^{1}H–^{1}H spin-diffusion NMR spectra of sample 1S3a.

The top of the HETCOR spectrum shows the ^{1}H projection as well as ^{1}H MAS NMR. The HETCOR measurement shows that boron nuclei do not 'see' the imidazolate protons that resonate at 7 ppm and as well as protons that belong to DMSO at 2.1 ppm in their proximity. Also, the coupling with the borohydride signal resonating close to 0 ppm is rather weak but observable. Boron nuclei are most strongly coupled with protons that resonate between 2 and 3 ppm. At this point, the only question was the assignment of those protons that resonate between 2 and 3 ppm. Since those protons are obviously close to the boron atoms, but do not belong to the borohydride group, it might be reasonable to assume that an additional B−H moiety is also present in structure.

The [1]H–[1]H spin-diffusion spectrum shows that signals from two protons, located off-diagonal, first one resonating at -0.3 ppm and second one resonating at 2.8 ppm, are strongly mutually coupled and thus close in space. In general, off-diagonal cross peaks in the spin-diffusion

spectrum indicate that polarization was transferred between the different types of H nuclei, suggesting that the corresponding H atoms have to be close in space. The narrow signal resonating at 2.1 ppm is not coupled to any other proton. The lack of coupling might be due to the fact that DMSO is in a separate phase. The most important feature noticed in the spin-diffusion spectra is the fact that the protons resonating at 7 ppm, belonging to imidazole do show the off-diagonal cross peak with protons resonating close to 0 ppm, that belong to borohydride group indicating that, in fact, both ligands are present within the same crystalline phase.

In conclusion, NMR results, together with *in-situ* HT XRPD data, suggest that the crystalline phase in sample 1S3a in fact corresponds to hybrid compound that contains both imidazolate and borohydride ligands while DMSO, in some form, remains in the amorphous phase.

4.1.2.3. Mechanochemical reactions of NaBH₄, ZnCl₂ and NaIm

As an alternative to the utilization of mixed metal precursor $NaZn(BH_4)_3$, direct mechanochemical reactions, conducted by neat grinding, involving $NaBH_4$, $ZnCl_2$ and NaIm in different molar ratios have been investigated (Scheme 3).
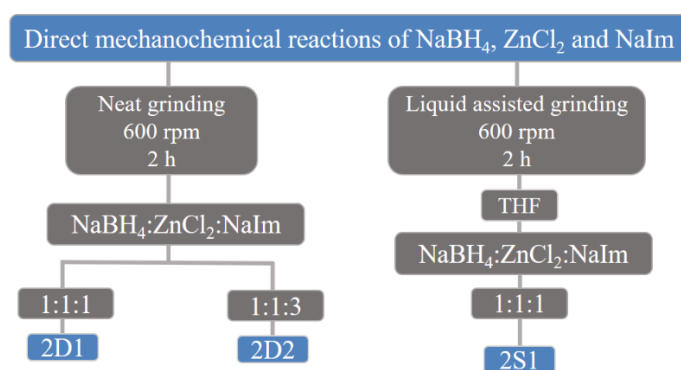
Scheme 3. Neat grinding of sodium borohydride, zinc chloride and sodium imidazolate. THF is used for liquid assisted grinding.

Rietveld refinements for samples 2D1 and 2D2, obtained by the dry mechanochemical reactions of $NaBH_4$, $ZnCl_2$ and NaIm in different molar ratios, are given in Figure 42.

Figure 42. Rietveld refinement on samples 2D1 and 2D2 obtained by the reaction involving NaBH$_4$, ZnCl$_2$ and NaIm in ratio: **a)** 1:1:1 and **b)** 1:1:3. Experimental diffraction data are shown in black, while calculated patterns are given in blue. Position of diffraction lines corresponding to sodium chloride are given by grey vertical marks.

Quantitative composition of samples 2D1 and 2D2 are summarized in Table 17.

Table 17. Quantitative composition of crystalline products in samples 2D1 and 2D2.

Sample	NaBH$_4$:ZnCl$_2$:NaIm ratio	Crystalline product composition as determined by the Rietveld refinement
2D1	1:1:1	small amount of the amorphous phase, NaCl
2D2	1:1:3	amorphous phase, NaCl

In both samples sodium chloride is present as the only crystalline phase that formed by cation exchange reaction of ZnCl$_2$ with either NaBH$_4$ or NaIm. Significant amount of amorphous phase can be observed in the case of sample 2D2 thus it has been additionally analyzed by *in-situ* SR-XRPD.

XRD patterns of sample 2D2 collected during a heating run in the temperature range from RT to 300 °C and during a cooling run back to RT are shown in Figure 43a, while Figure 43b shows phase analysis at temperatures: RT and 180 °C.
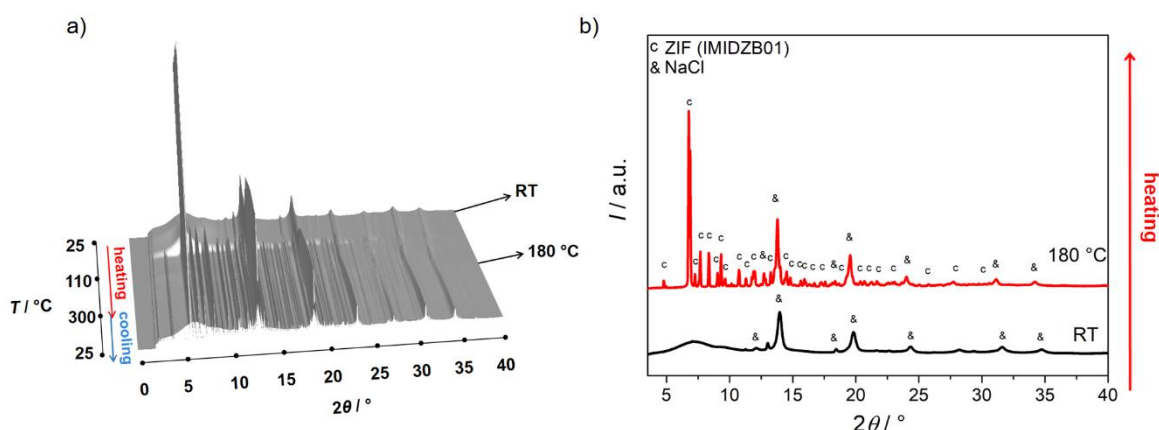
Figure 43. a) XRD patterns of sample 2D2 collected during heating run in temperature range from RT to 300 °C and during cooling run back to RT. **b)** Phase composition of sample 2D2 at RT and 180 °C. Diffraction lines of NaCl phase are marked with &, while the diffraction lines belonging to ZIF are represented by c. ($\lambda = 0.69449$ Å).

Temperature treatment of the sample 2D2, characterized by the significant amount of the amorphous phase at RT, led to crystallization of ZIF (IMIDZB01) above 160 °C. NaCl is present in the system all the time.

Diffraction pattern of sample 2S1 showed presence of a few unidentified diffraction lines but unfortunately, even the temperature treatment during the *in-situ* SR-XRPD, has not induced enhancement of crystallization that would allow the identification and/or structure solution (Figure AII SI, Table AII SI).

In summary, it can be concluded that dry mechanochemical milling of the bimetallic borohydride precursor with imidazolates often results in decomposition of the precursor followed by appearance of amorphous products, or even in some cases no reaction takes place. Additional thermal treatment usually results in the formation of a zeolitic imidazolate framework with zinc as metal centers while the sodium borohydride remains unreacted as a crystalline phase, forms solid solution with NaCl or transforms to an amorphous phase. Similar behavior has been noticed in the case when $NaBH_4$ and $ZnCl_2$ have been used instead of $NaZn(BH_4)_3$. On the other hand, it seems that liquid assisted grinding of the bimetallic borohydride with imidazolate can lead to the formation of a hybrid compound containing both borohydride and imidazolate anions, as proposed by the ss-NMR study.

4.2. MECHANOCHEMICAL REACTIONS OF MONOMETALLIC ALKALI BOROHYDRIDES MBH₄ (M = Li, Na AND K) WITH ALKALI METAL IMIDAZOLATES MIm (M = Li, Na AND K)

Previous chapter described the mechanochemical reactions of sodium imidazolate and a mixed, sodium containing, metal borohydride precursor [NaZn(BH₄)₃]. After initial assessment of those results, during the experimental stage of this dissertation, it was found that zeolitic imidazolate frameworks preferentially form when zinc cations are present together with imidazolate anions thus it seemed reasonable to conclude that the reactions with slightly less complex composition, in terms of number of metal centers present, might be more beneficial in providing the insight into the reactivity of imidazolates and borohydrides. Therefore dry mechanochemical reactions, by neat grinding, of alkali monometallic borohydrides MBH₄ (M = Li, Na and K) with alkali imidazolates MIm (M = Li, Na and K) in different ratios have been investigated (Scheme 4).
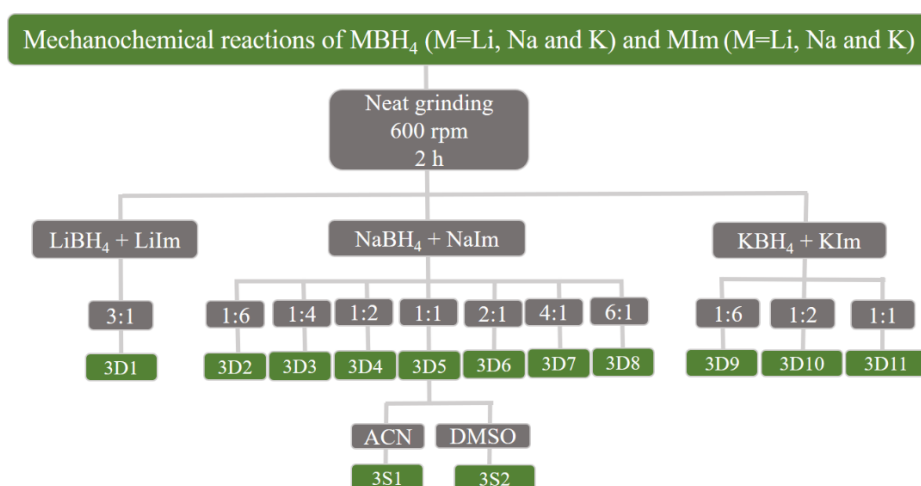
Scheme 4. Mechanochemical reactions of monometallic alkali borohydrides with alkali metal imidazolates.

Rietveld refinements for sample 3D1, obtained by the dry mechanochemical reactions of LiBH₄ and LiIm in the molar ratio 3:1 is given in Figure 44.
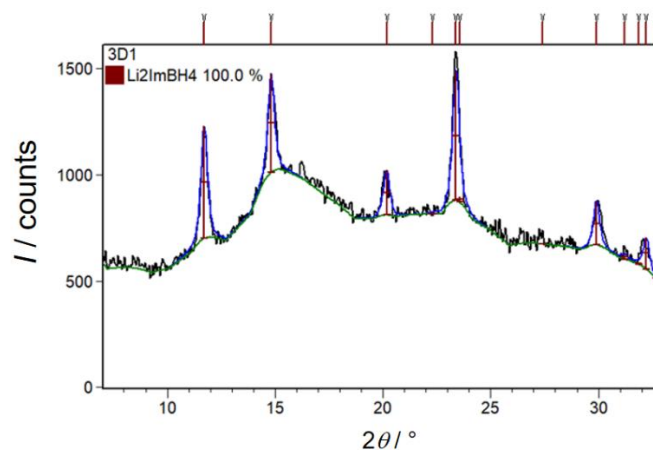
Figure 44. Rietveld refinement of sample 3D1 obtained by the dry mechanochemical reaction of LiBH$_4$ and LiIm in molar ratio 3:1. Experimental diffraction data are shown in black, while calculated pattern is given in blue. Diffraction lines position of Li$_2$ImBH$_4$ are represented by ochre vertical marks.

Rietveld structure refinement of sample 3D1 revealed that the hybrid compound Li$_2$ImBH$_4$ is formed. Until now, this compound was prepared either by solvent-assisted mechanochemical reactions or by an additional thermal treatment at 100 °C, while our results show that lithium borohydride imidazolate can form even by the neat-grinding reaction of LiIm and LiBH$_4$. After the reaction, the appearance of some amount of an amorphous phase cannot be avoided but nevertheless it has been clearly demonstrated that Li$_2$ImBH$_4$ can be formed at RT, as an only crystalline phase in the sample. It is interesting to notice that the direct mechanochemical reaction yielded a hybrid compound Li$_2$ImBH$_4$ in the case of the 3:1 molar ratio (with borohydride in excess) while in the case of 1:1 ratio the reaction was not sucesfull without the utilization of solvents or additional thermal treatment[110] which indicates that excess of borohydride in the system is necessary condition for the preparation of Li$_2$ImBH$_4$ *via* neat grinding.

Rietveld refinements for samples 3D2–3D8 (Scheme 4), obtained by the dry mechanochemical reactions of NaBH$_4$ and NaIm in the 1:6, 1:4, 1:2, 1:1, 2:1, 4:1 and 6:1 molar ratios, are given in Figure 45.
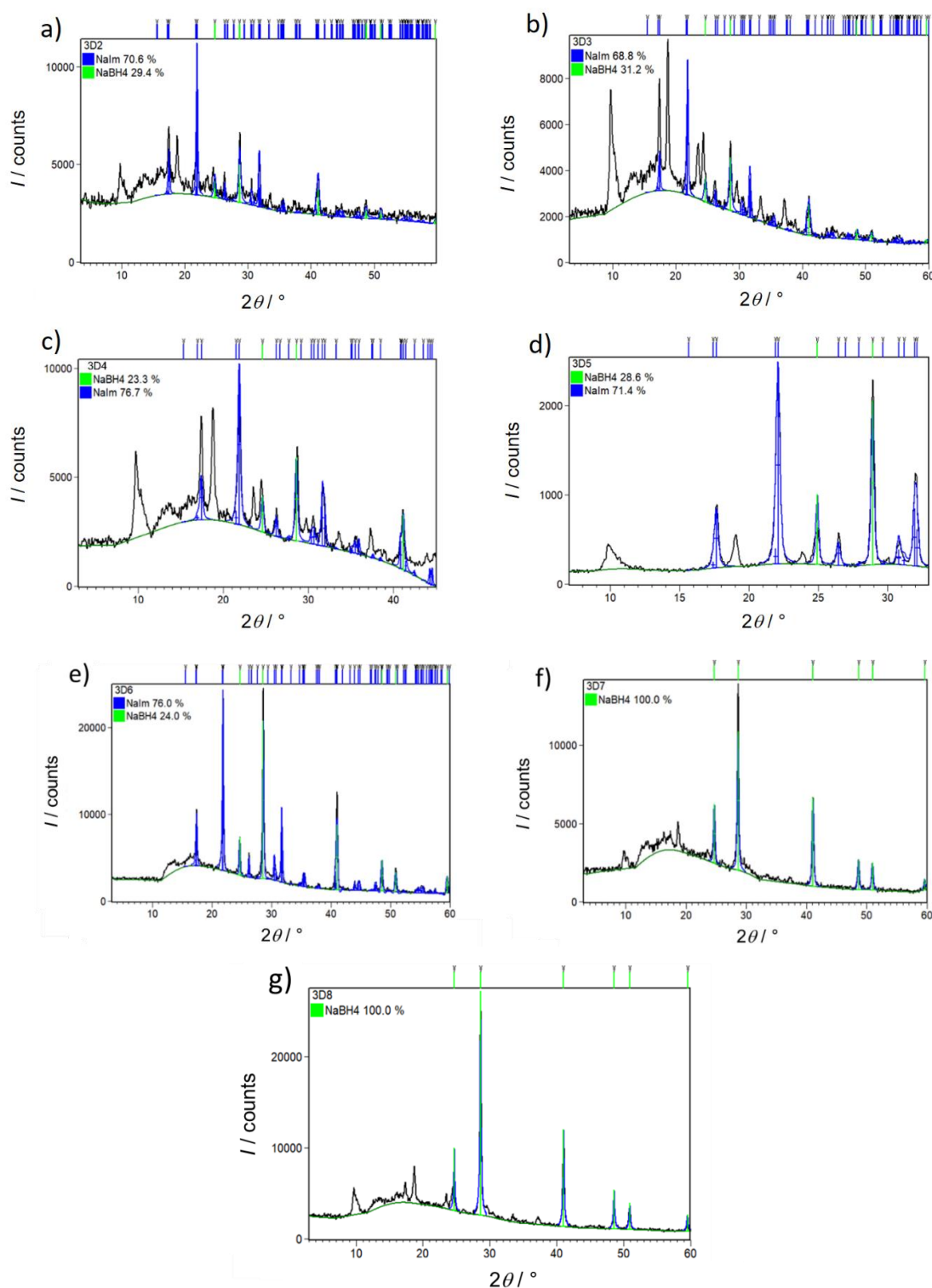
Figure 45. Rietveld refinement of samples 3D2–3D8 obtained by the dry mechanochemical reactions of $NaBH_4$ precursor and NaIm in different molar ratios: **a)** 1:6, **b)** 1:4, **c)** 1:2, **d)** 1:1, **e)** 2:1, **f)** 4:1 and **g)** 6:1. Experimental diffraction data are shown in black, while calculated patterns are given in blue. Diffraction lines position of $NaBH_4$ are represented by green vertical marks and NaIm by dark blue.

Quantitative composition of samples 3D2–3D8 are summarized in Table 18.

Table 18. Quantitative composition of crystalline products in samples 3D2–3D8.

Sample	$NaBH_4$: NaIm ratio	Crystalline products composition as determined by the Rietveld refinement
3D2	1:6	amorphous phase, NaIm (70.6 wt. %), $NaBH_4$ (29.4 wt. %), few unidentified peaks
3D3	1:4	amorphous phase, NaIm (68.8 wt. %), $NaBH_4$ (31.2 wt. %), few unidentified peaks
3D4	1:2	amorphous phase, NaIm (76.7 wt. %), $NaBH_4$ (23.3 wt. %), few unidentified peaks
3D5	1:1	NaIm (71.4 wt. %), $NaBH_4$ (28.6 wt. %), few unidentified peaks
3D6	2:1	amorphous phase, NaIm (76 wt. %), $NaBH_4$ (24 wt. %)
3D7	4:1	amorphous phase, $NaBH_4$ (100 wt. %), few unidentified peaks
3D8	6:1	amorphous phase, $NaBH_4$ (100 wt. %), few unidentified peaks

Rietveld structure refinement on XRPD data showed that in samples 3D2–3D4 (when excess NaIm has been used), NaIm can be detected as a major crystalline phase and $NaBH_4$ as a minor indicating that the reaction, in fact, has not occurred. But nevertheless, in all of the samples, few unidentified diffraction lines are present, indicating formation of a new crystalline phase. By comparing the position and intensities it was realized that in each sample those reflections belong to the same novel phase. In case of 3D6 sample, only unreacted reactants, NaIm and $NaBH_4$ are observed as crystalline products, while in samples 3D7 and 3D8 only $NaBH_4$ and unknown phase, same as in samples 1D1–1D5 (Scheme 2), are present as crystalline phases.

In order to elucidate the structural features of novel phase, sample 3D5, showing the smallest amount of amorphous phase, has been characterized by the solid state NMR. The ^{1}H, ^{13}C, ^{23}Na and ^{11}B solid state-NMR spectra of sample 3D5 are shown in Figure 46.
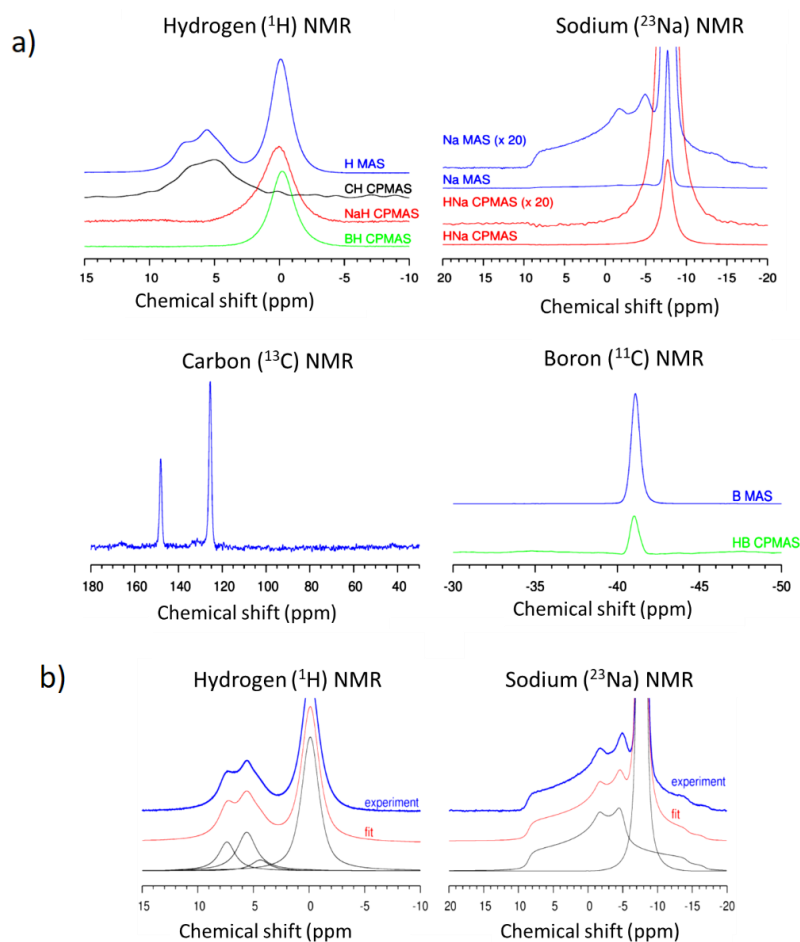
Figure 46. **a)** ¹H, ¹³C, ¹¹B and 23Na NMR spectra for sample 3D5.
b) Decomposition of the ¹H and ²³Na MAS NMR spectra.

Proton spectrum of sample 3D5 is composed of four contributions resonating at 7.4, 5.6, 4.4 and -0.1 ppm. Relative intensities of these contributions are roughly 2:(3–4):1:(9–10). From the two-dimensional ¹H–¹³C heteronuclear correlation spectrum (shown as a black CH-CPMASS line below the ¹H MAS spectrum), one can see that only the first three signals are close to carbon nuclei. On the contrary, the ¹H signal resonating at -0.1 ppm is close to Na and B nuclei; cross-polarization between these H nuclei and Na and B nuclei is efficient as visible by red and green spectra denoted as NaH- and BH-CPMAS, respectively. The lack of the -0.1 ppm proton signal in the CH heteronuclear correlation spectrum suggests that H atoms of this specie are not close to imidazole or that the specie is rather mobile and that therefore the H–C dipolar coupling is suppressed by fast motion. The sodium spectrum exhibits two very different signals, one narrow and symmetric resonating at about -7 ppm, and one with a typical broad quadrupolar line-shape extending between 9 and -16 ppm. Their relative intensities are approximately 3:1. The H–Na CPMAS spectrum shows that only the narrow contribution is efficiently cross-

polarized from protons. Narrow symmetric line for ^{23}Na nuclei indicates a highly symmetric position (like in cubic-like environment) or motionally averaged-out environment. However, since H–Na cross-polarization works well, motion is probably not very fast. The weaker, broader signal in the Na spectrum belongs to a less symmetric environment, not close to hydrogen atoms. In the boron NMR spectrum, only one symmetric signal can be seen. Since ^{11}B nuclei are quadrupolar nuclei (like ^{23}Na, and unlike ^{1}H), narrow symmetric line again indicates either a highly symmetric environment or fast motion. Here again also H–B CPMAS works, though less effectively than the H–Na CPMAS.

In summary, NMR detected one ^{11}B signal from $NaBH_4$ and two ^{23}Na signals presumably from $NaBH_4$ and NaIm. The question is, which elements could then be contained within the third crystalline phase visible in the diffraction pattern? The fact that NMR spectra showed the presence of only two phases containing sodium atoms, was an indication that the phase transition of one of the phases (NaIm or $NaBH_4$) took place during the ss-NMR measurement (that includes rotation and consequent increase in temperature).

In order to determine the crystal structure of the new crystalline compound, *in-situ* high temperature diffraction measurements with synchrotron radiation were performed at SNBL, ESRF. XRD patterns of sample 3D5 collected during the heating run in temperature range from RT to 240 °C and during the cooling run back to RT are shown in Figure 47a, while Figure 47b shows phase analysis at RT and 212 °C during heating and 210 °C and RT during the cooling run.
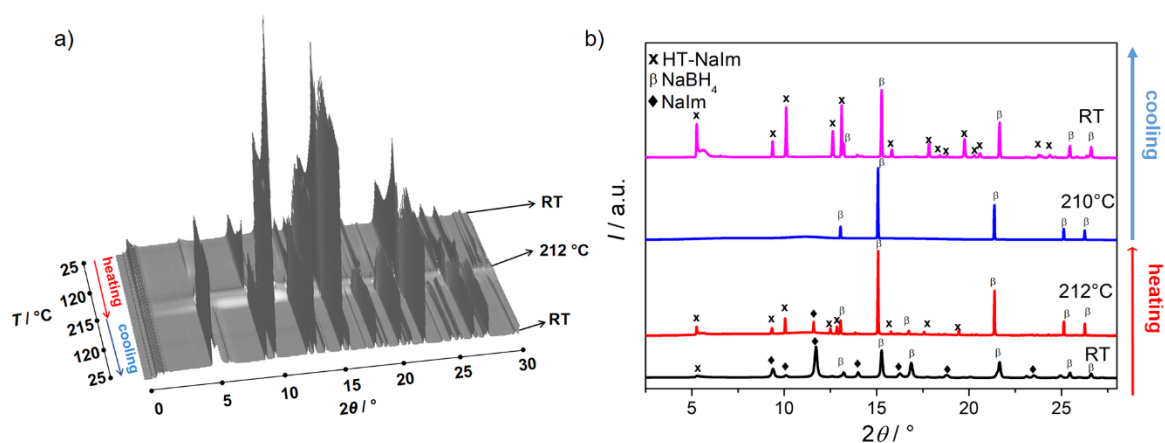
Figure 47. a) XRD patterns of sample 3D5 collected during heating run in temperature range from RT to 240 °C and during cooling run back to RT. **b)** Phase composition of sample 3D5 at RT and 212 °C during heating and 210 °C and RT during the cooling run. Diffraction lines belonging to NaIm are marked with diamonds, $NaBH_4$ with beta and HT-NaIm with x. Wavelength $\lambda = 0.8187$ Å.

Sample 3D5, in the temperature range from RT up to 172 °C, contained unreacted NaIm and NaBH$_4$ and a small amount of an unidentified phase; further discussion will reveal that those reflections belong to the second polymorph of NaIm, in particular the high-temperature polymorph. Between 172 °C and 213 °C NaIm slowly disappears while the diffraction lines of the second polymorph become more pronounced, until finally it melts around 216 °C. NaBH$_4$ is stable in the whole temperature range from RT to 220 °C. During cooling, the second NaIm polymorph recrystallizes below 190 °C, and it is stable down to the RT. NaBH$_4$ was stable during cooling. Second NaIm polymorph does not transform to the first one.

An interesting effect has been noticed during the recrystallization process of the second NaIm polymorph. Figure 48 shows diffraction patterns at 168 °C and 212 °C during heating and at 68 °C during cooling. With the grain growth diffuse scattering around the first diffraction line appears and with further cooling pronounced streaks, instead of a defined diffraction rings, are observed. Morphology of the sample changed from fine to quite grainy (Figure 49). Such a diffuse feature is an indication of the prominent increase of defects and/or disorder within the structure.
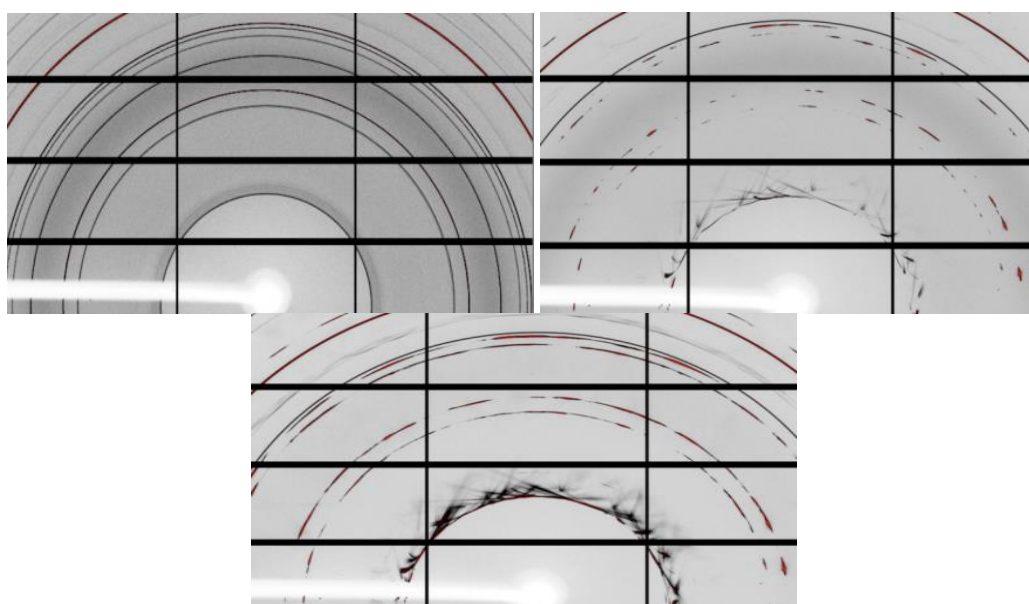
Figure 48. Diffraction patterns of sample 3D5, collected at 168 °C and 212 °C during heating and at 68 °C during cooling.
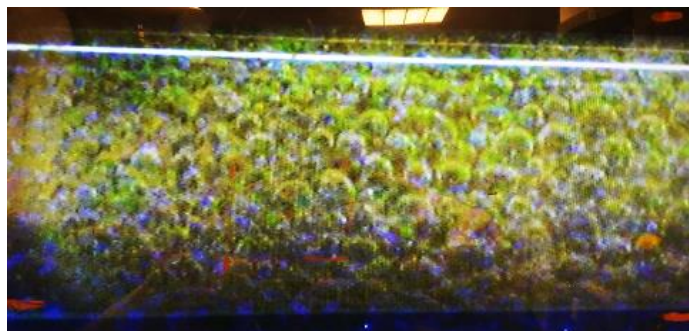
Figure 49. Sample 3D5 transformed from powder to grainy, during the synchrotron experiment.

Diffraction pattern collected at 139 °C during the cooling cycle has been indexed in the trigonal cell by the FOX program, however the significant overlap of diffraction lines, as well as disorder of the structure, prevented a successful structure determination thus the proposed unit-cell and space group could not have been ambiguously confirmed. In order to solve the structure an additional attempt to prepare single crystals has been carried out. Experimental setup is shown in Figure 50.

Figure 50. Experimental setup for the crystallization of high temperature NaIm polymorph in the form of the single crystal.

Pure NaIm was heated on a heating plate for 20 min in a capillary in a sand bath at 210 °C, a temperature well above the phase transformation. After this thermal treatment, the sample has been slowly cooled down to the room temperature, yielding single crystals of an adequate size for the structure solution (Figure 49).

Single crystal determination revealed that the HT polymorph of NaIm crystallizes in the trigonal $P3_112$ space group with cell parameters $a = 10.3164(4)$ Å and $c = 21.4192(11)$, confirming that the indexing process of the powder pattern was indeed correct.

The structure was solved as a racemic twin. Besides the inversion twin, no other twinning is involved. In general, a twinned crystal is an aggregate in which different domains are joined together according to a specific symmetry operation; the twin law. The diffraction patterns derived from different domains are rotated, reflected or inverted with respect to each other, depending on the nature of the relationship between the different domains, and weighted according to the quantity of a particular domain present in the crystal. The diffraction pattern measured during data collection is a superposition of all of these. During structure refinement, only Na1 and Na2 have been refined as fully occupied, the remaining sodium (Na3 and Na4) atoms are present in a 73/27 ratio. Crystal data and summary of refinement are given in Table 19 while the crystal structure is shown in Figure 51.

Table 19. Crystal data and summary of structure refinement for HT-NaIm

	HT-NaIm
Space group	$P3_112$
a/ Å	10.3164(4)
c/ Å	21.4192(11)
V/ Å^3	1974.21(18)
Chemical formula	C9 H9 N6 Na3
Chemical formula weight/ gmol^{-1}	270.19
Formula units, Z	6
F(000)	828
No. of measured reflections	13271
Goodness-of-fit	1.098
Rall	0.0682
Rgt	0.0516
wR	0.1619

Figure 51a shows two different chains with 3_1 screw axis along the c-direction, first one consisting of Na1- and Na2-imidazolate polyhedras and the second one consisting of Na3- and Na4-imidazolate polyhedras. Those chains are mutually connected and form a sheet that runs parallel to ab plane. Repeating sequence can be described as a trimeric unit with formula Na$_3$Im$_6$. Those three sodium atoms that form a trimeric unit are two Na1 atoms and one Na2 atom in the case of first chain, and two Na3 atoms and one Na4 atom in the case of the second chain. Sodium atoms Na2 and Na4 are octahedrally coordinated by six imidazolate rings while

atoms Na1 and Na3 are coordinated by four imidazolate ligands, forming highly deformed polyhedra.
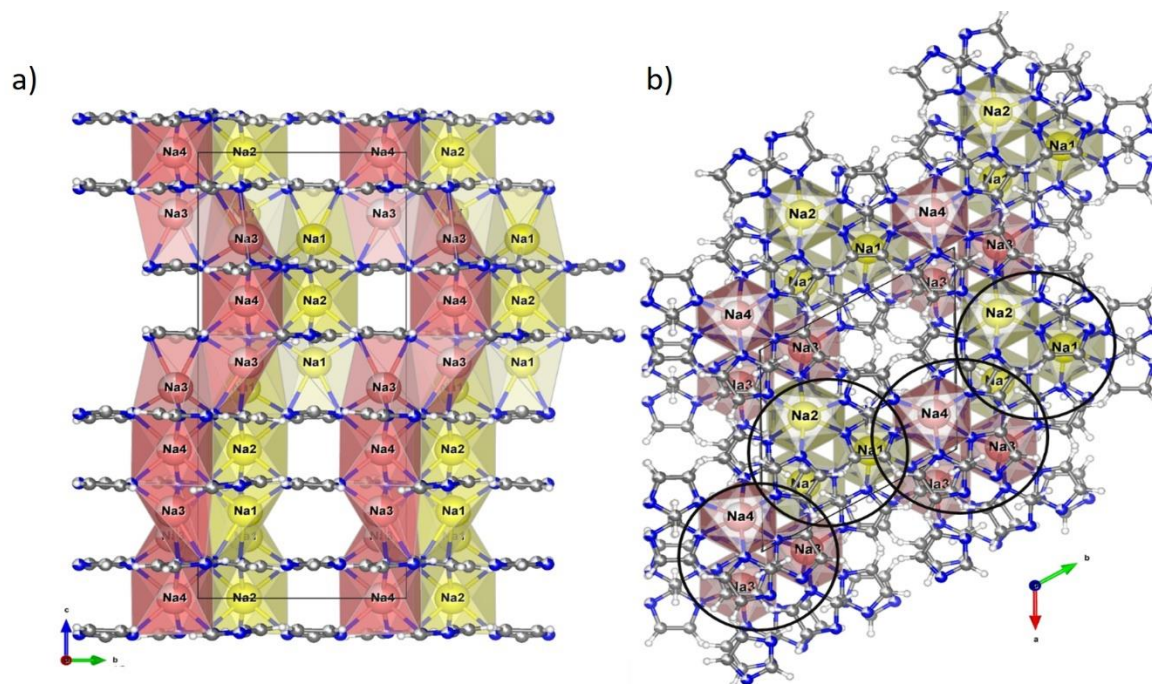
Figure 51. Crystal structure of HT-NaIm. **a)** Sheets along *b*-direction consisting of chains with 3_1 screw axis along *c*-direction. **b)** Helices viewed along *c*-direction.

Imidazolate rings, exhibiting different surroundings are shown in Figure 52.
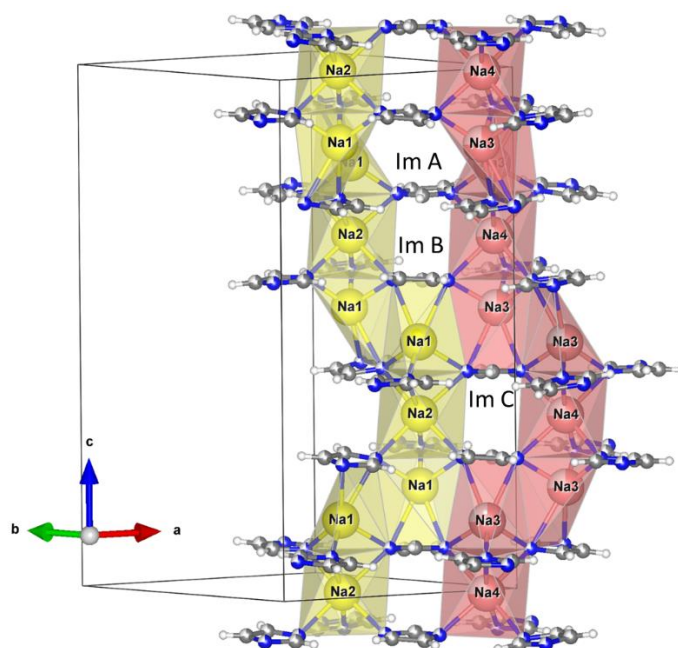
Figure 52. Different environments of imidazolate rings within the HT-NaIm structure

Imidazolate ring denoted as Im A acts like a bridging ligand towards four sodium atoms, Na1 and Na2 atoms *via* one nitrogen atom, and towards the Na3 and Na4 atoms *via* the other N atom. Imidazolate Im B exhibits even more complex environment, having Na2, Na3, Na4 and two Na1 atoms at the distances around 2.4–2.8 Å from nitrogen atoms, while Im C is surrounded by Na1, Na2, Na4 and two Na3 atoms at similar distances as in the case of Im B.

Figure 53 shows the hexagonal planes containing the triplet of coordination polyhedra. The planes are packed along c-axis in hexagonal close packing (HCP) (yellow-red or yellow-blue) with cubic close packed (CCP) domains (yellow-red-blue). This is a typical example of stacking faults between HCP and CCP, what explains also the diffuse streaks observed on diffraction pattern images of the single crystal on cooling.
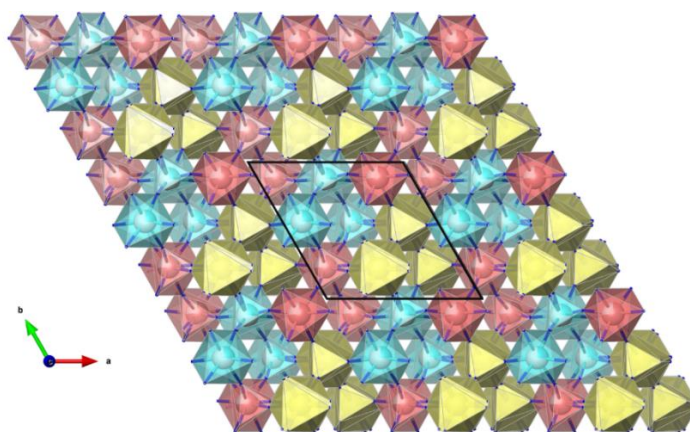
Figure 53. 3D framework of HT-NaIm in *ab* plane. Helicoidal chains containing fully occupied Na positions are given in yellow, while the majority and the minority helixes are given in pink and turqiuse, respectively.
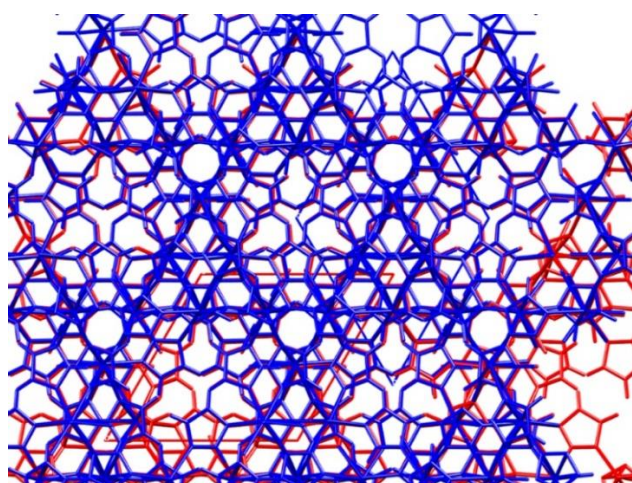
Figure 54. Overlapped structures of HT-NaIm. Positions of Na3 and Na4 sodium atoms are occupied in ratio 73/27. Component 1 with higher occupancies of Na atoms (73%) is shown with red model, while the component with lower occupancy (27 %) is shown with blue model.

Unlike the low temperature sodium imidazolate polymorph that shows tetrahedral coordination of sodium atom, in the structure of HT-NaIm polymorph the sodium atoms exhibit both tetrahedral coordination as well as a distorted octahedral coordination. The interatomic distances around the tetrahedrally coordinated sodium atoms, $d(Na_{tet}-N_{Im})_{HT-NaIm} = 2.39(3)$ Å, are found to be a bit shorter in the case of the high temperature polymorph of NaIm compared to the RT polymorph [$d(Na_{tet}-N_{Im})_{NaIm} = 2.45(3)$ Å]. The interatomic distances in the case of octahedrally coordinated sodium atoms are longer, as expected for higher coordination number, compared to tetrahedrally coordinated sodium atoms and amount to $d(Na_{oct}-N_{Im})_{HT-NaIm} = 2.65(2)$ Å.

Rietveld refinements for samples 3S1 and 3S2 (Scheme 4), obtained by the liquid assisted grinding of the sample obtained by mechanochemical reaction of NaBH$_4$ and NaIm in 1:1 molar ratio with acetonitrile (sample 3S1) and dimethylsulfoxide (sample 3S2), are given in Figure 55.
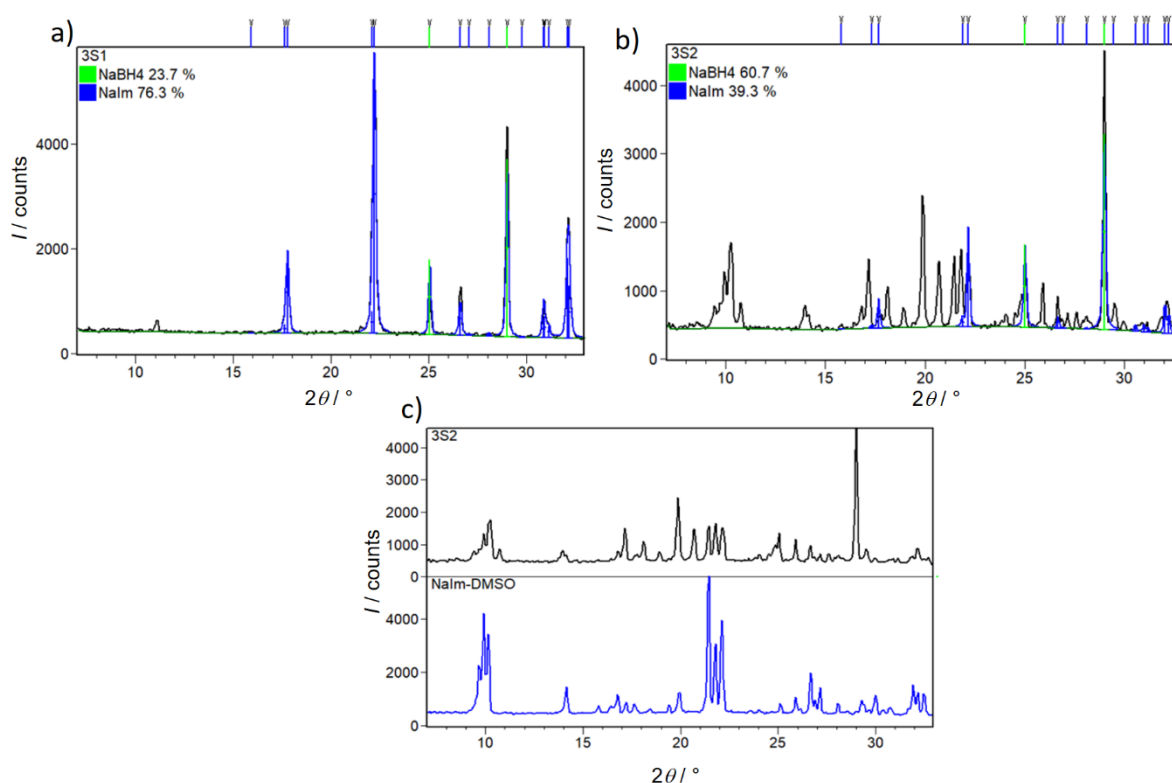
Figure 55. Rietveld refinements for samples 3S1 and 3S2, obtained by the liquid-assisted mechanochemical reactions of NaBH$_4$ and NaIm in molar ratio 1:1 with different solvents: **a)** ACN and **b)** DMSO. **c)** Unknown phase present in sample 3S2 can be identified as a DMSO solvate of NaIm.

Quantitative composition of mechanochemical products in samples 3S1 and 3S2 are summarized in Table 20.

Table 20. Quantitative composition of crystalline products in samples 3S1 and 3S2.

Sample	NaBH$_4$: NaIm ratio	Solvent	Crystalline products composition as determined by the Rietveld refinement
3S1	1:1	ACN	NaBH$_4$ (23.7 wt. %), NaIm (76.3 wt. %)
3S2	1:1	DMSO	NaBH$_4$, NaIm and NaIm-DMSO solvate

Both samples 3S1 and 3S2 contain starting reactants, NaBH$_4$ and NaIm indicating that reaction has not occurred, similar as in the case of neat grinding. It is interesting to notice that in the case of solvent-assisted grinding, compared to neat-grinding, a HT polymorph of NaIm has not been formed. In the case of reaction with DMSO, beside unreacted components, a DMSO solvate of NaIm is observed.

Rietveld refinements for samples 3D9–3D11 (Scheme 4), obtained by the dry mechanochemical reactions of KBH$_4$ and KIm in molar ratios 1:6, 1:2 and 1:1 are given in Figure 56.

Figure 56. Rietveld refinement of samples 3D9–3D11 obtained by the dry mechanochemical reactions of KBH$_4$ and KIm in different molar ratios: **a)** 1:6, **b)** 1:2 and **c)** 1:1. Experimental diffraction data are shown in black, while calculated patterns are given in blue. Diffraction lines position of KIm are represented by purple vertical marks, while the vertical marks in the case of KBH$_4$ are colored khaki.
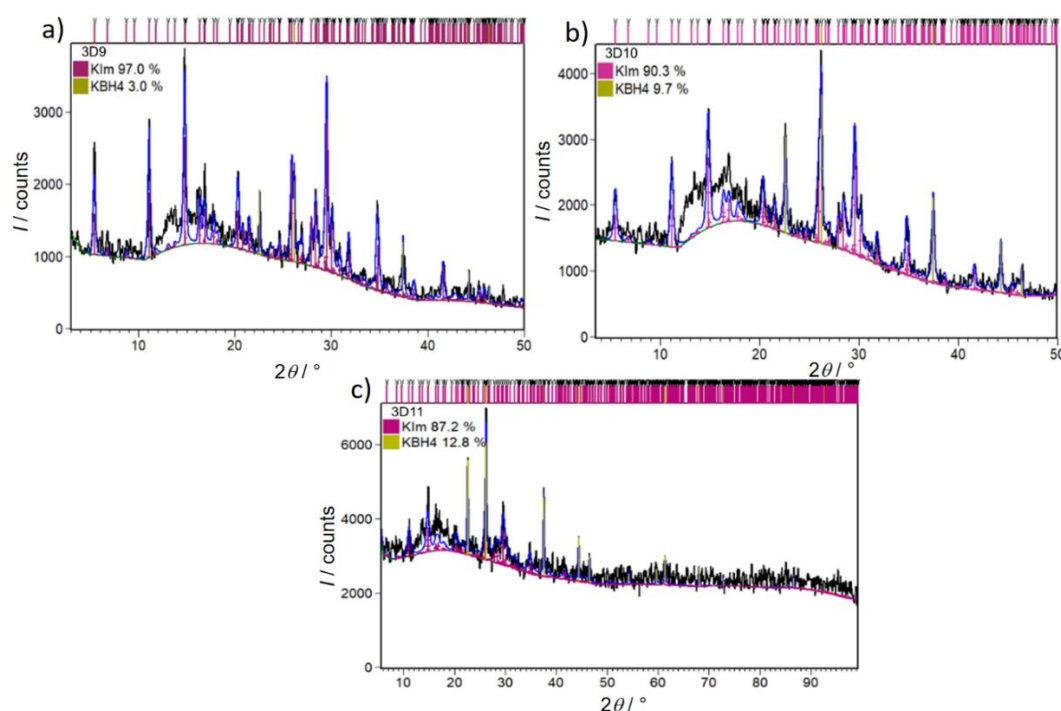
Quantitative composition of mechanochemical products in samples 3D9–3D11 are summarized in Table 21.

Table 21. Quantitative composition of crystalline products in samples 3D9–3D11, milled for 2h.

Sample	KBH_4: KIm ratio	Crystalline products composition as determined by the Rietveld refinement
3D9	1:6	KIm (97 wt. %), KBH_4 (3 wt. %)
3D10	1:2	KIm (90.3 wt. %), KBH_4 (9.7 wt. %), few unidentified peaks
3D11	1:1	KIm (87.2 wt. %), KBH_4 (12.8 wt. %), few unidentified peaks

Diffraction pattern of sample 3D11 showed the presence of few unidentified diffraction lines but even the temperature treatment during the *in-situ* SR-XRPD, have not induced a reaction of reactants; both being present at 142 °C, neither have induced further enhancement of crystallization that would allow identification of a new phase (Figure AIII SI, Table AIII SI). Above 159 °C, KIm melts and only KBH_4 remains in the sample.

In summary, it seems that the stability and the reactivity of borohydrides and imidazolates differ significantly for different metals of the alkali group. In the case of lithium, borohydride and imidazolate react swiftly and form the hybrid compound Li_2ImBH_4. This work demonstrates that crystallization of Li_2ImBH_4 is feasible simply by employing only neat grinding. No thermal treatment nor solvent assisted grinding is necessary. On the other hand, sodium and potassium imidazolates in reaction with sodium and potassium borohydride do not result in the formation of a similar hybrid compound. Moreover, even an additional thermal treatment that followed the mechanochemical grinding, have not resulted in the formation of hybrid compounds. Nevertheless, in the scope of this work, a novel polymorph of sodium imidazolate was discovered. It is particularly interesting to notice that the structure consists of imidazolate sheets with sodium atoms located in between those layers; sodium atoms might prove to be quite mobile thus this compounds will further be investigated for applications as solid state electrolytes. It is important to highlight that this compound has been identified during the mechanochemical milling of NaIm (in excess) with $NaBH_4$ which means that simple mechanochemical milling of the RT polymorph can induce the phase transformation to the high temperature form. Nevertheless, it seems that milling-induced phase transition of NaIm is not a straightforward process and that it is dependant on the amount of $NaBH_4$ present in the system; one would expect that the largest amount of HT-NaIm will be observed when the starting amount of NaIm is the largest, i.e. in the case when NaIm is used in excess compared to $NaBH_4$, but in fact the quantitative Rietveld refinements (Figure AIV and Table AIV in SI) showed that

highest amount of NaIm has been transformed to the high temperature polymorph in the case of NaBH$_4$:NaIm = 1:4 ratio, not in the case of 1:6 ratio, as might be expected. Here it has to be noted that while the HT-NaIm can be obtained by the neat-grinding, DMSO or ACN assisted grinding do not result in the phase transformation to the high temperature form. Alternatively, HT polymorph can also be prepared by heating RT-NaIm at 210 °C. Especially important feature, application-wise, is related to fact that during the cooling to RT, the high temperature polymorph of NaIm recrystallizes at 190 °C and remains stable in the whole temperature range.

4.3. MECHANOCHEMICAL REACTIONS OF MONOMETALLIC ALKALINE EARTH BOROHYDRIDE Mg(BH₄)₂ WITH ALKALI METAL IMIDAZOLATES MIm (M = Na, Li AND K)

After the investigations of the reactions of alkali metal imidazolates and alkali monometallic borohydrides, the research was further extended to the mechanochemical reactions of alkaline earth borohydrides. Mechanochemical reactions, conducted by neat grinding, of alkaline earth monometallic borohydride $Mg(BH_4)_2$ with alkali imidazolates MIm (M = Na, Li, K) in different ratios have been investigated (Scheme 5).
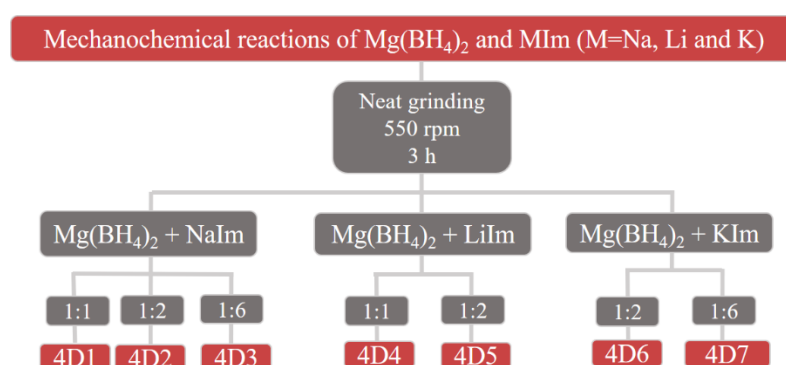
Scheme 5. Mechanochemical reactions of monometallic alkaline earth borohydride and alkali metal imidazolates.

Rietveld refinements for samples 4D1–4D7, obtained by neat grinding of $Mg(BH_4)_2$ and MIm (M = Na, Li and K) in different molar ratios, are given in Figure 57.
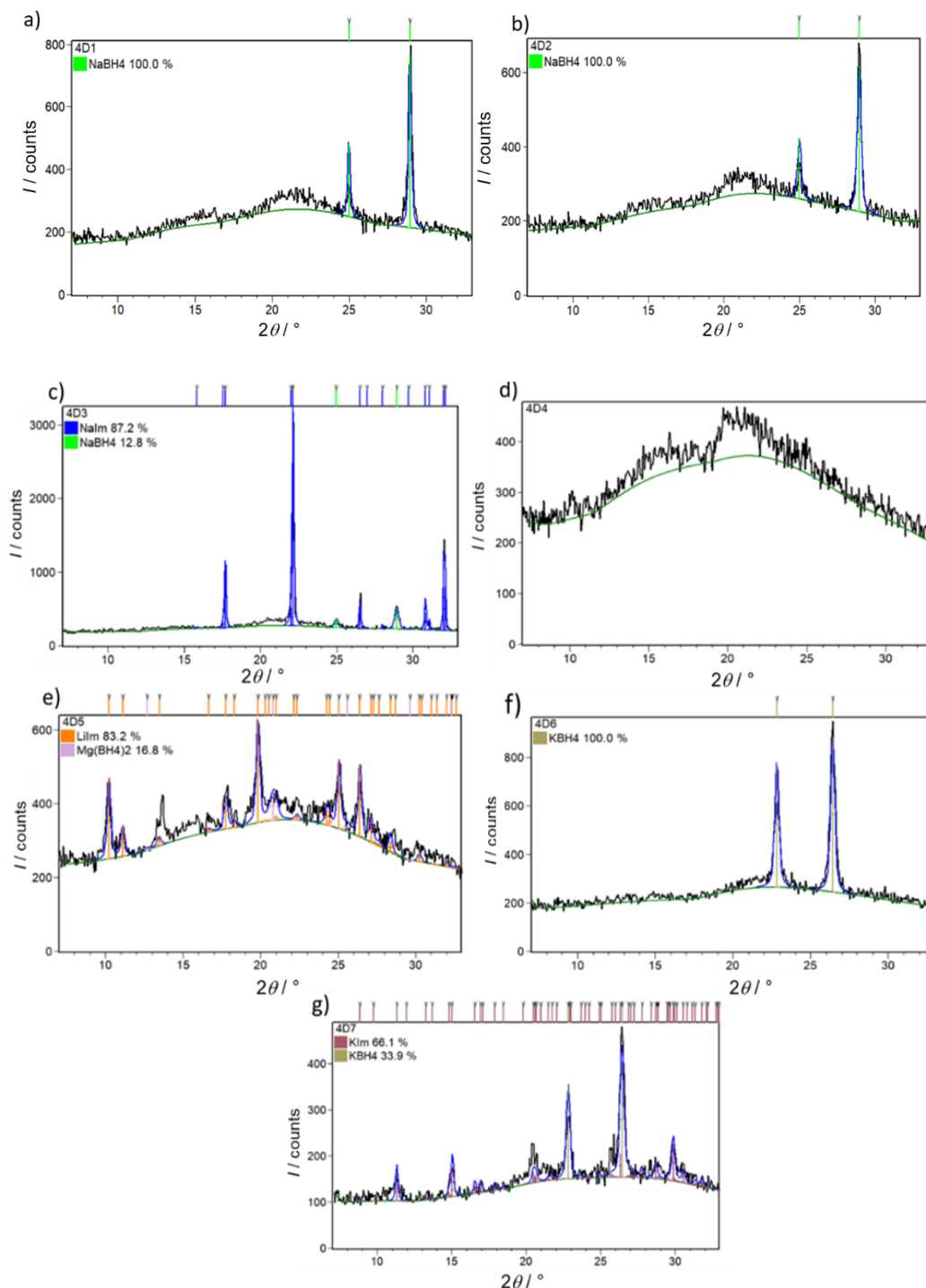
Figure 57. Rietveld refinement of samples 4D1–4D7 obtained by the dry mechanochemical reactions of Mg(BH$_4$)$_2$ and NaIm in different molar ratios: **a)** 1:1, **b)** 1:2 and **c)** 1;6; of Mg(BH$_4$)$_2$ and LiIm in different molar ratios: **d)** 1:1 and **e)**1:2,; of Mg(BH$_4$)$_2$ and KIm in different molar ratios: **f)** 1:2 and **g)** 1:6. Experimental diffraction data are shown in black, while calculated patterns are given in blue. Diffraction lines position of NaBH$_4$ are represented by green vertical marks, LiIm by orange, Mg(BH$_4$)$_2$ by light purple, NaIm by dark blue, KIm by purple while the vertical marks in the case of KBH$_4$ are colored khaki.

Table 22 shows quantitative composition of mechanochemical products (samples 4D1–4D7).

Table 22. Quantitative composition of crystalline products in samples 4D1–4D7

Sample	Reaction	Crystalline products composition as determined by the Rietveld refinement
4D1	$Mg(BH_4)_2$:NaIm = 1:1	amorphous phase, $NaBH_4$ (100 wt. %)
4D2	$Mg(BH_4)_2$:NaIm = 1:2	amorphous phase, $NaBH_4$ (100 wt. %)
4D3	$Mg(BH_4)_2$:NaIm = 1:6	NaIm (87.2 wt. %), $NaBH_4$ (12.8 wt. %)
4D4	$Mg(BH_4)_2$:LiIm = 1:1	amorphous phase
4D5	$Mg(BH_4)_2$:LiIm = 1:2	amorphous phase, LiIm (83.2 wt. %), $Mg(BH_4)_2$(16.8 wt. %), few unidentified peaks
4D6	$Mg(BH_4)_2$:KIm = 1:2	amorphous phase, KBH_4 (100 wt. %)
4D7	$Mg(BH_4)_2$:KIm = 1:6	amorphous phase, KIm (66.1 wt. %), KBH_4 (33.9 wt. %), few unidentified peaks

The only crystalline product in samples 4D1 and 4D2, obtained after the mechanochemical reaction of $Mg(BH_4)_2$ and NaIm for 2 h in the 1:1 and 1:2 ratio, was sodium borohydride. Those results suggest that cation exchange reaction took place but the energy during milling was not sufficient for crystallization of $MgIm_2$, which probably is contained in the amorphous phase. Similar behavior is noticed for the reaction in the 1:6 ratio, in the sample 4D3, where additionally NaIm is also observed which is, of course, consequence of the starting ratio where excess NaIm has been used. Sample 4D4 contains only amorphous products. Sample 4D5 showed unreacted reactants and some unidentified diffraction lines, similar as sample 4D7. Obviously, the energy brought to the reaction system during the milling, in most cases was not enough to induce the chemical reaction, thus thermally induced reaction during *in-situ* high temperature synchrotron radiation experiments have been performed for 4D3 and 4D5 while in the case of 4D7 the products have been *ex-situ* thermally treated and then measured.

XRD patterns of sample 4D3 collected during the heating run in the temperature range from RT to 385 °C and during the cooling run back to RT are shown in Figure 58a, while Figure 58b shows phase analysis at RT, 137, 209, 212, 249 and 349 °C.

Figure 58. a) XRD patterns of sample 4D3 collected during heating run in temperature range from RT to 385 °C and during cooling run back to RT. **b)** Phase composition of sample 4D3 at RT, 137, 209, 212, 249 and 349 °C. Diffraction lines of NaIm are marked with diamonds, NaMgIm$_3$ phase with circles while the unknown phase is denoted with x.

As known from laboratory data, sample 4D3 contains unreacted NaIm and some amount of an amorphous phase(s) at RT. At 118 °C, an unidentified phase started to crystallize; further discussion will reveal that this is novel compound NaMgIm$_3$. With further thermal treatment, the diffraction lines of NaIm disappear at 209 °C. Simultaneously, HT-NaIm starts to crystallize and it is stable from 209 up to 218 °C. Above 218 °C, only NaMgIm$_3$ diffraction peaks are present. It remains stable up to 340 °C.

XRD patterns of sample 4D5 collected during the heating run in the temperature range from RT to 450 °C and during the cooling run back to RT are shown in Figure 59a, while Figure 59b shows phase analysis at RT, 198 °C and 320 °C.
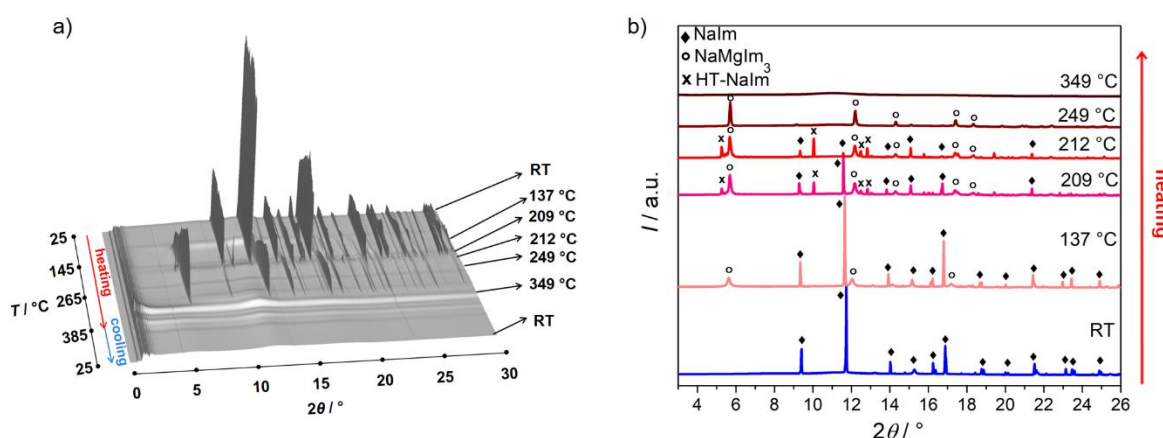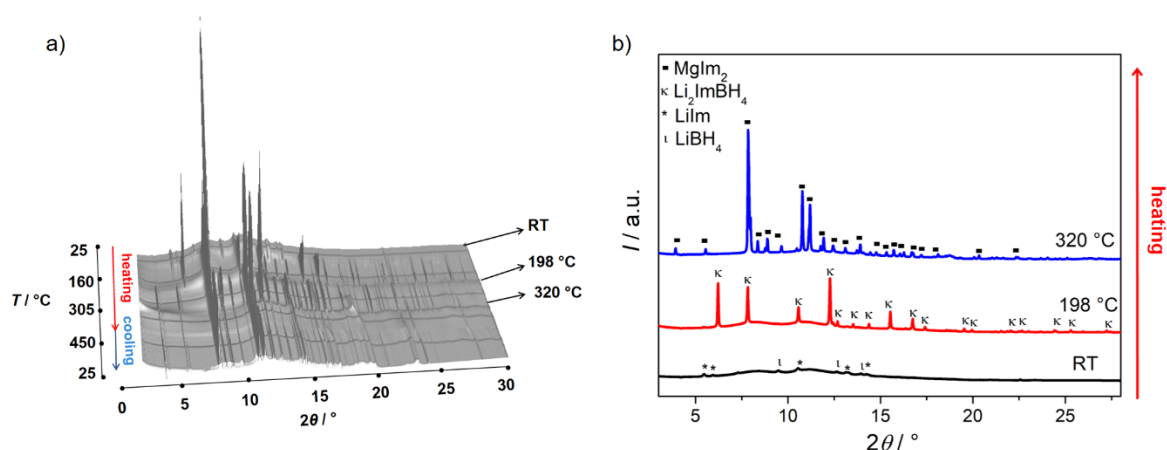

Figure 59. a) XRD patterns of sample 4D5 collected during heating run in temperature range from RT to 450 °C and during cooling run back to RT. **b)** Phase composition of sample 4D5 at RT, 198 and 320 °C. Diffraction lines of MgIm$_2$ are marked with squares, Li$_2$ImBH$_4$ with κ, LiIm with *, while the LiBH$_4$ is denoted with ι. (λ = 0.8212 Å).

If pattern at RT collected during the synchrotron experiment is compared to the pattern collected on the laboratory diffractometer (Figure 57e), it can be seen that the composition of sample 4D5 changed with aging; in particular the partial cation exchange occurred and $Mg(BH_4)_2$ is not present anymore, instead $LiBH_4$ is observed. The aged sample 4D5 at RT contained LiIm and $LiBH_4$ and some amount of an amorphous phase. Slowly with disappearance of LiIm and $LiBH_4$, a hybrid compound with both ligands incorporated in its structure, Li_2ImBH_4, starts to crystallize above 100 °C. Interestingly, this demonstrates that Li_2ImBH_4 can also be prepared from magnesium borohydride and lithium imidazolate, however, a partial cation exchange reaction that results in the formation of $LiBH_4$ occurs first, so additional thermal treatment has to be applied in order to initiate the reaction of $LiBH_4$ and LiIm. Even more interesting fact has been realized with further increase in temperature; simultaneously with disappearance of Li_2ImBH_4 around 240 °C, $MgIm_2$ begins to crystallize and it is stable as only crystalline phase in the system, without decomposition during heating to 450 °C as well as during cooling back to the RT. Until now it has been considered that crystalline $MgIm_2$ can only be prepared by the reaction in liquid ammonia from $NaNH_2$, $Mg(NO_3)_2$ and ImH[115] while this work shows that $MgIm_2$ can also be prepared by the partial exchange reactions during mechanochemical milling of LiIm and $Mg(BH_4)_2$ followed by the additional thermal treatment at 240 °C. This pathway represents an excellent alternative for the preparation of magnesium imidazolate by simple cation exchange starting with lithium imidazolate and magnesium borohydride. This is, however, limited only to lithium imidazolate; when sodium (or potassium; as further discussion will show) imidazolates are used in the reaction with magnesium borohydride, mixed metallic imidazolates form, and the crystallization of $MgIm_2$ does not occur during the thermal treatment.

Since the diffraction lines of an unidentified phase have been noticed in the sample 4D7 (Scheme 5; Figure 57g), obtained by the mechanochemical reaction of $Mg(BH_4)_2$ and KIm in the 1:6 ratio, sample 4D7 has been thermally treated in an autoclave at 155 °C, in order to improve the reaction of $Mg(BH_4)_2$ and KIm. Rietveld refinements for sample 4D7 at RT and 155 °C are given in Figure 60.
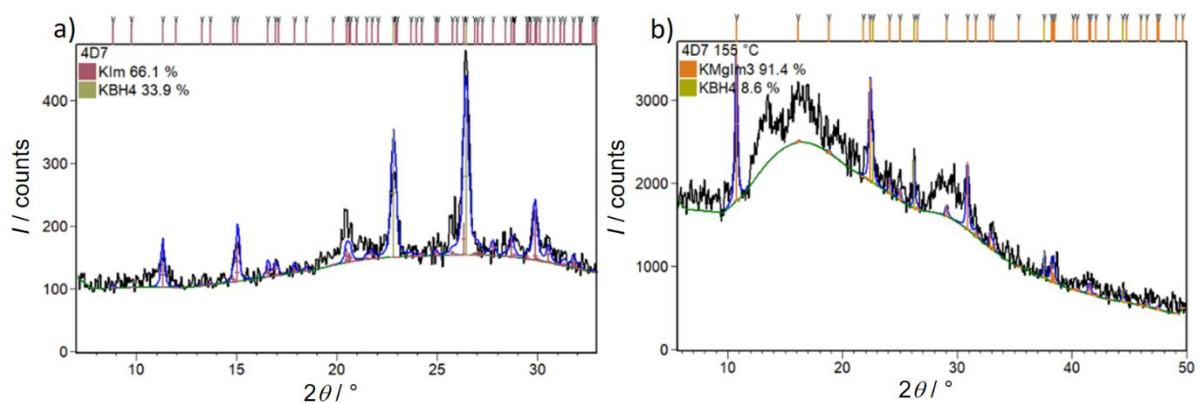
Figure 60. Rietveld refinement on sample 4D7 at RT **a)** as milled and **b)** thermally treated in an autoclave at 155 °C. Experimental diffraction data are shown in black, while calculated patterns are given in blue. Diffraction lines position of KIm are represented by purple vertical marks, $KMgIm_3$ by ocher, while the vertical marks in the case of KBH_4 are colored khaki.

Thermal treatment at higher temperature indeed induced crystallization of, at this point, an unknown phase; later discussion will show that diffraction lines correspond to the new compound $KMgIm_3$.

4.4. MECHANOCHEMICAL REACTIONS OF MONOMETALLIC ALKALINE EARTH IMIDAZOLATE Mg(Im)₂ WITH ALKALI METAL IMIDAZOLATES MIm (M = Na, K AND Li)

In order to prepare pure bimetallic imidazolates without borohydride and to gain further insight into its structural evolution and thermal stability, additional mechanochemical synthesis were conducted by neat grinding of $MgIm_2$ and MIm (M = Na, K and Li) in the 1:1 molar ratio (Scheme 6).
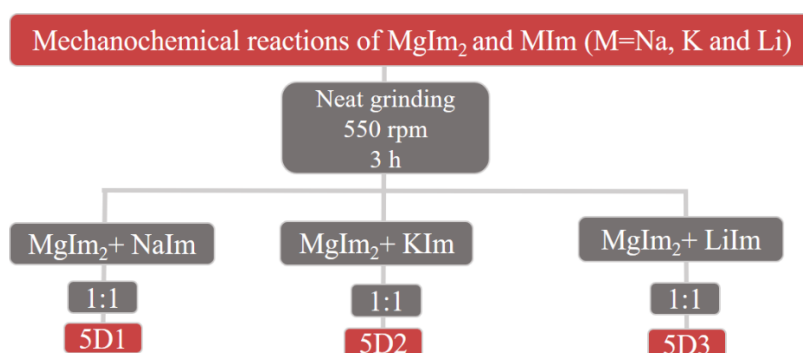
Scheme 6. Mechanochemical reactions of monometallic alkaline earth imidazolate and alkali metal imidazolates.

XRD patterns of sample 5D1 collected during the heating run in the temperature range from RT to 390 °C and during the cooling run back to RT are shown in Figure 61a, while Figure 61b shows phase analysis at RT, 159, 306, 341 and 391 °C.

Figure 61. a) XRD patterns of sample 5D1 collected during heating run in temperature range from RT to 390 °C and during cooling run back to RT. **b)** Phase composition of sample 5D1 at RT, 159, 306, 341 and 391 °C. Diffraction lines belonging to $NaMgIm_3$ phase are marked with circles and the diffraction lines belonging to $MgIm_2$ phase with squares.

As one can see from Figure 61, sample 5D1 is amorphous up to 149 °C when $NaMgIm_3$ starts to crystallize. It remains stable up to 310 °C. At 310 °C, the diffraction lines of $NaMgIm_3$ disappear and $MgIm_2$ starts to crystallize. Magnesium imidazolate was stable up to 366 °C. Interestingly, one can notice that $NaMgIm_3$ displays a wider range of thermal stability (118−340 °C) when borohydride is present in the system (chapter 4.3).

The crystal structure of $NaMgIm_3$ was determined using the diffraction data of sample 5D1 at 333 °C. The diffraction lines were indexed using the hexagonal system (space group $P6_322$). For structure determination, positions of one Na atom, one Mg atom, and one imidazolate group were varied using the corresponding antibump restraints. A Rietveld plot from the refinement of $NaMgIm_3$ is given in Figure 62, while the crystal structure is shown Figure 63. Crystal data for $NaMgIm_3$ and a summary of structure refinement data are listed in Table 23.
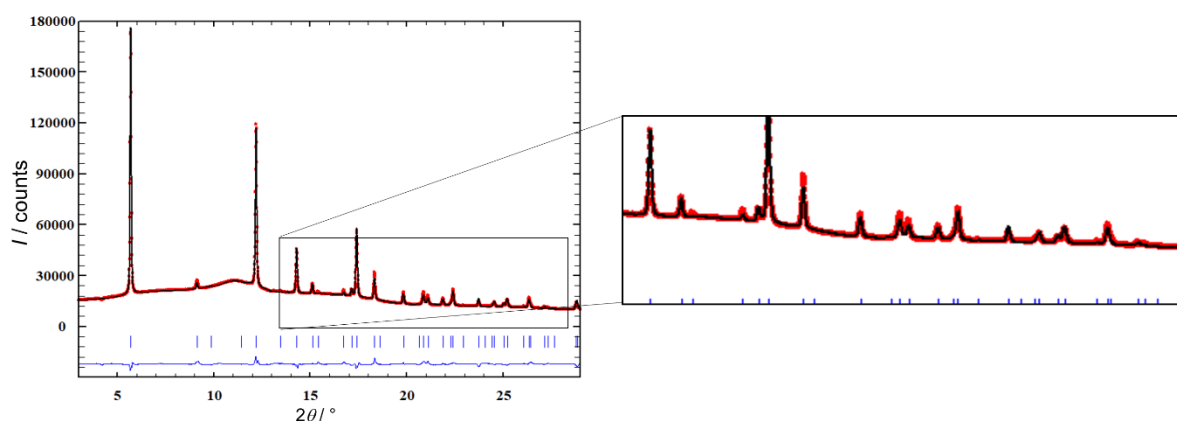
Figure 62. Rietveld refinement of $NaMgIm_3$. Experimental pattern is given as red dots, black curve shows calculated profile and the difference curve is given in blue. Vertical marks represent Bragg reflections of $NaMgIm_3$. Enlarged part of diffraction pattern is also shown in order to illustrate the quality of refinement.
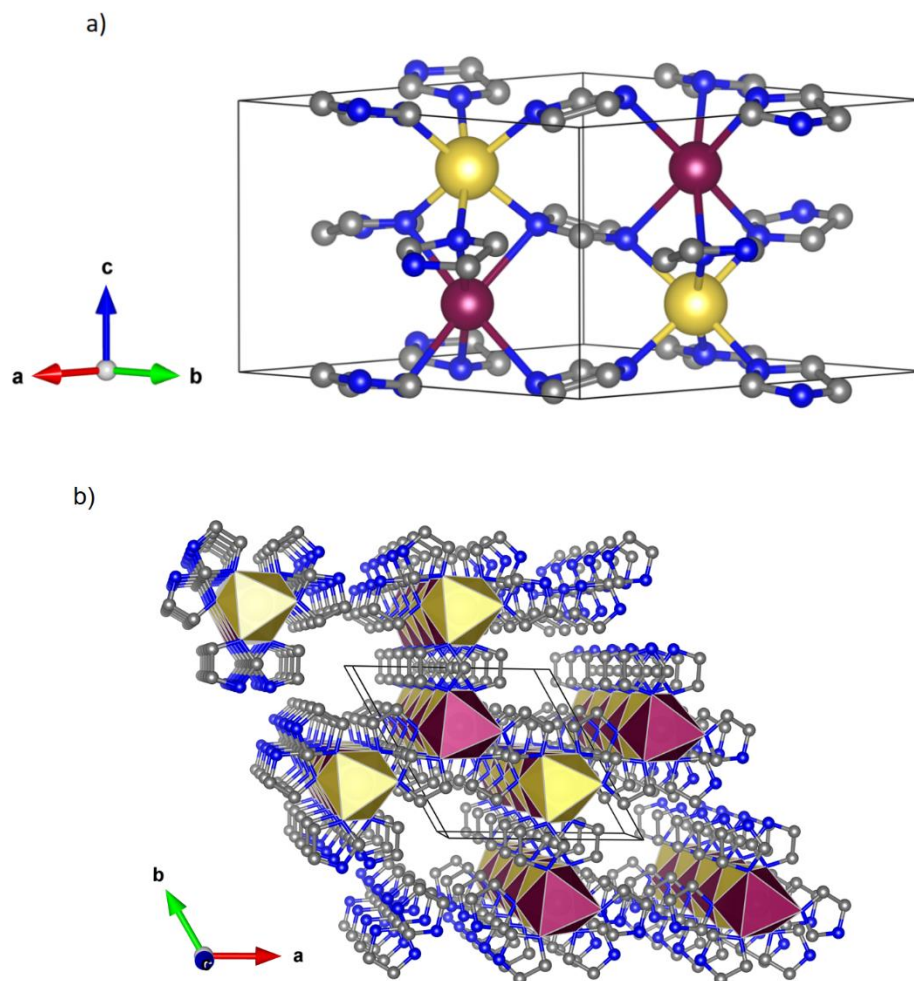
Figure 63. a) Crystal structure of NaMgIm₃; magnesium atoms are shown as purple balls, sodium is given in yellow, carbon is grey while nitrogen is shown in blue colour. **b)** Extended crystal packing of NaMgIm₃ showing channels along the *c*-direction.

Table 23. Crystal data and summary of structure refinement for NaMgIm₃

	NaMgIm₃
Profile function	Pseudo Voigt
R (profile)/ %	16.9
R (weighted profile)/ %	10.7
χ^2	$7.01 \cdot 10^3$
Space group	$P6_3 22$
a/ Å	9.5053(4)
c/ Å	6.57606(15)

Unlike monometallic imidazolates (NaIm and MgIm₂) that show tetrahedral coordination of metal atoms,[114] in NaMgIm₃ both Na and Mg cations exhibit a distorted octahedral coordination. The interatomic distances, d(M−N$_{im}$), are found to be longer in the case of mixed-metal imidazolates, as expected for a higher coordination number, compared to those of tetrahedrally coordinated metal cations in the case of NaIm and MgIm₂

$[d(Na_{tet}-N_{Im})_{NaIm} = 2.45(3)$ Å, and $d(Na_{oct}-N_{Im})_{NaMgIm3} = 2.5851(2)$ Å; $d(Mg_{tet}-N_{Im})_{MgIm2} = 2.04(1)$ Å, and $d(Mg_{oct}-N_{Im})_{NaMgIm3} = 2.3701(2)$ Å]. While the imidazolate ligands in MgIm$_2$ are connected only to two metallic centers (one Mg atom via each nitrogen atom) forming a porous structure, in NaMgIm$_3$, same as in NaIm, the imidazolate ligand is connected to four metal cations, where each N atom from the imidazolate anion is coordinated to two cations forming a more closely packed three-dimensional network. Along the *c*-direction, Na and Mg are connected *via* bridging N atoms from three imidazole rings forming the chain of face-shared metal octahedra. Those chains along the *c*-direction are mutually connected by bridging imidazolate anions, forming a zig-zag net in the *ab* plane. A crystal packing view also reveals channels running along the *c*-direction, located on the 6$_3$ screw axis. The channel is defined by a diameter of ~6.6 Å, and the empty volume calculated from the contact surface amounts to 28.5 Å^3 (assuming a spherical probe of $r = 1.4$ Å). The topology analysis of NaMgIm$_3$ has found that the underlying net is of the *stp* type. There are few MOFs with this topology type and they all have a common structure type belonging to iron phosphonate Fe$_2$(HPO$_3$)$_3$. It is not a structural prototype of NaMgIm$_3$, because the anion is different (phosphonate instead of imidazolate), and therefore, the space group is P6$_3$/m instead of P6$_3$22. One more difference between NaMgIm$_3$ and Fe phosphonate is that in the latter structure two octahedral nodes are occupied by atoms of the same type (Fe).

Because the mechanochemical reaction of MgIm$_2$ and NaIm yielded a novel bimetallic imidazolate compound, further attempts have been made to prepare novel mixed metal imidazolates containing K or Li, instead of Na.

Product obtained by mechanochemical reaction of MgIm$_2$ and KIm have been characterized by the *in situ* high-temperature diffraction measurements using the syncrotron radiation. XRD patterns of the sample 5D2 collected during the heating run in the temperature range from RT to 325 °C and during the cooling run back to RT are shown in Figure 64a, while Figure 64b shows phase analysis at RT, 348 °C and 368 °C during heating and at 269 °C during cooling run.
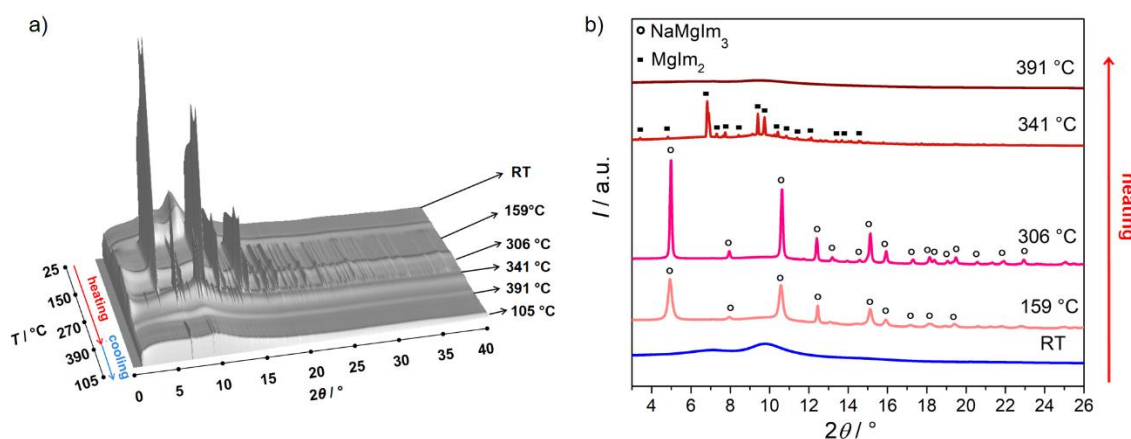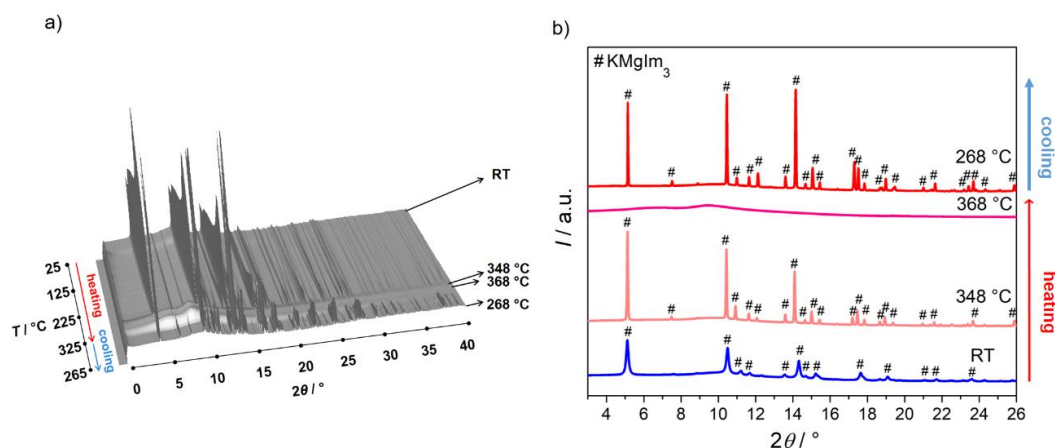
Figure 64. a) XRD patterns of sample 5D2 collected during heating run in temperature range from RT to 325 °C and during cooling run back to RT. **b)** Phase composition of sample 5D2 at RT, 348, 368 in heating and 268 °C in cooling. Diffraction lines belonging to KMgIm$_3$ phase are marked with ladders.

In the case of KIm, unlike that of NaIm, grinding without any thermal treatment proved to be sufficient for the formation of the mixed-metal imidazolate phase, KMgIm$_3$. This compound is stable in a wide temperature range, from RT to 353 °C, when it melts. The same compound recrystallizes below 298 °C during cooling.

The crystal structure of KMgIm$_3$ has been determined from powder X-ray diffraction data collected at 333 °C. For structure determination, positions of one K atom, one Mg atom, and one imidazolate group were varied using the corresponding antibump restraints. A Rietveld plot from the refinement of KMgIm$_3$ is given in Figure 65, while the crystal structure is shown Figure 66. Crystal data for KMgIm$_3$ and a summary of structure refinement data are listed in Table 24.
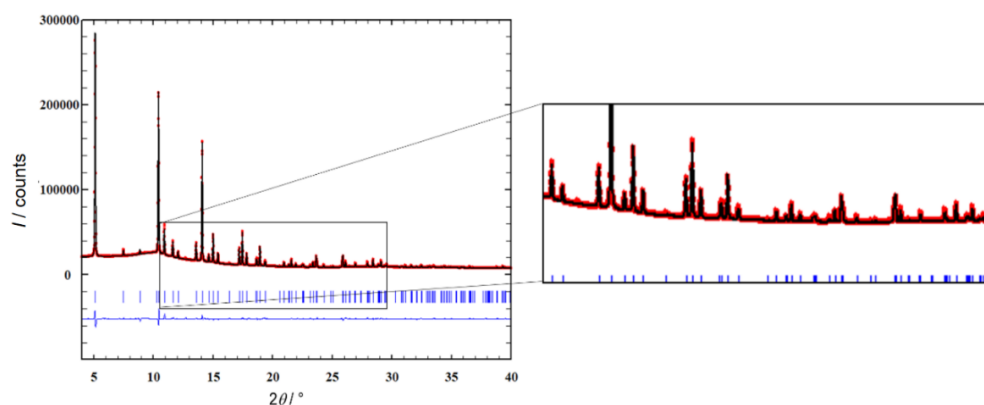
Figure 65. Rietveld refinement of KMgIm$_3$. Experimental pattern is given as red dots, black curve shows calculated profile and the difference curve is given in blue. Vertical marks represent Bragg reflections of KMgIm$_3$. Enlarged part of diffraction pattern is also shown in order to illustrate the quality of refinement.
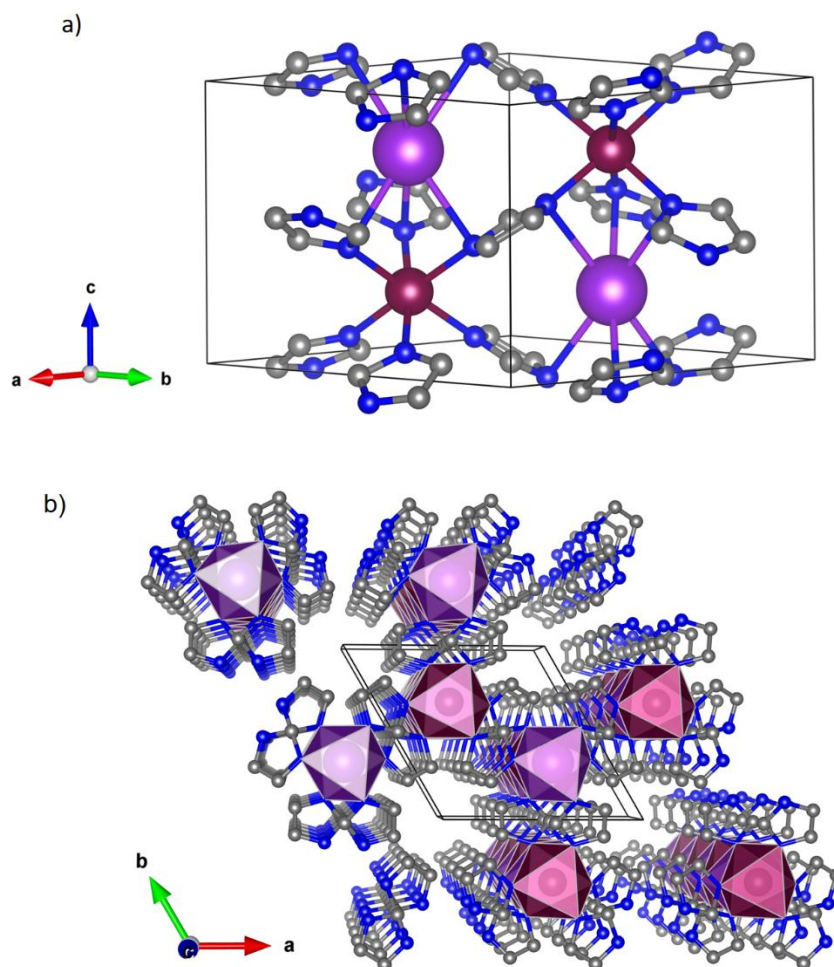
Figure 66. **a)** Crystal structure of KMgIm$_3$; magnesium atoms are shown as purple balls, potassium is given in violet, carbon is grey while nitrogen is shown in blue colour. **b)** Extended crystal packing of KMgIm$_3$ showing channels along *c*-direction.

Table 24. Crystal data and summary of structure refinement for KMgIm$_3$

	KMgIm$_3$
Profile function	Pseudo Voigt
R (profile)/ %	11.8
R (weighted profile)/ %	10.9
χ^2	$8.03 \cdot 10^4$
Space group	$P6_322$
a/ Å	9.22628(15)
c/ Å	7.50903(13)

It was found that the crystal structure of KMgIm$_3$ is similar to that of its sodium derivative. The main difference between crystal structures of NaMgIm$_3$ and KMgIm$_3$ is related to the orientation of the imidazolate rings. Although the imidazolate rings in the case of the sodium compound deviate slightly from an ideal planar configuration, the rings can be considered as

almost parallel to the *ab* plane, which is not the case for the potassium compound. Additionally, the two compounds show different degrees of polyhedral deformation around the alkali-metal cation; a pronounced distortion of octahedra around sodium can be observed [$\angle(N_{ax}-Na-N_{eq}) = 76.65°$], compared to the octahedra surrounding the potassium centre [$\angle(N_{ax}-K-N_{eq}) = 84.45°$].

According to bond valence sum (BVS) calculations, in NaMgIm₃, the valence sums for magnesium and sodium cations amount to 1.5 and 1, respectively. In the case of KMgIm₃, the valence sums for magnesium and potassium are 1.6 and 0.65, respectively. The calculated values are lower than expected because the tables of calculated R_{ij} values correspond to an isolated N^{3-} anion.

Sample 5D3, obtained by the mechanochemical reaction of MgIm₂ and LiIm have been characterized by the *in situ* high-temperature diffraction measurements using the synchrotron radiation. XRD patterns of sample 5D3 collected during heating run in temperature range from RT to 300 °C are shown in Figure 67a, while Figure 67b shows phase analysis at RT, 179 °C and 225 °C.
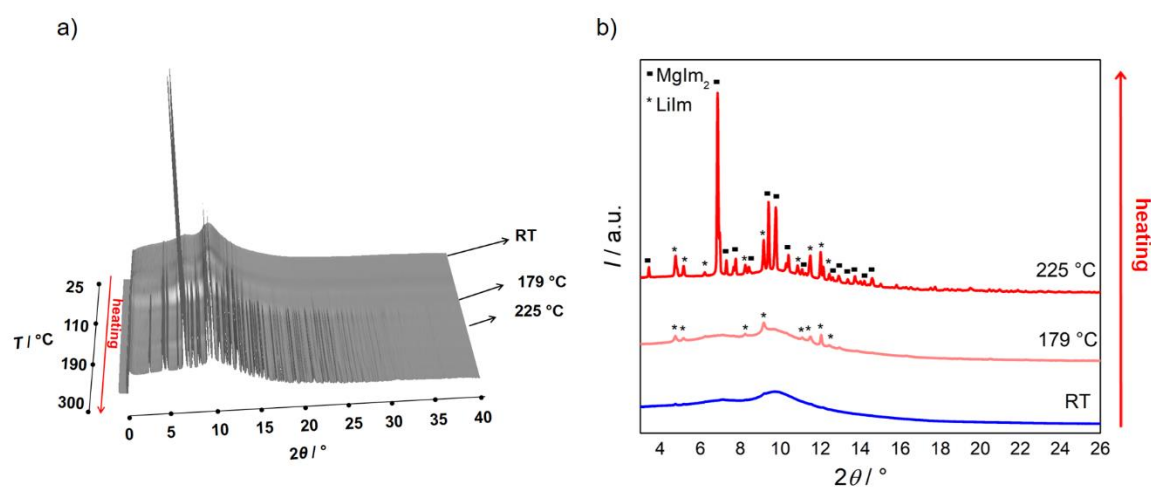
Figure 67. a) XRD patterns of sample 5D3 collected during heating run in temperature range from RT to 300 °C. **b)** Phase composition of sample 5D3 at RT, 179 °C and 225 °C. Squares are denoting the diffraction lines of MgIm₂ phase and asterisks are denoting the diffraction lines of the LiIm phase.

Diffraction lines of LiIm started to appear at 149 °C, and the second reactant, MgIm₂, started to crystallize at 185 °C. Both compounds remained stable up to 296 °C. No formation of a mixed-metal imidazolate was observed.

In conclusion, it appears that the formation of mixed metallic AMgIm₃ compounds, where A is Li, Na and K, is governed by the thermodynamic stability of the alkali metal imidazolates versus

the energy of formation of mixed metal imidazolate compounds; while lithium imidazolate does not react with magnesium imidazolate likely due to the limitation imposed by a small Li cation (A cations in $AMgIm_3$ have the coordination number 6), potassium imidazolate swiftly reacts with $MgIm_2$ and forms $KMgIm_3$.

4.5. MECHANOCHEMICAL REACTIONS OF MONOMETALLIC TRANSITIONAL BOROHYDRIDE Mn(BH₄)₂ WITH ALKALI METAL IMIDAZOLATES MIm (M = Na, K and Li)

After the reactions of alkali imidazolates and alkaline earth borohydrides resulted in the formation of a new group of bimetallic imidazolates, the research was further extended to the reactions of transitional monometallic borohydrides. Mechanochemical reactions, conducted by neat grindingof transitional monometallic borohydride, $Mn(BH_4)_2$, with alkali imidazolates MIm (M = Na, K, Li), in different ratios, have been investigated (Scheme 7).
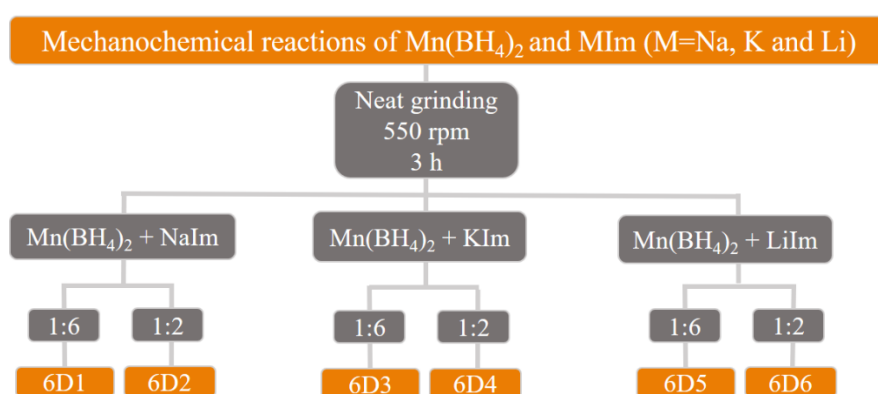
Scheme 7. Mechanochemical reactions of transitional monometallic borohydride and alkali metal imidazolates.

Rietveld refinements for samples 6D1–6D6, obtained by the dry mechanochemical reactions of $Mn(BH_4)_2$ and MIm (M = Na, K and Li) in different molar ratios, are given in Figure 68.
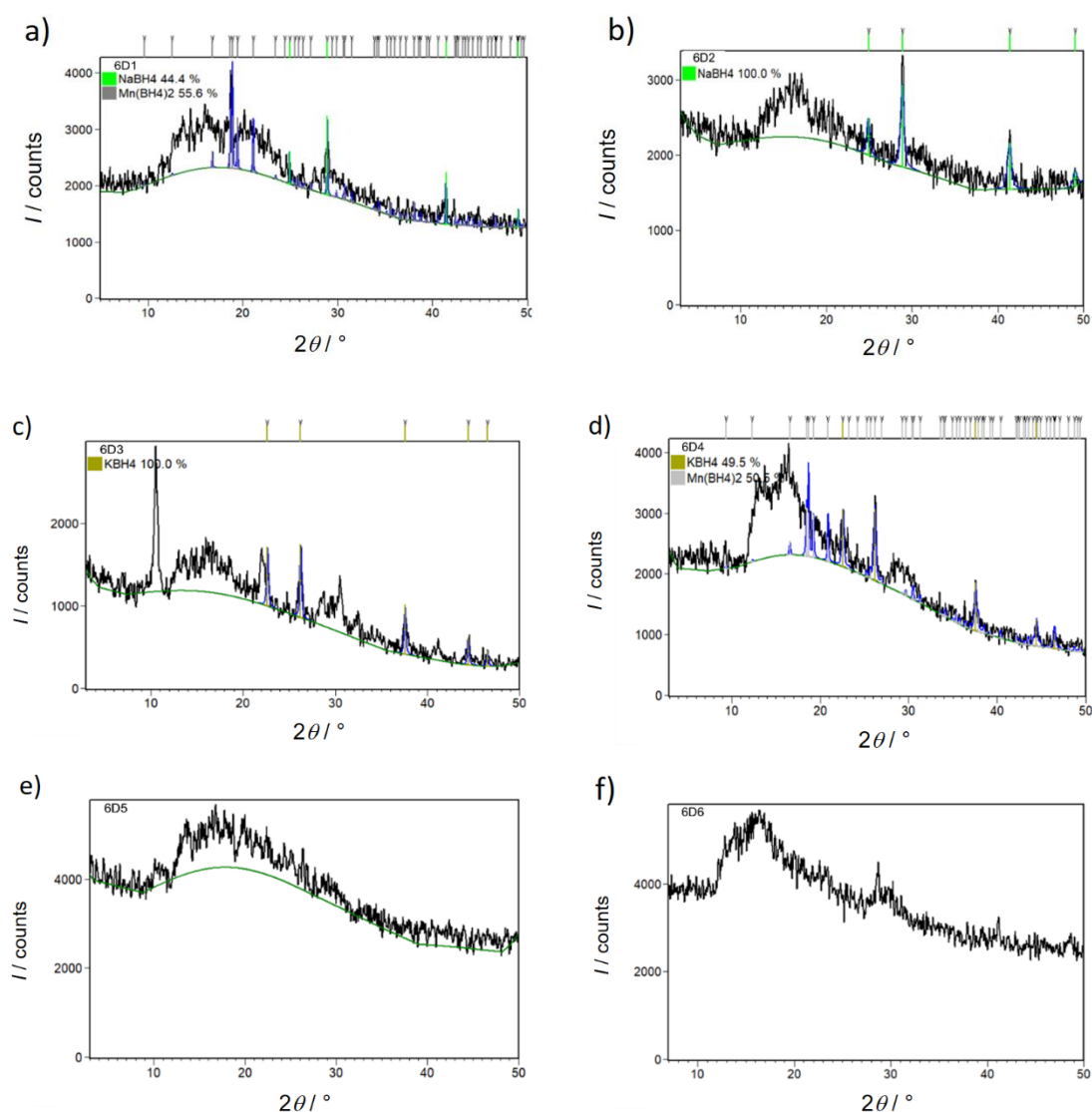
Figure 68. Rietveld refinement of samples 6D1–6D6 obtained by the neat grinding of $Mn(BH_4)_2$ and NaIm in different molar ratios: **a)** 1:6 and **b)** 1:2; $Mn(BH_4)_2$ and KIm in different molar ratios: **c)** 1:6 and **d)** 1:2; $Mn(BH_4)_2$ and LiIm in different molar ratios: **e)** 1:6 and **f)** 1:2. Experimental diffraction data are shown in black, while calculated patterns are given in blue. Diffraction lines position of $NaBH_4$ are represented by green vertical marks, $Mn(BH_4)_2$ by silver, while the vertical marks in the case of KBH_4 are colored khaki.

Quantitative composition of mechanochemical products (samples 6D1–6D6) are summarized in Table 25.

Table 25. Quantitative composition of crystalline products in samples 6D1–6D6

Sample	Reaction	Crystalline products composition as determined by the Rietveld refinement
6D1	MnBH$_4$)$_2$: NaIm = 1:6	amorphous phase, NaBH$_4$ (44.4 wt. %), Mn(BH$_4$)$_2$ (55.6 wt. %),
6D2	Mn(BH$_4$)$_2$:NaIm = 1:2	amorphous phase, NaBH$_4$ (100 wt. %),
6D3	Mn(BH$_4$)$_2$:KIm = 1:6	amorphous phase, KBH$_4$ (100 wt. %), unidentified phase(s)
6D4	Mn(BH$_4$)$_2$:KIm = 1:2	amorphous phase, KBH$_4$ (49.5 wt. %), Mn(BH$_4$)$_2$ (50.5 wt. %), unidentified phase(s)
6D5	Mn(BH$_4$)$_2$:LiIm = 1:6	amorphous product
6D6	Mn(BH$_4$)$_2$:LiIm = 1:2	amorphous product

The sample 6D1 formed in the mechanochemical reaction of Mn(BH$_4$)$_2$ and NaIm in 1:6 ratio contains unreacted borohydride Mn(BH$_4$)$_2$ and NaBH$_4$, that formed by the ionic exchange whereas the excess of NaIm exists in the amorphous phase. Quite similar, sample 6D2, obtained by the mechanochemical reaction of Mn(BH$_4$)$_2$ and NaIm in 1:2 ratio resulted in the formation of crystalline NaBH$_4$, formed during ionic exchange, and an amorphous part. Sample 6D3 showed the presence of KBH$_4$, that is formed by ionic exchange, but also contained unidentified diffraction lines. Similar was found for sample 6D4 but along with unidentified phase(s) and KBH$_4$, some unreacted Mn(BH$_4$)$_2$ remained in the sample. Reactions of Mn(BH$_4$)$_2$ and LiIm both in ratio 1:6 (6D5) and 1:2 (6D6), did not result in the formation of any crystalline phases, only amorphous halo was present.

Diffraction pattern of the sample 6D1 shows the presence of amorphous phase, thus the effect of thermal treatment on the sample 6D1 was additionally investigated by *ex-situ* heating at 220 °C and by the *in-situ* high temperature synchrotron radiation experiment. Rietveld refinement for sample 6D1 thermally treated in autoclave at 220 °C is shown in Figure AV SI, Table AV SI. Formation of a new unidentified phase, together with disappearance of the amorphous halo, during the thermal treatment in an autoclave was great motivation to conduct *in-situ* high temperature synchrotron radiation experiment. XRD patterns of the sample 6D1 collected during the heating run in the temperature range from RT to 295 °C and during the cooling run back to RT are shown in Figure 69a, while Figure 69b shows phase analysis at RT, 121 and 267 °C in heating and RT after cooling.
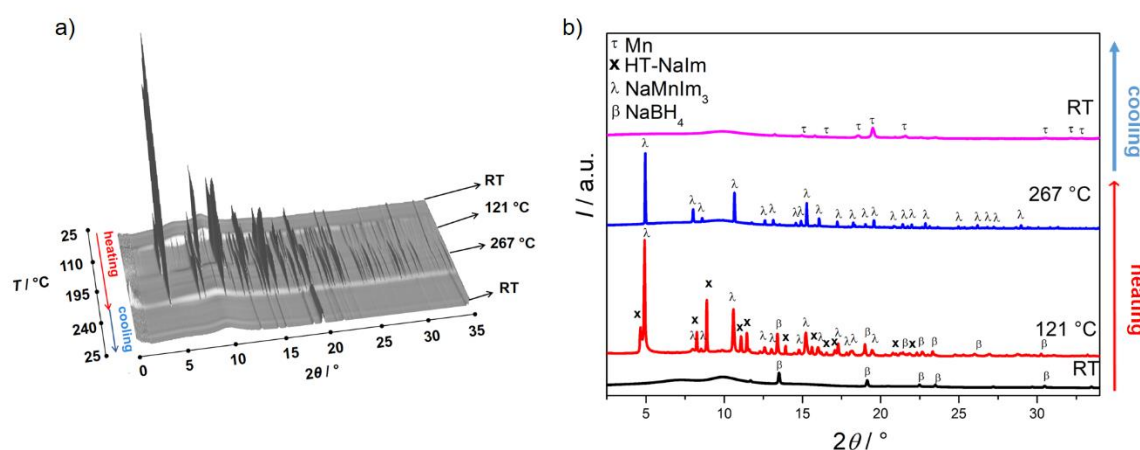
Figure 69. a) XRD patterns of sample 6D1 collected during heating run in temperature range from RT to 295 °C and during cooling run back to RT. **b)** Phase composition of sample 6D1 at RT, 121 and 267 °C in heatingand RT after cooling. Diffraction lines of HT-NaIm are marked with times sign, NaMnIm₃ phase with λ, while the NaBH₄ is denoted with β.

As previously known from the laboratory data, sample 6D1 at RT contains unreacted $Mn(BH_4)_2$, $NaBH_4$ formed by ionic exchange, and a significant amount of an amorphous phase. At 87 °C, an unidentified phase started to crystallize; further discussion will reveal that this phase is a new compound $NaMnIm_3$. At almost the same temperature, high temperature polymorph of NaIm also crystallizes and it is stable up to 180 °C. With further increase of temperature, only $NaMnIm_3$ is present in the sample and remains stable up to 280 °C. Above 280 °C, $NaMnIm_3$ melts and small amount of metallic Mn crystallizes.

The crystal structure of $NaMnIm_3$ was determined using the diffraction data of the sample 6D1 collected at 200 °C. The fact that the sample is phase-pure at 200 C, since HT-NaIm is stable up to T= 180 °C, to some extent facilitated the procedure of structure solution. The diffraction lines were indexed in the hexagonal system (space group $P6_322$). For structure determination, positions of one Na atom, one Mn atom, and one imidazolate group were varied using the corresponding antibump restraints. The Rietveld refinement plot for $NaMnIm_3$ is given in Figure 70, while the crystal structure is shown Figure 71. Crystal data for $NaMnIm_3$ and a summary of structure refinement data are listed in Table 26.

Figure 70. Rietveld refinement of NaMnIm₃. Experimental pattern is given as red dots, black curve shows calculated profile and the difference curve is given in blue. Vertical marks represent Bragg reflections of NaMnIm₃. Enlarged part of diffraction pattern is also shown in order ro illustrate the quality of refinement.
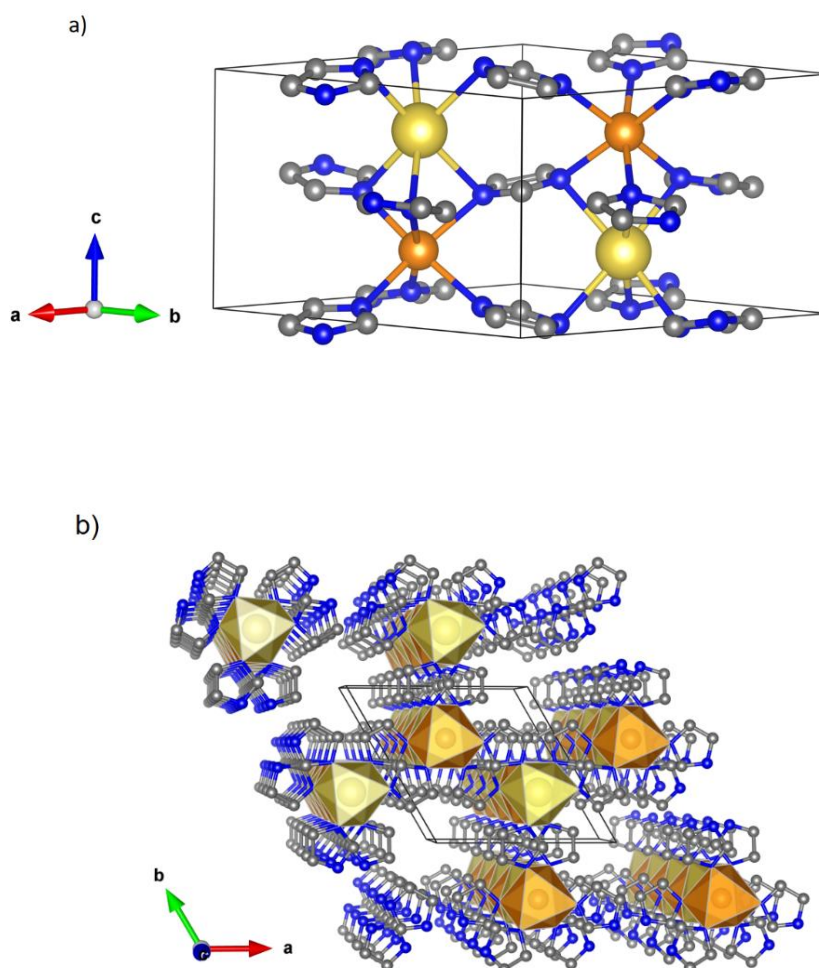
Figure 71. **a)** Crystal structure of NaMnIm₃; manganese atoms are shown as orange balls, sodium is given in yellow, carbon is grey while nitrogen is shown in blue. **b)** Extended crystal packing of NaMnIm₃ showing channels along *c*-direction.

Table 26. Crystal data and summary of structure refinement for NaMnIm$_3$

	NaMgIm$_3$
Profile function	Pseudo Voigt
R (profile)/ %	15.3
R (weighted profile)/ %	12.0
χ^2	$1.16 \cdot 10^3$
Space group	$P6_322$
a/ Å	9.64595(13)
c/ Å	6.57337(9)

NaMnIm$_3$ is isostructural with its magnesium analogue, NaMgIm$_3$. That was, in fact, quite expected if one considers the structural similarities between Mn- and Mg-borohydride compounds. In sodium imidazolate, Na atom exhibits the tetrahedral coordination[114] however in the case of NaMnIm$_3$ both Na and Mn cations exhibit a distorted octahedral coordination. It is interesting to note that the coordination of Mn in Mn(BH$_4$)$_2$ is not octahedral but tetrahedral. The interatomic distances, d(M−N$_{Im}$), are found to be longer in the case of mixed-metal imidazolate NaMnIm$_3$, as expected for a higher coordination number, compared to the tetrahedrally coordinated metal cation in the case of NaIm [d(Na$_{tet}$−N$_{Im}$)$_{NaIm}$ = 2.45(3) Å, and d(Na$_{oct}$−N$_{Im}$)$_{NaMnIm3}$ = 2.66859(3) Å]. The imidazolate ligand is connected to four metal cations, two Na and two Mn, where each N atom from the imidazolate anion is coordinated to two cations forming a complex three-dimensional network. Along the c-direction, Na and Mn are connected *via* bridging N atoms from three imidazole rings forming the chain of face-shared metal octahedra. Those chains running along the c-direction are mutually connected in an imidazolate bridged fashion, forming a *zig-zag* net in the *ab* plane. A crystal packing view also reveals channels running along the c-direction, located on the 6-fold screw axis. The channel is defined by a diameter d of ~6.6 Å, and the empty volume calculated from the contact surface amounts to 26 Å^3 (assuming a spherical probe of r = 1.4 Å). Similar porosity in the structure has been noted in the case of Mn(BH$_4$)$_2$,[105–107] having isolated voids of an estimated volume of 21 Å^3.

Bond between manganese atom and nitrogen atom from imidazolate ring in NaMnIm$_3$ [d(Mn−N$_{Im}$)$_{NaMnIm3}$ = 2.37226(2) Å] is a bit longer than bond between magnesium atom and nitrogen atom from imidazolate ring in NaMgIm$_3$ [d(Mg−N$_{Im}$)$_{NaMgIm3}$ = 2.3701(2) Å]. As it is case with borohydrides, larger Mn^{2+} in γ-Mn(BH$_4$)$_2$ forms a larger unit cell compared to γ-Mg(BH$_4$)$_2$ ($V_{NaMnIm3}$ = 529.674(18) Å^3, $V_{NaMgIm3}$ = 514.55(5) Å^3).

Diffraction pattern of sample 6D3, obtained by the mechanochemical reaction of $Mn(BH_4)_2$ and KIm in 1:6 ratio, showed presence of the amorphous phase, and also formation of new, unidentified phase, thus the effect of thermal treatment on sample 6D3 was additionally investigated by *ex-situ* heating at 175 °C and by the *in-situ* high temperature synchrotron radiation experiment. Rietveld refinement for sample 6D3 thermally treated in autoclave at 175 °C is shown in Figure AVI SI, Table AVI SI. In order to elucidate the structure of the novel phase obtained by milling, the sample 6D3 was additionally characterized by *in-situ* high temperature synchrotron radiation experiment. XRD patterns of sample 6D3 collected during the heating run in the temperature range from RT to 290 °C and during the cooling run back to RT are shown in Figure 72a, while Figure 72b shows phase analysis at RT and 173 °C in heating and RT after cooling.

Figure 72. a) XRD patterns of sample 6D3 collected during heating run in temperature range from RT to 290 °C and during cooling run back to RT. **b)** Phase composition of sample 6D3 at RT and 173 °C in heating and RT after cooling. Diffraction lines of KIm are marked with ψ, KBH_4 with σ, while the $KMnIm_3$ is denoted with φ.

At room temperature crystalline KBH_4 formed by ionic exchange during milling is present together with unreacted KIm and a new, unidentified phase which has crystallized already during milling. Further discussion will reveal that this phase is a new compound, $KMnIm_3$. KIm decomposes at 152 °C while $KMnIm_3$ remains stable from RT up to 289 °C. Above that temperature, it melts and only KBH_4 remains crystalline in the sample.

The crystal structure of $KMnIm_3$ was determined using the diffraction data of sample 6D3 collected at 173 °C. The diffraction peaks were indexed in the hexagonal system (space group $P6_322$). For structure determination, positions of one K atom, one Mn atom, and one imidazolate group were varied using the corresponding antibump restraints. The Rietveld plot

is given in Figure 73, while the crystal structure of KMnIm$_3$ is shown Figure 74. Crystal data
for KMnIm$_3$ and a summary of structure refinement data are listed in Table 27.
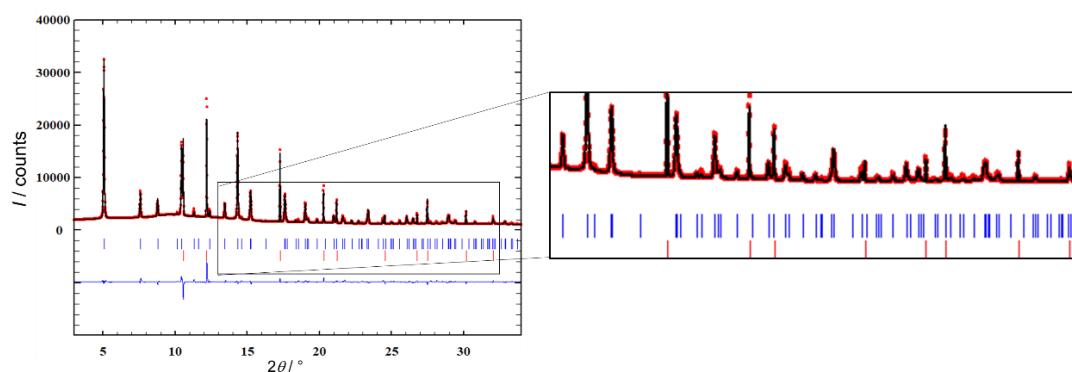
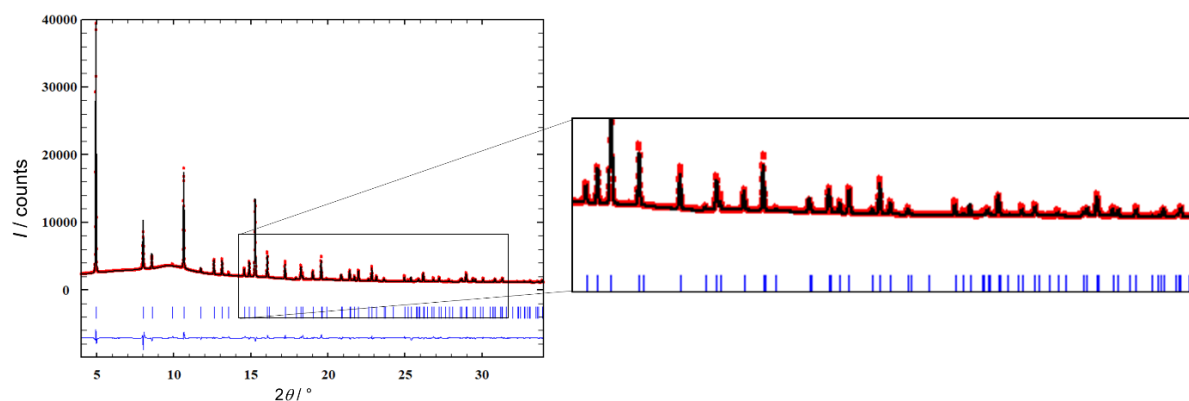
Figure 73. Rietveld refinement of sample 6D3 used for the structural determination
of KMnIm$_3$. Experimental pattern is given as red dots, black curve shows calculated
profile and the difference curve is given in blue. Blue vertical marks represent Bragg
reflections of KMnIm$_3$ and red represents KBH$_4$. Enlarged part of diffraction pattern
is also shown in order ro illustrate the quality of refinement.
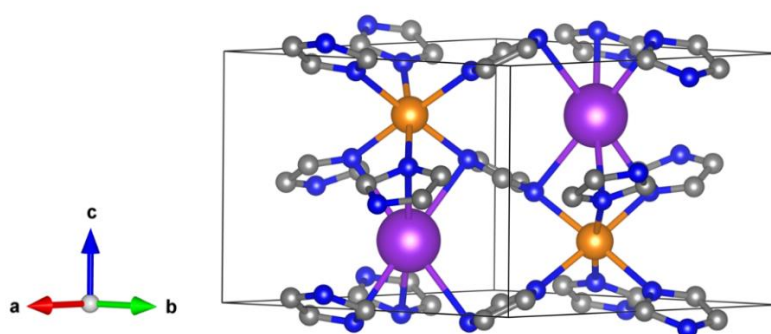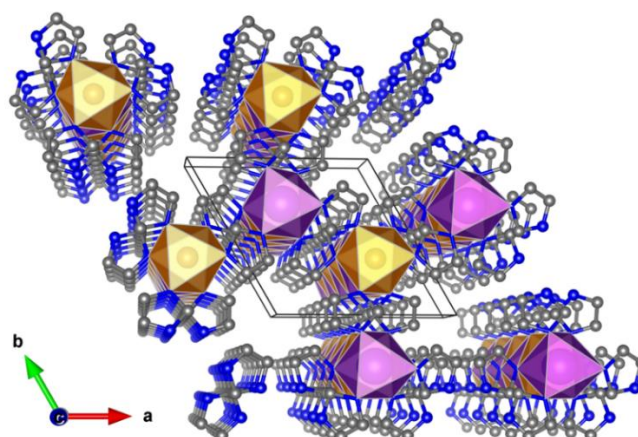
Figure 74. a) Crystal structure of KMnIm$_3$; manganese atoms are shown as
orange balls, potassium is given in purple, carbon is grey while nitrogen is
shown in blue colour. **b)** Extended crystal packing of KMnIm$_3$ showing
channels along *c*-direction.

Table 27. Crystal data and summary of structure refinement for KMnIm$_3$

	KMnIm$_3$
Profile function	Pseudo Voigt
R (profile)/ %	17.3
R (weighted profile)/ %	14.0
χ^2	5.16·10^3
Space group	$P6_3$22
a/ Å	9.42180(6)
c/ Å	7.3322(3)

Same as for magnesium compounds, crystal structure of KMnIm$_3$ is similar to that of its sodium derivative, however, a difference can be noted regarding the orientation of the bridging imidazolate rings, those that mutually connect two chains running along *c*-direction. In the case of sodium compound the ring is almost parallel to the *ab* plane, while the imidazolate rings in the case of potassium compound are tilted in respect to *ab* plane. Additionally, polyhedra around the potassium atom is more regular, compared to the polyhedra in the case of sodium compound. Both NaMnIm$_3$ and KMnIm$_3$ structures are validated by BVS calculations.

Main difference between the magnesium group of compounds and the manganese group is regarding the structure solution process. While AMgIm$_3$ have been solved by parallel tempering procedure, using billion trials per run, for AMnIm$_3$ a different strategy in global optimization process was used, as explained in Černý,[125] small number of runs and trials, but by using the least squares refinement procedure after every run. In the case of AMnIm$_3$ the former strategy resulted in the false minimum structures, with doubled imidazolate ring. Both in AMgIm$_3$ and AMnIm$_3$, imidazolate ring has been rigidified and the corresponding antibump restraints have been used for each pair of atoms.

Diffraction patterns of the sample 6D5, obtained by the mechanochemical reaction of Mn(BH$_4$)$_2$ and LiIm in 1:6 ratio, showed only an amorphous halo, so in order to gain an insight into the temperature-induced structural changes it was additionally heat-treated *ex-situ* in autoclave at 175 °C. Thermal treatment induced the crystallization of Li$_2$ImBH$_4$ as well as a new, unidentified phase as shown in Figure AVII SI, Table AVII SI. Sample 6D5 was further investigated by thermally induced reaction during *in-situ* high temperature synchrotron radiation experiment.

XRD patterns of sample 6D5 collected during the heating run in the temperature range from RT to 305 °C and during the cooling run back to RT are shown in Figure 75a, while Figure 75b shows phase analysis at RT and 197 °C in heating and RT after cooling.
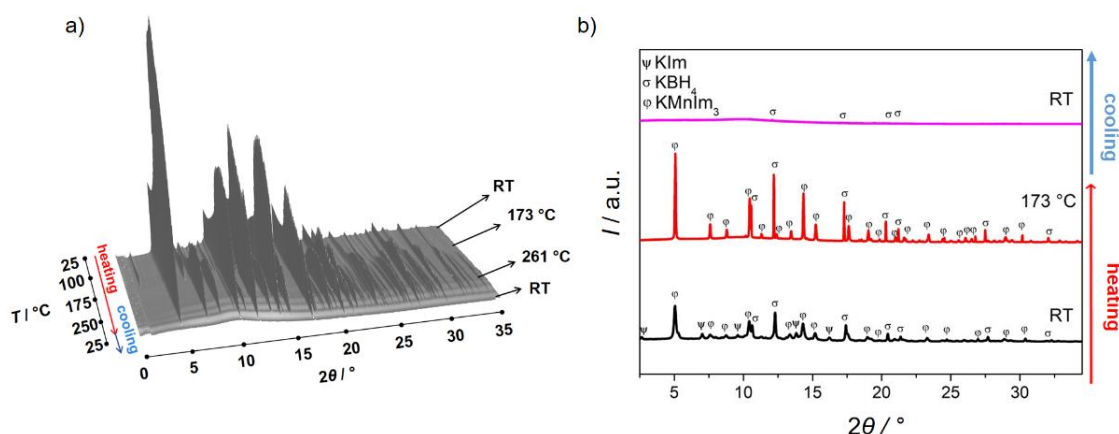
a)

b)
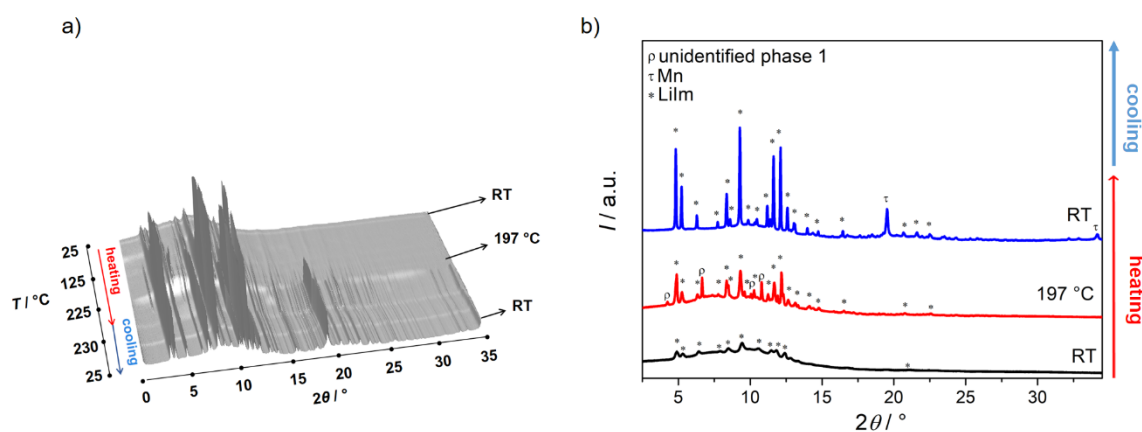
Figure 75. a) XRD patterns of sample 6D5 collected during heating run in temperature range from RT to 305 °C and during cooling run back to RT. **b)** Phase composition of sample 6D5 at RT and 197 °C in heating and RT after cooling. Diffraction lines of LiIm are marked with asterisks, first unidentified phase with ρ, while Mn is denoted with τ.

At room temperature, only LiIm is crystalline, while the rest of the sample is amorphous. During heating, the rate of the amorphous part decreases and around 145 °C a few unidentified diffraction lines appear. At 222 °C this phase disappears simultaneously with crystallization of metallic Mn, that remains stable in the sample in the cooling to RT. At this point, unfortunately, the structure of unknown phase remains undetermined but based on the recation of $Mg(BH_4)_2$ with LiIm, one might expect that this phase, in fact, is manganese imidazolate.

In summary, the reactivity of $Mn(BH_4)_2$ towards the alkali imidazolates seems to be quite similar to the $Mg(BH_4)_2$; both NaIm and KIm easily form $AMnIm_3$, while the reaction with LiIm after thermal treatment in the autoclave results in the formation of Li_2ImBH_4.

§ 5. CONCLUSIONS

In the scope of this work the reactivity between borohydride and imidazolate compounds has been studied in the comprehensive and systematic manner; the mechanochemical reactions between various monometallic and bimetallic borohydrides with alkali and alkaline earth metal imidazolates have been investigated. Interestingly, beside lithium, it seems that none of those metal centers are able to form hybrid compounds that would incorporate both borohydride and imidazolate anions but nevertheless in the majority of cases, milling induced mechanochemical reactions that resulted in the formation of novel mixed-metal imidazolates.

While the preparation of Li_2ImBH_4, the one and only known compound that crystallizes as a hydride-organic framework, until now involved either solvent-assisted mechanochemical reactions or thermal treatment at 100 °C, this work shows that lithium borohydride imidazolate can form even by the neat-grinding reaction of LiIm and $LiBH_4$. After the reaction, the appearance of some amount of amorphous phase cannot be avoided but nevertheless it has been clearly demonstrated that Li_2ImBH_4 can be formed at RT, as an only crystalline phase in the sample. The compound can also be obtained by the reactions involving LiIm and $Mg(BH_4)_2$ or $Mn(BH_4)_2$ however in those cases a subsequent thermal treatment is necessary in order to induce the crystallization of Li_2ImBH_4 since the energy of ball-milling seems to result only in the partial cation exchange i.e. the formation of $LiBH_4$.

Unlike in the case of lithium, when NaIm was used as a reactant with $NaBH_4$, no hybrid compounds were formed but nevertheless, interesting behavior has been noted; the sample obtained after the mechanochemical reaction, besides unreacted reactants, showed the presence of second polymorph of NaIm. As it turned out, this novel polymorph is, in fact, the high temperature polymorph of NaIm that crystallized as a racemic twin. The high temperature structure contains two different chains along the *c*-direction with 3_1 screw axis that are mutually interconnected and form a quite complex 3D framework. It is interesting to notice that HT polymorph of NaIm also appears as a product of mechanochemical reactions of NaIm and $Mg(BH_4)_2$ or $Mn(BH_4)_2$ but only after the heat treatment, while in the case of reaction with $NaBH_4$ the HT-NaIm phase crystallizes at RT, without any additional heat treatment.

Particularly interesting behavior was noticed in the case of the mechanochemical reactions of NaIm and $Mg(BH_4)_2$. Again the mechanochemical milling of NaIm with $Mg(BH_4)_2$, as well as subsequent thermal treatment, have not yielded hybrid compounds, however, a formation of

novel mixed-metal imidazolates with the formula $NaMgIm_3$ has been observed. Unlike monometallic imidazolates ($NaIm$ and $MgIm_2$) which show tetrahedral coordination of metals, in $NaMgIm_3$ both Na and Mg cation exhibit a distorted octahedral coordination. The structure is characterized by channels of diameter $d \sim 6.6$ Å running along the c-direction, located on the 6_3 screw axis. It has been shown that the same compound can be prepared by the direct reaction of $MgIm_2$ and $NaIm$ but, interestingly, $NaMgIm_3$ displays a wider range of thermal stability when borohydride is present in the system. Similarly, the reaction of $MgIm_2$ with both KIm or $LiIm$ have been investigated and it appears that the formation of $AMgIm_3$ (A=Na, K and Li) compounds is governed by the thermodynamic stability of the alkali metal imidazolates *vs.* the energy of formation of mixed metal imidazolate compounds; while lithium imidazolate does not react with magnesium imidazolate likely due to the limitation imposed by a small Li cation (A cations in $AMgIm_3$ have the coordination number 6), while potassium imidazolate swiftly reacts with $MgIm_2$ and forms $KMgIm_3$. The double cation imidazolates of magnesium and sodium or potassium are the first members of a new family of imidazolate frameworks with *stp* topology.

New mixed-metal imidazolates with the formula $AMnIm_3$ (A=Na and K), isostructural to their magnesium analogues, have been observed as the product of $Mn(BH_4)_2$ with alkali imidazolates. The main difference between the magnesium group of compounds and manganese group is regarding the structure solution process. For $AMgIm_3$ (A=Na and K) parallel tempering procedure with billion trials per run was good choice, but for $AMnIm_3$ (A=Na and K) this strategy resulted in the false minimum structures, with doubled imidazolate rings, so for $AMnIm_3$ (A=Na and K) a different strategy in global optimization process was used: small number of runs and trials, but by using the least squares refinement procedure after every run.

Additionally, in the course of the conducted research, it has been found that it is possible to prepare magnesium imidazolate by mechanochemical reaction; until now it has been considered that crystalline $MgIm_2$ can only be prepared by the reaction in liquid ammonia from $NaNH_2$, $Mg(NO_3)_2$ and ImH while this work shows that $MgIm_2$ can also be prepared by the partial exchange reaction during mechanochemical milling of $LiIm$ and $Mg(BH_4)_2$ followed by the additional thermal treatment at 240 °C. Prepared $MgIm_2$ remains stable after cooling to RT. The proposed pathway for the preparation of $MgIm_2$ provides a great alternative compared to the

liquid ammonia reaction where special attention has to be paid in order to avoid the violent redox reaction of NH_2^- and NO_3^-.

Last, but not the least, a comment about the reactivity of bimetallic borohydrides with metal imidazolates is in order. Products obtained after the mechanochemical reactions of $NaZn(BH_4)_3$ with NaIm, in the majority of cases contain only amorphous products, unreacted reactants or products of decomposition of the precursors. Additional thermal treatment often resulted in the crystallization of zeolitic imidazolate frameworks, in particular IMIDZB01, indicating that the reaction of bimetallic borohydrides with metal imidazolates does not result in the formation of a hybrid compound containing both borohydride and imidazolate anions. However, based on the results of the solid-state NMR, it seems that in the case of the liquid-assisted reaction of $NaZn(BH_4)_3$ and NaIm in DMSO, a hybrid compound in fact might have crystallized. Since in the spin-diffusion spectrum the off-diagonal cross peak of protons resonating at 7 ppm, belonging to imidazole with protons resonating close to 0 ppm, that belong to the borohydride group have been noted, it is suggested that the corresponding H atoms are, in fact, close in space i.e. that they are present in the same crystalline phase. Further attempts to determine the structure will be undertaken.

§ 6. ABBREVIATIONS

ACN-acetonitrile

BVS-bond valence sum

CF-chloroform

DCM-dichloromethane

DMSO-dimethylsulfoxide

DOE-US Department for Energy

DoF-degrees of freedom

ESRF-European Synchrotron Radiation Facility

FKKT-Faculty of Chemistry and Chemical Technology, Ljubljana, Slovenia

HINA-isonicotinic acid

HOF-metal-hydride-organic framework

HT-high temperature

ILAG-ion and liquid assisted grinding

LAG-liquid assisted grinding

MAS-magic angle spinning

MOF-metal-organic framework

NG-neat grinding

NU-Northwestern University

PM-pattern modelling

PSI-Paul Scherrer Institute

RT-room temperature

SLS-Swiss Light Synchrotron

SNBL-Swiss-Norwegian Beamline

SR-PXRD-synchrotron radiation X-ray powder diffraction

SSNMR-solid-state nuclear magnetic resonance

THF-tetrahydrofuran

TMB-trimethoxybenzene

XRPD-X-ray powder diffraction

ZIF-zeolitic imidazolate framework

§ 7. REFERENCES

1. A. Züttel, in A. Züttel, A. Borgschulte and L. Schlapbach (ed.), *Hydrogen as a Future Energy Carrier*, Vol. 1, Wiley-VCH Verlag GmbH&Co. KGaA, Weinheim, 2008, page 1–6.

2. I. Dovgaliuk, Synthesis, structure and properties of Al-based borohydrides for hydrogen storage, Ph.D. Dissertation, Univerité catholique de Louvain, Louvain-la-Neuve, Belgium, 2017.

3. R. Mohtadi, and S.-I. Orimo, *Nat. Rev. Mater.* **2** (2016) 16091.

4. https://www.energy.gov/eere/fuelcells/hydrogen-storage (accessed 15 March 2019).

5. L.E. Klebanoff, and J.O. Keller, *Int. J. Hydrogen Energy* **38** (2013) 4533–4576.

6. E. Callini, Z.Ö.K. Atakli, B.C. Hauback, S.-I. Orimo, C. Jensen, M. Dornheim, D. Grant, Y.W. Cho, P. Chen, B. Hjörvarsson, P.E. de Jongh, C. Weidenthaler, M. Baricco, M. Paskevicius, T.R. Jensen, M.E. Bowden, T.S. Autrey, and A. Züttel, *Appl Phys A-Matter* **122** (2016) 353.

7. Y. Filinchuk, B. Richter, T.R. Jensen, V. Dmitriev, D. Chernyshov, and H. Hagemann, *Angew. Chem. Int. Ed.* **50** (2011) 11162–11166.

8. B.D. James, and M.G.H. Wallbridge, *Prog. Inorg.Chem.* **11** (1970) 99–231.

9. T.J. Marks, and J.R. Kolb, *Chem. Rev.* **77** (1977) 263–293.

10. W. Grochala, and P.P. Edwards, *Chem. Rev.* 104 (2004) 1283–1315.

11. Y. Filinchuk, D. Chernyshov, and V. Dmitriev, in U.B. Demirci and P. Miele (Ed.), *Boron hydrides, high potential hydrogen storage materials*, Nova Publishers, New York, 2010.

12. D.B. Ravnsbæk, Y. Filinchuk, R. Černý, and T.R. Jensen, *Z. Kristallogr.* **225** (2010) 557–569.

13. D. Ravnsbæk, Y. Filinchuk, Y. Cerenius, H.J. Jakobsen, F. Besenbacher, J. Skibsted, and T.R. Jensen, A*ngew. Chem. Int. Ed.* **48** (2009) 6659–6663.

14. U. Eberle, M. Felderhoff, and F. Schüth, *Angew. Chem. Int. Ed.* **48** (2009) 6608–6630.

15. M.P. Suh, H.J. Park, T.K. Prasad, and D.-W. Lim, *Chem. Rev.* **112** (2012) 782–835.

16. K.M. Thomas, *Catal. Today* **120** (2007) 389–398.

17. O.K. Farha, A.O. Yazaydin, I. Eryazici, C.D. Malliakas, B.G. Hauser, M.G. Kanatzidis, S.T. Nguyen, R.Q. Snurr, and J.T. Hupp, *Nat. Chem.* **2** (2010) 944.

18. H. Furukawa, N. Ko, Y.B. Go, N. Aratani, S.B. Choi, E. Choi, A.O. Yazaydin, R.Q. Snurr, M. O'Keeffe, J. Kim, and O.M. Yaghi, *Science* **329** (2010) 424.

19. S.S: Kaye, A. Dailly, O.M. Yaghi, and J.R. Long, *J. Am. Chem. Soc.* **129** (2007) 14176.

20. Project „Metal-Hydride Organic Frameworks (HOF)–new solids for gas adsorption and separation", Geneva, 2015.

21. H.H. Giese, T. Habereder, J. Knizek, H. Nöth, and M. Warchhold, *Eur. J. Inorg. Chem.* **5** (2001) 1195–1205.

22. R. Černý, unpublished results

23. K.S. Park, Z. Ni, A.P. Côté, J.Y. Choi, R. Huang, F.J. Uribe-Romo, H.K. Chae, M. O'Keeffe, and Omar M. Yaghi, *Proc. Natl. Acad. Sci. U.S.A.* **103** (2006) 10186–10191.

24. L. Takacs, *J. Therm. Anal. Calorim.* **90** (2007) 81–84.

25. J. Huot, D.B. Ravnsbæk, J. Zhang, F. Cuevas, M. Latroche, and T.R. Jensen, *Prog Mater Sci* **58** (2013) 30–75.

26. S.L. James, C.J. Adams,C. Bolm, D. Braga, P. Collier, T. Friščić, F. Grepioni, K.D.M. Harris, G. Hyett, W. Jones, A. Krebs, J. Mack, L. Maini, A.G. Orpen, I.P. Parkin, W.C. Shearouse, J.W. Steedk and D.C. Waddelli, *Chem. Soc. Rev.* **41** (2012) 413–447.

27. A. D. McNaught and A. Wilkinson, *IUPAC Compendium of Chemical Terminology*, Blackwell Scientific Publications, Oxford, 1997.

28. V.V. Boldyrev, *Russ. Chem. Rev.* **75** (2006) 177–189.

29. T. Friščić, I. Halasz, V. Štrukil, M. Eckert-Maksić, and R.E. Dinnebierd, *Croat. Chem. Acta* **85** (2012) 367–378.

30. https://ninithi.wordpress.com/topdown_methods/ (accessed 18 March 2019).

31. https://www.chemistryworld.com/features/introducing-mechanochemistry/3009223.article (accessed 18 March 2019).

32. P. Baláž, M. Achimovičová, M. Baláž, P. Billik, Z. Cherkezova-Zheleva, J.M. Criado, F. Delogu, E. Dutkova, E. Gaffet, F.J. Gotor, R. Kumar, I. Mitov, T. Rojac, M. Senna, A. Streletskii, and K. Wieczorek-Ciurowa, *Chem. Soc. Rev.* **42** (2013) 7571–7637.

33. E. Gaffet, and G. Le Caër, in C. Bréchignac, P. Houdy and M. Lahmani (Ed.), *NanoMaterials and NanoChemistry,* Springer, Berlin, 2008.

34. https://www.fritsch-international.com/sample-preparation/milling/planetary-mills/details/product/pulverisette-7-premium-line/ (accessed 18 March 2019).

35. M. C. Etter, G. M. Frankenbach, and J. Bernstein, *Tetrahedron Lett.* **30** (1989) 3617–3620.

36. M. A. Mikhailenko, T. P. Shakhtshneider, and V. V. Boldyrev, *J. Mater. Sci*. **39** (2004) 5435–5439.

37. R. Trotzki, M. M. Hoffmann, and B. Ondruschka, *Green Chem.* **10** (2008) 767–772.

38. A. Bruckmann, A. Krebs, and C. Bolm, *Green Chem.* **10** (2008) 1131–1141.

39. V. Štrukil, M. D. Igrc, L. Fábián, M. Eckert-Maksic, S. L. Childs, D. G. Reid, M. J. Duer, I. Halasz, C. Mottillo, and T. Friščić, *Green Chem.* **14** (2012) 2462–2473.

40. J. Stojaković, B. S. Farris, and L. R. MacGillivray, *Chem. Commun.* **48** (2012) 7958–7960.

41. G.-W. Wang, *Chem. Soc. Rev.* **42** (2013) 7668–7700.

42. D. Braga, D. D'Addario, L. Maini, M. Polito, S. Giaffreda, K. Rubini, and F. Grepioni, in E. R. T. Tiekink and J. J. Vittal (Ed.), *Frontiers in Crystal Engineering*, John Wiley & Sons, Ltd, Chichester, 2006.

43. A. M. Belenguer, T. Friščić, G. M. Day, and J. K. M. *Chem. Sci.,* **2** (2011) 696–700.

44. A. Delori, T. Friščić, and W. Jones, *CrystEngComm* **14** (2012) 2350–2362.

45. C. F. Burmeister, and A. Kwade, *Chem. Soc. Rev.* **42** (2013) 7660–7667.

46. K. Ralphs, C. Hardacre, and S. L. James, *Chem. Soc. Rev.* **42** (2013), 7701–7718.

47. F. K. Urakaev, and V. V. Boldyrev, *Russ. J. Phys. Chem.* **79** (2005) 563–572.

48. V. K. Smolyakov, O. V. Lapshin, and V. V. Boldyrev, Int. J. Self-Propag. High-Temp. Synth. **17** (2008) 20–29.

49. S. M. Hick, C. Griebel, D. T. Restrepo, J. H. Truitt, E. J. Buker, C. Bylda, and R. G. Blair, *Green Chem.* **12** (2010) 468–474.

50. T. Kleine, J. Buendia, and C. Bolm, Green Chem. **15** (2013) 160–166.

51. V. Šepelák, A. Düvel, M. Wilkening, K.-D. Becker and P. Heitjans, *Chem. Soc. Rev.* **42** (2013), 7507–7520.

52. I.G. Konstanchuk, E.Y. Ivanov, and V.V. Boldyrev, *Russ. Chem. Rev.* **67** (1998) 69–79.

53. W. Jones, and M.D. Eddleston, *Faraday Discuss.* **170** (2014) 9–34.

54. S. E. Zhu, F. Li, and G. W. Wang, *Chem. Soc. Rev.* **42** (2013) 7535–7570.

55. C.S.B. Gomes, P.T. Gomes, and M.T. Duarte, *J. Organomet. Chem.* **760** (2014) 101.

56. K. M. Wiggins, J. N. Brantley, and C. W. Bielawski, *ACS Macro Lett.* **1** (2012) 623–626.

57. V. Štrukil, M. D. Igrc, M. Eckert-Maksić, and T. Friščić, *Chem. Eur. J.* **18** (2012) 8464–8473.

58. G.A. Bowmaker, *Chem. Commun.* **49** (2013) 334–348.

59. D. Braga, L. Maini, and F. Grepioni, *Chem. Soc. Rev.* **42** (2013) 7638–7648.

60. P.J. Beldon, L. Fabian, R.S. Stein, A. Thirumurugan, A.K. Cheetam, and T. Friščić, *Angew. Chem. Int. Ed.* **49** (2010) 9640–9643.

61. G. Rothenberg, A.P. Downie, C.L. Raston, and J.L. Scott, *J. Am. Chem. Soc.* **123** (2001) 8701–8708.

62. A.A.L. Michalchuk, I.A. Tumanov, and E.V. Boldyreva, *CrystEngComm* **15** (2013) 6403–6412.

63. K.S. McKissic, J.T. Caruso, R.G. Blair, and J. Mack, *Green Chem.* **16** (2014) 1628–1632.

64. J.J. Gilman, *Science* **274** (1996) 65.

65. I. Halasz, S.A.J. Kimber, P.J. Beldon, A.M. Belenguer, F. Adams, V. Honkimäki, R.C. Nightingale, R.E. Dinnebier, and T. Friščić, *Nat. Protoc.* **9** (2013) 1718–1729.

66. S. Lukin, T. Stolar, M. Tireli, M.V. Blanco, D. Babić, T. Friščić, K. Užarević, and I. Halasz, *Chem. Eur. J.* **23** (2017) 13941–13949.

67. A.D. Katsenis, A. Puškarić, V. Štrukil, C. Motillo, P.A. Julien, K. Užarević, M.-H. Pham, T.-O. Do, S.A.J. Kimber, P. Lazić, O. Magdysyuk, R.E. Dinnebier, I. Halasz, and T. Friščić, *Nature Commun.* **6** (2015) 6662.

68. V. Ban, Y. Sadikin, M. Lange, N.A. Tumanov, Y. Filinchuk, R. Černý, and N.P.M. Casati, *Anal. Chem.* **89** (2017) 13176–13181.

69. N. Tumanov, V. Ban, A. Poulain, and Y. Filinchuk, *J. Appl. Crystallogr.* **50** (2017) 994–999.

70. M. Paskevicius, L.H. Jepsen, P. Schouwink, R. Černý, D.B. Ravnsbæk, Y. Filinchuk, M. Dornheim, F. Besenbacher, and T.R. Jensen, *Chem. Soc. Rev.* **46** (2017) 1565–1634.

71. N.N. Maltseva, K.G. Myakishev, B.I. Saidov, N.S. Kedrova, N.I. Gorbacheva, V.V. Potapova, and V.V. Volkov, *Zh. Neorg. Khim.* **34** (1989) 1430.

72. J. Huot, D.B. Ravnsbæk, J. Zhang, F. Cuevas, M. Latroche, T.R. Jensen, *Prog Mater Sci* **58** (2013) 30–75.

73. A. Pichon, A. Lazuen-Garay, and S.L. James, *CrystEngComm* **8** (2006) 211–214.

74. T. Friščić, *Mechanochemical Approaches to Metal-Organic Frameworks,* John Wiley & Sons, Ltd., published online, 2014, page 12.

75. T. Friščić, in L. R. MacGillivray (Ed.), Towards mechanochemical synthesis of metalorganic frameworks (MOFs): from coordination polymers and lattice inclusion compounds to porous materials, John Wiley & Sons, Inc., Iova, 2010, page 267.

76. P. Schouwink, M.B. Ley, A. Tissot, H. Hagemann, T.R. Jensen, Ĺ. Smrčok, and R. Černý, *Nat. Commun.* **5** (2014) 5706.

77. A.V. Skripov, A.V. Soloninin, O.A. Babanova, H. Hagemann, and Y. Filinchuk, *J. Phys. Chem. C* **114** (2010) 12370–12374.

78. M.B. Ley, D.B. Ravnsbak, Y. Filinchuk, Y.-S. Lee, R. Janot, Y.W. Cho, J. Skibsted, and T.R. Jensen, *Chem. Mater.* **24** (2012) 1654–1663.

79. M.B. Ley, L.H. Jepsen, Y.-S. Lee, Y.W. Cho, J.M. Bellosta von Colbe, M. Dornheim, M. Rokni, J.O. Jensen, M. Sloth, Y. Filinchuk, J.E. Jorgensen, F. Besenbacher, and T.R. Jensen, *Mater. Today* **17** (2014) 122–128.

80. L.H. Jepsen, M.B. Ley, Y.-S. Lee, Y.W. Cho, M. Dornheim, J.O. Jensen, Y. Filinchuk, J.E. Jorgensen, F. Besenbacher, and T.R. Jensen, *Mater. Today* **17** (2014) 129–135.

81. A. Unemoto, M. Matsuo, and S.-I. Orimo, *Adv. Funct. Mater.* **24** (2014) 2267–2279.

82. A. Züttel, A. Borgschulte, and S.-I. Oriomo, *Scr. Mater.* **56** (2007) 823–828.

83. L. George, and S.K. Saxena, *Int. J. Hydrogen Energy* **35** (2010) 5454–5470.

84. U. Bösenberg, S. Doppiu, L. Mosegaard, G. Barkhordarian, N. Eigen, A. Borgschulte, T.R. Jensen, Y. Cerenius, O. Gutfleisch, T. Klassen, M. Dornheim, and R. Bormann, *Acta Mater.* **55** (2007) 3951–3958.

85. H. Hagemann, and R. Černý, *Dalton Trans.* **39** (2010) 6006–6012.

86. C. Frommen, N. Aliouane, S. Daledda, J.E. Fonnelop, H. Grove, K. Lieutenant, I. Llamas-Jansa, S. Sartori, M.H. Sorby, and B.C. Hauback, *J. Alloys Compd.* **496** (2010) 710–716.

87. H.I. Schlesinger, H.C. Brown, and A.E. Finholt, *J. Am. Chem. Soc.* **75** (1953) 205–209.

88. Y. Wu, M.T. Kelly, J.V. Ortega, Review of Chemical Processes for the Synthesis of Sodium Borohydride, Millenium Cell Inc. 2004.

89. J.-Ph. Soulié, G. Renaudin, R. Černý, and K. Yvon, *J. Alloys Compd.* **346** (2002) 200–205.

90. O.A. Babanova, A.V. Soloninin, A.P. Stepanov, A.V. Skripov, and Y. Filinchuk, *J. Phys. Chem. C* **114** (2010) 3712–3718.

91. Y. Filinchuk, D. Chernyshov, and V. Dmitriev, in U.B. Demirci, and P. Miele, *Crystal chemistry of light metal borohydrides*, Nova Science Publishers, New York, 2010, Chapter 6.

92. D.T. Hurd, *Preparation of Boron Compounds*, US Patent 2469879, 1949.

93. L. Johnston, and N.C. Hallett, *J. Am. Chem. Soc.* **75** (1953) 1467–1468.

94. W.H. Stockmayer, and C.C. Stephenson, *J. Chem. Phys.* **21** (1953) 1311–1312.

95. Y. Filinchuk, and H. Hagemann, *Eur. J. Inorg. Chem.* (2008) 3127–3133.

96. Y. Filinchuk, R. Černý, and H. Hagemann, *Chem. Mater.* **21** (2009) 925–933.

97. J.H. Her, P.W. Stephens, Y. Gao, G.L. Soloveichik, J. Rijssenbeek, M. Andrus, and J.C. Zhao, *Acta Crystallogr. Sect. B: Struct. Sci.* **63** (2007) 561–568.

98. R. Černý, Y. Filinchuk, H. Hagemann, and K. Yvon, *Angew. Chem., Int. Ed.* **46** (2007) 5765–5767.

99. M.P. Pitt, C.J. Webb, M. Paskevicius, D. Sheptyakov, C.E. Buckley, and E.M. Gray, *J. Phys. Chem. C* **115** (2011) 22669–22679.

100. M. Paskevicius, M.P. Pitt, C.J. Webb, D.A. Sheppard, U. Filso, E.M. Gray, and C.E. Buckley, *J. Phys. Chem. C* **116** (2012) 15231–15240.

101. W.I.F. David, S.K. Callear, M.O. Jones, P.C. Aeberhard, S.D. Culligan, A.H. Pohl, S.R. Johnson, K.R. Ryan, J.E. Parker, P.P. Edwards, C.J. Nuttall, and A. Amieiro-Fonseca, *Phys. Chem. Chem. Phys*. **14** (2012) 11800–11807.

102. A. Amieiro-Fonseca, S.R. Ellis, C.J. Nuttall, B.E. Hayden, S. Guerin, G. Purdy, J.P. Soulie, S.K. Callear, S.D. Culligan, W.I.F. David, P.P. Edwards, M.O. Jones, S.R. Johnson, and A.H. Pohl, *Faraday Discuss*. **151** (2011) 369–384.

103. Y. Filinchuk, R. Černý, and H. Hagemann, *Chem. Mater.* **21** (2009) 925–933.

104. R. Černý, and P. Schouwink, Acta Crystallogr., Sect. B: Struct. Sci., *Cryst. Eng. Mater.* **71** (2015) 619–640.

105. B. Richter, D.B. Ravnsbaek, N. Tumanov, Y. Filinchuk, and T.R. Jensen, *Dalton Trans.* **44** (2015) 3988–3996.

106. R. Černý, N. Penin, H. Hagemann, and Y. Filinchuk, *J. Phys. Chem. C* **113** (2009) 9003–9007.

107. N.A. Tumanov, E. Roedern, Z. Łodziana, D.B. Nielsen, T.R. Jensen, A.V. Talyzin, R. Černý, D. Chernyshov, V. Dmitriev, T. Palasyuk, and Y. Filinchuk, *Chem. Mater*. **28** (2016) 274–283.

108. D.B. Ravnsbæk, L.H. Sørensen, Y. Filinchuk, F. Besenbacher, and T.R. Jensen, *Angew. Chem. Int. Ed.* **51** (2012) 3582–3586.

109. R. Černý, P. Schouwink, Y. Sadikin, K. Stare, Ĺ. Smrčok, B. Richter, and T.R. Jensen, Inorg. Chem. **52** (2013) 9941–9947.

110. F. Morelle, V. Ban, Y. Filinchuk, Towards hydridic nanoporous frameworks: the first imidazolate-borohydride compound Li_2ImBH_4 (Im = $[C_3H_3N_2]^-$). International symposium on metal-hydrogen systems (MH2014); Manchester, UK, July 20–25, 2014.

111. Y.-Q. Tian, H.-J. Xu, Y.-Z. Li, and X.-Z. You, *Z. Anorg. Allg. Chem.* **630** (2004) 1371–1373.

112. D.M. Schubert, M.Z. Visi, and C.B. Knobler, *Main Group Chem.* **7** (2008) 311–322.

113. J.A. Graden, L.M. Ellerby, J.A. Roe, and J.S. Valentine, *J. Am. Chem. Soc*. **116** (1994) 9743–9744.

114. N.T.T. Nguyen, T.N.H. Lo, J. Kim, H.T.D. Nguyen, T.B. Le, K.E. Cordova, and H. Furukawa, *Inorg. Chem.* **55** (2016) 6201–6207.

115. F. Morelle, Hybrid hydridic frameworks by the combination of complex hydrides and nitrogen-based organic ligands. Ph.D. Dissertation, Univerité catholique de Louvain, Louvain-la-Neuve, 2017.

116. D.A. Safin, K. Robeyns, and Y. Filinchuk, *Acta Crystallogr., Sect. A: Found. Adv.* **72** (2016) 402.

117. https://link.springer.com/chapter/10.1007/978-3-319-48933-9_17#Sec3 (accessed 23 March 2019).

118. V.K. Pecharsky, and P.Y. Zavalij, Fundamentals of powder diffraction and structural characterization of materials, Springer, New York, 2009.

119. M. Font-Bardia, and X. Alcobé, X-ray single crystal and powder diffraction: possibilities and applications, CCiTUB Handbook, Barcelona, 2010.

120. http://www.tulane.edu/~sanelson/eens211/x-ray.htm (accessed 23 March 2019).

121. Q.Q. Pan, P. Guo, J. Duan, Q. Cheng, and H. Li, *Chin Sci Bull* **57** (2012) 3867–3871.

122. https://www.psi.ch/sites/default/files/import/sls-techno-trans-ag/HomeEN/ScienceOmega3-ESS-August7th-2.pdf (accessed 24 March 2019).

123. A. Bergamaschi, A. Cervellino, R. Dinapoli, F. Gozzo, B. Henrich, I. Johnson, P. Kraft, A. Mozzanica, B. Schmitt, and X. Shi, *J. Synchrotron Rad.* **17** (2010) 653–668.

124. A. Meden, *Croat. Chem. Acta* **71** (1998) 615–633.

125. R. Černý, *Crystals* **7** (2017) 142–152.

126. A. Boultif, D. Louër, *J. Appl. Crystallogr.* **37** (2004) 724–731.

127. A. Altomare, C. Giacovazzo, A. Guagliardi, A.G.G. Moliterni, R. Rizzi, and P.-E. Werner, *J. Appl. Crystallogr.* **33** (2000) 1180–1186.

128. A. Le Bail, *Powder Diffraction* **19** (2004) 249–254.

129. V. Favre-Nicolin, and R. Černý*, J. Appl. Crystallogr.* **35** (2002) 734–743.

130. R. Černý, V. Favre-Nicolin, J. Rohlĺcek, M. Hušak, Z. Matej, and R. Kužel, *CPD Newsl.* **35** (2007) 16–19.

131. A. Altomare, M.C. Burla, M. Camalli, B. Carrozzini, G.L. Cascarano, C. Giacovazzo, A. Guagliardi, A.G.G. Moliterni, G. Polidori, and R. Rizzi, *J. Appl. Crystallogr.* **32** (1999) 339–340.

132. R. W. Cheary, and A.A. Coelho, *J. Appl. Crystallogr.* **25** (1992) 109–121.

133. M.A. Neumann, *J. Appl. Crystallogr.* **36** (2003) 356–365.

134. W.I.F. David, and K. Shankland, *Acta Cryst.* **A64** (2008) 52–64.

135. A. LeBail, H. Duray, and J. L. Fourquet, *Mat. Res. Bull.* **23** (1988) 447–452.

136. G. S. Pawley, *J. Appl. Crystallogr.* **14** (1981) 357–361.

137. D. S. Sivia and W. I. F. David, *Acta Cryst.* **A50** (1994) 703–714.

138. R. Černý, and V. Favre-Nicolin, *Z. Kristallogr.* **222** (2007) 105–113.

139. R. A. Young (Ed.), *The Rietveld Method,* University Press, Oxford, 1993.

140. N. Döbelin, XRD and Rietveld Refinement, RMS Foundation, Lyon, 2015.

141. B.E. Warren, and B.L. Averbach, *J. Appl. Phys.* **21** (1950) 595–599.

142. D. Taupin, *J. Appl. Crystallogr.* **6** (1973) 266–273.

143. D. Balzar, in R.L. Synder, H.K. Bunge, and J. Fiala (Ed.), *Voigt-function model in diffraction line-broadening anlysis*, IuCr, Riverside, 1999.

144. W. Su, Y.-P. Zhou, L.-F. Wei, Y.Sun, and L. Zhou, *New Carbon Mater.* **22** (2007) 135–140.

145. G. Mali, in F. Zafar, and E. Sharmin, Looking into Metal-Organic Frameworks with Solid-State NMR Spectroscopy, IntechOpen, 2016.

146. M. Feike, D.E. Demco, R. Graf, J. Gottwald, S. Hafner, and H.W. Spiess, *J Magn Resonance, Ser A.* **122** (1996) 214–221.

147. https://www.fritsch-international.com/sample-preparation/milling/planetary-mills/details/product/pulverisette-7-premium-line/ (accessed 28 March 2019).

148. https://dqmp.unige.ch/cerny/glove-boxes/ (accessed 28 March 2019).

149. https://www.google.com/search?q=schlenk+line+setup&tbm=isch&source=iu&ictx=1&fir=2yn6 C-XiTVyInM%253A%252CKjOTfBqe0KhyeM%252C_&vet=1&usg=AI4_-kQI3toL-jndFiLhwCIGewyTw9IiMA&sa=X&ved=2ahUKEwi3sOvwhebhAhUO0qYKHcKpAL8Q9QEw AHoECAsQBg#imgrc=2yn6C-XiTVyInM:&vet=1 (accessed 28 March 2019).

150. https://dqmp.unige.ch/cerny/powder-diffraction/ (accessed 28 March 2019).

151. https://dqmp.unige.ch/cerny/single-crystal-diffraction/ (accessed 29 March 2019).

152. V. Dyadkin, Ph. Pattison, V. Dmitriev, D. Chernyshov, *J. Synchrotron Radiat.* **23** (2016) 825–829.

153. N. E. Brese and M. O'Keeffe, *Acta Crystallogr., Sect. B: Struct. Sci.* **B47** (1991) 192−197.

154. J. Rodriguez-Carvajal, *Phys. B* **192** (1993) 55−69.

155. V. A. Blatov, *Struct. Chem.* **23** (2012) 955−963.

156. K. Momma and F. Izumi, *J. Appl. Crystallogr.* **44** (2011) 1272−1276.

157. R. Černý, K. C. Kim, N. Penin, V. D'Anna, H. Hagemann, and D. S. Sholl, *J. Phys. Chem. C* **114** (2010) 19127–19133.

§ 8.   APPENDICES

❖
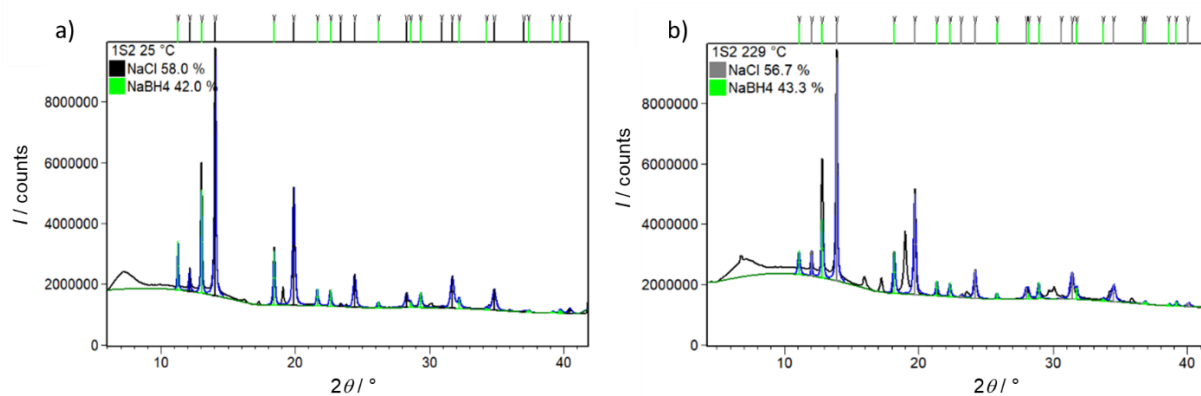
Figure AI. Rietveld refinement on sample 1S2 at temperatures **a)** 25 °C and **b)** 229 °C. ($\lambda = 0.69449$ Å). Experimental diffraction data are shown in black, while calculated patterns are given in blue. Diffraction lines position of NaCl are represented by gray vertical marks, while the positions of NaBH$_4$ are given by green marks.

Table AI. Temperature-induced changes in the phase composition for sample 1S2

Sample	Temperature / °C	Crystalline products composition as determined by the Rietveld refinement
1S2	25	NaCl (58 wt. %) and NaBH$_4$ (42 wt. %) and few small unknown peaks
	229	NaCl (56.7 wt. %) and NaBH$_4$ (43.3wt. %), unidentified phase

❖
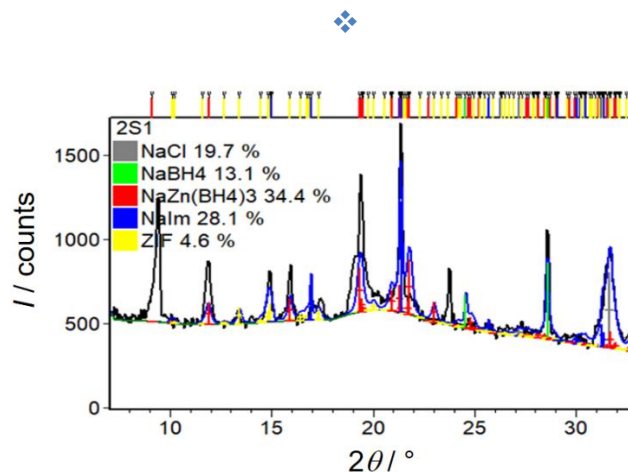
Figure AII. Rietveld refinement on sample 2S1 obtained by the reaction involving $NaBH_4$, $ZnCl_2$ and NaIm in molar ratio 1:1:1 with THF as solvent. Experimental diffraction data are shown in black, while calculated patterns are given in blue. Diffraction lines position of $NaBH_4$ are represented by green vertical marks, NaCl by grey, NaIm by blue, ZIF(IMIDZB01) by yellow while the diffraction lines in case of $NaZn(BH_4)_3$ are colored in red.

Table AII. Quantitative composition of crystalline products in sample 2S1.

Sample	$NaBH_4$:$ZnCl_2$: NaIm ratio	Solvent	Crystalline product composition as determined by the Rietveld refinement
2S1	1:1:1	THF	NaCl (19.7 wt. %), $NaBH_4$ (13.1 wt. %), $NaZn(BH_4)_3$ (34.4 % wt. %), NaIm (28.1 wt. %), ZIF(IMIDZB01)(4.6 wt. %) and few unidentified diffraction lines are present.
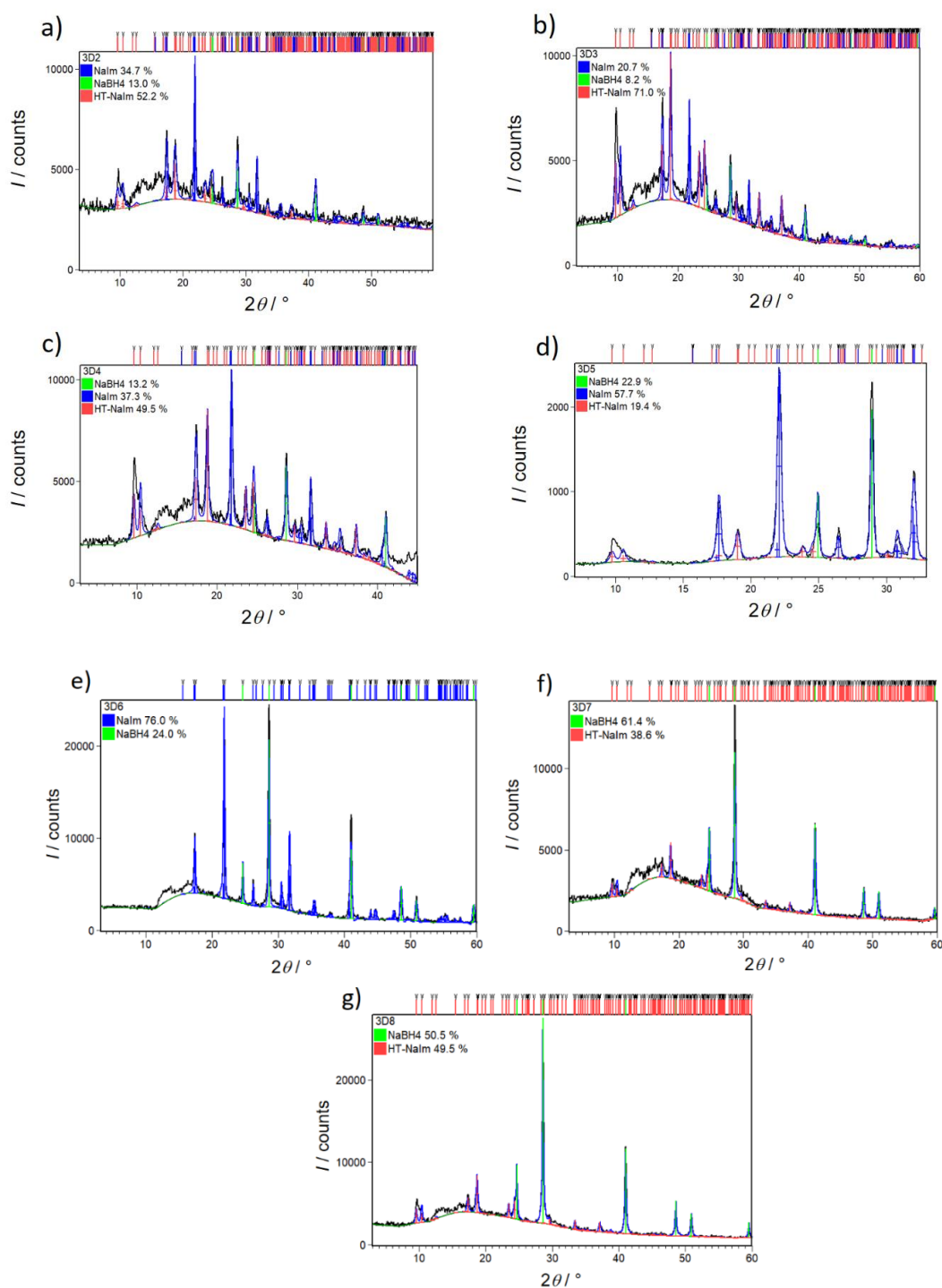
Figure AIII. Rietveld refinement of samples 3D2–3D8 obtained by the dry mechanochemical reactions of $NaBH_4$ precursor and NaIm in different molar ratios: **a)** 1:6, **b)** 1:4, **c)** 1:2, **d)** 1:1, **e)** 2:1, **f)** 4:1 and **g)** 6:1. Experimental diffraction data are shown in black, while calculated patterns are given in blue. Diffraction lines position of $NaBH_4$ are represented by green vertical marks, NaIm by deep blue and HT-NaIm by red.

Table AIII. Quantitative composition of crystalline products in samples 3D2–3D8, milled for 2h.

Sample	NaBH$_4$: NaIm ratio	NaIm wt. %	NaBH$_4$ wt. %	HT-NaIm wt. %
3D2	1:6	34.7	13	52.2
3D3	1:4	20.7	8.2	71
3D4	1:2	37.3	13.2	49.5
3D5	1:1	57.7	22.9	19.4
3D6	2:1	76	24	/
3D7	4:1	/	61.4	38.6
3D8	6:1	/	50.5	49.5
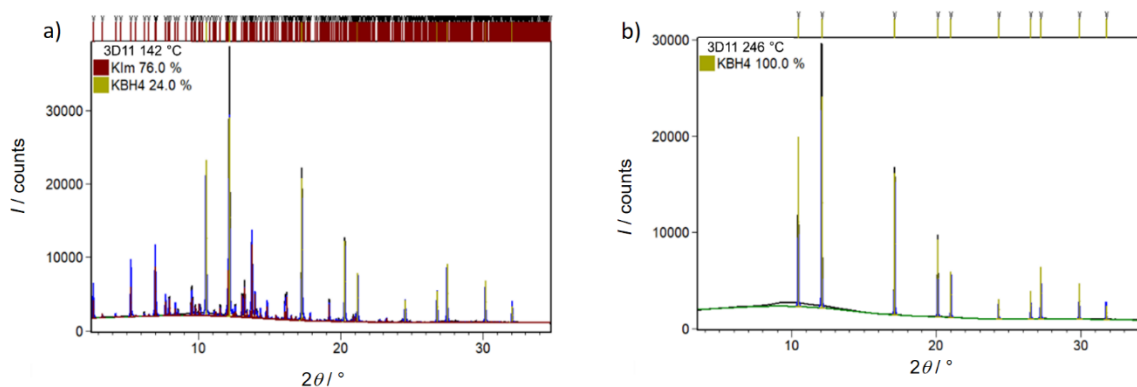
Figure AIV. Rietveld refinement on sample 3D11 at temperatures **a)** 142 °C and **b)** 246 °C. (λ = 0.7225 Å). Experimental diffraction data are shown in black, while calculated patterns are given in blue. Diffraction lines position of KIm are represented by purple vertical marks, while the vertical marks in the case of KBH_4 are colored in khaki.

Table AIV. Temperature-induced changes in the phase composition for sample 3D11.

Sample	Temperature / °C	Crystalline products composition as determined by the Rietveld refinement
3D11	142	KIm (76 wt. %) and KBH_4 (24 wt. %)
	246	KBH_4 (100 wt. %)

❖

Figure AV. Rietveld refinement on sample 6D1 at temperatures **a)** 25 °C and **b)** 220 °C. Experimental diffraction data are shown in black, while calculated patterns are given in blue. Diffraction lines position of $NaBH_4$ are represented by green vertical marks, $Mn(BH_4)_2$ by silver, HT-NaIm by gold while the vertical marks in the case of NaIm are colored by deep blue.

Table AV. Temperature-induced changes in the phase composition for sample 6D1.

Sample	Temperature / °C	Crystalline products composition as determined by the Rietveld refinement
6D1	25	amorphous phase, $NaBH_4$ (44.4 wt. %), $Mn(BH_4)_2$ (55.6 wt. %),
	220	$NaBH_4$ (9 wt. %), NaIm (49.3 wt. %), NaIm (41.4 wt. %) and unidentified phase(s)

Figure AVI. Rietveld refinement on sample 6D3 at temperatures **a)** 25 °C and **b)** 175 °C. Experimental diffraction data are shown in black, while calculated patterns are given in blue. Diffraction lines position of KBH_4 are represented by khaki vertical marks.

Table AVI. Temperature-induced changes in the phase composition for sample 6D3.

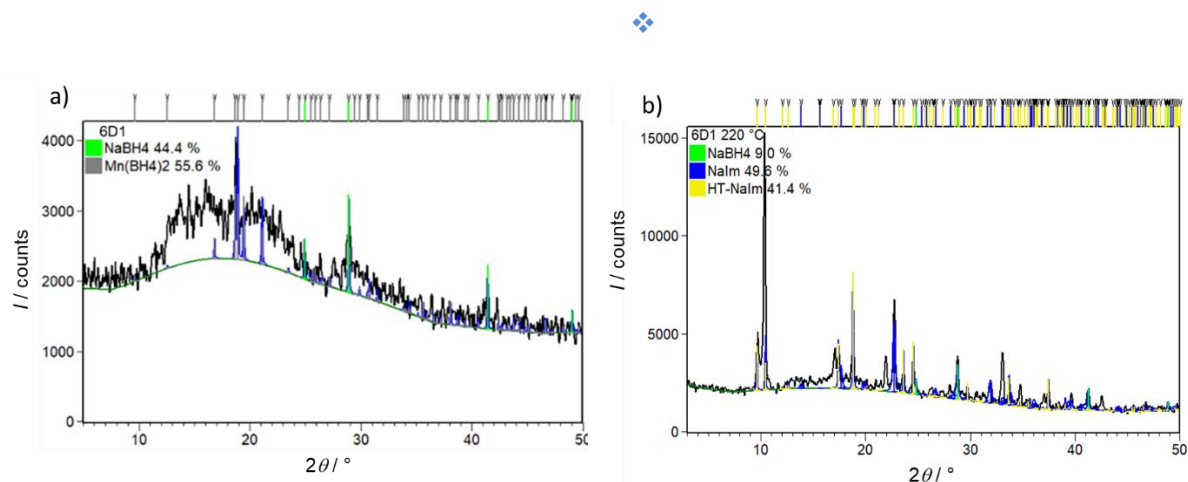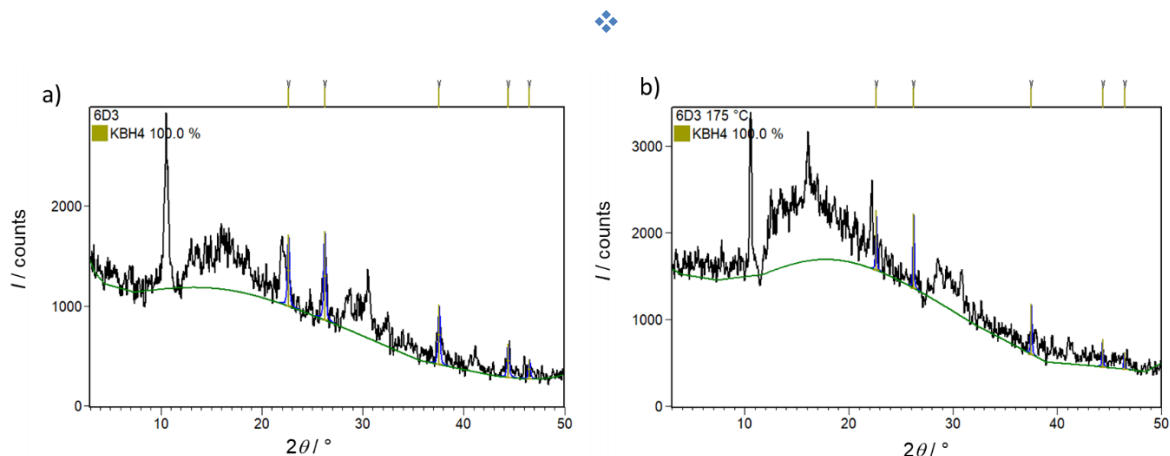| Sample	Temperature / °C	Crystalline products composition as determined by the Rietveld refinement
6D3	25	KBH_4 (100 wt. %), unidentified phase(s) and amorphous part
	175	KBH_4 (100 wt. %), unidentified phase(s) and amorphous part

❖
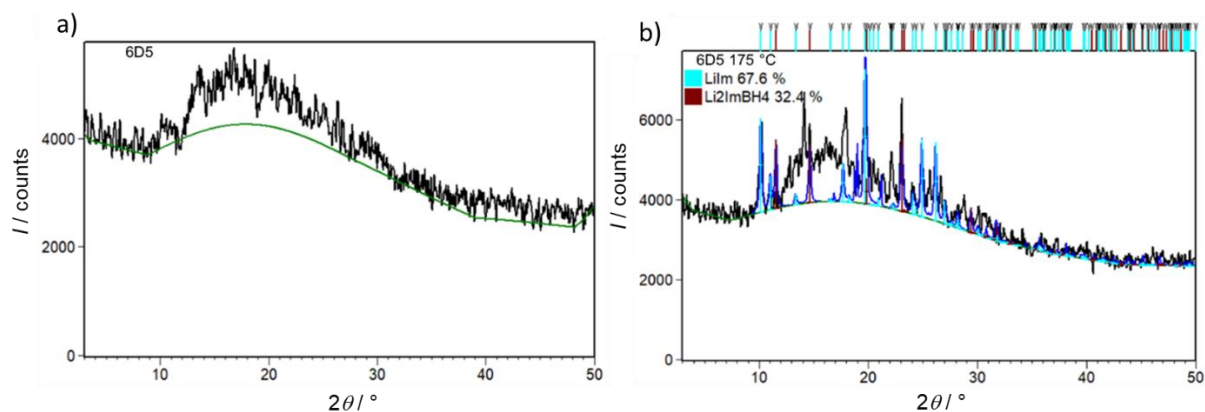
Figure AVII. Rietveld refinement on sample 6D5 at temperatures a) 25 ° C and b) 175 ° C. Experimental diffraction data are shown in black, while calculated patterns are given in blue. Diffraction lines position of LiIm are represented by aqua vertical marks, while the vertical marks in the case of Li_2ImBH_4 are colored maroon.

Table AVII. Temperature-induced changes in the phase composition for sample 6D5.

Sample	Temperature / °C	Crystalline products composition as determined by the Rietveld refinement
6D5	25	amorphous hump
	175	LiIm (67.6 wt. %), Li_2ImBH_4 (32.4 wt. %), unidentified phase(s), amorphous part

§ 9.   CURRICULUM VITAE

Personal information

Name : Sanja Burazer (born Brkić)

Address : Severinska 17, 10000 Zagreb, Croatia

Telephone : +385958484234

E-mail : Sanja.Burazer@irb.hr

Date of Birth : 28/11/1990

Nationality: Croatian

Work experience

01/2015–present	**PhD Student**, Laboratory for Synthesis and Crystallography of Functional Materials, Division for Materials Physics, Ruđer Bošković Institute, Zagreb (Croatia).
03/2014–07/2014	Technologist in the production and analyst of mechanical and thermal properties of materials, Dukat d.d., Lactalis Group, Production of Plastic Packaging;

Education

11/ 2014–present	**PhD Study** in Inorganic and Structural Chemistry, Faculty of Science, Department of Chemistry, Zagreb (Croatia).
2012–2014	**Master in Material Science and Engineering**, Faculty of Chemical Engineering and Technology, Zagreb (Croatia); Graduation thesis: *Lead dioxide and its composites as active cathode materials in electrochemical supercapacitor*; Prof. Zoran Mandić, PhD; 11 July 2014.
2009–2012	**univ.bacc.ing.cheming**, **Materials Science and Engineering**, Faculty of Chemical Engineering and Technology, Zagreb (Croatia); Graduation thesis: *Determination of pseudocapacitive properties of electrochemically deposited NiOOH*; Prof. Zoran Mandić, PhD; 17 July 2012.

Research visits at international instition

02–04/2017	Laboratory of Crystallography, Department of Quantum Matter Physics, University of Geneva, Switzerland;
12/2016	Department of Physics, University of Hong Kong, Hong Kong;
11/2016	Department of Physics, South University Shenzhen, PR China;
11/2016	The Swiss-Norwegian Beamlines, The European Synchrotron Radiation Facility, Grenoble, France;
11/2016	Faculty of Chemistry and Chemical Technology, University of Ljubljana

05/2016	Faculty of Chemistry and Chemical Technology, University of Ljubljana
02/2016	Faculty of Chemistry and Chemical Technology, University of Ljubljana
11/2015	The Swiss-Norwegian Beamlines, The European Synchrotron Radiation Facility, Grenoble, France
10/2015–11/2015	Faculty of Chemistry and Chemical Technology, University of Ljubljana
05/2015–06/2015	Faculty of Chemistry and Chemical Technology, University of Ljubljana
05/2015	National Institute of Chemistry, Ljubljana (Slovenia)

Training

08/2013–09/2013	Educational student practice, Faculty of Science, Zagreb (Croatia)
2013–2014	Teaching assistant in laboratory. Faculty of Chemical Engineering and Technology; Division of Electrochemistry; Zagreb (Croatia)
2011–2012	Teaching assistant in laboratory. Faculty of Chemical Engineering and Technology; Division of General and Inorganic Chemistry; Zagreb (Croatia)
08/2011–09/2011	Educational student practice. PLIVA, TAPI, Research and Development Department; Laboratory of Organic Chemistry; Zagreb.

Lectures and poster presentations at schools, conferences and workshops

09–12/04/2019	26th, Croatian Meeting of Chemists and Chemical Engineers, HSKIKI26 Šibenik (Croatia); **Lecture**: *Mechanochemical synthesis and crystal structure of new group of mixed-metal imidazolates $AMgIm_3$, A = Na, K.*
25/09–02/10/2016	3rd European Crystallography School, ECS3, Bol (Croatia); **Poster presentation:** *Metal-Hydride Organic Frameworks:synthesis and structure.*
21–25/09/2016	24th Croatian-Slovenian Crystallographic Meeting, Bol (Croatia); **Lecture**: *Mechanochemical pathway towards novel Metal-Hydride Organic Frameworks.*
28/08–01/09/2016	30th European Crystallographic Meeting, ECM30, Basel (Switzerland); **Poster presentation**: *Metal-Hydride Organic Frameworks (HOF)– new solids for gas adsorption and separation.*
27/09–03/10/2015	International School on Introduction in the Rietveld Structure Refinement, Sofia (Bulgaria); **Poster presentation:** *Tuning lithium ion battery performance: Effect of structure and microstructure on the capacity of the $CoMn_2O_4$ materials.*
23–28/08/2015	29th European Crystallographic Meeting, ECM28, Rovinj (Croatia);

	Poster presentation: *Facile route for preparation of nanocrystalline $ZnMn_2O_4$: effect of preparation conditions on structure and microstructure.*
10–15/05/2014	*Hot Topics in Contemporary Crystallography*, Šibenik (Croatia).
20/02/2014	*X Meeting of Young Chemical Engineers 2014*, Zagreb (Croatia);
	Poster presentation: *Electrodeposition and characterization of PbO_2 for hybrid supercapacitor application.*
17/06/2013	*3rd Workshop Polymers from the Perspective of Chemists and Mechanical Engineers*; Zagreb (Croatia);
	Lecture: *Polymer composite materials in surgery.*
16–21/09/2012	Attendance on *6th European Summer School on Electrochemical Engineering*; Zadar (Croatia).

Awards and grants

2016	The *"Annual Award by Director of Ruđer Bošković Institute"* for excellence in scientific research
09–10/2015	International Union for Crystallography (IUCr) grant for *International School on Introduction in the Rietveld structure refinement*, Sofia, Bulgaria.
20/10/2014	Award "*Vjera Marjanović-Krajovan*" for best Graduate student on Material Science and Engineering Division; medal for academic excellence by University of Zagreb, Končar d.d.-Institute for electronics and Faculty of Chemical Engineering and Technology, Zagreb (Croatia).
11/07/2014	mag.ing.cheming. *Magna cum laude* (With great honor); Faculty of Chemical Engineering and Technology; Zagreb (Croatia).
22/10/2012	"*Dean's Award for best Undergraduate student on Material Science and Engineering Division*"
	"Medal for academic excellence by Faculty of Chemical Engineering and Technology"; Faculty of Chemical Engineering and Technology; Zagreb (Croatia).
17/07/2012	univ.bacc.ing.cheming. *Magna cum laude* (With great honor); Faculty of Chemical Engineering and Technology; Zagreb (Croatia).

Scientific articles

[1] **S. Burazer,** F. Morelle, Y. Filinchuk, R. Černý and J. Popović, *Inorg. Chem.* **58** (2019) 6927–6933.

[2] Q. Sun, M. Bijelić, A. Djurišić, C. Suchomski, X. Liu, M. Xie, A.M.C. Ng, H. Kong Li, K. Shih, **S. Burazer,** et al., *Nanotechnology* **28 (**2017) 455401.

[3] I. Lončarić, J. Popović, V. Despoja, **S. Burazer,** I. Grgičević, D. Popović and Ž. Skoko, *Cryst. Growth Des.* **17** (2017) 4445–4453.

[4] M. Valant, J. Popović, M. Vrčon Mihelj, **S. Burazer,** A. Altomare, and A. Moliterni, *ACS Sustain. Chem. Eng.* **5** (2017) 5562–5568.

[5] **S. Burazer,** S. Sopčić and Z. Mandić, *J Solid State Electrochem* **20** (2016) 3053–3059.

Associate on international projects

01/01/2016–31/12/2017	German-Croatian bilateral project: *New generation of actuators based on thermosalient effect.*
01/01/2016–31/12/2017	Chinese-Croatian bilateral project: *High performance batteries via utilization of spinel anode materials.*
01/04/2014–01/04/2017	SCOPES project (Swiss National Science Fondation): *Metal-Hydride Organic Frameworks (HOF)–new solids for gas adsorption and separation.*
01/01/2014–31/12/2015	Slovenian-Croatian bilateral project: *Nonconventional multiferroics.*

Organization of international conferences and schools

2015/2016	3rd European Crystallography School, Bol (Croatia), 2016; Member of organizing committee, Community manager.
2015	29th European Crystallography Meeting, Rovinj (Croatia), 2015; Participation in organization

Popularisation of science and research

2015, 2016	RBI, Open doors on RBI; Guide for visitors.
01/2019-	RBI, Representative in the Assistant Council

Membership in scientific societies

2016–	Croatian Crystallographic Association